



HAL
open science

Cosmic-ray flux and propagation in magnetised atomic clouds

François R. Kamal Youssef

► **To cite this version:**

François R. Kamal Youssef. Cosmic-ray flux and propagation in magnetised atomic clouds. Astrophysics [astro-ph]. Université Paris Cité, 2023. English. NNT : 2023UNIP7176 . tel-04633148

HAL Id: tel-04633148

<https://theses.hal.science/tel-04633148>

Submitted on 3 Jul 2024

HAL is a multi-disciplinary open access archive for the deposit and dissemination of scientific research documents, whether they are published or not. The documents may come from teaching and research institutions in France or abroad, or from public or private research centers.

L'archive ouverte pluridisciplinaire **HAL**, est destinée au dépôt et à la diffusion de documents scientifiques de niveau recherche, publiés ou non, émanant des établissements d'enseignement et de recherche français ou étrangers, des laboratoires publics ou privés.

THÈSE DE DOCTORAT DE PHYSIQUE DE L'UNIVERS

présentée pour obtenir le grade de
DOCTEUR d'Université Paris Cité

par
FRANÇOIS R. KAMAL YOUSSEF

Cosmic-ray flux and propagation in magnetised atomic clouds

Thèse dirigée par ISABELLE A. GRENIER

Présentée et soutenue publiquement le 15 décembre 2023

Devant un jury composé de :

Pr.Fabien CASSE, Professeur des universités, *Université Paris-Cité*, APC PRÉSIDENT DU JURY
Pr.Isabelle GRENIER, Professeure des universités, *Université Paris-Cité*, CEA-AIM DIRECTRICE DE THÈSE
Pr.Pierre JEAN, Professeur des universités, *Université Toulouse III Paul Sabatier*, IRAP RAPPORTEUR
Dr.Alexandre MARCOWITH, Directeur de recherche CNRS, *LUPM* RAPPORTEUR
Dr.Luigi TIBALDO, Astronome adjoint, *Université Toulouse III Paul Sabatier*, IRAP EXAMINATEUR
Pr.Julia TJUS, University professor, *Ruhr University - Bochum*, RAPP EXAMINATRICE

THÈSE DE DOCTORAT DE PHYSIQUE DE L'UNIVERS
Spécialité Astronomie et Astrophysique

présentée pour obtenir le grade de

DOCTEUR d'Université Paris Cité

par

FRANÇOIS R. KAMAL YOUSSEF

**Cosmic-ray flux and propagation
in magnetised atomic clouds**

Thèse dirigée par ISABELLE A. GRENIER

Présentée et soutenue publiquement le 15 décembre 2023

Devant un jury composé de :

Pr.Fabien CASSE, Professeur des universités, *Université Paris-Cité*, APC PRÉSIDENT DU JURY
Pr.Isabelle GRENIER, Professeure des universités, *Université Paris-Cité*, CEA-AIM DIRECTRICE DE THÈSE
Pr.Pierre JEAN, Professeur des universités, *Université Toulouse III Paul Sabatier*, IRAP RAPPORTEUR
Dr.Alexandre MARCOWITH, Directeur de recherche CNRS, *LUPM* RAPPORTEUR
Dr.Luigi TIBALDO, Astronome adjoint, *Université Toulouse III Paul Sabatier*, IRAP EXAMINATEUR
Pr.Julia TJUS, University professor, *Ruhr University - Bochum*, RAPP EXAMINATRICE

" TU DECIDERAS UNE CHOSE, ET ELLE TE RÉUSSIRA,
ET LA LUMIÈRE RESPLENDIRA SUR TES VOIES "
– JOB 22:28

Abstract

Context. Cosmic rays have aroused the interest of many scientists since their discovery in 1912 during Victor Hess's balloon flight. Since then, several theories and models have been developed to understand their propagation and their interactions with the interstellar medium of the Galaxy. Observations with *Fermi*-LAT of the γ rays produced by hadronic interactions between cosmic rays and gas have been used to probe the spectrum of particles from a few GeV to several TeV across the Galaxy. Given the 10-15% uncertainty inherent in 21-cm observations regarding the gas mass traversed by cosmic rays, the γ -ray measurements made in several nearby clouds show a fairly uniform cosmic-ray flux within about 1 kpc of the Sun. This local uniformity has recently been challenged by the observation of a nearby cirrus cloud called Eridu, located in the vicinity of the Orion-Eridanus superbubble, where an unexplained 30-50% deficit in cosmic-ray flux has been measured.

Aims. We have examined how the cosmic-ray spectrum deduced from the γ -ray emissivities in local clouds, notably in the Eridu cloud, compares with direct cosmic-ray observations near the Solar System. We have then studied whether the magnetic configuration of the Eridu cloud, which is largely ordered and directed towards the southern Galactic halo, could favour the escape of cosmic rays from the cloud. To do this, we have studied the cosmic-ray flux in another similar cloud in the constellation Reticulum. This cloud shares many characteristics with Eridu in terms of distance, geometry, orientation, gas state, and magnetic configuration.

Methods. Using the most recent spectra of cosmic nuclei and leptons inferred from direct measurements outside the heliosphere, as well as recent cross sections for hadronic interactions, we have calculated the γ -ray emissivity per gas nucleon that is expected near the Sun and we have compared it with more distant measurements made in nearby clouds. In order to measure the emissivity per gas nucleon in the Reticulum cloud, we have used 14 years of data from the *Fermi*-LAT satellite, in the energy range from 0.16 to 63 GeV. We have estimated the gas column densities in the atomic and molecular phases of Reticulum and of the various clouds visible in this region of the sky in order to model the observed interstellar γ -ray emission by combining their contributions.

Results. The expected emissivity per gas atom near the Sun depends significantly on the choice of hadronic cross section among the most recent parameterisations available. The difference exceeds thirty percent in γ rays near one GeV. The current uncertainty about these effective cross sections makes it impossible to know whether the cosmic-ray flux diffusing through Eridu is comparable to or less than that reaching the heliosphere. It also prevents us from knowing whether the average cosmic-ray spectrum measured within ~ 1 kpc around the Sun is greater than or comparable to that reaching the heliosphere.

In the Reticulum cloud, we have found a γ -ray emissivity spectrum per gas atom that is fully compatible with the local average spectrum and that is $57\% \pm 9\%$ larger than in the similar Eridu cloud. We have found no significant differences between the two clouds in the properties of the interstellar gas (density and compressibility of the gas, ratio between magnetic and thermal pressures, gas velocity dispersion, amplitude of the magnetic field (projected onto the sky) and dispersion in the orientation of field lines). We have found similar diffusion coefficients along the magnetic field in the cosmic-ray self-confinement scenario. These similarities between the Reticulum and Eridu clouds do not explain the loss of cosmic-ray flux in the latter. All these investigations were carried out on a scale of about 1 pc and not on the much smaller scale of the particle gyroradius, which is inaccessible to observations. Even

if the loss of cosmic rays in the Eridu cloud remains unexplained, the comparison of these two clouds will provide important constraints for studying how magnetohydrodynamic turbulence and its damping by ion-neutral interactions, together with the tangling of magnetic field lines by turbulent gas motions, regulate the scattering of cosmic rays in the atomic phase of clouds, which forms the main phase of the interstellar medium.

Key words : Gamma rays - Cosmic rays - Intertellar medium – Dust - Magnetic field – Propagation – Diffusion coefficient - Hadronic cross sections - Bremsstrahlung - Solar neighbourhood

Résumé

Contexte. Les rayons cosmiques ont suscité l'intérêt de nombreux scientifiques depuis leur découverte en 1912 lors du vol de Victor Hess en ballon. Depuis ce jour, plusieurs théories et modèles ont été élaborés pour comprendre leur propagation et leurs interactions avec le milieu interstellaire de la Galaxie. Les observations avec *Fermi-LAT* des rayons γ produits par les interactions hadroniques entre les rayons cosmiques et le gaz ont été utilisées pour sonder le spectre des particules de quelques GeV à plusieurs TeV à travers la Galaxie. Compte tenu de l'incertitude de 10 à 15% inhérente aux observations Hi à 21 cm sur la masse du gaz traversée par les rayons cosmiques, les mesures γ effectuées dans plusieurs nuages proches montrent un flux de rayons cosmiques assez uniforme à moins d'environ 1 kpc du Soleil. Cette uniformité locale a récemment été remise en question par l'observation d'un cirrus proche nommé Eridu, situé à proximité de la superbulle d'Orion-Eridanus, où un déficit inexpliqué de 30 à 50% du flux de rayons cosmiques a été mesuré.

Objectifs. Nous avons examiné comment le spectre des rayons cosmiques déduit des émissivités γ dans les nuages locaux, notamment dans le nuage Eridu, se comparait aux observations directes des rayons cosmiques près du Système Solaire. Nous avons ensuite étudié si la configuration magnétique du nuage Eridu, largement ordonnée et pointant vers le halo sud de la Galaxie, pouvait favoriser l'évasion des rayons cosmiques hors du nuage. Pour cela nous avons étudié le flux de rayons cosmiques dans un autre nuage similaire dans la constellation de Réticulum. Celui-ci présente de nombreuses caractéristiques communes avec Eridu en distance, géométrie, orientation, état du gaz et configuration magnétique.

Méthodologie. En utilisant les spectres les plus récents de noyaux et de leptons cosmiques déduits des mesures directes hors de l'héliosphère, ainsi que des sections efficaces récentes pour les interactions hadroniques, nous avons calculé l'émissivité γ par nucléon de gaz que l'on pourrait attendre près du Soleil et nous l'avons comparée aux mesures plus lointaines effectuées dans les nuages proches. Pour mesurer l'émissivité γ par nucléon de gaz dans le nuage Réticulum, nous avons utilisé 14 ans de données du satellite *Fermi-LAT*, dans la gamme d'énergie de 0,16 à 63 GeV. Nous avons estimé les densités de colonne de gaz dans les phases atomique et moléculaire de Reticulum et des différents nuages visibles dans cette région du ciel pour modéliser l'émission γ interstellaire observée en combinant leurs contributions.

Résultats. L'émissivité γ attendue par atome de gaz près du Soleil dépend de manière importante du choix de section efficace hadronique parmi les paramétrisations les plus récentes disponibles. La différence dépasse trente pour cent dans les rayons γ proches d'un GeV. L'incertitude actuelle sur ces sections efficaces empêche de savoir si le flux de rayons cosmiques qui diffusent dans Eridu est comparable ou inférieur à celui qui atteint l'héliosphère. Elle empêche également de savoir si le spectre moyen de rayons cosmiques mesuré sur ~ 1 kpc autour du Soleil est supérieur ou comparable à celui qui atteint l'héliosphère.

Dans le nuage de Réticulum, nous avons trouvé un spectre d'émissivité γ par atome de gaz entièrement compatible avec le spectre moyen local et plus élevé de $57\% \pm 9\%$ que dans le nuage similaire d'Eridu. Nous n'avons trouvé aucune différence notable entre les deux nuages en ce qui concerne les propriétés du gaz interstellaire (densité volumique et compressibilité du gaz, rapport entre les pressions magnétique et thermique, dispersion de vitesse du gaz, amplitude du champ magnétique (projeté sur le ciel) et dispersion dans l'orientation des lignes de champ). Nous avons trouvé des coefficients de diffusion similaires le long du champ magnétique dans le scénario d'auto-confinement des rayons cosmiques.

Ces ressemblances entre les nuages de Reticulum et Eridu ne permettent pas d'expliquer la perte de flux de rayons cosmiques dans ce dernier. Toutes ces investigations ont été menées à une échelle d'environ 1 pc et non à l'échelle beaucoup plus petite du rayon de giration des particules qui est inaccessible aux observations. Même si la perte de rayons cosmiques dans le nuage d'Eridu demeure inexplicée, la comparaison de ces deux nuages fournira des contraintes importantes pour étudier comment la turbulence magnétohydrodynamique et son amortissement par les interactions ions-neutres ainsi que l'emmêlement des lignes de champ magnétique par les mouvements turbulents du gaz régulent la diffusion des rayons cosmiques dans la phase atomique des nuages qui forme la phase principale du milieu interstellaire.

Version détaillée. Le milieu interstellaire contient 99% de gaz. Ce gaz est constitué à 90% d'hydrogène, se présentant sous trois phases distinctes : 23% en phase ionisée, 60% en phase atomique et 17% en phase moléculaire. A cause d'une instabilité thermique, le gaz de la phase atomique se divise en deux groupes stables. Le premier, appelé Warm Neutral Medium (WNM), est un gaz atomique chaud avec une densité moyenne d'environ 0.5 cm^{-3} , une température d'environ 10^4 K et une fraction d'ionisation d'environ 10^{-2} . Le second, appelé Cold Neutral Medium (CNM), est un gaz atomique froid avec une densité moyenne autour de 30 cm^{-3} , une température d'environ 10^2 K et une fraction d'ionisation d'environ 10^{-4} . La phase intermédiaire instable entre ces deux états stables est appelée souvent Lukewarm Neutral Medium (LNM). La phase atomique est observée dans le domaine radio par la raie H α à 21 cm, offrant une information sur la vitesse projetée le long de la ligne de visée grâce à l'effet Doppler. Cette information permet de séparer les différents nuages atomiques présents sur la ligne de visée. Cependant, l'auto-absorption pose un inconvénient, car plus il y a de gaz sur la ligne de visée, plus la raie est absorbée. Les données doivent être corrigées en utilisant la température de spin, variant de quelques dizaines de Kelvins pour un gaz optiquement épais (CNM) à une valeur aux alentours de 10^4 pour un nuage optiquement mince (WNM). Dans notre étude, nous avons utilisé les données radio du Galactic All-Sky Survey (GASS) avec une résolution angulaire de $16.2'$ et une résolution en vitesse de 0.82 km/s . En ce qui concerne la phase moléculaire, la molécule H $_2$ se forme à une densité supérieure à quelques centaines d'atomes par cm^{-3} . Sa température tombe en dessous d'une cinquantaine de Kelvins. Cette phase, appelée Dark Neutral Medium (DNM), est sombre car la molécule H $_2$ ne possède pas de dipôle électrique permanent pour produire un rayonnement induit par la rotation des molécules dans les zones froides. À des densités plus élevées, d'autres molécules se forment, notamment la molécule de ^{12}CO qui émet par rotation un rayonnement à 2.6 mm de longueur d'onde. Cependant, le facteur de conversion X_{CO} , permettant d'estimer la densité de colonne de H $_2$ à partir de l'intensité des raies CO, n'est pas très bien connu à ce jour.

Outre le gaz, le milieu interstellaire contient de la poussière, un champ magnétique et des rayons cosmiques qui se propagent. Les grains de poussière peuvent absorber et émettre des rayonnements, et en plus de cela, ils s'alignent perpendiculairement aux lignes du champ magnétique ambiant. L'orientation du champ magnétique dans le plan du ciel peut être mesurée grâce à la polarisation de l'émission thermique des grains de poussière. Pour étudier cette émission et le champ magnétique dans nos nuages, nous avons utilisé les données des satellites *Planck* et *IRAS*, avec une résolution de 5 arcmin .

Pendant la propagation des rayons cosmiques, ceux-ci interagissent avec le gaz des nuages interstellaires, produisant par des réactions hadroniques des pions neutres qui se désintègrent ensuite en photons γ . L'intensité de ces photons est observée à l'aide du Large Area Telescope situé à bord du satellite *Fermi* Gamma-ray Space Telescope, capable d'observer des photons γ d'énergie entre 20 MeV et 1 TeV . Il est capable d'obtenir une localisation précise des sources de rayons γ grâce à sa résolution de quelques

degrés à basse énergie et qui diminue jusqu'à 0.1° à haute énergie.

En analysant l'intensité γ produite par les rayons cosmiques dans un nuage et en estimant la masse du gaz dans le nuage, notamment dans la phase atomique du nuage où l'émission des raies H α permet d'estimer le nombre d'atomes présents de manière plus fiable que dans les autres phases, nous pouvons mesurer l'émissivité γ par atome de gaz. Celle-ci reflète le flux de rayons cosmiques dans le nuage. Des observations d'intensité γ dans les nuages situés à moins de 1 kpc du Système Solaire ont montré des émissivités γ assez uniformes, avec de faibles variations imputables aux incertitudes de mesure de la masse de gaz dans ces nuages. Une émissivité moyenne a été calculée et appelée "Emissivity of the Local Interstellar Spectrum" q_{LIS} .

Eridu est un filament de gaz atomique situé à proximité de la superbulle d'Orion-Eridanus à environ 300 parsecs du Soleil. Il a été découvert avec une émissivité γ inférieure de 30 à 40% par rapport à q_{LIS} , impliquant un net déficit de rayons cosmiques dans ce filament comparé aux autres nuages locaux. Étant donné que le nuage d'Eridu se trouve dans la même vallée interstellaire que le Soleil, nous avons cherché à comparer son émissivité γ à celle des environs immédiats du Soleil. Pour calculer celle-ci, nous avons utilisé les spectres de rayons cosmiques déduits des mesures directes effectuées à l'intérieur du Système Solaire et juste à l'extérieur de l'héliosphère. Ces spectres sont corrigés de l'effet de modulation solaire grâce au modèle HelMod de Boschini et al. pour les noyaux et aux travaux d'Orlando et al. pour les leptons. En ce qui concerne les sections efficaces d'interactions hadroniques, nous avons utilisé deux versions qui s'appuient sur les données et paramétrisations les plus récentes : les matrices obtenues par les simulations de FLUKA d'une part, et une combinaison des matrices QGSJET-II-04m avec les paramétrisations de Kamae et al. d'autre part. À partir de ces spectres et sections efficaces, nous avons calculé l'émissivité γ attendue par nucléon de gaz auprès du Soleil et nous l'avons comparée aux mesures plus lointaines effectuées en rayons γ dans des nuages situés à quelques centaines de parsecs du Soleil. Nous avons constaté que cette émissivité γ dépend de manière significative du choix de section efficace hadronique. La différence entre les sections efficaces dépasse trente pour cent pour les rayons γ proches d'un GeV. L'incertitude actuelle sur ces sections efficaces ne permet donc pas de déterminer si le flux de rayons cosmiques qui diffusent dans Eridu est comparable ou inférieur à celui qui atteint l'héliosphère, ni même de savoir si le spectre moyen de rayons cosmiques mesuré sur ~ 1 kpc autour du Soleil est supérieur ou comparable à celui qui atteint l'héliosphère.

Eridu est un filament de gaz atomique incliné par rapport au plan Galactique. Il présente un champ magnétique ordonné et globalement parallèle à l'axe du filament, donc fortement incliné par rapport au plan Galactique et presque perpendiculaire à la direction du champ magnétique moyen de la vallée locale. Pour examiner si une telle configuration magnétique est à l'origine du déficit de rayons cosmiques dans le nuage, nous avons décidé d'étudier un autre filament de gaz atomique, Reticulum, présentant les mêmes caractéristiques générales qu'Eridu. Reticulum est également incliné par rapport au plan Galactique, son champ magnétique est ordonné et parallèle à son axe, et il se trouve à une distance comparable du Soleil qu'Eridu.

Grâce aux informations en vitesse des raies H α et grâce aux différentes morphologies des nuages, nous avons pu séparer le filament Reticulum d'autres nuages visibles dans cette région de ciel. Nous avons isolé sept nuages atomiques (Reticulum, Hydre Nord, Hydre Sud, Hydre Lointain, Dorade Est, Dorade West, Horologium). En utilisant les données H α GASS, nous avons estimé la densité de colonne de gaz atomique dans chacun des nuages pour différents niveaux d'absorption. À l'aide de la carte de photons γ de *Fermi-LAT* et de celle des poussières vues par *Planck* et *IRAS*, nous avons estimé la quantité totale de gaz dans cette zone. En calculant le résidu entre le gaz total et le gaz atomique observé en H α , nous

avons obtenu une estimation de la densité de colonne de gaz moléculaire sombre. Nous avons trouvé du gaz sombre dans le nuage d'Hydre Nord et quelques grumeaux à l'intérieur du filament de Reticulum.

Pour mesurer l'émissivité γ par nucléon de gaz dans le nuage Réticulum, nous avons utilisé 14 ans de données du satellite *Fermi*-LAT, dans la gamme d'énergie de 0,16 à 63 GeV. Nous avons modélisé l'émission γ interstellaire observée par *Fermi*-LAT dans cette région en combinant les contributions de chaque nuage. Nous avons ainsi mesuré un spectre d'émissivité γ par atome de gaz dans le nuage de Reticulum qui se trouve être entièrement compatible avec la moyenne locale q_{LIS} et plus élevé de $57\% \pm 9\%$ que dans le nuage similaire d'Eridu.

Pour comprendre cette différence de flux de rayons cosmiques dans les deux filaments, nous avons étudié les propriétés de propagation des particules de quelques GeV dans les deux nuages. Nous nous sommes focalisés sur la comparaison de paramètres du gaz qui peuvent influencer la vitesse de diffusion des particules : la densité volumique du gaz, le rapport entre sa pression magnétique et thermique, le niveau de turbulence dans le champ de vitesse du gaz et dans l'orientation du champ magnétique, la compressibilité de la turbulence et l'amplitude du champ magnétique en projection sur le ciel. Nous n'avons trouvé aucune différence notable entre les deux nuages en ce qui concerne ces propriétés. Nous avons également utilisé ces propriétés pour calculer le coefficient de diffusion des particules le long du champ magnétique dans le scénario d'auto-confinement par excitation d'ondes d'Alfvén. Nous avons trouvé des coefficients similaires dans les deux nuages et des valeurs proches de la moyenne Galactique déduites d'autres informations.

Cette forte ressemblance entre les nuages de Reticulum et d'Eridu à l'échelle du parsec où nous avons pu comparer leurs propriétés ne permet pas d'expliquer la perte de flux de rayons cosmiques dans ce dernier. Malheureusement les propriétés des nuages à l'échelle beaucoup plus petite du rayon de giration des particules est inaccessible aux observations. Mais, même si la perte de rayons cosmiques dans le nuage d'Eridu demeure inexpliquée à l'issue de nos travaux, la mise en évidence d'une nette différence de flux de rayons cosmiques entre les deux et la comparaison de ces deux nuages avec des modèles et simulations numériques pourront à l'avenir contraindre encore davantage notre compréhension encore très incertaine de la propagation des rayons cosmiques dans la phase majeure (neutre) du milieu interstellaire. Ils serviront notamment à explorer comment la turbulence magnétohydrodynamique et son amortissement par les interactions ions-neutres et/ou comment l'emmêlement des lignes de champ magnétique par les mouvements turbulents du gaz régulent la diffusion des rayons cosmiques Galactiques.

Mots-clés : Rayons gammas - Rayons cosmiques - Milieu interstellaire – Poussières - Champ magnétique – Propagation – Coefficient de diffusion - Sections efficace hadronique - Bremsstrahlung - Milieu local

Acknowledgements

I would like to express my gratitude to my thesis advisor, Isabelle Grenier, for her guidance throughout these three years. Thank you for sharing your knowledge with me and humbly imparting your vast expertise. It is thanks to her determination and boundless curiosity that the work I can present today is what it is. Special thanks for helping me in the writing part.

I acknowledge the financial support by the LabEx UnivEarthS for this work. I extend my gratitude to all the members of the *Fermi* collaboration for the scientific discussions and feedback.

I am thankful to the staff of the STEP-UP doctoral school for their administrative support and ensuring the smooth progress of the theses.

A big thank you to the members of the jury who agreed to evaluate this work : Fabien Casse, Pierre Jean, Alexandre Marcowith, Luigi Tibaldo, and Julia Tjus.

Thanks to my friends and cousins who have accompanied me during this journey from my undergraduate studies, whether in Alexandria, Nantes or Paris. Thanks to those who were by my side during the last year and especially the last months ; without you, I would not have reached this stage. You are the best.

Because a thesis is a long-term endeavor, it would not have been possible without the daily support I have counted on for three years. For that, I am deeply grateful to my parents, Réda & Réna, and my brother Chris for always being by my side. Thanks for all the love you give me.

And to those whom I may not mention by name but who know what I owe them, Thank you. Happy reading.

Table des matières

Acknowledgements

Introduction	1
1 Interstellar medium	5
1.1 The atomic phase	6
1.1.1 21 cm lines emission	6
1.1.2 Absorption	8
1.1.3 GASS survey measurements	10
1.2 The molecular phase	11
1.2.1 CO radiation	12
1.2.2 Dark gas	14
1.3 H α	15
1.4 Thermal properties	16
1.4.1 Heating and cooling	16
1.4.2 Thermal instability	17
1.4.3 Equilibrium and stability	18
1.5 Global appraisal of interstellar contents	20
2 Magnetic field	25
2.1 Dust polarisation and magnetic field orientation	26
2.2 Plane-of-sky magnetic-field strength	28
2.2.1 DCF method	28
2.2.2 ST method	30
2.3 Line-of-sight magnetic-field strength	31
2.4 Turbulence and Alfvén Mach number	32
2.5 Interstellar values of the magnetic field	35
3 Galactic cosmic rays	39
3.1 Brief history	39
3.2 CR composition	41
3.3 Direct detection	42
3.4 CR abundances and inelastic interactions	46

3.5	CR Spectra	47
3.5.1	The knee break	47
3.5.2	The ankle break	49
3.5.3	Hardening near 300 GV	49
3.5.4	Electron and positron spectra	51
3.6	CR anisotropy	53
3.7	Indirect detection	56
3.8	Acceleration sources of CRs	58
3.9	Galactic CR distribution	61
4	Gas tracers : data and analyses	69
4.1	Fermi-LAT	70
4.1.1	The LAT in Space	70
4.1.2	Detector structure	71
4.1.3	Event reconstruction	72
4.1.4	Instrument response functions	73
4.1.5	Data likelihood analysis	76
4.2	Modelling γ rays	77
4.3	Planck	80
4.4	Modelling the dust optical depth	80
4.5	The search for dark neutral gas	82
5	Cosmic-ray propagation	85
5.1	Diffusion modes	86
5.2	Wave growth and damping rates	88
5.2.1	Growth rate of Alfvén waves	88
5.2.2	Damping modes	89
5.3	Diffusion models	94
5.3.1	Leaky box model	94
5.3.2	Simulation models	98
6	γ-ray emissivities in local clouds	101
7	The CR flux in Eridu and near the Solar System	105
7.1	The Eridu cloud	105
7.2	The CR flux in Eridu	107
7.3	A loss of cosmic rays?	107
7.3.1	CR flux in the Solar System	107
7.3.2	Cross sections	110
7.3.3	γ -ray emissivity	115
7.4	First Paper (2021)	115
8	CRs in Reticulum vs Eridu	125
8.1	General characteristics of Reticulum	126

8.2	Gas estimates	127
8.2.1	HI gas phase	127
8.2.2	Molecular phase	128
8.3	Second Paper (2023)	130
8.4	Complementary results : γ -ray point sources	157
9	Conclusions and perspectives	159
	Bibliographie	165

Introduction

In the field of astroparticles, our quest to unravel the mysteries of the universe takes us to the far reaches of the cosmos. This exciting domain of science combines the principles of particle physics with the study of cosmic phenomena, offering us a unique perspective on the universe's fundamental building blocks and its grand structures.

The journey begins with understanding the fundamental particles that make up our universe. Particle physics, the science that explores the tiniest constituents of matter, reveals a diverse spectrum of particles, from electrons and protons to neutrinos and more. These particles play a crucial role in the universe, from the formation of atoms to the birth and evolution of stars.

One of the most remarkable tools at our disposal for peering into the universe's secrets is the telescope, which has been our window to the cosmos for centuries. Telescopes have enabled us to observe distant galaxies, nebulae, and celestial bodies, shedding light on the vastness of the universe and the processes that govern it. But the wonders of the universe are not limited to what we can see with our eyes.

In the modern era, space-based observatories and satellites have expanded our observational capabilities beyond the visible spectrum. One such satellite, *Fermi*-LAT, has provided us with a unique opportunity to study the cosmos through γ -ray observations. These observations allow us to explore cosmic-ray interactions with interstellar gas. Cosmic rays, especially in the GeV energy range, play a significant role in the evolution of galaxies. Their pressure, equal to the gas pressure and that of the magnetic field in the interstellar medium, is a crucial factor.

My thesis delves into the intriguing field of astroparticles, focusing on the data obtained from the *Fermi*-LAT satellite. It is divided into two distinct parts, each offering valuable contributions to our understanding of the cosmic-ray interactions with the medium.

The first part of my work revolves around investigating the cosmic-ray spectrum using γ -ray observations and hadronic cross sections in order to unravel the local cosmic-ray spectrum within our Solar System. This part also involves revisiting earlier measurements and using the latest cosmic-ray spectra to refine our understanding. I specifically focused on Eridu, a cloud exhibiting an unexplained deficit in cosmic-ray flux. To shed light on this mystery, I turned my attention to another cloud in the Reticulum constellation, which shares similar characteristics with Eridu. In the second part, I estimated the gass mass and measured the cosmic-ray flux in the Reticulum cloud. Aiming to uncover the origin of the cosmic-ray deficit in Eridu, I compared diffusion properties including the cosmic-ray propagation and their interaction with the

magnetic field in both cloud media.

Intriguingly, both parts of my thesis contribute to our broader understanding of astroparticles and their interactions with the interstellar medium. They invite us to explore the depths of our universe, where particles and phenomena come together to weave the complex fabric of the cosmos. The results of these both parts led to publications that are integrated in the manuscript.

Before presenting the results, I introduce, in a few chapters, the key concepts from various fields of astrophysics that will be used later on.

[Chapter 1](#) is an overview on the interstellar medium, including the chemical and thermodynamics properties of different phases especially the atomic and the molecular ones.

[Chapter 2](#) presents various methods for measuring the magnetic field orientation and strength in the interstellar medium, whether the magnetic field is projected onto the plane of the sky or along the line of sight.

[Chapter 3](#) is related to the cosmic rays. I show a brief history of their discovery and the major particle detectors used to directly observe them. Then, I present their composition and abundance and almost all the important features in their spectra. In the following section, I talk about the techniques used to detect them far from the Sun using indirect observations. In the end of the chapter, I present possible cosmic-ray acceleration sources and their distribution in our Galaxy.

[Chapter 4](#) shows the gas tracers used in this thesis. I begin by presenting the *Fermi-LAT* satellite. Then I explain the γ -ray and dust models that I use to estimate the dark gas in an interstellar cloud.

[Chapter 5](#) is an overview on the different diffusive modes for CRs in the Galaxy, and especially the self-streaming. Then, I present the growth rate of the Alfvén waves and the different damping modes in the interstellar medium. The second part consists of presenting the models of propagation that exist nowadays. Here I show the Leaky-Box model and the numerical simulations like GALPROP, USINE, DRAGON and PICARD.

[Chapter 6](#) is an overview on the γ -ray emissivities, discovered in the last decade, in the local clouds at few hundreds of parsecs around the Solar System. Among these findings, the Eridu cloud that stands out with its distinct nature.

[Chapter 7](#) compares the cosmic-ray flux in the Eridu cloud with that in our Solar System and the one found in the other local clouds. The first paper has been integrated in that chapter.

[Chapter 8](#) presents another filamentary cloud, Reticulum, which has been studied to understand the different cosmic-ray flux found in Eridu. I also explore the propagation properties of cosmic rays and the level of gas and magnetic field turbulences in both clouds. The results are presented in the second paper, integrated in that chapter.

[Chapter 9](#) provides a summary of the obtained results, along with proposed avenues for further exploration.

TABLE 1 : Important units used in this manuscript

Gega electron-volt	GeV	$10^9 \text{ eV} = 10^9 \times 1.6 \times 10^{-19} \text{ J}$	Energy
Light-years	ly	$9.46 \times 10^{15} \text{ m}$	Distance
Parsec	pc	$3.26 \text{ ly} = 3.09 \times 10^{16} \text{ m}$	Distance
Astronomical unit	au / AU	$4.8481 \mu\text{pc} = 1.495 \times 10^{11} \text{ m}$	Distance
milli Barn	mbarn	$10^{-3} \text{ barn} = 10^{-31} \text{ m}^2$	Surface
Rayleigh	R	$(10^{10}/4\pi) \text{ photons m}^{-2} \text{ s}^{-1} \text{ sr}^{-1}$	Column emission rate
Debye	D	$3.34 \times 10^{-30} \text{ C m}$	Dipole moment in CGS
Gauss	G	$10^{-4} \text{ tesla} = 10^{-4} \text{ weber m}^{-2}$	Magnetic field intensity

Interstellar medium

The interstellar medium (ISM) is an important component of galaxies. It is composed of gas and dust found between stars and it is responsible for star formation which are the main sources of energy in the galaxies besides gravitation. In the Milky Way, most of that baryonic matter has been transformed into stars or stellar remnants but even today, 10% of the baryons are to be found in the ISM of our galaxy (Draine, 2011). In Figure 1.1 we can see that most of the interstellar gas and dust is located within a relatively thin gaseous disk, with a thickness of a few hundred parsecs. That is the region where almost all the stars are formed.

About 90% of interstellar atoms are hydrogen. They are presented as atomic, molecular or even ionised gas. This baryonic matter, found in the dynamic ISM, has a wide range of temperatures and densities forming characteristic phases, in particular, seven distinct phases :

- Hot Ionised Medium (HIM)
- Ionised gas (HII) or Warm Ionised Medium (WIM)
- Warm atomic gas or Warm Neutral Medium (WNM)
- Cold atomic gas or Cold Neutral Medium (CNM)
- HI-HII transition or Dark Neutral Medium (DNM)
- Dense molecular gas (H_2 and other molecules)
- Stellar outflows

Therefore, the ISM is composed of gas organised into several phases of density, temperature, and chemical composition. To determine the amount of gas and trace it, it is first necessary to understand the different phases and how to observe them. In the following sections, we will discuss more about the atomic and molecular phases.

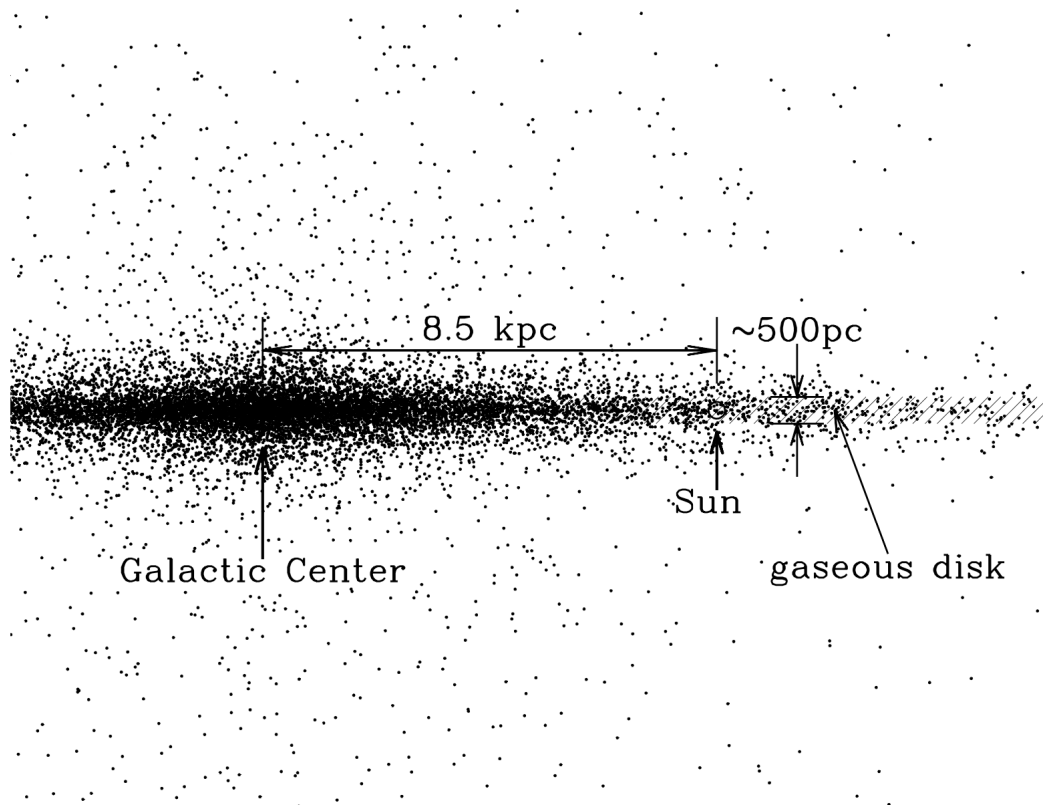


FIGURE 1.1 : An edge-on view of the Milky Way galaxy. The black dots represent the stars and the volume containing most of the interstellar gas and dust is shaded (Draine, 2011).

1.1 The atomic phase

Most of the interstellar gas mass in the Milky Way is neutral, and $\sim 78\%$ of the neutral hydrogen is atomic (H I)¹ (Draine, 2011). That neutral atomic phase serves as an intermediary between ionised gas and cold molecular clouds. We can directly infer the atomic gas mass from the observation of the H I 21 cm lines (e.g. Dickey et al. (2000); Heiles and Troland (2003))

1.1.1 21 cm lines emission

A neutral hydrogen atom consists of electron bound to a nucleus composed of one proton. The lowest stationary energy state of that bound electron is the ground state and it equals to 13.6 eV in energy. Both electron and proton have intrinsic angular momentum which is the spin. As a result of the quantum angular momentum of that system, there are two states in spin, therefore, the electron's spin can be parallel or antiparallel to that of the proton. The electron's ground state becomes slightly higher in energy when its spin is parallel to that of the proton. This amount of energy equals to 5.9×10^{-6} eV which is very small compared to the hydrogen ground state energy.

¹A chemical component of an atom followed by the Roman numeral I indicates that it is in a neutral state, while the numeral II indicates that it is once ionised. For example, CII means that carbon is ionised C^+ .

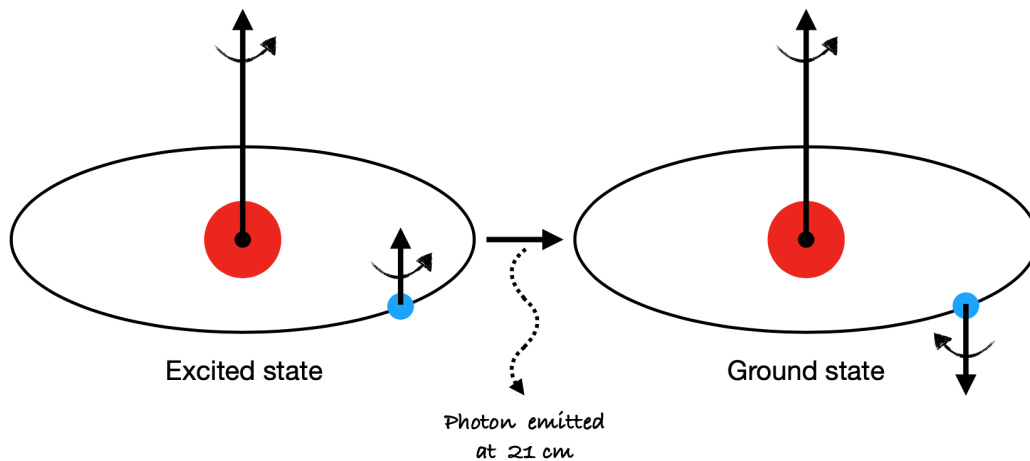


FIGURE 1.2 : A diagram representing the spin-flip transition in the hydrogen atom leading to emission of a photon at 1420 MHz or 21 cm. The proton and the electron are represented by the red and blue circles respectively. Note that spin is not classical spinning charge sphere as represented here. It is a quantum angular momentum and does not have any classical analogy.

During collisions between atoms, the electron's spin can change state and become antiparallel to the one of the nucleus. Therefore, a photon is emitted carrying the difference in energy, which corresponds to a wavelength of 21 cm and a frequency of 1420 MHz. The probability of this phenomenon is very low with a transition rate $2.9 \times 10^{-15} \text{ s}^{-1}$, so the mean lifetime of the excited state is around 11 million years. However, the huge quantity of hydrogen in the interstellar clouds and the collisions between atoms can help promote the 21 cm emission.

The advantage is that 21 cm line allows the detection of hydrogen atoms in their most fundamental state without the need for radiation excitations. The map obtained by H I 21 cm radiation is shown in Fig.1.3.

Since it is a narrow line, velocity information can be obtained by the Doppler effect, but only the component projected onto the line of sight. The 21 cm line therefore allows the mapping of the amounts of H I gas by calibrating the frequencies based on the object's movement and distance (Dickey et al., 2000 ; Heiles & Troland, 2003).

This 21 cm line was predicted by the Dutch astronomer H. C. van de Hulst in 1944, but was observed for the first time in 1951 by Harold Ewen and Edward M. Purcell at Harvard. It was the birth of spectral-line radio astronomy. Few years after 1952, the first maps of the H I gas in the Galaxy were made, and revealed for the first time the spiral structure of the Milky Way (van de Hulst et al., 1954 ; Westerhout, 1957).

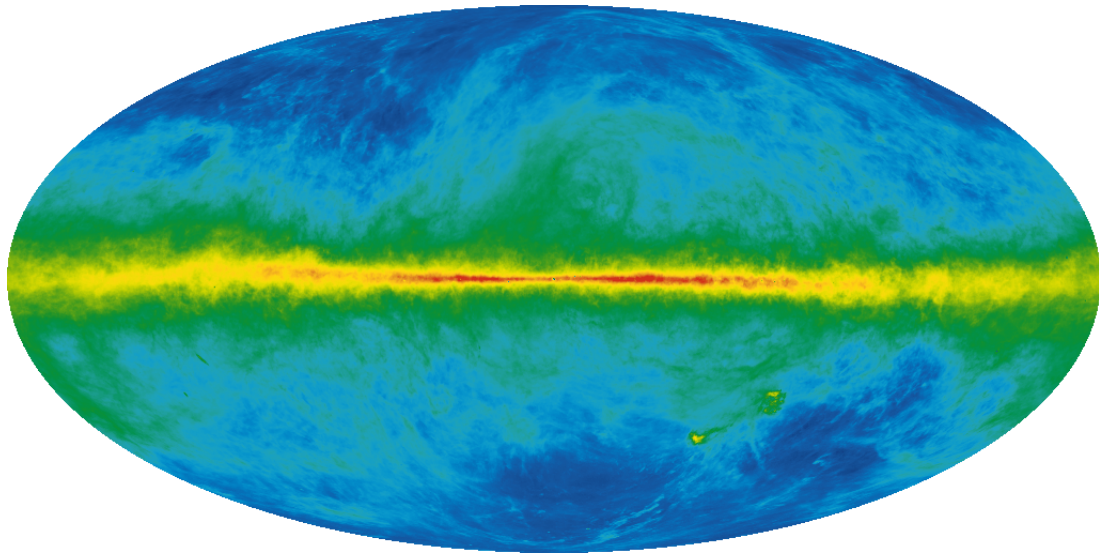


FIGURE 1.3 : Intensity map of the integrated HI lines at 21 cm (HI4PI Collaboration et al., 2016).

1.1.2 Absorption

By observing an intense radio source, the hydrogen atoms found on the line of sight between that source and the telescope can absorb the 21 cm lines if the gas is dense enough. By measuring the depth of the absorption line, one can estimate the HI density in the ISM and infer the total amount of hydrogen in that specific direction.

Figure 1.4 is an example of the absorption and emission spectra in the direction of J003824–742212. There are mainly two major absorption lines but more emission lines, about four between 100 and 150 km.s^{-1} , and one intense line at the velocity of 160 km.s^{-1} . We can see that the most intense emission line is the one related to the highest absorption. Because the more there is emission, the more there is gas on the line of sight and consequently the absorption is not negligible.

The 21 cm line width is influenced by the kinetic temperature of the HI gas. A broader line suggests a wider range of velocities, hence higher temperatures and/or turbulent motions inside the cloud. The emission spectra typically exhibit broader line widths compared to the absorption one, indicating the presence of colder, denser clumps within a surrounding, less dense, and warmer medium.

1.1.2.1 Self-absorption

The main difficulty in HI observations is self-absorption. It occurs when the emitted photon can reverse the spin of another electron given that it carries the right energy for this process. Therefore, HI lines must be corrected for partial self absorption in order to estimate the gas mass (Murray et al. (2015), and references therein).

The populations of parallel (higher energy) and antiparallel (lower energy) spin states are

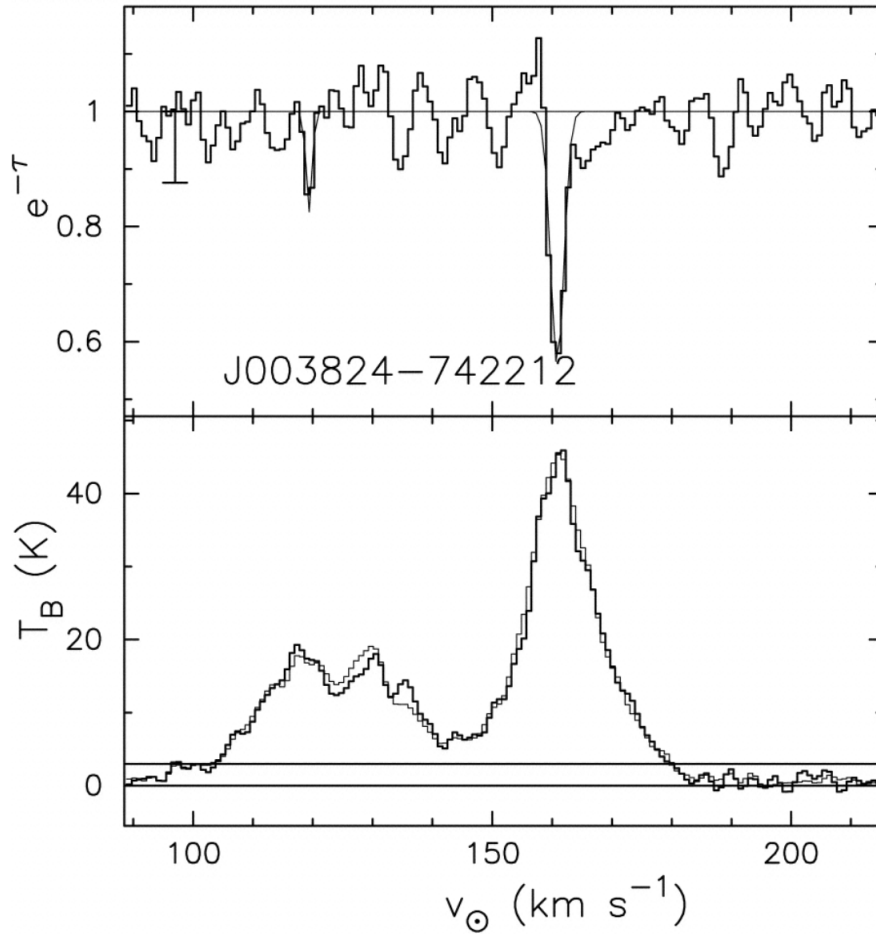


FIGURE 1.4 : An example of absorption (top) and emission (bottom) spectra in the direction of J003824–742212, as a function of the velocity projected onto the line of sight. The Gaussian fits to the line components are indicated and the 3σ threshold for detection of absorption is shown on the left side of the upper spectrum. In emission, the two different lines (dark and light) are for two different measurements. (Dickey et al., 2000)

governed by the Boltzmann distribution, which is determined by the relative energies of the different states and the temperature of the system. The spin temperature, T_S , represents the gas temperature at which the populations of the two spin states would be in thermal equilibrium, following the Boltzmann distribution.

For a hotter temperature, more atoms will exist in the higher-energy parallel state. In that case, the hydrogen gas will emit 21 cm radiation more than it absorbs, leading to a net emission of the H I radiation and the gas is considered as optically thin. However, if the gas is colder than T_S , more atoms will exist in the lower-energy antiparallel state. Therefore, the gas will preferentially absorb 21 cm radiation leading to a characteristic dip in the observed spectrum and this is the optically thick case.

1.1.3 GASS survey measurements

Many surveys exist aiming at studying the neutral atomic H I gas. Among these surveys, there is the Leiden-Argentine-Bonn survey (LAB), the Effelsberg-Bonn H I Survey (EBHIS) and the Galactic All-Sky Survey (GASS).

The all-sky LAB survey is substituted using the latest data from the EBHIS and GASS. The result of merging both datasets is called the HI4PI Survey (HI4PI Collaboration et al., 2016).

		LAB	GASS	EBHIS	HI4PI	Unit
Declination range	δ	Full	$\leq 1^\circ$	$\geq -5^\circ$	Full	
Angular resolution	θ_{FWHM}	36'	16.2'	10.8'	16.2'	
Velocity interval	$ v_{\text{LSR}} $	$\leq 460^*$	≤ 470	≤ 600	$\leq 600^{**}$	km s^{-1}
Channel separation	Δv	1.03	0.82	1.29	1.29	km s^{-1}
Spectral resolution	δv	1.25	1.00	1.49	1.49	
Temperature noise	σ_{rms}	80	55	90	~ 43	mK
	$N_{\text{HI}}^{\text{lim}}$	3.9	2.5	4.7	~ 2.3	10^{18} cm^{-2}
	$S_{\text{HI}}^{\text{lim}}$	16.1	2.1	1.8	~ 2.0	Jy km s^{-1}

TABLE 1.1 : Comparison of basic parameters of selected H I surveys of the Milky Way. The bottom two rows quote theoretical 5σ detection limits (velocity-integrated intensity) integrating over a Gaussian profile of 20 km s^{-1} line width (FWHM) for surface brightness and point sources, respectively. * Northern (LDS) part : $v_{\text{LSR}} \leq 400 \text{ km s}^{-1}$. ** Southern (GASS) part : $|v_{\text{LSR}}| \leq 470 \text{ km s}^{-1}$.

In that work, we are using GASS III data (Kalberla & Haud, 2015) aimed at studying the distribution and properties of H I gas in the Southern sky. The observations began in January 2005 and stopped in October 2006 using 64-m Parkes Radio Telescope. Lines in our analyses span velocities from -125 to +495 km/s.

To quantify the amount of neutral hydrogen H I, two key observables are employed. The first one is the brightness temperature, denoted as T_b , which indicates the intensity of the emitted spectral line, and the second one is the line-of-sight velocity relative to the Local Standard of Rest (LSR). The T_b translates the intensity detected by the telescope into the temperature of a blackbody of equivalent specific intensity. This intensity is converted into the total gas column density along the line of sight, expressed in units of cm^{-2} .

Radiative transfer equations provide relationships between the column density of H I along a given line of sight N_{HI} , the optical depth of the spectral line $\tau(v)$ at velocity v , the spin temperature T_S , and the brightness temperature T_b .

$$N_{\text{HI}} = \int n_{\text{HI}} dL_{\text{sight}} = C \int T_S (1 - e^{-\tau(v)}) dv \quad (1.1)$$

Here, $C = 1.823 \times 10^{28}$ atoms cm^{-2} $(\text{K km s}^{-1})^{-1}$. When considering the background brightness temperature as T_{BG} , the quantity detected by the telescope is the difference denoted as $\Delta T = T_b - T_{BG}$, where :

$$\Delta T = T_b - T_{BG} = (T_S - T_{BG})(1 - e^{-\tau(\nu)}) \quad (1.2)$$

The background temperature primarily includes the Cosmic Microwave Background (CMB) radiation with $T_{BG} = 2.66$ K at the 21 cm wavelength. By expressing τ in terms of T_b and assuming a uniform spin temperature, the column density can be expressed as :

$$N_{\text{HI}} = CT_S \int \ln\left(\frac{T_S}{T_S - T_b}\right) dv \quad (1.3)$$

In situations where the optical depth is small (optically thin case with $\tau < 1$), we can simplify Eq.1.2 using a first-order Taylor expansion, resulting in $T_b = T_S \tau(\nu)$. This simplifies the expression for column density to :

$$N_{\text{HI,thin}} = C \int T_b dv \quad (1.4)$$

The value of T_S varies depending on the phase of the atomic gas. For cold gas, spin temperatures typically range from 40 to 200 K, while in the warm phase, they vary between 4000 and 9000 K (Murray et al., 2015). In most subsequent analyses in this thesis, the column densities are relatively low ($N_{\text{HI}} < 2 \times 10^{21}$ cm^{-2}). A correction with a uniform T_S temperature over a cloud is generally sufficient to yield reliable results (Nguyen et al., 2018).

1.2 The molecular phase

When the gas becomes sufficiently dense, individual hydrogen atoms form H_2 molecules on the surface of dust grains and the molecules are then released into the gas phase. The major phenomenon which endangers the existence of these molecules is the photo-dissociation by interstellar ultraviolet (UV) photons.



The molecules at the periphery of a cloud are quickly dissociated into hydrogen atoms, but UV absorption by this dissociation and by dust grains in the atomic envelope can leave behind denser and more shielded clumps of molecular hydrogen. That is why, the H_2 molecules are found in dense clumps at the cores of atomic clouds, shielded from photo-dissociation.

These surviving clumps are the resilient remnants of the molecular cloud, a testament to the complex interplay between interstellar UV radiation and the formation and dissociation of molecular hydrogen in the diverse regions of the interstellar medium.

1.2.1 CO radiation

The H_2 molecule is symmetric and homonuclear therefore it possesses no permanent electric dipole moment. This absence of a dipole moment makes it an inefficient radiator of electromagnetic radiation, emitting only weak quadrupole transitions $\Delta J = 2$.

Another significant factor influencing H_2 molecule's radiative behavior is its small moment of inertia. This property has important implications for the energy levels within the molecule. At low temperatures, the spacing between these levels becomes relatively wide which leads to inefficient population of the energy states. In other words, at the typical temperatures of molecular clouds, the majority of H_2 molecules occupy their lowest energy states, making them less likely to transition to higher states that could result in radiative emissions.

One must rely on surrogate observations such as the rotational lines of CO and its isotopologues which is the next most abundant molecule. Their abundance compared to H_2 molecules varies between 10^{-7} and 10^{-4} . The most abundant isotope is $^{12}C + ^{16}O$. In order to quantify the H_2 mass, the abundance and excitation temperature of CO molecules should be large enough. The CO molecule has a permanent dipole moment of 0.1098 D and its rotation causes emission at microwave frequencies at 115 GHz and a wavelength of 2.6 mm, thanks to the transition $J : 1 \rightarrow 0$. The CO molecules are formed in the cold dense molecular phase at larger densities than H_2 formation, therefore CO clouds are not diffuse as in the HI phase (see Fig.1.5). However, the emission from CO molecules in the cores of clumps are partially observed because the CO dipole radiation is easily absorbed.

To study the gas molecular phase, we need to count the CO molecules and then convert this count into H_2 molecules that occupy this dense phase. Similarly to HI measurements, the CO surveys conducted by radio telescopes provide the brightness temperature of the emission as a function of longitude, latitude, and gas velocity. The quantity of molecular gas traced by CO emission is proportional to the integrated CO intensity along a line of sight, expressed in $K.km.s^{-1}$:

$$W_{CO} = \int T_b dv \quad (1.5)$$

The conversion factor translates the observed W_{CO} intensity, into a column density of molecular hydrogen N_{H_2} in cm^{-2} .

$$X_{CO} = \frac{N_{H_2}}{W_{CO}} \quad (1.6)$$

In the local environment, X_{CO} varies around $10^{20} cm^{-2}K^{-1}km^{-1}s$, while outside the Galaxy it is almost double due to the low abundance of interstellar C and O atoms when star formation is low. The curve of X_{CO} values is given by Fig.1.6. This factor has been studied theoretically and observationally (Bolatto et al. (2013); Gong et al. (2018); Remy et al. (2017a) and references therein), but the variations are too large and too uncertain to reliably use the CO data to measure the cosmic ray flux in the dense molecular phase of clouds.

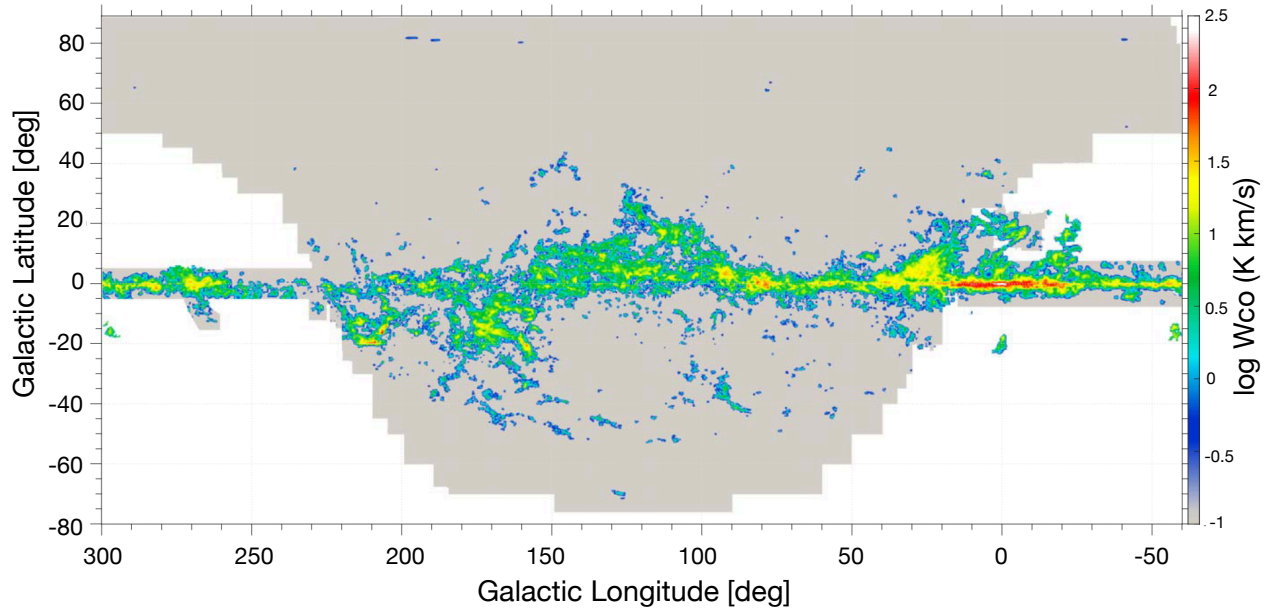


FIGURE 1.5 : Map of the integrated intensity of rotational lines of ^{12}CO over velocity from -36 to 36 km.s^{-1} , the range over which significant emission is detected. For cosmetic purposes, the map was interpolated to $1/8^\circ$ spacing and smoothed slightly by convolution with a 0.3° Gaussian. The white area is unobserved. (Dame & Thaddeus, 2022)

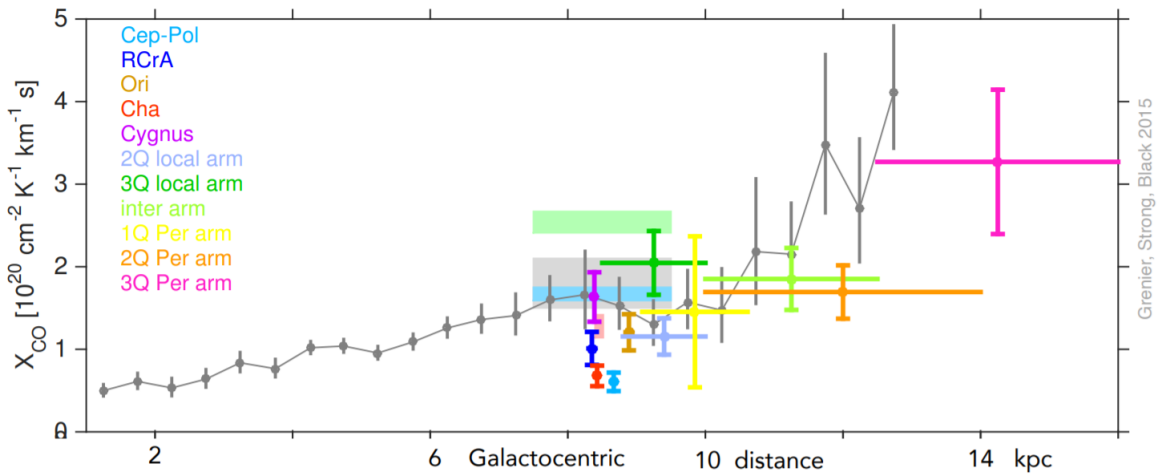


FIGURE 1.6 : The X_{CO} values deduced from observations of several clouds and spiral arms in our local environment and outside the galaxy. (Grenier et al., 2015)

1.2.2 Dark gas

The dark gas, referred to as the Dark Neutral Medium (DNM), represents the gas accumulation at the H_I-H₂ transition within clouds (Liszt et al., 2019). This substantial quantity of gas remains invisible to the 21 cm and 2.6 mm lines, thus eluding H_I and CO line observations (Grenier et al., 2005). It remains undetectable in emission due to self-absorption within dense H_I clumps, and CO molecules are efficiently dissociated by photons or insufficiently excited in the diffuse H₂ gas because the gas lacks the density required for collisions that would induce CO molecules to rotate and emit radiation. Therefore, the dark gas comprises a mixture of optically thick H_I and diffuse H₂, in proportions that remain unknown. This DNM introduces significant uncertainty in estimating the total interstellar gas content as its mass corresponds to about 20% of the overall gas mass. It compares or exceeds the CO-bright molecular mass (Remy et al., 2018).

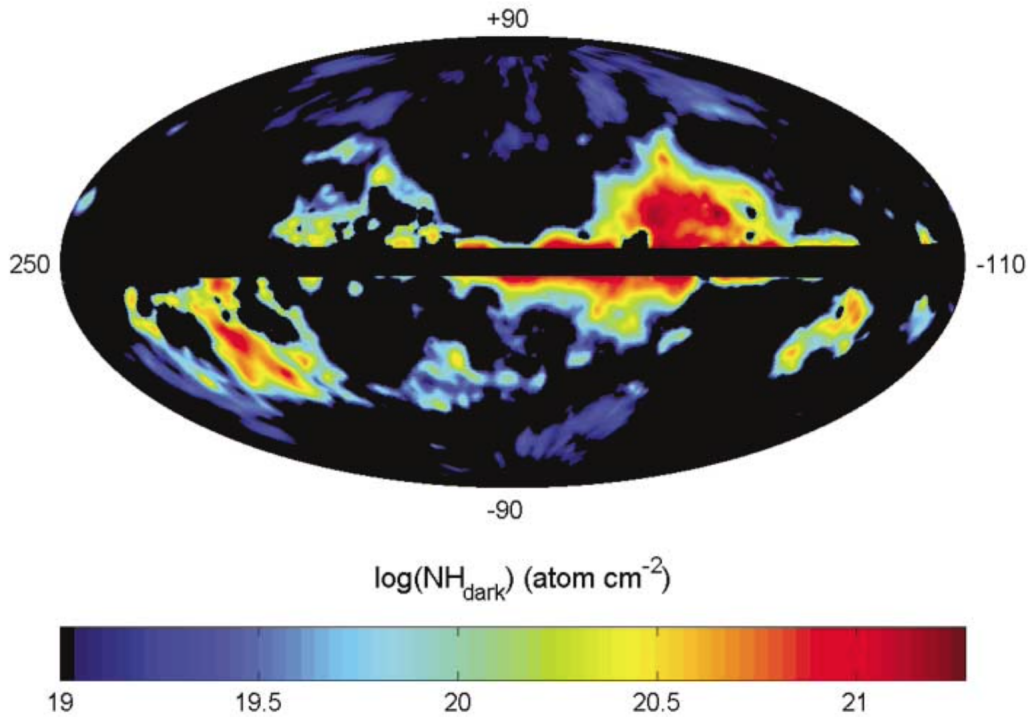


FIGURE 1.7 : Map by Grenier et al. (2005) of the DNM column densities found in the dust halos. The map is shown in Galactic coordinates centered on $l = 70^\circ$. This dark gas complements that visible in HI and CO.

Molecules are formed in the diffuse molecular gas prior to CO, and some of these molecules act as precursors to CO formation. They can thus be employed to detect the molecular component of the dark gas, such as CH, OH, or HCO⁺. Observing them directly is less susceptible to line-of-sight confusion issues compared to other commonly used tracers like the CII line emitted at 158 μm . This is because the CII line is emitted in various gas phases (H_I, H_{II}) apart from the dark gas phase. However, observations of CH, OH, or HCO⁺ molecules are only effective in absorption and require long point-by-point observation times, making them quite

sparse. Initial measurements suggest that H_2 appears to dominate the dark gas column density (Liszt et al., 2019). An analysis of H α absorption lines leads to the same conclusion (Murray et al., 2018), but the composition is likely to vary from cloud to cloud and within the DNM phase itself (Remy et al., 2018).

Tracers of the gas total column density are required to unveil this large-scale neutral dark gas. Only the combination of thermal dust emission and interstellar γ radiation is currently capable of fulfilling this role (Grenier et al., 2005 ; Planck Collaboration, Fermi Collaboration, et al., 2015 ; Remy et al., 2018). The missing dark gas manifests as an excess of γ photons or dust above the expected quantities from H α and CO data as represented in Fig.1.7. This technique is explained in details in Chap.4.

1.3 H α

H α line emission traces the recombination of ionised hydrogen (H $^+$) back into its neutral state (H) in the ISM. Hydrogen is ionised by energetic photons from massive stars or other astrophysical sources, often in the form of ultraviolet radiation. However, the interstellar medium is not static ; it's a dynamic environment filled with various energy sources and physical processes. Over time, the ionised hydrogen atoms naturally recombine as electrons and protons rejoin, transitioning back to their neutral state. It's during this recombination process that H α emission occurs. If the electron is captured into some specific state $n\ell$, that was initially unoccupied, the "radiative recombination" is represented by :

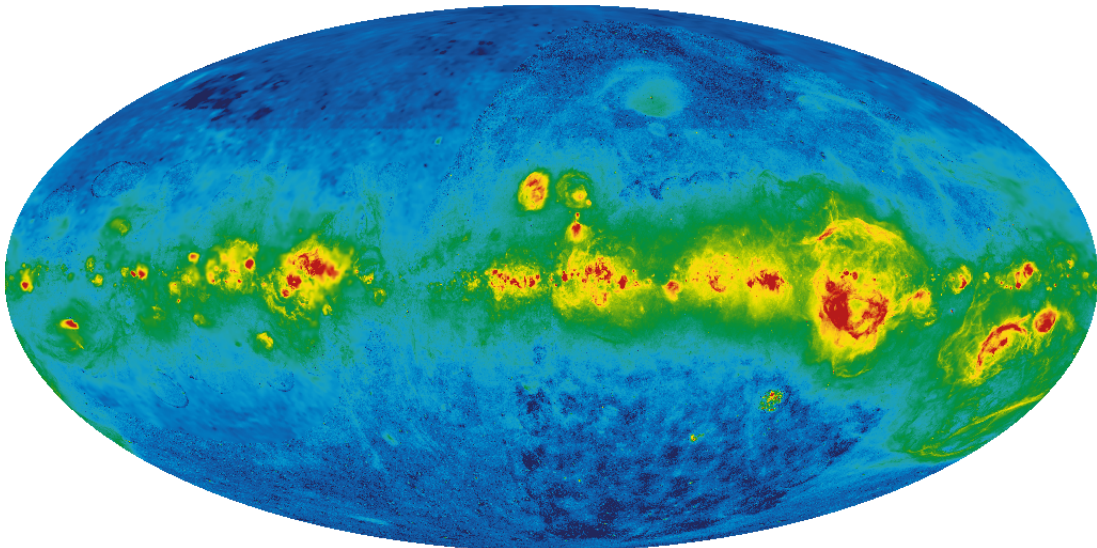
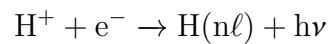


FIGURE 1.8 : H α map at 6' resolution. The data is combined by (Finkbeiner, 2003) from the Wisconsin H-Alpha Mapper (WHAM), the Virginia Tech Spectral-Line Survey (VTSS) and the Southern H-Alpha Sky Survey Atlas (SHASSA).

This specific transition involves the electron falling from the third energy level to the second

in the hydrogen atom, releasing a photon with a wavelength of approximately 656.3 nm, which falls within the red part of the visible spectrum. H_α emission is a valuable tool for astronomers as it serves as a tracer for regions of ionised gas, highlighting areas of intense star formation and providing insights into the structure and dynamics of the interstellar medium.

In this work, we are using the 6' (FWHM) resolution H_α map reprocessed by Finkbeiner (2003) from the Southern Halpha Sky Survey Atlas (SHASSA) data (Gaustad et al., 2001). In our analysis, this map is used as a crude gas template even though the H_α emission measure does not scale with the N_{H^+} column density, in cm^{-2} , but it integrates the product of the electron and ion volume densities along the line of sight, $EM_\alpha \propto \int n_e n_{H^+} dL_{\text{sight}}$.

1.4 Thermal properties

1.4.1 Heating and cooling

A thermal equilibrium must have a balance between heating and cooling rates $\Gamma = \Lambda(T)$. Heating is represented by the amount of energy E that the gas receives per unit volume V and per unit time t . This term $dE/dVdt$ is proportional to the volumetric density of the gas n and the heating rate Γ . There are several processes that can heat the gas :

- The transfer of kinetic energy by fast electrons that have been ejected from dust grains by photoelectric effect and give up their energy through collision or re-absorption.
- Localised heating by thermodynamic processes such as the shock wave of a stellar wind or a supernova explosion, which pass through, compress and heat the gas abruptly to temperatures of millions of degrees.
- The ultraviolet (UV) photons that dissociate H_2 molecules at the edge of molecular clouds. The hydrogen atoms then transfer their kinetic energies to the gas through collisions.

Cooling is represented by the total amount of energy radiated per unit volume and time. To cool down the gas, there are several means, mainly radiative :

- Radiative recombination of free electrons on ionised atoms, especially the recombination of C^+ (CII) lines at $158 \mu\text{m}$.
- Free-Free radiation² emitted by a fast-moving electron or a cosmic-ray electron, slowed down by the electric field of an atomic nucleus.
- Radiation of $H\text{I}$ at 21 cm and rotational radiation of molecules with a dipole moment such as CO and H_2O .

²Free-Free radiation is the braking radiation or bremsstrahlung, and it is so named because the electron is free before and after deviation.

Each cooling process must be summed, according to the volume densities of electrons n_e and ions n_i , and the temperature dependencies T of the various processes.

$$\frac{dE_{ray}}{dVdt} = \frac{dE_{brem}}{dVdt} + \frac{dE_{recomb}}{dVdt} + \dots \propto n_e n_i T^{1/2} + n_e n_i T^{-1/2} + \dots \quad (1.7)$$

At first order, the gas is neutral in the main atomic and molecular phases. There are then as many electrons as ions $n_e = n_i$ per unit volume, therefore, the cooling is proportional to the square of the gas volume density n^2 and the cooling rate $\Lambda(T)$.

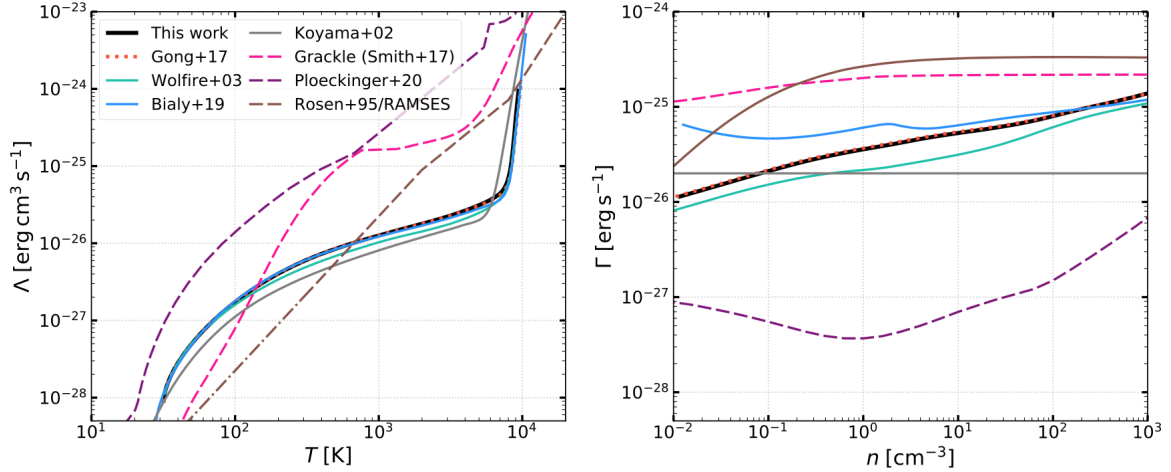


FIGURE 1.9 : The cooling function Λ as a function of temperature (left) and the heating rate per H nucleon Γ as a function of density (right) for different models at solar metallicity and for a cosmic-ray ionisation rate of $2 \times 10^{-16} \text{ s}^{-1}$. The label "this work" refers to the model of Kim et al. (2023) used for the present thesis work.

We observe that, in the ISM, when we compress the gas by increasing its density, unlike in thermodynamics, heating increases with density n but cooling, which depends on n^2 , varies more quickly and the gas cools down !

1.4.2 Thermal instability

If two media with different temperatures are in contact, they will not necessarily converge to a median temperature, on the contrary, there may be divergence.

As a first approximation, the interstellar medium is isobaric thanks to sound waves circulating everywhere with velocities of the order of a few km/s to smooth out pressure changes. By the ideal gas law $P = nkT$ and taking the pressure, P , as a constant, the product of gas volume density by temperature, nT , becomes constant. Therefore, if T decreases, n increases. Since the heating increases with n but the cooling increases with n^2 , the temperature decreases even more. The HI phase has therefore two phases (Field et al., 1969) :

- Warm Neutral Medium (WNM) stable around 10^4 K and $\sim 0.5 \text{ cm}^{-3}$ of volume density. The ionisation fraction is around 10^{-2} .

- Cold Neutral Medium (CNM) stable around 10^2 K and density $\sim 30 \text{ cm}^{-3}$ with a lower ionisation fraction around 10^{-4} .

The warm atomic phase WNM of the ISM is a critical component of the galactic environment. Despite the presence of ionising radiation from nearby massive stars, the WNM has a relatively low degree of ionisation therefore, most of the hydrogen remain in the neutral state.

The molecular phase, including the DNM phase and especially the phase visible in CO, is even colder than the cold atomic phase CNM. It is around 10-30 K which is due to the high density, $10^2 - 10^7 \text{ H}_2.\text{cm}^{-3}$, and the cooling effect of CO radiation.

1.4.3 Equilibrium and stability

1.4.3.1 Thermal equilibrium

The time required to reach thermal equilibrium is represented by all the thermal energy divided by the rate of energy loss. Thermal energy is of the order of nkT , and the loss due to radiation is proportional to $n^2\Lambda(T)$. The time needed to achieve this thermal equilibrium is given by :

$$\tau_{\text{th}} = \frac{nkT}{n^2\Lambda} \quad (1.8)$$

Wich can be written as (Tielens, 2010) :

$$\tau_{\text{th}} \simeq 1.4 \times 10^6 \text{ yr} \left(\frac{P_{\text{th}}}{3000 \text{ K.cm}^{-3}} \right) \left(\frac{n}{1 \text{ cm}^{-3}} \right)^{-1} \left(\frac{n\Lambda}{10^{-33} \text{ J.s}^{-1}.(\text{Hatom})^{-1}} \right)^{-1} \quad (1.9)$$

For a typical CNM density of $n \sim 30 \text{ cm}^{-3}$, a temperature of $T \sim 80 \text{ K}$, and a radiation rate of $n\Lambda \sim 6 \times 10^{-33} \text{ W}$ per H atom, the cooling time τ_{th} is on the order of few 10^3 years. In contrast, for the WNM gas, the typical density of $n \sim 0.5 \text{ cm}^{-3}$ and the radiation rate $n\Lambda \sim 2 \times 10^{-33} \text{ W}$ per H atom lead to a cooling time τ_{th} on the order of few 10^6 years.

Therefore, the WNM gas phase at 10^4 K is a stable phase, but it takes time to reach this stability. CNM phase, on the other hand, is more stable and reaches equilibrium more quickly.

1.4.3.2 Ionisation equilibrium

Ionisation equilibrium is the time it takes for an electron to undergo recombination. It is calculated as the volumetric ion density, n_i , divided by the recombination energy loss, which is the volumetric ion density multiplied by that of electrons, n_e , and the reaction rate, Λ_{rec} . The radiative recombination time scale is as follows (Tielens, 2010) :

$$\tau_{\text{rec}} = \frac{n_i}{n_i n_e \Lambda_{\text{rec}}} \simeq 200 \text{ yr} \left(\frac{T}{1 \text{ K}} \right)^{0.6} \left(\frac{n_e}{1 \text{ cm}^{-3}} \right)^{-1} \quad (1.10)$$

In the CNM phase, the electron fraction is of the order of 10^{-3} , resulting in a recombination time on the order of few 10^5 years. However, for the WNM phase, the electron fraction is approximately 10^{-1} , leading to $\tau_{\text{rec}} \sim 10^6$ years.

1.4.3.3 Pressure equilibrium

Pressure equilibrium is achieved by the speed of sound, c_s , which makes the gas isobaric. The equation is as follows :

$$c_s = \sqrt{\frac{\gamma_{IG} k_B T}{m_{\text{tot}}}} \approx 10^2 \text{ m.s}^{-1} \left(\frac{T}{1 \text{ K}}\right)^{1/2} \quad (1.11)$$

With γ_{IG} the adiabatic index for ideal gas, k_B the Boltzmann constant, T the temperature in Kelvin and m_{tot} the total gas mass. Therefore, the time it takes for sound to traverse a cloud is the time to establish pressure equilibrium. The equation for this time, τ_s , is given by :

$$\tau_s = \frac{L_{\text{cloud}}}{c_s} \quad (1.12)$$

In the cold CNM phase, the sound speed is approximately 1 km.s^{-1} , resulting in an equilibrium time of 10^6 years for a cloud with a length of 1 pc. Therefore, the cold gas can be considered in thermal and ionisation equilibrium. On the other hand, in the WNM phase, the time is on the order of few 10^5 years for a c_s of around 10 km.s^{-1} and a cloud of 1 pc. This phase is therefore easily perturbed from thermal equilibrium and the cold gas is relatively more stable.

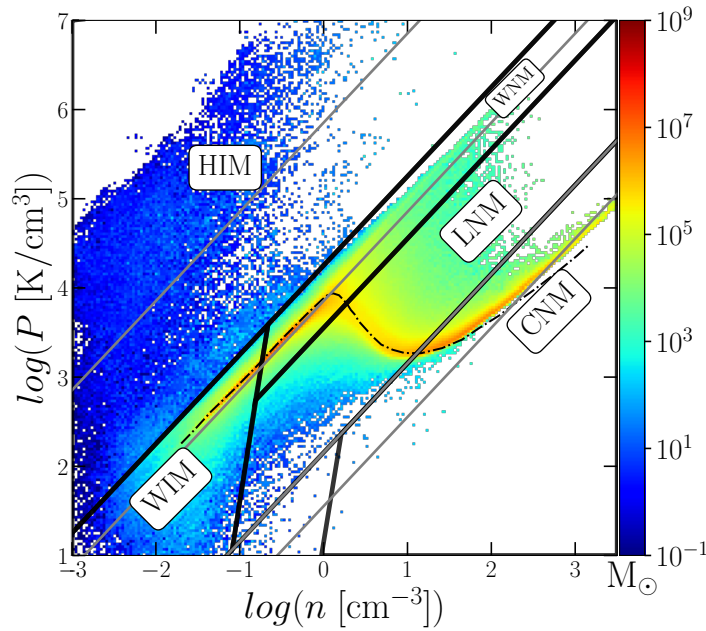


FIGURE 1.10 : Gas phase diagram of a simulation performed by (Nuñez-Castiñeyra et al., 2022). Solid black boundaries are given to partition the gas phases between the WNM and CNM phases, the unstable LNM and the warm and hot ionised media (WIM and HIM respectively). The dot-dashed curve corresponds to the gas in thermal equilibrium according to Wolfire et al. (1995). Grey oblique lines from bottom to top represent the isothermal lines at 50, 200, 10^4 and 10^6 K.

However, about 30% of the H_I gas is in the cold CNM phase (Nuñez-Castiñeyra et al., 2022), with the remainder in the WNM. This is because there are continual sources of turbulence, remnants of supernovae, and stellar winds operating on timescales of 10⁵ years, constantly causing the gas to change states. This is why nearly 20% of the gas is in the Lukewarm Neutral Medium (LNM), an intermediate unstable phase that attempts to reach stable phases but may or may not succeed (Murray et al., 2018).

Figure 1.10 is a diagram of five different gas phases obtained by a simulation performed by Nuñez-Castiñeyra et al. (2022). The grey isothermal lines represent the temperature at the different phases; Hot Ionised Medium (HIM) at 10⁶ K, Warm Ionised Medium (WIM) and Warm Neutral Medium (WNM) at 10⁴ K, Lukewarm Neutral Medium (LNM) at 200 K and Cold Neutral Medium (CNM) at 50 K. The plot shows the bimodal distribution of the H_I neutral gas in the warm and cold phases.

The Wolfire curve, represented by the black dot-dashed curve, shows the gas at thermal equilibrium (Wolfire et al., 1995). The best resolution in the simulation, which is 9 pc, does not allow to follow the Wolfire curve to the coldest and densest part of the distribution, where the transition to H₂ occurs.

1.5 Global appraisal of interstellar contents

Approximately 99% of the ISM mass is gas. About 60% of that gas in the Milky Way is in H_I regions, 23% of the hydrogen is ionised, and ~ 17% is in molecular clouds (Draine, 2011). In Figure 1.11, the diagram shows several phases of the interstellar gas. The small grey dots represent dust grains observed at a frequency of 353 GHz and used to trace the gas (see chapter 4). It can be observed that H_I, in light turquoise, forms a diffuse envelope and occupies the largest volume. It contains the majority of the mass. Between the atomic part visible at 21 cm and the green phase visible in CO at 115 GHz, there exists a phase represented by dark turquoise. This phase contains H₂ molecules that shield themselves from UV photons but have very low density to form CO molecules and/or make CO molecules radiate. It is the Dark Neutral Medium (DNM). It represents the second most massive phase after the H_I phase.

Figure 1.12 shows the spectrum of the 21 cm HI line, in gray, as a function of the velocity projected onto the line of sight in km/s. The black curve corresponds to the 2.6 mm CO lines. We note that the atomic phase is more diffuse because it covers velocity ranges where the molecular phase is absent.

The molecular phase, including hydrogen molecules H₂ and especially CO molecules, forms inside the CNM atomic gas. That is why, the detection of the CO line proves the presence of CNM in the region. This dense CNM absorbs 21 cm photons rapidly, which explains the presence of self-absorption notches of the 21 cm line at the same velocities as CO lines for nearby clouds in Fig.1.12. For distant molecular clouds, there is much more WNM along the line of sight, so even if there is a self-absorption notch, it is too weak to be detected. The loss of signal will be negligible against the strong emission background of the WNM.

Figure 1.13 describes the abundance of some chemical components as a function of extinction

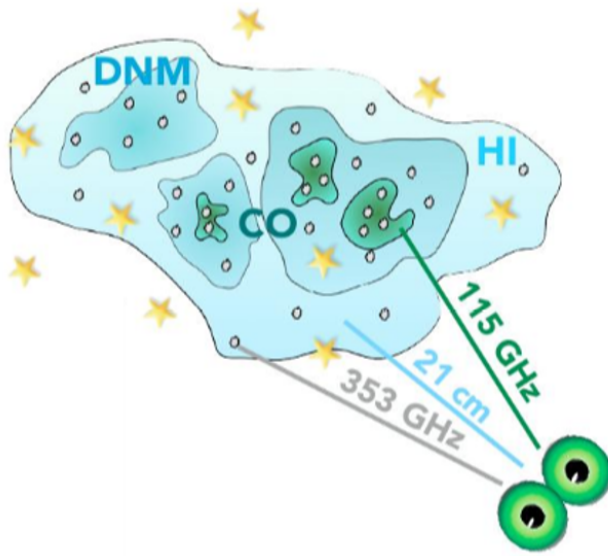


Figure 1.11 : Sketch representing the three neutral phases of the interstellar gas ; atomic hydrogen HI detected at 21 cm (light turquoise), the dark gas phase (DNM) that is undetectable (dark turquoise) and the dense molecular phase detectable in CO at 115 GHz (green). The observed dust grains at 353 GHz are shown in grey. (courtesy of I. Grenier)

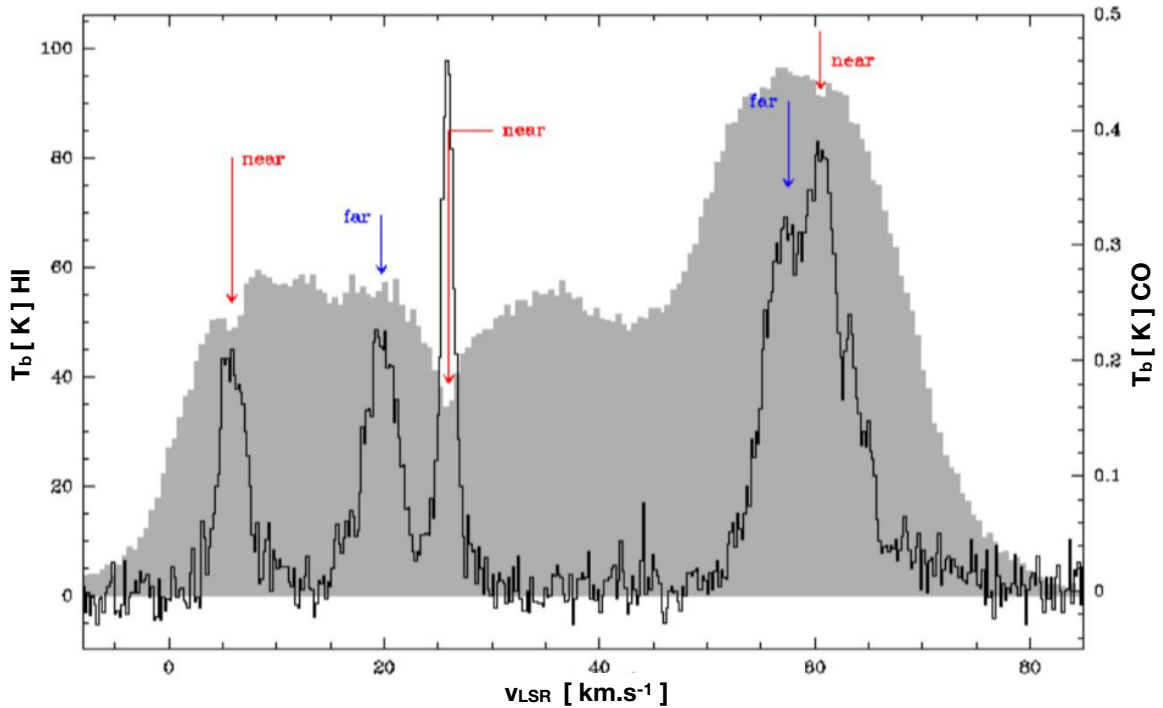


FIGURE 1.12 : Spectrum of the HI line at 21 cm and the 2.6 mm of CO molecular line, as a function of the velocity of the clouds projected onto the line of sight in km/s. The y-axes give the intensities of the HI and CO lines, expressed in equivalent temperature of a blackbody.

in the visible A_V in magnitude. This extinction, caused by the dust mixed with gas, describes the attenuation of starlight as one penetrates into the cloud. The left side of the graph represents the edge of the cloud. As we move towards the right, we approach the cloud core composed of

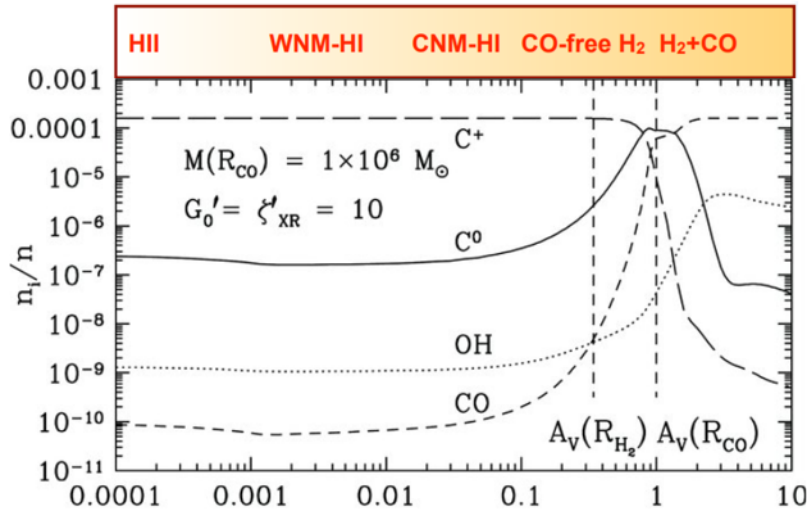


Figure 1.13 : The abundance of some chemical components in the various thicknesses of an arbitrary slab cloud, as a function of extinction in the visible A_v . (Wolfire et al., 2010)

CO, indicating an increasingly dense gas region. In the ionised phase (HII), starlight and especially UV radiation penetrates effortlessly, leading to a higher concentration of ions compared to atoms. Moving deeper into the cloud, ionisation decreases, and the warm atomic gas WNM is formed. Reaching the cloud's core, WNM cools to form the cold gas CNM. In this CNM phase, starlight is attenuated by approximately 10%, particularly in the optical and UV spectra. As the gas cools further, the dark molecular phase DNMM, CO-free, begins. From this point onward, starlight is significantly attenuated, giving rise to the cold molecular phase, in which the gas becomes dense enough to form molecules such as HCO^+ , CH, OH, then CO and many others.

On the ordinate axis of Fig.1.13, we have the abundance of various elements compared to the total number of atoms. The curve for C^+ remains relatively constant, even within the HI region, because light penetrates and ionises carbon. This occurs because the ionisation energy of carbon (11.26 eV) is lower than that of hydrogen (13.6 eV). Subsequently, carbon recombines into neutral C^0 when there is a decrease in the presence of ultraviolet radiation. As the shielding increases, the formation of CO dominates and locks up most of the carbon.

The decline in HI contribution becomes noticeable at an extinction level of $A_v \approx 0.4$ mag, which marks the H_2 molecule formation and its shielding effect against UV photons. This transition is indicated by the left vertical line. In contrast, CO emission increases within the range of extinctions between 1 and 2.5 mag, effectively preserving these molecules (Remy et al., 2018). The corresponding region is denoted by the right vertical line. The dark gas DNMM is primarily situated between the zone where HI intensity decreases and W_{CO} increases.

In Fig.1.14, the x-axis represents the column density of hydrogen regardless of its state, therefore, one should divide by two for H_2 column densities. On the y-axis, we have the optical depth of dust, τ , which reflects the column density of dust grains. This graph is a two-dimensional histogram across all directions of the sky, with the highest intensity value shown in red and the lowest in blue.

In the diffuse atomic phase, a linear relationship is observed, indicating a strong correlation between the quantities of gas and dust. Starting from 10^{20} cm^{-2} , a bump begins to appear indicating that the count of dust grains exceeds that of hydrogen atoms. This marks the phase of

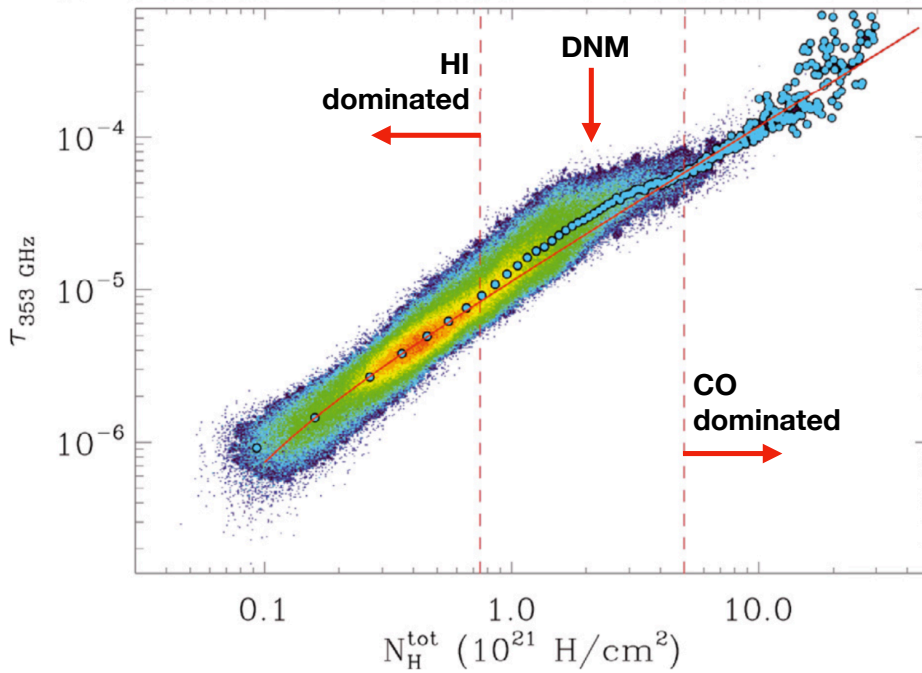


FIGURE 1.14 : A two-dimensional histogram of the dust optical depth at 353 GHz as a function of the total column density of hydrogen, $N(\text{H}_I + 2\text{H}_2)$. The highest intensity value shown in red and the lowest in blue. (Planck Collaboration et al., 2011)

dark gas (DNM), which is challenging to precisely quantify.

In the dense molecular phase, through the observation of CO lines and the use of the conversion factor X_{CO} , we can estimate the quantity of hydrogen molecules H_2 and consequently the hydrogen atoms. This should restore the expected correlation with dust. However, it is consistently found that the data points systematically deviate from the linear relationship. This suggests the possibility of missing gas, as CO is easily absorbed. Another possibility, that has been demonstrated, is that dust grains in dense CO cores become more emissive and inherently brighter, which contributes to the deviation from linearity (see Remy et al. (2017a) and references therein).

To conclude, the H_I gas is mainly warm and low-density, WNM, within which there are cold and dense clumps, CNM, giving rise to the molecular phase H_2 . The densest clumps are rich in CO molecules. Given the uncertainty in gas mass estimates in the dark and molecular phases of clouds, one can only infer the cosmic ray spectrum with adequate precision in the atomic phase.

Magnetic field

Our Galaxy is permeated by magnetic fields intimately linked to the ISM and cosmic rays. On large scales, its structure appears predominantly parallel to the Galactic plane on scales of at least several kpc (Zweibel, 2017). The results of Han (2017) show that magnetic field lines are oriented along the spiral arms, with possible reversals of direction between the arms and interarm regions. They also show that the azimuthal components are reversed in the halo on each side of the Galactic plane. On large scales, the magnetic field opposes the gravitational collapse of gas and confines cosmic rays in the Galactic halo. On a more local level, it affects turbulent movements such as supernova expansions and it regulates star formation.

The origin of the overall magnetic field remains uncertain. The most accepted hypothesis being that of a hydromagnetic dynamo where the differential rotation of a conducting fluid in a magnetic field generates currents that, in turn, amplify the initial field (Federrath, 2016). The magnetic field is directly coupled to ionised gas and indirectly to the rest of the neutral gas through ion-neutral interactions.

The total magnetic field, B_{tot} , can be separated into several distinct components ; the regular and turbulent fields, B_0 and δB respectively.

$$B_{\text{tot}} = B_0 + \delta B \quad (2.1)$$

The regular field has a well-defined direction, while the turbulent one exhibits numerous changes in direction. The turbulent field can be isotropic, denoted as B_{iso} , but can also preferentially align in response to gas flow compression or shearing, known as B_{aniso} . MHD¹ Magnetic turbulence is likely highly anisotropic, with eddies being elongated along the mean field direction and narrower in the perpendicular direction (Federrath, 2016). All these magnetic field components can be further divided into their projection on the plane of sky, B_{sky} , and along the line of sight, B_{los} .

$$B_{\text{tot}} = \sqrt{B_{\text{sky}}^2 + B_{\text{los}}^2} \quad (2.2)$$

¹Magnetohydrodynamics (MHD) is a branch of plasma physics that studies the behavior of electrically conducting fluids in the presence of magnetic fields.

2.1 Dust polarisation and magnetic field orientation

Interstellar dust grains are present throughout the universe and can absorb, emit, and scatter light. They are typically irregularly shaped and elongated, and can become aligned with the ambient magnetic field due to a physical process called "paramagnetic alignment". When light from a background source, such as a star, passes through a region containing aligned dust grains, it interacts with them and becomes polarised, meaning that the electromagnetic waves oscillate predominantly in one direction. The degree and the angle of polarisation are related to the orientation of the aligned dust grains. These parameters can be detected using a polarimeter and the direction of the magnetic field in the plane of the sky is perpendicular to the polarisation angle. This effect is most efficient for grains with sizes comparable to the wavelength of stellar radiation.

Another process is the emission of linearly polarised thermal radiation by dust grains, which peaks at far infrared and sub-mm wavelengths according to the dust temperature. After a 90° rotation, this radiation allows the characterisation of the magnetic field structure projected in the plane of the sky, B_{sky} , for example, with observations from the *Planck* telescope as shown in Figure 2.1.

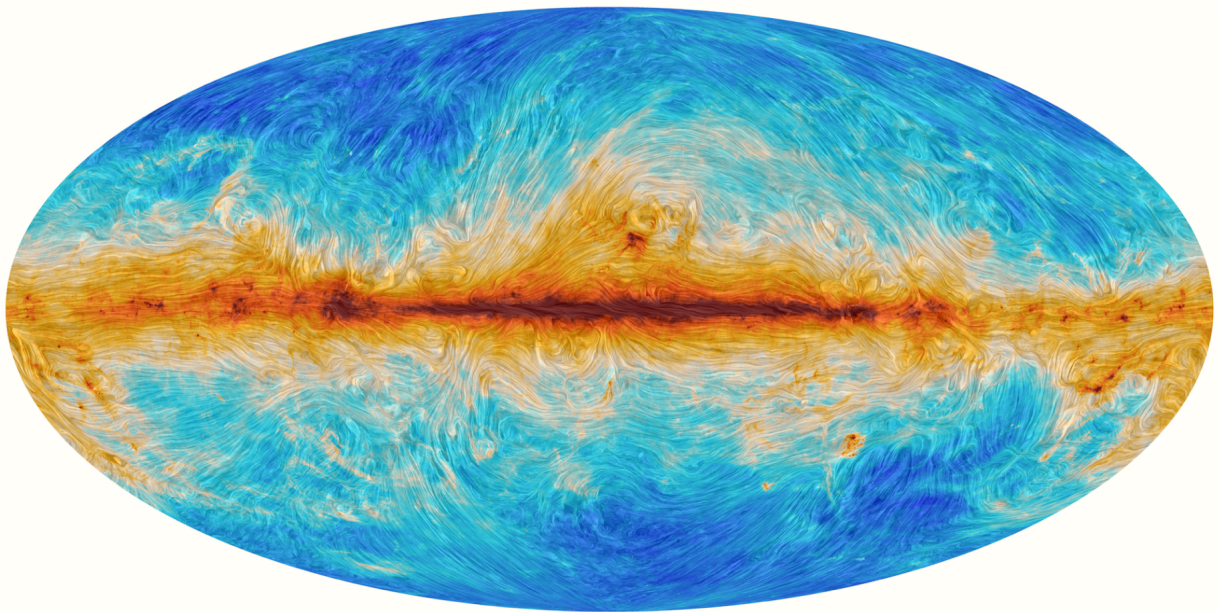


FIGURE 2.1 : Mollweide projection sky map of the HI column density. The overlaid transparency was generated using the Line Integral Convolution (LIC) method (Cabral & Leedom, 1993) to depict the orientation of the magnetic field in the plane of the sky, based on observations of polarised dust emission at 353 GHz by the *Planck* satellite. This map is taken from the gallery of the *Planck*'s website [<https://www.cosmos.esa.int/web/planck/picture-gallery>]

One way to quantify the regularity or disorderliness of the magnetic field in a given region is by using the polarisation angle dispersion function, S_ψ . By analysing the polarisation data and

the S_ψ dispersion, one can reveal important information about the properties of cosmic dust, such as its composition, size, and also the magnetic field's strength, orientation, and organisation in different regions of space.

Dust polarisation data are expressed as Stokes parameters (I, Q, U). The parameter I represents the real polarisation intensity while the measured one is calculated by $P = \sqrt{Q^2 + U^2}$. The Q and U Stokes parameters are defined with respect to the Galactic coordinates, but with a convention opposite to that of the International Astronomical Union (IAU) along the longitude axis. Consequently, the polarisation angle is defined as follows :

$$\psi_{IAU} = \frac{1}{2} \arctan(-U, Q) \quad (2.3)$$

ψ is zero at the North Galactic pole and it follows the IAU convention by increasing counter-clockwise with increasing longitude. The $\arctan(\sin, \cos)$ is the arc-tangent function that solves the π ambiguity taking into account the sign of the cosine.

When a cloud is the predominant dust cloud along its specific line of sight, dust polarisation measurements provide information about the magnetic field within that cloud, projected onto the plane of the sky, B_{sky} . To assess the consistency of the B_{sky} direction, we can employ the polarisation angle dispersion function (Planck Collaboration, Ade, et al., 2015) :

$$S_\psi(\vec{x}, \delta) = \sqrt{\frac{1}{N} \sum_{i=1}^N \left[\psi(\vec{x}) - \psi(\vec{x} + \vec{\delta}_i) \right]^2} \quad (2.4)$$

where $\Delta\psi_{xi} = \psi(\vec{x}) - \psi(\vec{x} + \vec{\delta}_i)$ is the difference between the polarisation angle in a given direction \vec{x} and in a displaced direction $\vec{x} + \vec{\delta}_i$. In practice, we can calculate $\Delta\psi_{xi}$ from the Stokes parameters as (Planck Collaboration, Ade, et al., 2015) :

$$\Delta\psi_{xi} = \frac{1}{2} \arctan(Q_i U_x - Q_x U_i, Q_i Q_x + U_i U_x) \quad (2.5)$$

where the x and i indices stand for the central and displaced directions, respectively. The average in S_ψ is taken over displaced directions spanning an annulus around the \vec{x} direction with an inner radius $\delta/2$ and an outer radius $3\delta/2$. We have degraded the original 4.8' resolution to an angular resolution of 14' (FWHM) in order to increase the signal to noise ratio. Therefore, we decided to take 15' for the δ lag.

The S_ψ dispersion values span from 0° , indicating a highly ordered B_{sky} magnetic field, to $S_\psi = 90^\circ$, signifying a disordered field configuration. In situations where the polarisation signal is overwhelmed by noise, S_ψ tends to converge to $\pi/\sqrt{12}$ ($\approx 52^\circ$) (Planck Collaboration, Ade, et al., 2015).

2.2 Plane-of-sky magnetic-field strength

The total magnetic field is composed of a mean component, \vec{B}_0 , and a small fluctuating one, $|\vec{\delta B}| \ll |\vec{B}_0|$. These fluctuations arise from Alfvén waves² and can be due to turbulent gas motions. The magnetic energy density, in the CGS unit system, is therefore :

$$\epsilon_B = \frac{B^2}{8\pi} = \frac{1}{8\pi} [B_0^2 + \delta B^2 + 2\vec{\delta B} \cdot \vec{B}_0] \quad (2.6)$$

2.2.1 DCF method

The Davis-Chandrasekhar-Fermi (DCF) method is a widely employed technique for estimating the strength of magnetic fields in the interstellar medium (ISM) projected onto the plane of the sky. This method was originally introduced by Davis (1951) and subsequently refined by Chandrasekhar and Fermi (1953).

The DCF method is grounded in the assumption that isotropic turbulent motions initiate the propagation of Alfvén waves, responsible for the observed polarisation of dust grains within the ISM. These Alfvén waves are presumed to be incompressible and transverse ($\vec{\delta B} \cdot \vec{B}_0 = 0$) within the frozen-in magnetic field.

The method uses both polarisation and spectroscopic data to derive the magnetic field strength. Polarisation data is utilised to determine the direction of the magnetic field, while spectroscopic data is employed to estimate the velocity dispersion of the gas. This velocity dispersion is directly related to the Alfvén velocity, serving as an indicator of magnetic field strength. Consequently, the DCF method assumes that the kinetic energy of turbulence is equal to the fluctuating magnetic energy density, and that the dispersion in polarisation angle ψ reflects the dispersion in magnetic-field orientation.

From the equipartition condition :

$$\frac{1}{2}\rho\delta v^2 = \frac{\delta B^2}{8\pi} \quad (2.7)$$

By dividing both sides by B_0^2 :

$$\frac{\rho}{B_0^2}\delta v^2 = \frac{1}{4\pi} \frac{\delta B^2}{B_0^2} \quad (2.8)$$

And from $S_\psi \approx \delta B/B_0$, one obtains :

$$B_{sky}^{DCF} = f \sqrt{4\pi\rho} \frac{\delta v}{S_\psi} \quad (2.9)$$

where f is added as a correction factor.

²Alfvén waves are a type of MHD wave that propagates through a magnetised plasma. These waves are characterised by their ability to transmit disturbances or fluctuations in magnetic fields and can play a significant role in the dynamics of plasmas. They are transverse waves and magnetosonic, meaning that the oscillations are perpendicular to the direction of the magnetic field lines and they propagate at the Alfvén velocity, v_A .

The DCF method offers several advantages due to its simplicity and versatility. It stands out for its ease of application, avoiding the need for intricate modeling or simulations. It can be effectively employed to estimate magnetic field strength across a wide array of astrophysical settings. Researchers have utilised the DCF method to investigate magnetic fields in diverse objects, including molecular clouds, HII regions, and supernova remnants.

Nevertheless, the DCF method carries certain limitations and assumptions that impact its accuracy. A primary assumption is the isotropic nature of turbulence within the interstellar medium (ISM). However, observations suggest that ISM turbulence is often anisotropic, potentially leading to significant deviations from actual values (Goldreich & Sridhar, 1995). Another assumption concerns the dominance of Alfvén waves as the primary mode of wave propagation in the ISM. Yet, recent studies have indicated that compressible modes, also known as fast and slow magnetosonic modes, might also play a significant role especially in regions characterised by high density and strong magnetic fields (Heyvaerts & Priest, 1983).

Furthermore, the DCF method neglects the effects of projection and line-of-sight integration in the polarisation data, introducing potential inaccuracies in inferred magnetic field strength. It assumes a uniform magnetic field and perfect alignment of dust grains with the magnetic field. In reality, magnetic fields can exhibit complexity, and dust grains may deviate from perfect alignment or possess varying polarisation properties.

The correction factor, denoted as f , plays a crucial role in rectifying the limitations of the classical DCF method by accounting for the influence of compressible modes of wave propagation, which were previously neglected. This factor is defined as the ratio between the true Alfvén velocity and the velocity dispersion estimated using the DCF method. It quantifies the extent to which compressible modes of wave propagation contribute to the observed velocity dispersion. Assuming to be independent of the specific physical conditions within the ISM, f is typically treated as a constant.

In the original work by (Chandrasekhar & Fermi, 1953), a value of $f = 1/\sqrt{3}$ was proposed, based on the assumption of isotropic turbulence versus 2D polarisation information. However, subsequent research introduced variations in the suggested values, ranging from 0.3 to 0.7 based on MHD simulations. Notably, Skolidis and Tassis (2021) challenged the commonly adopted constants, revealing that they do not apply across all ISM conditions. They demonstrated that f is contingent on the turbulent sonic Mach number, a parameter reflecting compressibility. In simulations, the value of f is observed to decrease as the Mach number increases. For instance, in the context of supersonic models with a sonic Mach number $M_s = 0.7$, the DCF method, without the inclusion of the f factor, deviates from the true value by a factor of ≈ 5 . This suggests that, in such cases, the correction factor f needs to equal $1/5$ to yield accurate estimations. Conversely, in subsonic models with M_s of 1.2, 4.0, and 7.0, an appropriate correction factor is $\approx 1/3$ to align with the actual conditions.

In summary, the DCF method is a widely used technique for estimating the strength of magnetic fields in the ISM, projected onto the plane of the sky. It is relatively simple and easy to apply, but it has several limitations and assumptions. Skolidis and Tassis (2021) proposed a new method (hereafter the ST method) for estimating the strength of plane-of-sky magnetic fields in the ISM that does not require a correction factor.

2.2.2 ST method

This new method is based on a statistical approach that takes into account the anisotropic nature of turbulence in the ISM which is a major source of uncertainty in the classical DCF method. It also takes into account the compressible modes of wave propagation, also known as fast and slow magnetosonic modes, which are neglected in the DCF method. To include these modes, the cross-term of eq.2.6 is not omitted $\vec{\delta B} \cdot \vec{B}_0 \neq 0$ (Skalidis & Tassis, 2021). The energy equation will therefore be :

$$\frac{1}{2}\rho\delta v^2 = \frac{\delta B B_0}{4\pi} \quad (2.10)$$

In that equation, the perturbation δB is aligned with the magnetic field B_0 . This is due to the local alignment between δB and δv , which is called "dynamic alignment". This alignment has been observed in simulations of both incompressible and compressible turbulence (Skalidis & Tassis, 2021).

After dividing both terms by B_0^2 and replacing $\delta B/B_0$ by S_ψ , Skalidis and Tassis (2021) propose an alternative formulation that agrees within 20-30% with MHD simulation data :

$$B_{sky}^{ST} = \sqrt{2\pi\rho} \frac{\delta v}{\sqrt{S_\psi}} \quad (2.11)$$

Another advantage of the new method is that it does not require a correction factor and it is independent of the sonic Mach number.

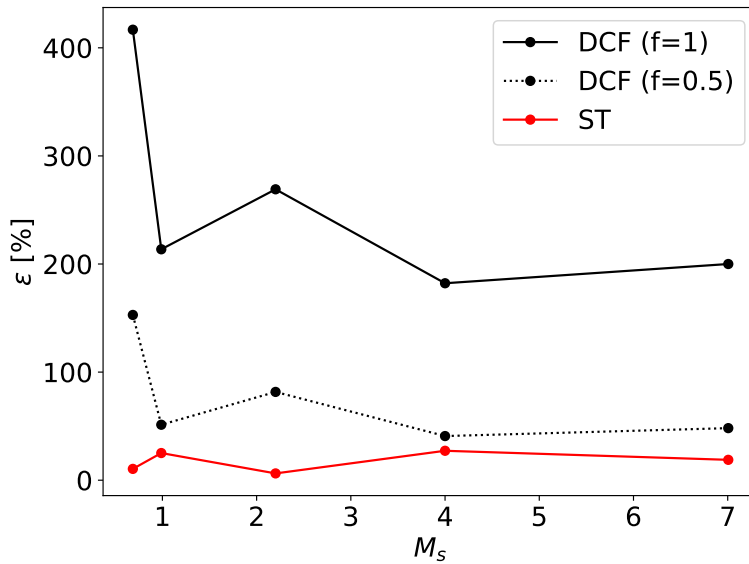


FIGURE 2.2 : Relative deviation between DCF and ST B_{sky} estimates with respect to the true simulated value, as a function of the sonic Mach number. (Skalidis & Tassis, 2021)

The simulations of Skalidis and Tassis (2021) showed that B_{sky}^{DCF} using a correction fraction $f = 0.5$ systematically overestimates the real values of plane-of-sky magnetic field, as shown

in Fig.2.2. Therefore, it represents an upper limit to the true B_{sky} . They also showed that B_{sky}^{ST} slightly underestimates the real magnetic field strength, and therefore represents a lower limit to B_{sky} .

2.3 Line-of-sight magnetic-field strength

The line-of-sight magnetic field, B_{los} , refers to the component of magnetic field that lies along the direction of observation. The direct measurement of B_{los} is based on the Zeeman effect or the Faraday rotation in spectroscopic observations.

The Faraday rotation is based on the Faraday effect, which is the rotation of the plane of polarisation of linearly polarised light as it passes through a magnetised plasma. Counterclockwise rotation occurs if the magnetic field is oriented toward the observer and clockwise if the field points away from the observer. The rotation angle $\Delta\theta$ is given by (Burn, 1966) :

$$\Delta\theta = \lambda^2 \times \Phi \quad (2.12)$$

Where λ is the light wavelength and Φ the rotation measure, in rad.m^{-2} , and described as :

$$\Phi \propto \int_{\text{source}}^{\text{observer}} B_{0,\text{los}} n_e dL_{\text{sight}} \quad (2.13)$$

with $B_{0,\text{los}}$ the magnetic field strength projected in the line of sight and n_e the electron number density of the plasma. It's important to note that the amount of rotation depends on the wavelength of the light. Therefore, observations at multiple wavelengths are often necessary to calculate the magnetic field's properties accurately. Another important effect is the Faraday depolarisation. It can happen in regions of space where the magnetic field varies significantly with position or where there are turbulent magnetic fields (Sokoloff et al., 1998). In that case, a range of frequencies within a linearly polarised wave experiences different amounts of Faraday rotation. As a result, different parts of the wave become polarised in different directions or to different degrees and therefore, the wave becomes elliptically polarised or even fully depolarised. This effect can make it difficult to observe or measure the polarisation properties of radio sources accurately.

The Zeeman effect is the altering or splitting of spectral lines in the electromagnetic spectrum into multiple components due to the influence of a magnetic field. The spectral lines are narrow with discrete wavelengths in the electromagnetic spectrum. They correspond to specific transitions by electrons within atoms or molecules, when changing their energy levels. Therefore, these spectral lines serve as unique signatures for the elements present in celestial objects. In a star's atmosphere or interstellar cloud, the magnetic field interacts with charged particles such as electrons. This interaction modifies the atomic energy levels leading to a split of the original spectral line into multiple components which appear at slightly different wavelengths compared to the unaffected spectral line. The extent of this splitting depends on the magnetic field strength, the properties of the atomic or molecular species involved, and the specific spectral

line being observed. This effect is more significant for molecular lines (OH, CN, H₂O) (Heiles & Crutcher, 2005). In the interstellar neutral hydrogen clouds, the Zeeman effect is the splitting of the 21 cm line (Davies et al., 1968). There are two types of Zeeman effect :

- Normal Zeeman effect where the spectral line splits into three components ; One at the original wavelength and two additional components at slightly longer and shorter wavelengths. The three resulting components are symmetrically distributed around the original spectral line. The separation between these components is directly proportional to the strength of the magnetic field along the line of sight (LOS).
- Anomalous Zeeman effect occurs in more complex atoms or molecules, typically those with larger numbers of electrons and more intricate energy-level structures. Unlike the normal Zeeman effect, the anomalous one leads to an array of additional components with more irregular patterns of spectral line splitting. This irregularity results from the complex relationships between the magnetic field and various quantum properties of electrons, such as their spins and angular momenta, This effect does not adhere to the straightforward proportional splitting.

2.4 Turbulence and Alfvén Mach number

The ISM collapses within the gravitational potential of the Galaxy, but most of the gas mass remains within approximately 300 pc from the Galactic plane. To do so, it necessitates support from a pressure of $P_{\text{tot}}/k_B \sim 2 \times 10^4 \text{ K.cm}^{-3}$, which is roughly ten times its thermal pressure (Cox, 2005). The total pressure encompasses non-thermal contributions originating from supersonic turbulence and magnetic fields. Therefore, understanding the characteristics of interstellar turbulence is crucial, as it serves as the primary mechanism preventing molecular clouds from collapsing under their self-gravity (Hennebelle & Falgarone, 2012). However, before delving into that, I would like to introduce an important physical quantity.

The Alfvén Mach number, M_A , is a dimensionless quantity that compares the strength of the magnetic-field energy density (e_B) and the kinetic energy of the turbulent fluid motions in a plasma (e_{kin}).

$$M_A^2 = \frac{e_{\text{kin}}}{e_B} = \frac{(1/2)\rho \delta v^2}{B_{\text{tot}}^2/(8\pi)} \quad (2.14)$$

in the CGS system. The mass density of the plasma is ρ and the total magnetic field strength, B_{tot} , is the sum of the mean field and the turbulent one $B_{\text{tot}} = B_0 + \delta B$. The Alfvén Mach number therefore compares the characteristic velocity of the turbulence, δv , with the Alfvén velocity, $v_A = B/\sqrt{4\pi\rho}$. Beattie et al. (2022) introduce three different Alfvén Mach numbers that are relevant for compressible³ MHD turbulence depending on the magnetic field. The first one is the mean-field Alfvén Mach number, $M_{A,0}$, which compares the kinetic energy of fluid motions with the large-scale magnetic energy. It is defined as

$$M_{A,0} = \sqrt{4\pi\rho} \frac{\delta v}{B_0} = \frac{\delta v}{v_{A,0}} \quad (2.15)$$

³Compressible means that the fluid density varies significantly during the flow

The second one is the turbulent-field Alfvén Mach number, $M_{A,\text{turb}}$, which compares the turbulent magnetic energy with the kinetic energy :

$$M_{A,\text{turb}} = \sqrt{4\pi\rho} \frac{\delta v}{\delta B} = \frac{\delta v}{v_{A,\text{turb}}} \quad (2.16)$$

The total-field Alfvén Mach number, $M_{A,\text{tot}}$, compares the total magnetic energy, including the large-scale and the turbulent ones, with the kinetic energy.

$$M_{A,\text{tot}} = \sqrt{4\pi\rho} \frac{\delta v}{B_{\text{tot}}} = \frac{\delta v}{v_{A,\text{tot}}} \quad (2.17)$$

The total-field Alfvén Mach number relates directly to the energy equilibrium of the plasma and gives information about the efficiency of magnetic fields in controlling the plasma dynamics. In other words, it tells us how fast the fluid is moving relative to the magnetic field.

A high Alfvén Mach number means that the fluid motions can easily drag the magnetic field, and the latter is not able to control the plasma dynamics. This is often the case in highly turbulent plasmas, where the fluid motions are chaotic. On the other hand, a low Alfvén Mach number means that the magnetic field is stiff and able to control the plasma dynamics. The simulations by Beattie et al. (2022) showed that if the three Alfvén Mach numbers increase, the actual rate of increase differs for each one of them. The mean-field Alfvén Mach number, $M_{A,0}$, increases more slowly than the other two numbers. This is because the large-scale magnetic field is less affected by the turbulent motions than the turbulent magnetic field. As a result, the large-scale magnetic field remains relatively strong even as the fluid motions become stronger. The turbulent-field Alfvén Mach number, $M_{A,\text{turb}}$, increases more rapidly than the other two numbers. This is because the turbulent magnetic field is more affected by the fluid motions than the large-scale magnetic field. As a result, the turbulent magnetic field becomes weaker more quickly as the fluid motions become stronger. The total-field Alfvén Mach number, $M_{A,\text{tot}}$, is a combination of the mean-field and turbulent-field Alfvén Mach numbers. As a result, it increases more slowly than $M_{A,\text{turb}}$ but more rapidly than $M_{A,0}$.

Let's return to interstellar turbulence. Turbulence is a phenomenon characterised by the presence of irregular eddy motions. It is the instability of smooth, ordered (laminar) flows when inertial forces, $\vec{v} \cdot \nabla \vec{v}$ associated with fluid motion, significantly surpass the viscosity-induced forces $\nu \Delta \vec{v}$, where ν is the kinematic viscosity. This occurs when the Reynolds number $Re = \ell v_\ell / \nu$ at a characteristic scale ℓ and velocity v_ℓ exceeds a few hundred. As a result of this instability, turbulent motion passes from larger to smaller scales, transferring kinetic energy down to the dissipation scale ℓ_D , where energy is converted into heat due to particle viscosity. This process is known as the turbulent energy cascade. The time-scale for the growth of this instability is of the order of the eddy turnover time $\tau_\ell = \ell / v_\ell$ at each length scale ℓ .

The work of Kolmogorov (1941) introduced the fundamental concept of a dissipationless cascade, characterised by a transfer rate of kinetic energy that remains independent of scale between the injection and dissipation scales. For incompressible turbulence (constant ρ), the ϵ rate of kinetic energy⁴ supplied to the fluid from scale to scale per unit time and per unit mass

⁴Kinetic energy of the turbulent fluid is : $\frac{1}{2}\rho v^2$

is $\epsilon \propto v_\ell^2/\tau_\ell \propto v_\ell^2/\tau_\ell = v_\ell^3/\ell$. Because the ϵ rate is constant, $v_\ell \propto \ell^{1/3}$, so the velocity of eddies and turbulence intensity slowly decrease with decreasing ℓ scale. A dimensional analysis shows how the energy spectrum per unit mass is distributed with wavenumber $k = 2\pi/\ell$ such as $[k] = L^{-1}$. The total energy in the spectrum $\int_0^\infty E(k) dk$ scales with the total input kinetic energy per unit mass ($\frac{1}{2}v_\ell^2$), so $[E(k) dk] = L^2 T^{-2}$ and $[E(k)] = L^3 T^{-2}$. The transfer rate ϵ scales as $[\epsilon] = L^2 T^{-3}$, so the solution for $[E(k)] = [\epsilon]^a [k]^b$ is $E(k) \propto \epsilon^{2/3} k^{-5/3}$ known as the Kolmogorov spectrum even though the 5/3 slope was derived after the original Kolmogorov study. Another way to obtain that slope is by $E(k) dk \propto v_\ell^2 \propto (\epsilon^{1/3} \ell^{1/3})^2 \propto \epsilon^{2/3} k^{-2/3}$ which means that the total kinetic energy spectrum scales as $E(k) \propto k^{-5/3}$ (see Fig.2.3).

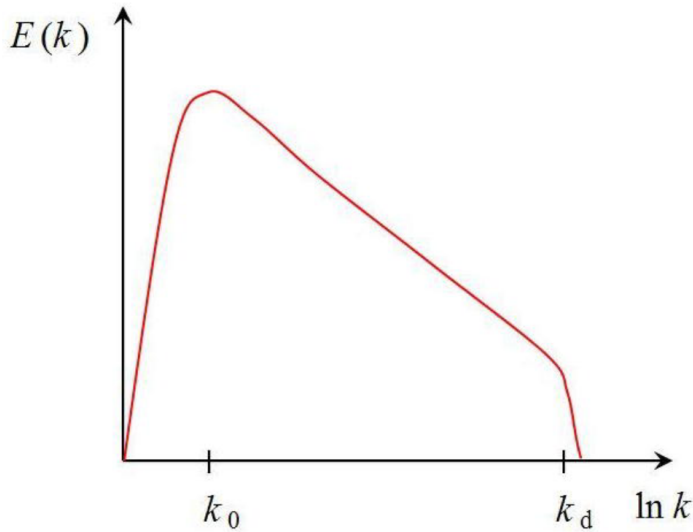


Figure 2.3 : A representation of the Kolmogorov energy spectrum per unit mass, as a function of the wavenumber k , for an incompressible, homogeneous, isotropic fluid turbulence. Kinetic energy is injected at $k = k_0$ and cascades to larger k , to be dissipated and converted into heat at $k = k_d$. The $k_0 < k < k_d$ represents the inertial range where the flow is controlled by inertia forces, and kinetic energy does not dissipate.

However, the MHD turbulence, where magnetic fields interact with fluid flows, poses challenges. The characteristic of MHD turbulence is that Alfvén wave packets traveling in the same direction along magnetic field lines don't interact with each other. The interactions only occur between waves moving in opposite directions. Iroshnikov (1964) and Kraichnan (1965) formulated the first phenomenological theory of MHD turbulence. They found that the energy spectrum scales as $E(k) \propto k^{-3/2}$. An essential assumption of their approach is that the eddies are isotropic. However, MHD turbulence is largely anisotropic, with energy transfer from large to small scales predominantly occurring perpendicular to the mean magnetic field direction, as supported by observations (Biskamp, 2003).

Therefore, Goldreich and Sridhar (1995) have developed a theory known as critical balance which takes into account the anisotropy in incompressible MHD turbulence. As the energy cascade proceeds to smaller scales, turbulent eddies progressively become elongated along the large-scale field. The Alfvén wave frequency (propagating at the Alfvén velocity v_A) and the non-linear cascade frequency are in critical balance $k_{\parallel} v_A \approx v_{\perp} k_{\perp}$. Therefore they found that the energy spectrum per unit mass is $E(k_{\perp}) \propto \epsilon^{2/3} k^{-5/3}$ and $E(k_{\parallel}) \propto \epsilon^{3/2} v_A^{-5/2} k_{\parallel}^{-5/2}$

The nature and properties of turbulence in the ISM are still highly debated and controversial. This is due in part to the huge range of scales separating those of the energy injection at the Galaxy scale, from those where it is dissipated, presumably below the milliparsec scale. It is also due to the fact that the turbulence is compressible, magnetised and multi-phasic. Given the

complexity of the problem, analytical rigor is scarce, and our understanding primarily stems from numerical simulations conducted over the past two decades.

2.5 Interstellar values of the magnetic field

In ideal MHD, where the fluid is treated as a perfect conductor, the magnetic field lines are "tied" or "frozen" and advected along with fluid. When the fluid moves, it carries along the embedded magnetic field lines without allowing them to slip or disconnect. This concept is the magnetic flux freezing. The break down of the ideal MHD conditions allows magnetic reconnection⁵ which releases the stored energy from the magnetic field (Priest & Forbes, 2000). The concept of magnetic fields being frozen into fluids with infinite electrical conductivity was first proposed by Alfvén (1942). The frozen-in condition leads to a relationship between magnetic intensity (B) and gas density (ρ) which reflects the movements of the gas relative to magnetic field lines. That relation is $B \propto \rho^\kappa$ with κ a constant determined by the specific conditions of the system.

If the gas contraction occurs parallel to the field lines, the magnetic field is not amplified and remains constant ($\kappa = 0$). In cases where motion is perpendicular to the field lines, it can be demonstrated that $B \propto \rho$. When contraction takes on a spherical form, the mass enclosed is $(4\pi R^3)\rho$ and the magnetic field through the surface is $(4\pi R^2)B$. The magnetic intensity is therefore $B \propto \rho^{2/3}$. However, maintaining a spherical shape during contraction is unlikely, particularly in the presence of a non-negligible magnetic field. Under these conditions, it is expected that equilibrium along the field lines will be established. According to Virial theorem, there is a balance between the thermal and potential energies of a system in a stable equilibrium state, $2E_{\text{th}} + E_{\text{pot}} = 0 \Rightarrow 3nk_B T = \frac{3}{5} \frac{GM^2}{R}$. Introducing the sound speed $c_s^2 = \frac{5}{3} \frac{k_B T}{M}$, the Virial relation leads to $c_s^2 \propto \phi$, where ϕ is the gravitational potential. In that case, $B \propto c_s \rho^{1/2}$. Basu (2000) compared data from Crutcher (1999) with this expression, achieving good agreement, which further improves when using velocity dispersion σ , related to the kinetic energy of the gas movement, instead of c_s , related to the thermal energy. Another simpler interpretation of this relationship is equipartition between magnetic and kinetic energy densities : $B^2/(8\pi) \propto \frac{1}{2}\rho\sigma^2$.

The overall strength of the magnetic field in the solar neighborhood is $5.62 \pm 0.01 \mu\text{G}$, as measured by Voyager 1 (Burlaga et al., 2013). Burlaga et al. (2015) provide first insights into in situ measurements of turbulent magnetic fields in the local ISM based on the results of the magnetometer onboard Voyager 1. They identified a weak turbulent component exhibiting an energy distribution consistent with a Kolmogorov spectrum. The ratio of turbulent fluctuations to the average field is relatively small, ~ 0.023 . Additionally, their findings suggest that the turbulence is predominantly compressible.

On a Galactic scale, the mean magnetic field strength varies across different regions across the Milky Way. According to Wielebinski (2005), magnetic field lines in the Milky Way are concentrated in the Galactic plane, with a typical strength of $\sim 10 \mu\text{G}$ in the inner regions, decreasing to about $\sim 5 \mu\text{G}$ at radii beyond 15 kpc. In certain areas, such as those near massive

⁵Magnetic reconnection is a physical process occurring in electrically conducting plasmas, in which the magnetic topology is rearranged and magnetic energy is converted to kinetic energy, thermal energy, and particle acceleration (Mozer & Pritchett, 2010).

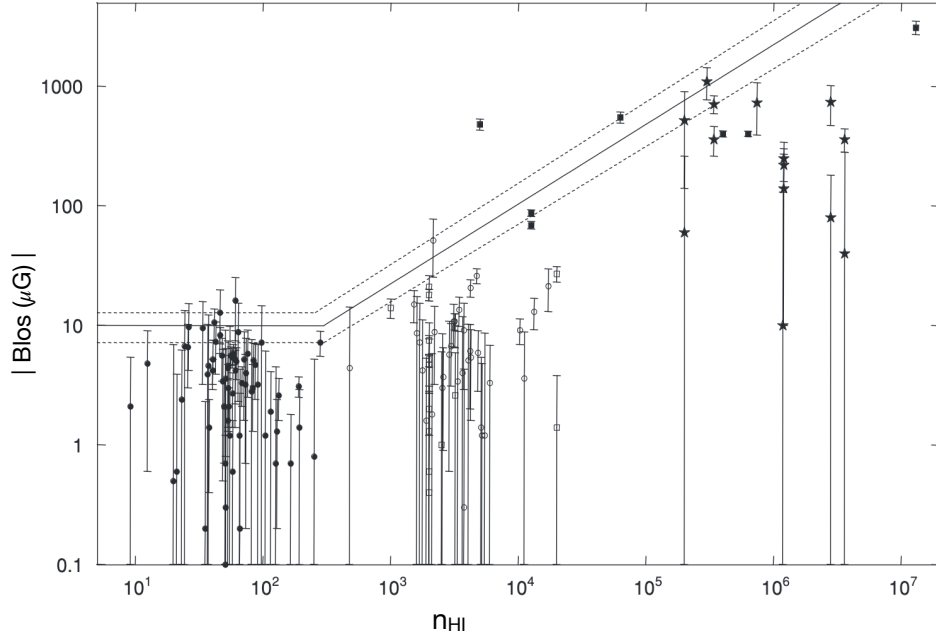


FIGURE 2.4 : Line-of-sight magnetic field strength B_{los} , as determined through Zeeman effect measurements, plotted against HI volume density (in cm^{-3}) for a selection of diffuse and molecular clouds. The accompanying error bars represent 1σ uncertainties in the measurements. Various symbols are employed to denote the cloud type and the source of the measurement. Filled circles represent HI diffuse clouds measured by Heiles in 2004, open circles correspond to dark clouds measured by Troland in 2008, and open squares represent other clouds surveyed by Crutcher in 1999. Additionally, filled squares represent molecular clouds from Crutcher’s 1999 study, while stars represent molecular clouds surveyed by Falgarone in 2008. The solid line illustrates the most likely maximum $B_{\text{tot}}(n_{\text{HI}})$ values derived through Bayesian analysis of the plotted B_{los} data. Dotted line segments encompass the ranges determined by acceptable alternative model parameters, indicating the inherent uncertainty within the model. (Crutcher et al., 2010)

star-forming regions or supernova remnants, the magnetic field strength can exceed $10\ \mu\text{G}$ and may even reach several hundred μG . The Galactic Centre region exhibits unique non-thermal radio arcs and filaments with field strengths of 100 to $400\ \mu\text{G}$ (Yusef-Zadeh et al., 2022) and a $100\ \mu\text{G}$ field has been estimated in the envelope of the massive Sgr B2 cloud in the central molecular zone (Yusef-Zadeh et al., 2024). Orlando and Strong (2013) conducted a model of synchrotron emission and predicted values for the local magnetic field. They predicted a regular magnetic field component of $2\ \mu\text{G}$ and a total magnetic field strength of $\sim 6\ \mu\text{G}$, which aligns with measurements from Voyager. Additionally, J. Xu and Han (2019) demonstrated that the local magnetic field in the Galactic disc, where a significant portion of the ISM resides, follows the local spiral arms and has a field strength of $1.6\ \mu\text{G}$.

Crutcher et al. (2010) examined the density-dependent behavior of magnetic fields in molecular clouds, utilising four Zeeman surveys to estimate the line-of-sight magnetic field strength, B_{los} , in each cloud. The first survey, conducted by Crutcher himself in 1999, focused on a set of 27 molecular clouds. The second survey, carried out in 2008 by Falgarone et al., utilised the IRAM 30 m telescope to measure the Zeeman effect in the CN spectral line. The third survey, performed in 2012 by Li and Henning, employed the Atacama Pathfinder EXperiment (APEX) telescope to measure the Zeeman effect in the 3 mm spectral line in the Taurus molecular cloud. The last survey, conducted in 2014 by Heiles, utilised the Green Bank Telescope (GBT) to measure the Zeeman effect in the 21 cm spectral line of atomic hydrogen within the Milky Way. Figure 2.4 displays the results of the B_{los} measurements and their corresponding 1σ uncertainties for both diffuse and molecular clouds, plotted as a function of the n_{HI} . Zeeman measurements also provide the direction of the line-of-sight component. In the plot, only the magnitudes $|B_{\text{los}}|$ are represented. The study by Crutcher et al. (2010) revealed that, for atomic gas densities between a few cm^{-3} and 300 cm^{-3} typical of the CNM, the most probable maximum values for the total magnetic field strength B_{tot} are approximately $10\ \mu\text{G}$. The field strength then rises in denser molecular clouds by compression with the gas infall.

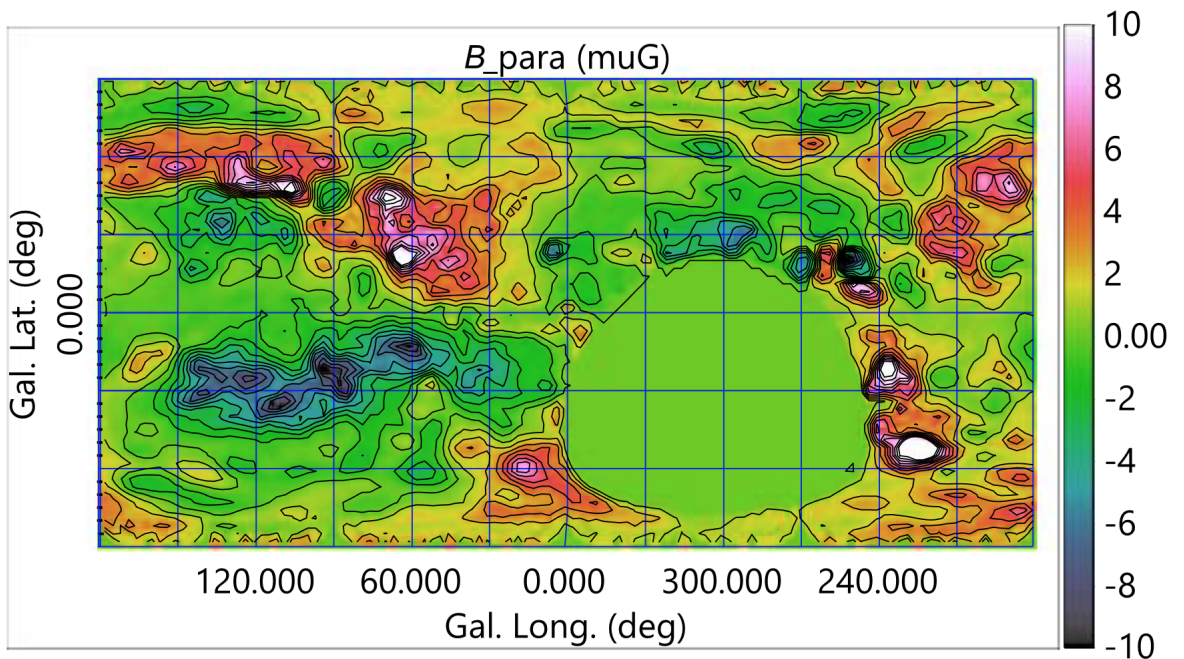


FIGURE 2.5 : Map of $\langle B_{\parallel} \rangle$ with contours at intervals of $1\ \mu\text{G}$. Positive values in red indicate a magnetic field away from the observer, and negative ones in blue indicate a field approaching the observer.

In Fig. 2.4, one observation at a density of $10^{3.7}\text{ cm}^{-3}$ notably exceeds the upper limit of the magnetic field strength inferred from the analysis. The authors noted that this outlier corresponds to the giant molecular cloud Sgr B2 North, which is thought to be the most massive in the Galaxy. It features highly active star formation, distinctive chemical properties, and a high ionisation rate, making it a prominent source of complex molecule emissions. The large ma-

agnetic field strength in/around this cloud has just been confirmed from synchrotron emission (Yusef-Zadeh et al., 2024).

However, it is essential to acknowledge that the Zeeman effect measures the direction-averaged line-of-sight magnetic field strength, which might not fully capture the magnetic-field tangling within a given region (Crutcher et al., 2010).

Sofue et al. (2019) has exploited the correlation between maps of rotation measure, H α column density, and radio thermal and synchrotron brightness to infer B_{los} strengths of 1 to 3 μG in the diffuse atomic gas (WNM) outside compressed bubble rims. Figure 2.5 shows the obtained all-sky map of $\langle B_{\parallel} \rangle$. This map is not affected by the line-of-sight depth and exhibits the field strength and direction only. It is interesting to note that both the northern and southern polar regions show positive B_{\parallel} around 1 μG , indicating that the vertical field directions are pointing away from the Sun.

Galactic cosmic rays

Cosmic rays (CRs) with a kinetic energy of a few GeV play a crucial role in the evolution of galaxies, especially through their various propagation processes. At this energy, their pressure is of the same order of magnitude as the magnetic or the gas pressure in the ISM. The challenge with these particles of moderate energies is their detection, which is why indirect observation methods based on hadronic interactions of CRs with interstellar gas have been used. In order to access the CR flux, it is necessary to know the column density of interstellar gas which is the integration of the volume density over the line of sight $\int n_{\text{gas}} dL_{\text{sight}}$.

3.1 Brief history

The story began in 1785 by an electroscope which was the first electrical measuring instrument. It detects an electric charge based on the Coulomb electrostatic force and was used only for high voltage sources. In that year, Coulomb found that electroscopes can spontaneously discharge in air. Fifty years later, Faraday confirmed this observation using better insulation technology. In the end of the XIXth century, radioactivity was discovered by Becquerel and Marie Curie found that radiations from the radioactive elements can discharge electroscopes. They concluded that there are radiations that ionise air and their sources are the radioactive elements in the ground.

In the beginning of the XXth century, experiments by Rutherford and others show that the ionisation rate is reduced when the electroscope is surrounded by metal shields. In 1907, Eve measured the ionisation over the center of the Atlantic Ocean and found no difference compared to the observations in England. One year after, they found a drop of 28 % in the ionisation rate when the observation was made at the bottom of a salt mine. They concluded that the Earth serves as the primary origin of penetrating radiation, while specific bodies of water, soil types and salt deposits are relatively devoid of radioactive elements, making them effective barriers against such radiation.

In parallel, the Wilson cloud chamber was invented. It is a particle detector used for visualising the passage of ionising radiation and played an important role in experimental particle physics from the 1920s to the 1950s, "the most original and wonderful instrument in scientific history" said Rutherford.

In 1909, Wulf improved the electroscope up to a sensitivity of 1 volt and made it transportable. On his Easter holiday trip in Paris, he measured the ionisation rate on top of the Eiffel tower during the day and at night. He was expecting an exponential decrease given that radioactivity was coming from the ground, but the decrease was small, not even to half of the ground value. He concluded there is another source of ionisation and he thought that might be due to the radioactive metal of the Eiffel tower.

The meteorologist Domenico Pacini compared the ionisation rate on mountains at different altitudes, over a lake, and over the sea. He found that radioactivity was reduced by 20% at a depth of 3 m in the sea. He therefore concluded that the soil is not the only source of radiation. So, scientists decided to fly on balloons.

Ascending up to 4 km, they found that the decrease in ionisation rate with height is not as expected from a terrestrial origin. Hess, in 1912, flew 7 times and reached an altitude of 5.2 km in the final one. He found that, after a specific minimum value, the ionisation was increasing again with height. Therefore, he thought that this radiation had extra-terrestrial origin. Kolhörster proved the same after a flight up to a height of 9.2 km. The latter found an ionisation rate ten times larger than the rate at sea level. This flight was on 28th of June 1914, the day of the beginning of the World War I.

During the war, improvements in electrometer performance were achieved. Some scientists were opposed to extraterrestrial radiation and concluded, from observations, that ionisation was due to the presence of radioactive elements in the atmosphere. After the war, the research was more focused in the United States. Millikan & Bowen flew up to 15 km above Texas and found a quarter of the ionization rate measured by Hess and Kolhörster. They thought about a turnover in radiation intensity at high altitudes, because they were yet unaware of the latitude-dependent geomagnetic effect found later (see below). Two years after, Millikan reversed his conclusions and introduced the term of "cosmic rays". He chose the term of rays because they believed that this cosmic radiation was gamma photons given their penetrating power. In the American media and according to the public opinion, the discovery of these cosmic rays was a success of American science as shown in Fig. 3.1. In this magazine publication, Hess and Kolhörster were not referenced. Hess published an article to blame Millikan and said that the latter's results were just a confirmation and extension of the work initiated by others and that refusing to acknowledge previous work was an error and unjustified.

Meanwhile, Clay travelled from the Indonesian island of Java to Genova in Italy while carrying his radiation detector. He accidentally discovered the geomagnetic effect in cosmic rays. One year later, he did another trip from Java to Amsterdam and confirmed his results. Compton organised a world-wide survey to see how the intensity of cosmic radiation (also called Höhenstrahlung) depends on geomagnetic latitude. They discovered in 1933 that the intensity is greater in the West than in the East. Knowing the direction of the Earth's magnetic field, they concluded that most of the primary cosmic rays are positively charged particles.

During these East-West experiments, Rossi discovered extensive air showers in Eritrea, but he did not study them in detail and unfortunately, published his results in Italian. Pierre Auger, three years later, re-discovered these air showers and studied them.

In parallel, in 1931, during a lecture at Caltech by Zwicky, the term "supernova" was introduced. Two years after studying these phenomena, Zwicky and Baade concluded that massive stars end their lives by an explosion that produce cosmic rays.

Super-Rays Reveal Secret of Creation

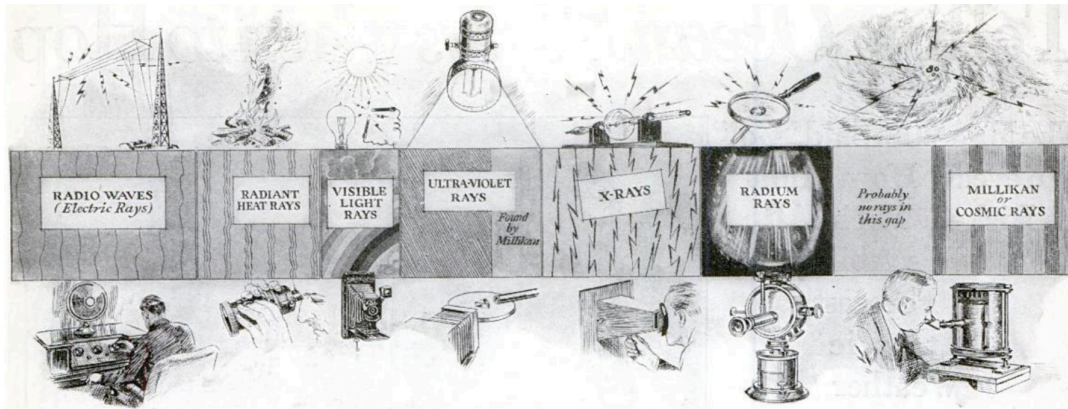


FIGURE 3.1 : (magazine, 1928)

Using the Wilson cloud chamber and the presence of a magnetic field, Anderson took pictures of different particles. He deduced the mass from the long range of the track; the more massive the particle, the shorter the distance it travels before stopping. In 1932, he found a particle that has the same mass as an electron, but by observing the curvature of that particle's path, due to the Lorentz force, he found that it carries a positive electrical charge. He had found the positron, the antimatter of the electron which is consistent with the Dirac's equation.

In 1937, a heavier electron was discovered and named a muon. The first meson was found in 1947 and called a pion. It had been predicted by Yukawa twelve years before. In the same year, they discovered a kaon which was the first strange particle. Four years after, the parity violation and the first strange baryon, lambda, were discovered. Cosmic-ray experiments are cheap and that is why, the research continued in Europe even after the bad conditions of the World War II. In 1953, the era of particle accelerators began and the CERN added the research on cosmic rays in its constitution. The field of particle physics, thus had its origins in the study of cosmic rays and numerous discoveries have arisen from this pursuit.

3.2 CR composition

Cosmic rays (CRs) are relativistic particles that circulate in the interstellar medium (ISM). These particles consist of approximately 99% nuclei and 1% electrons. The most abundant nucleus is the proton, which represents 89%, followed by alpha particles (helium nuclei) representing 10%, and the rest is antimatter and neutral particles. The CR flux of primary relativistic particles describes the number of particles $dN/(dS dt d\Omega dE)$ per unit surface dS , time dt , so-

lid angle $d\Omega$, and energy dE . It peaks at an energy close to 10^9 eV and decreases rapidly with energy according to an approximate $E^{-2.7}$ power law (see Fig.3.5).

CR energies span a range from approximately 10^6 eV up to at least 10^{20} eV with an average particle energy of 3 GeV (Armillotta et al., 2022). For an energy above 3 MeV/nucleon and > 3 MeV for electrons, the overall CR energy density in the solar neighborhood is between 0.83 - 1.02 eV.cm $^{-3}$ (Cummings et al., 2016), a value comparable to the thermal, turbulent, and magnetic energy densities found in the local ISM. The number density is 3×10^{-10} cm $^{-3}$, much lower than the average interstellar gas density of approximately 1 cm $^{-3}$ (Zweibel, 2017). The Larmor radii of Galactic CRs :

$$r_L = 1.2 \times 10^{-6} \text{ pc} \left(\frac{E_k}{10 \text{ GeV}} \right) \left(\frac{B}{10 \mu\text{G}} \right)^{-1} \quad (3.1)$$

range from 10^5 km at the lowest energies to 0.1 pc near 10^{15} eV, so that directional information on their sources is completely lost during their Galactic propagation.

In this thesis, we are going to describe primarily the Galactic Cosmic Rays (GCRs) that are produced in our Galaxy and do not exceed 10^{15} eV in energy. We only briefly comment spectral breaks and anisotropies at higher energies.

3.3 Direct detection

Cosmic-ray detection can be performed using ground-based particle detectors. One of these are the fluorescence detectors used by the Pierre Auger Observatory in Argentina in order to study ultra-high-energy cosmic rays (UHECRs), exceeding 1 EeV. They observe the faint fluorescent light emitted high in the Earth's atmosphere when UHECRs interact with air molecules. They also use Cherenkov detectors that cover an area of around 3000 km 2 in order to detect the secondary particles produced when UHECRs interact with the Earth's atmosphere. Another experiment is IceCube dedicated to study neutrinos energies greater than 100 GeV, from astrophysical sources and the ones produced by CR interactions in the Earth's atmosphere. They are using detectors deep within the Antarctic ice sheet that detect Cherenkov light emitted when neutrinos interact with the ice. There are also a lot of other ground-based detectors to observe high-energy CRs and especially air showers like High-Resolution Fly's Eye (HiRes) and Telescope Array (TA) in USA, High-Altitude Water Cherenkov Observatory (HAWC) in Mexico, Karlsruhe Shower Core and Array DETector (KASCADE) in Germany, Tunka Radio Extension (Tunka-Rex) in Russia, Tibet Air Shower Array (Tibet-AS γ) in China and Gamma Ray Astronomy PeV EnergieS Phase-3 (GRAPES-3) in India.

Direct detection in the atmosphere can be performed using balloons. Balloon-borne experiments have been widely used to study CRs due to their ability to reach high altitudes in the atmosphere. For example ATIC, SuperTIGER, CREAM and BESS. The details of these experiments are presented in Table 3.1.

Space particle detectors are used to directly detect CRs before arriving to the Earth's atmosphere. These detectors are located onboard satellites in orbit around the Earth like ACE and PAMELA. Other particle detectors are on the International Space Station (ISS) for example AMS, CALET and DAMPE. The objectives and energy range of these detectors are presented

in Table 3.1.

There are also longer-range space probes travelling in the Solar System. They are designed to travel long distances and operate far from the Earth and the Sun for example Voyager 1 & 2 and Ulysses (see Table 3.1).

In general, for light CR elements such as H and He, observations by AMS-1,2, ATIC-2, PAMELA-1, and BESS-polar are extremely useful. Heavier elements have been studied with CREAM, SuperTIGER and ACE. Leptons are detected by ATIC-1,2, AMS-02 and PAMELA.

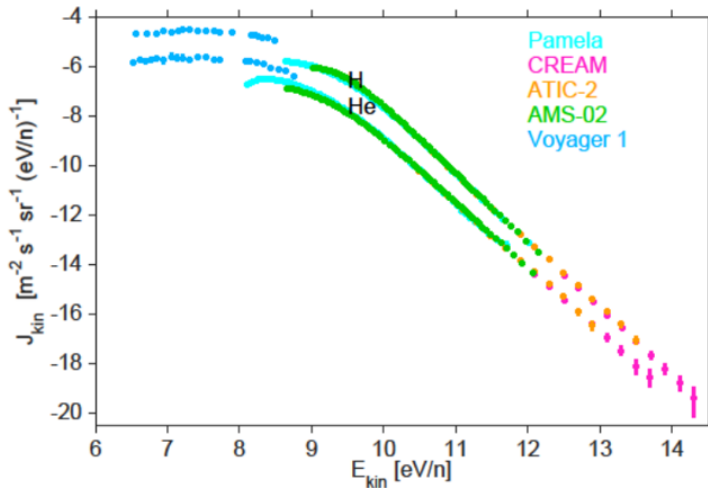


Figure 3.2 : The spectral intensity of cosmic protons and alphas, directly detected by particle detectors, displayed without solar demodulation as a function of kinetic energy per nucleon. The different colors represent different detectors. (Grenier et al., 2015)

Figure 3.2 represents the CR flux in $\text{m}^{-2} \text{s}^{-1} \text{sr}^{-1} (\text{eV/n})^{-1}$ for cosmic protons and alphas, directly detected by various particle detectors, as a function of kinetic energy per nucleon. At high energy, beyond approximately 10 GeV, Galactic cosmic rays (GCRs) penetrate the Solar System without difficulty. However, at low energies, the magnetic structure of the solar wind and heliosphere limit the inflow of Galactic particles into the Solar System. This effect is called the "solar modulation", first introduced by Parker (1965) and later modelled by a time-variable force-field approximation (Gleeson & Axford, 1968), and more recently by solving the Parker transport equation in a time variable configuration of the heliosphere (HelMod (Bobik et al., 2012, 2013)). This is why we observe a downward break in the spectrum at low energies. The two space probes, Voyager 1 and 2, which have just exited the heliosphere in 2012 and 2018 respectively, were able to detect low-energy Galactic cosmic rays (Stone et al., 2013). The spectrum obtained by one of the Voyagers is shown in blue.

The CR composition exhibits energy-dependent variations. For instance, at lower energies, CRs are predominantly composed of protons, while heavier nuclei gain significance as energy levels (rigidity¹) rise, as shown in Fig.3.3. At the mean energy, CRs are primarily composed of protons. The proton spectrum differs is steeper than the alpha one. The ratio of the proton to helium intensities decreases in the energy range from 30 GeV (where solar modulation is negligible) to about 1 TeV by a factor of approximately 1.5 (Erlykin & Wolfendale, 2015).

The spectral difference between protons and alphas remains unexplained. Tentative explanations involve differences in the acceleration process or the escape from CR sources. A spectral

¹Rigidity is a measure of the momentum of the particle, and it refers to the fact that a higher momentum particle will have a higher resistance to deflection by a magnetic field. It is defined as $R = pc/Ze$ and measured in Volt.

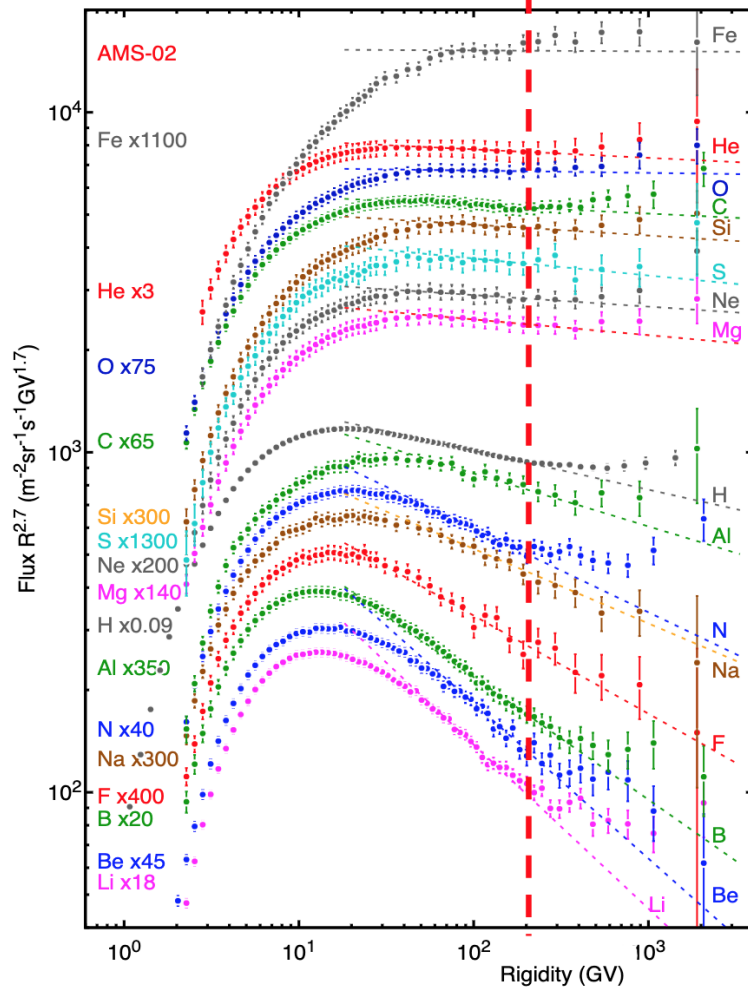


FIGURE 3.3 : CR species flux data obtained by AMS-02, where the 200 GV break is most clearly seen. The CR species are sorted by approximate order of their spectral index in 50-200 GV range. Iron has the flattest spectrum. The steeper spectra are observed beginning from protons and the steepest is Lithium.

difference should arise if protons and alphas are injected and accelerated at different stages of the source evolution. These scenarios may involve a shock with a decreasing velocity with time (Gabici et al., 2019). Consequently, alphas would predominantly undergo acceleration during the early stages when the sonic Mach number M_s is much greater than 1 and the particle spectrum is harder, while protons would be injected primarily when M_s is lower (Erlykin & Wolfendale, 2015). This scenario could potentially be due to a non-uniform distribution of helium in the surrounding medium of the accelerators. While elements like helium are typically found throughout the ISM with a nearly constant abundance ratio, such a particular configuration might arise within superbubbles, as suggested by Ohira and Ioka (2011).

Experiment Acronym	Launching	Objectives	Energy range	References
ATIC Advanced Thin Ionisation Calorimeter	3 flights 2000-2007	CR composition especially e^- spectrum	up to 100 TeV	Panov et al. (2009)
SuperTIGER Super Trans-Iron Galactic Element Recorder	Flight in 2012	Rare heavy nuclei $40 < Z \leq 60$	0.8 to 10 GeV/n	Binns et al. (2013) Murphy and Supertiger Collaboration (2016) Walsh et al. (2019)
CREAM Cosmic Ray Energetics And Mass	7 flights 2004-2016 altitude 40 km Sent on ISS in 2017	CR composition The "Knee" break	10^{10} to 5×10^{14} eV	Ahn et al. (2008) Yoon et al. (2017)
BESS Balloon-borne Experiment with a Superconducting Spectrometer	9 flights since 1993 BESS-Polar 2004 BESS-Polar II 2008	Antimatter	\bar{p} : 0.1 – 4.2 GeV	Yamamoto (2003) Yoshida et al. (2004)
ACE the Advanced Composition Explorer	Florida 1997 ended in 2016	CRs $3 \leq Z \leq 34$ Composition of solar corona	50 to 600 MeV/n	Stone et al. (1998)
PAMELA Payload for Antimatter -Matter Exploration and Light-nuclei Astrophysics	Russia 2006 ended in 2016	First satellite to detect CRs / Antimatter Dark matter annihilation	e^+ : 0.05 – 270 GeV e^- : up to 400 GeV $p(\bar{p})$: to 700(190) GeV $Z \leq 6$: to 200 GeV/n	Adriani et al. (2009) Adriani et al. (2014)
AMS Alpha Magnetic Spectrometer	California 2011	Antimatter within CRs Dark matter	0.5 GeV – 1.4 TeV	Aguilar et al. (2015)
CALET CALorimetric Electron Telescope	Japan 2015	Abundances CRs and γ rays searching for dark matter	$e^-(e^+)$: 1 GeV–20 TeV photons : to 10 TeV $Z \leq 28$: to 1 PeV	Adriani et al. (2019)
DAMPE DARk Matter Particle Explorer	China 2015	High-energy e^- and protons searching for dark matter	5 GeV – 100 TeV	An et al. (2019)
Voyager 1 & 2	Florida 1977	Outer planets Edge of Solar System	0.05 – 0.17 μm	Cummings et al. (2016)
Ulysses	Florida 1990 ended in 2009	Solar wind / Sun's polar magnetic	1.6 – 862 eV	Krüger et al. (2015)

TABLE 3.1 : Different experiments for CRs direct detection. The balloon-borne experiments are shown in red and the detectors located onboard satellites and ISS are represented in orange and blue respectively. The longer-range space probes are represented in magenta.

3.4 CR abundances and inelastic interactions

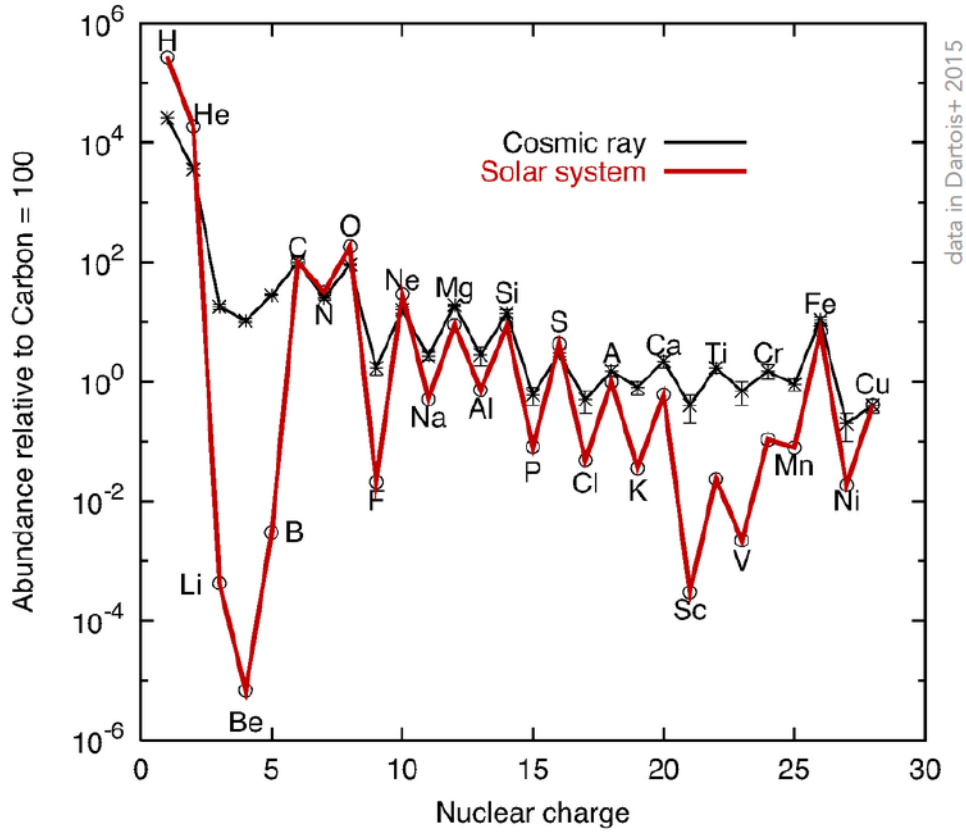


FIGURE 3.4 : Comparison between the mean composition of the Solar System (red) with the mean composition of CRs arriving Earth at 10 GeV (black)

In CR composition studies, it is common to observe certain elements being either more abundant (enhancements) or less abundant (depletions) than their counterparts in the ISM, as illustrated in Fig.3.4. The CR abundances do not differ much from those of the hydrogen and helium created in the nucleosynthesis phase of the Big Bang, or of the C, O, Fe, and Ne to A atoms created in massive stars, or of atoms heavier than iron created during SN explosions. Whereas, taking the CR carbon abundance as a reference, nuclei of the (Li, Be, B) group and sub-Iron group ($Z=20-25$) are overabundant by several orders of magnitude. The possible reason is the spallation reactions between primary CRs that interact through nuclear processes with interstellar atoms, producing lighter secondary CRs that alter the CR composition and abundance ratios. The path length of a primary p species is usually expressed in units of grammage² and defined as :

$$X = \int \rho_{ISM}(L) dL = \int \rho_{ISM}(L) v_{CR}(t) dt \quad (3.2)$$

Where ρ_{ISM} is the ISM mass density and v_{CR} is the CR velocity. Supposing that the only allowed spallation reaction is $p \rightarrow s$, with s the secondary species, and that there is no new generation of

²Amount of matter by cubic centimeter traversed by CRs in their propagation path. Its dimensions are [$g.cm^{-2}$].

primary CRs, the amount of secondaries depends on the grammage traversed by the primaries. CRs detected on Earth have traversed approximately 5 g.cm^{-2} (Zweibel, 2017) since they have left their source. Additionally, it is found that the grammage decreases with energy following a power law of $E^{-0.3}$ - $E^{-0.6}$ (Zweibel, 2017).

One particularly informative parameter in CR research is the energy dependence of the Boron-to-Carbon ratio, often denoted as B/C. Carbon is primarily generated through stellar nucleosynthesis during stars' standard life cycles. It remains relatively stable without undergoing significant nuclear reactions in the ISM. In contrast, Boron is enriched via spallation, resulting from interactions between carbon and the interstellar hydrogen. The evolution of the B/C ratio with energy, as observed by AMS-02 (Aguilar et al., 2016), serves as a diagnostic tool to infer the mean diffusion coefficient, its energy dependence, and the amount of reacceleration during the confinement time. The isotope ^{10}Be is unstable and undergoes radioactive decay reducing its abundance over time. The ratio of the radioactive and stable isotopes, $^{10}\text{Be}/^9\text{Be}$, suggest that GeV CRs remain confined within our Galaxy for approximately $(1 - 2) \times 10^7$ yr (Gabici et al., 2019). This confinement time diminishes with increasing energy according to $E^{-0.3}$ - $E^{-0.6}$, for an average gas volume density of 0.1 cm^{-3} (Zweibel, 2017).

The ratio of secondary-to-primary and of decaying-to-stable CRs are further discussed in Chap.5, especially the relationship between them and the diffusion coefficient.

3.5 CR Spectra

Fig.3.5 shows two marked breaks in slope in the CR spectrum, one around 3×10^{15} eV called the knee, and the other around 5×10^{18} eV called the ankle. It is also found that the spectra of all nuclei present the same break near 300 GeV/nucleon. The Greisen-Zatsepin-Kuzmin (GZK) cutoff, around 3×10^{19} eV for protons, represents an energy threshold beyond which the interactions between CRs and the cosmic microwave background (CMB) radiation become significant. Therefore, by the energy loss due to these interactions, the GZK cutoff represents an upper limit on the energy of CRs that can effectively reach us on Earth.

3.5.1 The knee break

The knee break occurs at energies around 3 to 5 PeV. Beyond this energy, the spectral index of the CR spectrum smoothly changes from $E^{-2.7}$ to $E^{-3.1}$ (Antoni et al., 2005), hence the name. The exact origin of the knee in the CR spectrum remains an active area of research and debate. Several hypotheses have been proposed. Certain models rely on the idea that the Galactic magnetic field has a reduced capacity to confine particles beyond the knee energy (Hillas, 2006). Therefore, CRs escape from our Galaxy more efficiently than at lower energies, leading to a drop in the observed flux.

However, according to the prevailing consensus, the observed spectral steepening above the knee is attributed to a reduced efficiency of Galactic CR sources to accelerate particles to such high energies. The knee essentially signifies the maximum energy attainable by protons at Galactic accelerators, particularly supernova remnants (SNRs) (this acceleration mechanism is described in the following section). In contrast, heavier nuclei are expected to contribute significantly more above the knee since their maximum energy achievable within a given accelerator

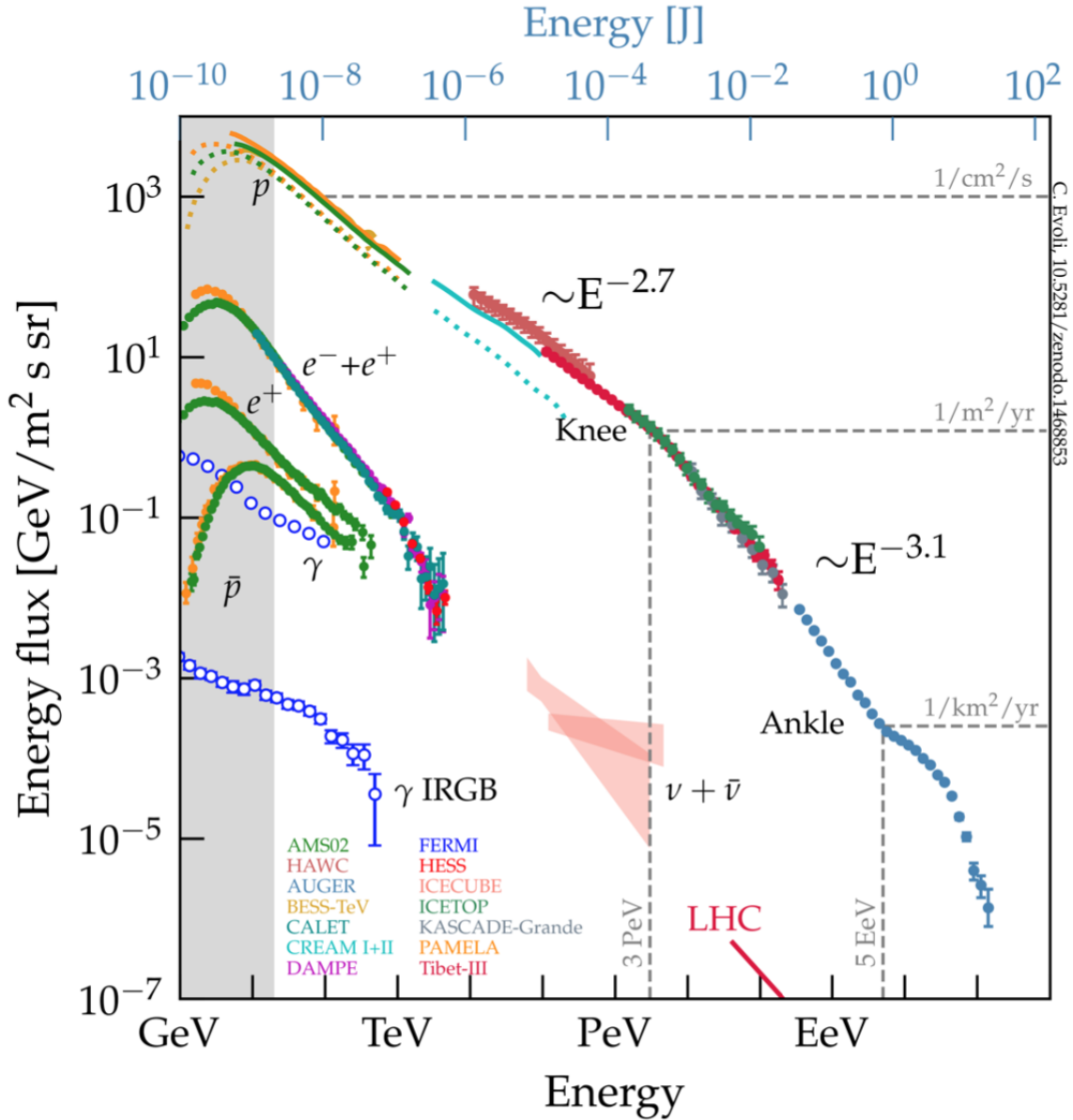


FIGURE 3.5 : Spectra of different particle of the CRs including the proton, the leptons and the antiproton. The IRGB is acronym of the isotropic γ -ray background. (Evoli, 2018)

surpasses that of protons. Studies have demonstrated that the sum of contributions from all nuclear species closely matches the observed $E^{-3.1}$ spectrum above the knee (Hillas, 2006).

From an observational perspective, conclusive proof of effective PeV proton acceleration at SNR shocks would require the detection of neutrinos or γ rays from these shocks, exhibiting an unattenuated spectrum extending into the multi-TeV domain (Gabici & Aharonian, 2007). However, the limited statistics of multi-TeV domain and the anticipated scarcity of presently active SNR PeVatrons (only a few in the entire Galaxy) pose significant challenges to these observations, even for the most sensitive instruments (Cristofari et al., 2018).

3.5.2 The ankle break

The ankle break corresponds to a hardening in the CR spectrum that occurs around energies of 3 to 5 EeV. The CR flux declines less steeply at energies above the ankle and the spectrum changes to E^{-3} . Several hypotheses have been proposed to understand the origin of this break. One of them suggests that the ankle may signal the transition from predominantly Galactic to extragalactic sources of CRs (Parizot, 2014). These sources could accelerate CRs to much higher energies, leading to the observed increase in flux.

As discussed earlier, the knee break is widely regarded as representing the maximum energy achievable by protons accelerated by Galactic sources. For heavier ions, this maximum energy increases linearly with the atomic number Z , considering the same shock properties for all nuclei (as seen in Eq. 3.11 in the following section). Among the heavy elements present in the ISM, Fe with $Z_{Fe} = 26$ is the most abundant. Consequently, the contribution to the overall CR spectrum from Galactic sources should extend up to an energy of approximately $E_{\max}^{Fe} \sim Z_{Fe} E_{\max}^H \approx 10^{17}$ eV (Gabici et al., 2019). This energy is about 30 times lower than the energy of the ankle, posing a challenge to the conventional scenario for the transition from Galactic to extragalactic CRs.

One possible solution to this discrepancy would involve postulating that the transition occurs much earlier than the ankle, at an energy around $\approx 10^{17}$ eV. Another feature in the CR spectrum, known as the second knee, is observed at this energy, albeit less pronounced (Hörandel, 2003). Such a transition at the second knee would, however, require an unusual degree of fine-tuning, as the extragalactic contribution should sharply emerge exactly where the Galactic contribution disappears (Parizot, 2014). Furthermore, this scenario would necessitate an alternative explanation for the ankle.

Alternatively, one could propose the existence of a third CR population that fills the gap between the Galactic component (by SNR acceleration) and the extragalactic one (Hillas, 2006), or suggest that a subset of the SNR population, rather than an entirely new source class, fills this gap (Ptuskin et al., 2010). A critical examination of these three-component scenarios is presented by (Parizot, 2014).

Finally, another potential solution involves reevaluating the entire SNR paradigm and considering that sources other than SNRs dominate the CR spectrum all the way up to the ankle. Superbubbles, rather than isolated SNRs, could account for the entire spectrum of Galactic CRs up to the ankle (Bykov, 2014; Lingenfelter, 2018; Parizot, 2014). Surprisingly, this scenario has received less attention than the SNR paradigm and therefore requires further investigation.

3.5.3 Hardening near 300 GV

In addition to the knee and ankle, there is a notable spectral hardening in the CR spectrum, by 0.1 or 0.2 in spectral index, occurring between 200 and 300 GeV/n. It has been seen by Dampe (An et al., 2019), AMS-02 (Aguilar et al., 2015), ATIC-2 (Panov et al., 2009), CREAM I+III (Ahn et al., 2010; Yoon et al., 2017), and also by PAMELA (Adriani et al., 2011) as shown in Fig.3.6. The break is in the same rigidity range (~ 300 GV) for nearly all CR species regardless of their spectrum shape (see Fig.3.3). The precise origin of that break is still under investigation, but there are potential explanations.

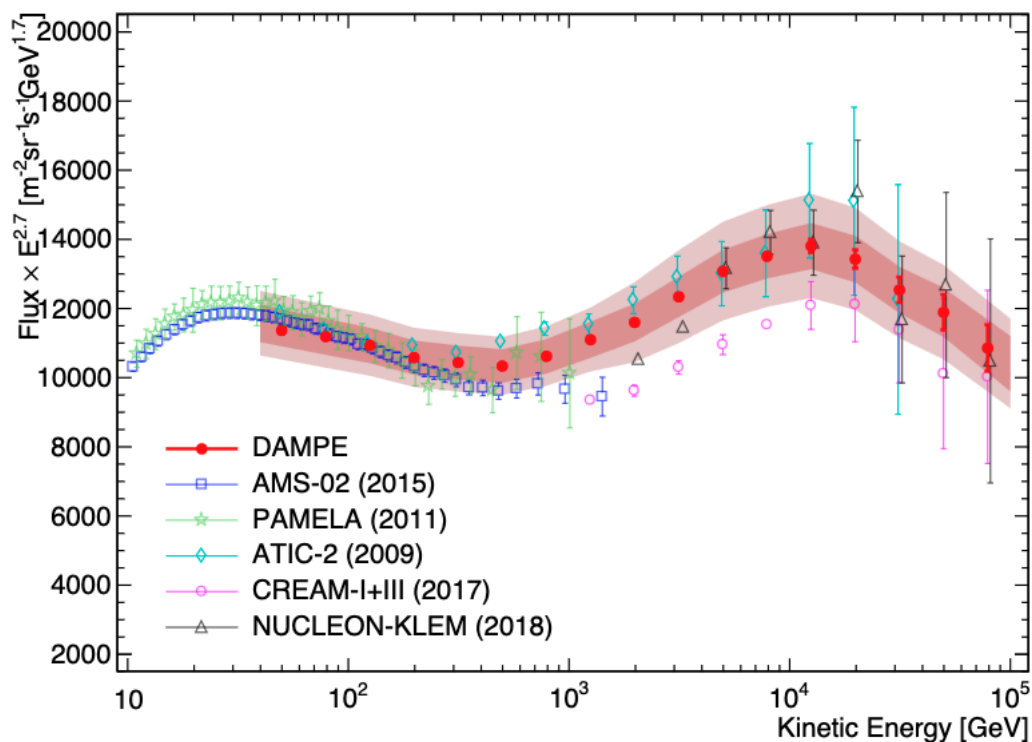


FIGURE 3.6 : Proton spectrum measured with different detectors. The data from DAMPE is shown in red filled dots with the statistical uncertainties represented by the red error bars. The inner shaded red band represents the estimated systematic uncertainties due to the analysis procedure and the outer band shows the total systematic uncertainties including also those from the hadronic models. The other direct measurements are obtained by PAMELA (green stars), AMS-02 (blue squares), ATIC-2 (cyan diamonds), CREAM I+III (magenta circles), and NUCLEON KLEM. For the PAMELA data, a $\sim 3.2\%$ correction of the absolute fluxes has been included according to (Adriani et al., 2014). The error bars of PAMELA and AMS-02 data include both statistical and systematic uncertainties but for ATIC, CREAM, and NUCLEON data, only statistical uncertainties are shown (An et al., 2019).

One possible explanation is the presence of a relatively nearby CR source (Ahn et al., 2010). Alternatively, this hardening could be attributed to the transport characteristics of CRs within the Galaxy (Aloisio & Blasi, 2013; Tomassetti, 2012), such as a feature in the CR diffusion coefficient. Another explanation could relate to a break in the overall spectrum of CRs injected into the ISM (Recchia & Gabici, 2018; Yuan et al., 2011; Zatsepin & Sokolskaya, 2006). The distinction between these two explanations can be elucidated by conducting precise measurements of secondary spallation nuclei. If it were solely a result of propagation effects, the break in the secondary spectra would be twice as prominent as that in the primary spectra. However, if the break exists in the injection spectrum, it should be the same for both primary and secondary species (Gabici et al., 2019). In a study by Génolini et al. (2017), which utilised B/C ratio data from the AMS-02 experiment up to \sim TeV energies, the authors found evidence favoring a dif-

fusive propagation origin for the broken primary species spectra. More recently, measurements of the absolute spectra of secondary species (Li, Be, and B) by AMS-02 have supported the hypothesis that the spectral slopes above the break are consistent with this scenario (Aguilar et al., 2018).

An alternative model, introduced by Blasi et al. (2012) and developed by Evoli, Blasi, et al. (2018), suggests that a change in the mode of CR transport may be responsible for the spectrum hardening. In general, the turbulence that scatters CRs is described by two components : external turbulence, traditionally attributed to injection by SNRs, and waves generated by CRs themselves through the streaming instability (R. Kulsrud & Pearce, 1969). The presence and amount of these waves is linked to the number density and gradients of CRs (This topic is discussed in details in Chap.5). Evoli, Blasi, et al. (2018) proposed that CRs above the break primarily diffuse on external turbulence, while self-generated turbulence dominates at lower rigidities because the turbulence injected at the large SNR scales does not have the time to cascade down to the micro-parsec scale resonant with CR gyroradii. This argument is, however, challenged by ISM observations that indicate that turbulence is continuously replenished (Hennebelle & Falgarone, 2012). Luo et al. (2023) applied a numerical simulation using the DRAGON propagation code (Evoli et al., 2008). In this simulation, they assumed that that Galactic halo has a double structure. The inner one near the Galactic disk has a high level of turbulence, due to the proximity of numerous SNRs, and a low diffusion coefficient. The outer one is characterised by a larger diffusion coefficient. By these assumptions, they found a resulting curve that fits well the data at the 300 GV hardening.

It is important to note that these explanations are not mutually exclusive, and the observed spectral break could be influenced by a combination of these factors.

3.5.4 Electron and positron spectra

Secondary electrons (e^-) and positrons (e^+) arise from the cosmic nuclei interactions with ISM, through decay chains involving particles like π^\pm and μ^\pm . These processes should produce approximately equal amounts of e^- and e^+ . However, the observed overabundance of e^- compared to e^+ in CRs suggests that a significant portion of electrons has a primary origin. Furthermore, observations of X-ray and TeV γ -ray emissions from SNRs provide compelling evidence for the acceleration of electrons in SNR shocks to energies reaching approximately 100 TeV (F. A. Aharonian, 2013).

More recently, the AMS-02 reported the most precise measurements to date of CR electron (e^-) and positron ($e^- + e^+$) fluxes (Aguilar et al., 2014). The electron-positron spectrum can be described by a single power-law function above 30 GeV, characterised by a spectral index $\gamma = -3.170 \pm 0.008$ (statistical + systematic) ± 0.008 (energy scale uncertainty). However, the electron spectrum exhibits a different behavior and cannot be fitted with a single power-law over an energy range (> 10 GeV) where it remains unaffected by solar modulation. In fact, it was discovered that the spectral index of electrons displays energy-dependent variations, with the spectrum undergoing hardening at around 30 GeV.

This observed electron spectrum is notably steeper than that of protons because e^- experience substantial energy losses during their propagation through the Galaxy. Even when accounting for these losses, it is necessary to consider different injection spectra for electrons and protons

to accurately reproduce the local electron spectrum (Gaggero et al., 2013; A. W. Strong et al., 2011). This could imply either that CR protons and electrons are emitted by the same sources but with different energy distributions or that they are accelerated in distinct source environments.

In a study by F. Aharonian et al. (2009), evidence was reported for a steepening in the energy spectrum at approximately 1 TeV. More recent data has revealed that this steepening is quite abrupt, with the spectral index transitioning from -3.04 to -3.78 (Kerszberg et al., 2017). Furthermore, the spectrum continues without further attenuation up to particle energies of approximately 20 TeV. Subsequently, the CALET and DAMPE experiments extended these measurements up to particle energies of 5 TeV with a high degree of precision, providing additional evidence for a break in the spectrum at around 1 TeV, beyond which the spectral index rapidly shifts to ~ -4.1 (Adriani et al., 2017; DAMPE Collaboration et al., 2017).

These observations carry a significant implication. Given the extremely short energy loss time of 20 TeV electrons within the Galaxy, it suggests that such particles must have originated from our local neighborhood, approximately 100 pc away (F. A. Aharonian et al., 1995; López-Coto et al., 2018; Recchia et al., 2019).

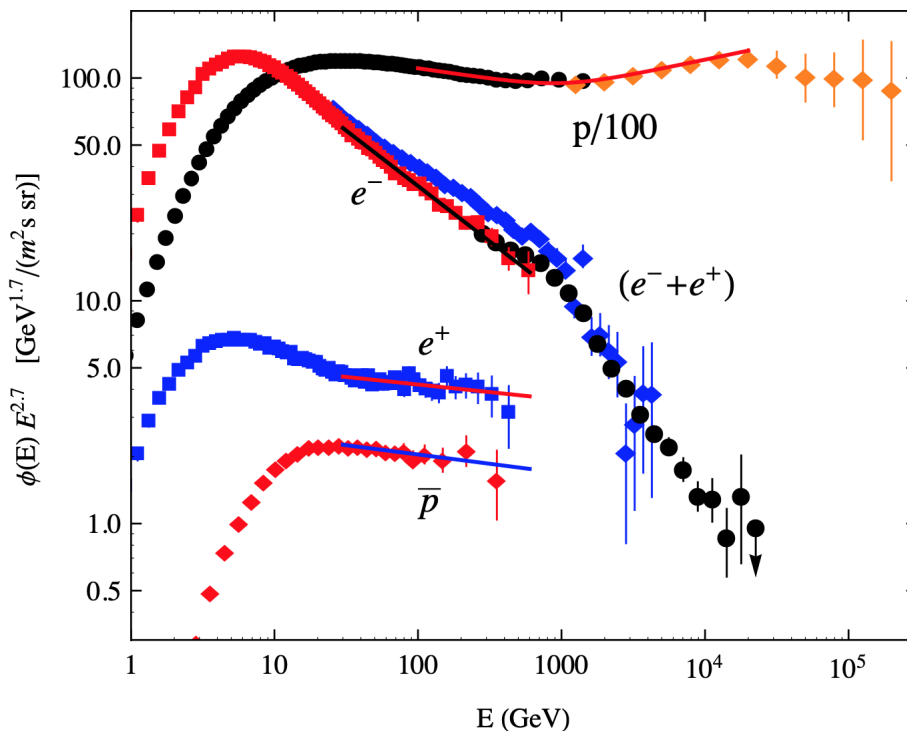


FIGURE 3.7 : Figure by (Lipari, 2019) of the spectra of proton (by CREAM), electron (by AMS-02), positron (by AMS-02), electron-positron (by DAMPE and HESS) and antiproton (by AMS-02). The line for the proton data is a broken power law fit. For the other, the lines are simple power law fits for $E > 30$ GeV.

Even more astonishing are the discoveries concerning the positron spectrum. The measurements of the CR positron fraction $e^+/(e^+ + e^-)$, conducted by PAMELA (Adriani et al., 2009), revealed an unexpected increase in this fraction beyond energies of ~ 8 GeV. According to the

conventional model of CR transport, positrons are primarily generated as secondary products in inelastic proton-proton collisions. Consequently, one would expect the positron ratio to decrease with increasing energy. Therefore, this unexpected rise in the fraction has led to the hypothesis of the existence of a source of primary positrons (Gabici et al., 2019). However, the presence of an upper limit on the age ($\sim 10^5$ yr) and distance (< 1 kpc) of astrophysical sources for 100 GeV e^+ , due to energy losses from processes like inverse Compton (IC) scattering on Cosmic Microwave Background (CMB) photons and synchrotron emission in the local magnetic field, has posed challenges to this hypothesis.

The observed excess of e^+ has been proposed to result from the annihilation or decay of dark matter particles in the Milky Way halo (Bergström et al., 2008). On the other hand, astrophysical sources such as nearby and young pulsars (F. A. Aharonian et al., 1995; Hooper et al., 2009), or nearby SNRs, which could produce and accelerate secondary positrons before they escape into the ISM (Blasi, 2009), have been suggested as alternative explanations to account for the observed population of these particles.

According to the most recent data from the AMS-02 experiment, the positron fraction appears to decrease above particle energies of $\sim 400 - 500$ GeV. This trend can only be explained if the local source(s) of TeV e^- do not produce e^+ in equal quantities, which casts doubt on scenarios involving pulsars or pulsar winds as the primary sources of high-energy leptons (Recchia & Gabici, 2018).

Figure 3.7 illustrates recent measurements of the CR spectrum for four different components. This figure clearly depicts the spectra's changes, which remain puzzling. Notably, the hardening around 500 GeV and the softening at 13.6 TeV in the p spectrum. Concerning the e^- , there is the softening at 1 TeV, affecting also the spectrum of $(e^- + e^+)$. Another puzzling concerns the spectra of e^+ and \bar{p} , which exhibit a similar shape above 30 GeV with the same spectral index. Consequently, the ratio of the two spectra remains constant at a value of $e^+/\bar{p} \approx 2$. Research and observations continue in an effort to interpret these spectra.

3.6 CR anisotropy

Based on Eq.3.1 and a Galactic mean magnetic-field strength of $\sim 3 \mu\text{G}$, the Larmor radius of a 10 GeV proton is of the order of few μpc in the Milky Way. Efficient scattering at these scales implies that CRs must undergo efficient randomisation (Gabici et al., 2019) during their journey through space. If the particles were travelling ballistically from their sources to the Earth (in straight-line trajectories), without any significant path randomisation, the anisotropy would be $\sim 1/\sqrt{N_{src}}$. Even with $N_{src} = 10^6$ sources, there would still be some level of anisotropy due to nearby sources (R. M. Kulsrud, 2005). The paths randomisation can be accomplished by resonant interactions with a turbulent magnetic field. The change in CR direction is therefore happening by pitch-angle³ scattering. Considering small magnetic field fluctuations, the scattering rate ν can be calculated by quasi-linear theory (Hasselmann & Wibberenz, 1970; Jokipii, 1966; Kennel & Engelmann, 1966), where scattering is approximated as a combination of the regular magnetic field and small perturbations. The pitch-angle scattering rate is directly proportional to the ratio of energy densities between the turbulent magnetic field, δB , and the

³The pitch angle is the angle between the CR momentum and the regular magnetic field.

regular magnetic field, B_0 :

$$\nu_{\text{scat}} = \left(\frac{\delta B^2}{B_0^2} \right) \Omega \quad (3.3)$$

with the relativistic gyrofrequency Ω . To achieve a high degree of isotropy, the turbulent field's energy density must be large compared to the regular one. In quasi-linear theory, a low level of turbulence is required for the perturbative approach to be valid, so diffusion can be noticeably anisotropic, with a large parallel diffusion coefficient, $\kappa_{\parallel} \approx c^2/(3\nu_{\text{scat}})$ (where c is the speed of light) and a much smaller perpendicular diffusion coefficient, $\kappa_{\perp}/\kappa_{\parallel} \approx (\delta B^2/B_0^2)^2$ (Jokipii, 1966; Schlickeiser, 2002). It is worth mentioning that even though Galactic diffusion may be anisotropic, it can effectively become isotropic on larger Galactic scales since the orientation of the regular background magnetic field varies over these scales.

If CRs undergo efficient randomisation, anisotropy in their arrival directions can be detected if the CR source distribution is locally inhomogeneous. In that case, a gradient in the isotropic part of the CR density will occur, inducing a dipole in the arrival directions of CRs. For isotropic diffusion, the dipole points in the upward direction of the CR gradient. This has led scientists to use these anisotropies to look for nearby sources of CRs (Borriello et al., 2012; Büsching et al., 2008; di Bernardo et al., 2011). The amplitude of dipole anisotropy is given by Ginzburg and Syrovatskii (1964) :

$$a = \frac{3\kappa}{c} \frac{|\vec{\nabla} n_{CR}|}{n_{CR}} \quad (3.4)$$

where n_{CR} is the CR space density. Taking ℓ_{cr} to be the typical scale of the CR gradient over large Galactic scales one gets :

$$a \approx 10^{-4} \left(\frac{\kappa}{10^{28} \text{ cm}^2 \text{ s}^{-1}} \right) \left(\frac{\ell_{cr}}{3 \text{ kpc}} \right)^{-1} \quad (3.5)$$

For anisotropic diffusion, the observed dipole will be aligned with the magnetic field lines. Therefore $\vec{\nabla} n_{CR}$ is replaced by $\vec{b} \cdot \vec{\nabla} n_{CR}$ where \vec{b} is the magnetic field direction $\vec{B}_0/|\vec{B}_0|$. In that case, the dipole amplitude will be reduced by the cosine of the angle between CR gradient and background magnetic field which limits the information on CR sources.

Another expected cause for dipole anisotropy is the motion of the Earth relative to the isotropic frame of CR density. The observer motion can make CRs appear slightly more concentrated in one direction than the opposite one. This effect is called the Compton-Getting effect (Compton & Getting, 1935; Gleeson & Axford, 1968). Figure 3.8 shows a remarkable degree of isotropy even for 10 TeV particles, but a dipole is clearly visible at the per mille level. The excess is caused by the alignment of the local magnetic field and the tail of heliosphere seen the strongest red hot spot. Figure 3.9 shows the phase (*upper* plot) and amplitude (*lower* plot) of the dipole anisotropy as recently measured by different experiments. Up to ~ 10 TeV, the amplitude is close to $\sim 10^{-3}$. Then, it decreases to a minimum of around 10^{-4} between 200 and 300 TeV, and increases again to $\sim 10^{-1}$ at a few tens of PeV. The phase significantly flips with energy. It is relatively constant at $\sim 45^\circ$ in right ascension up to 100 TeV, then quickly changes to $\sim 270^\circ$ at few tens of PeV, which is interestingly the direction of the Galactic centre. The energy of this phase transition is very close to the energy of the amplitude transition.

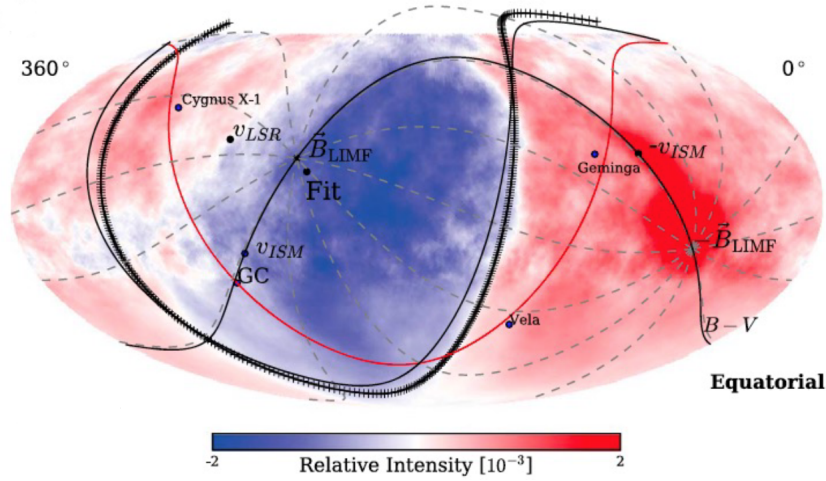


FIGURE 3.8 : Relative intensity variations of 10-TeV cosmic rays detected by HAWC and IceCube. The Galactic plane is shown as a red curve. The plane containing the local interstellar medium magnetic field (\vec{B}_{LIMF}) and solar velocity in the ISM (\vec{v}_{ISM}) is shown as a black curve (Zirnstern et al., 2016). Its equator is also shown (Abeysekara et al., 2019).

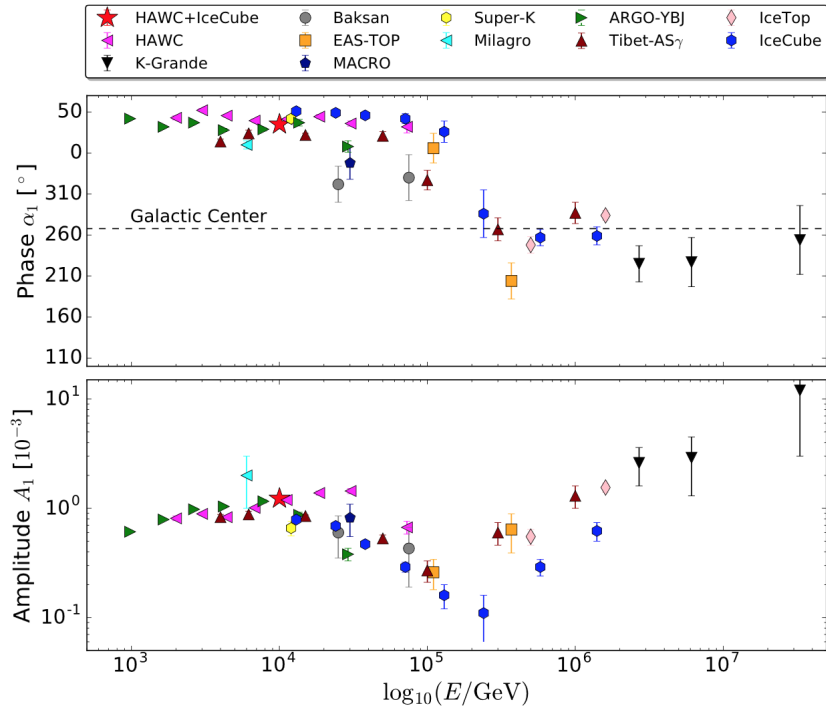
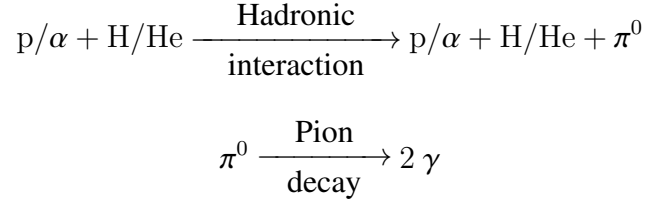


FIGURE 3.9 : Phase (top) and amplitude (bottom) of the dipole anisotropy from recent measurements. (Abeysekara et al., 2019)

3.7 Indirect detection

The only way to observe CRs beyond the immediate vicinity of the heliosphere is indirectly through γ rays and synchrotron radio emission. These radiations can cross the entire Galaxy without being absorbed thanks to the high energy of γ rays and the long wavelength of radio waves. However, the intensity decreases with distance squared and is integrated over the entire line of sight. For the γ -ray signal, there are four different processes.

The major channel for γ -ray production in the GeV energy band is the hadronic interaction :



That equation represents the hadronic interaction between CR nuclei, especially protons and alphas, with the gas nuclei of high abundances like hydrogen and helium. This interaction produces neutral pions which in turn decay to γ -ray photons. The majority of γ -ray photons detected in the Galaxy in the *Fermi*-LAT energy band are produced by this hadronic interaction. The photons have a typical energy 7 to 10 times lower than that of the parent CR nucleus.

The second process is the bremsstrahlung radiation produced by the interaction of cosmic electrons with the interstellar gas :



The emitted radiation has almost the same energy as the electron, which is an advantage. However, the signal is weak because electrons represent only 1% of total cosmic rays.

The third process is the Inverse Compton (IC) scattering, which is the interaction of cosmic electrons with the soft photons of the Cosmic Microwave Background (CMB) or the Far Infrared Radiation (FIR) produced by dust grains or even starlight.



The fourth process is the electron-positron annihilation :

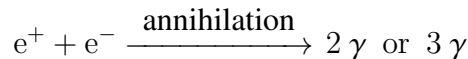


Figure 3.10 compares the intensity of γ rays produced by different types of interaction, as a function of radiation energy. The bremsstrahlung effect could not be separated from the hadronic emission at low energy, so it may contribute somewhat to the hadronic radiation below 300 MeV. Hadronic and bremsstrahlung interactions in the different gas phases are plotted in red for the atomic gas, magenta for the DNM, and green for the dense molecular phase visible in CO. The inverse Compton process, plotted in cyan, presents a harder spectrum than the gas-

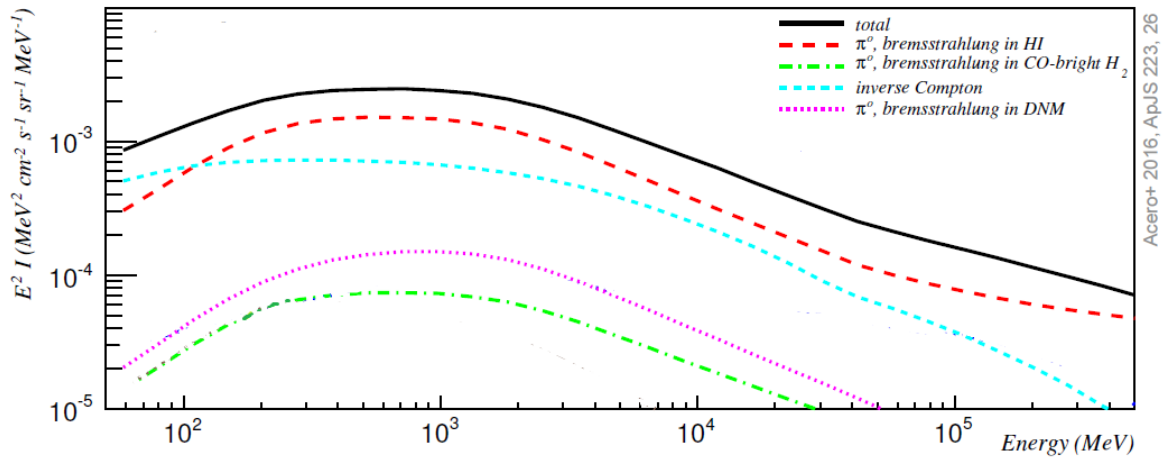


FIGURE 3.10 : Decomposition of the diffuse γ -ray intensity spectrum observed by *Fermi*-LAT at latitudes $|b| > 10^\circ$ and produced by different types of interactions. (Acero et al., 2016)

related interactions. The black curve results from the combination of all types of interactions that matches the data. Therefore, the most important signal originates from the HI phase, followed by the one in the DNM, and finally the one in CO-bright H_2 , which is logical given the mass and volumetric distribution of these phases. The inverse Compton contributes significantly at energies beyond tens or hundreds of GeV and is dominant below 100 MeV.

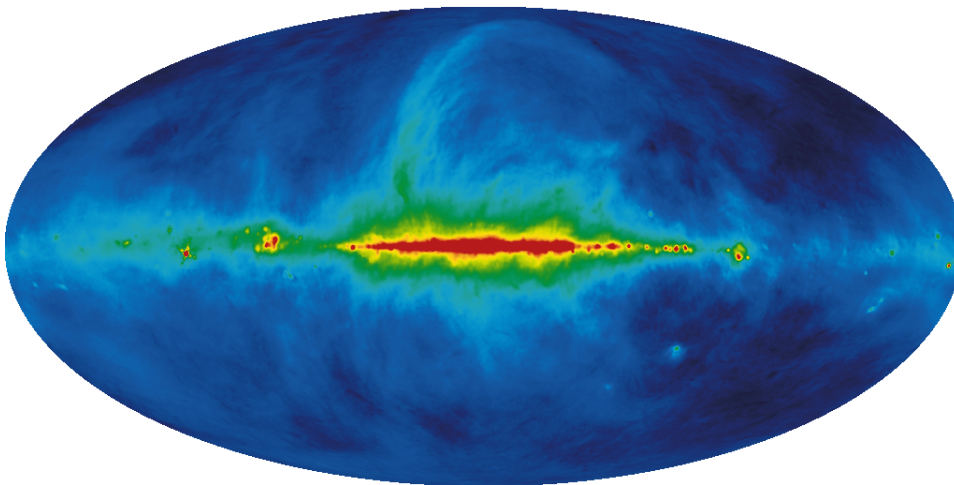


FIGURE 3.11 : Map of the radio emission at 408 MHz. (Remazeilles et al., 2015)

Another indirect observation of CRs is by using the radio signal. The allsky radio map at 408 MHz is shown in Fig.3.11. Almost all of the radiation observed are produced by leptons gyrating around the magnetic field because they are accelerated more by the Lorentz force than protons and heavier ions. The radiation is named magnetobremsstrahlung, but different names are used depending on the lepton speed : gyro-radiation or cyclotron for relativistic leptons with kinetic energies comparable to their rest mass and synchrotron for ultrarelativistic leptons (Condon & Ransom, 2016).

The radio signal mainly results from the synchrotron emission of leptons, especially primary and secondary CR electrons and positrons. Using the magnetic energy density in the CGS system $U_B = B^2/8\pi$, the synchrotron power radiated by a single electron, at velocity βc , is :

$$P_{syn} = 2 \sigma_T \beta^2 \gamma_L^2 c U_B \sin^2 \alpha \quad (3.6)$$

with the Thomson cross section $\sigma_T = 6.65 \times 10^{-25} \text{ cm}^2$, the Lorentz factor γ_L and α the pitch angle. The average synchrotron power in a source with an isotropic pitch-angle distribution is :

$$\langle P_{syn} \rangle = \frac{4}{3} \sigma_T \beta^2 \gamma_L^2 c U_B \quad (3.7)$$

We can notice that the synchrotron radiation is directly proportional to the magnetic energy density therefore to the strength of the ambient magnetic field squared $P_{syn} \propto U_B \propto B^2$.

The advantage of the radio signal is its angular resolution, which is much better than the γ -ray one. However, this signal strongly depends on the ambient intensity of the magnetic field, which is difficult to know. Another disadvantage is that high-energy electrons and positrons radiate very rapidly at high energy. Their spectra are steeper than that of CR nuclei and their spatial distribution is more contrasted.

3.8 Acceleration sources of CRs

The origin of CRs depends on their energy. Low-energy CRs, from approximately MeV to GeV, are primarily produced in our own Milky Way Galaxy. They mainly originate from stellar processes, such as stellar flares and coronal mass ejections. Additionally, there's a contribution from interactions of higher-energy primary CRs with the ISM.

It is currently believed that supernova (SN) shock waves are the likely sites for accelerating CRs to intermediate-energies between GeV and PeV, up to the knee break. The reason is that SN are one of the few objects numerous enough (2-3 per century in the Galaxy) and energetic enough (10^{44} J per SN) in a galaxy to produce the entire CR power observed in the Milky Way. This power requires that about 10% of the injected SN energy be transferred to CRs (Drury et al., 1994).

A preliminary version of this acceleration mechanism was proposed by (Fermi, 1949). It has since been referred to as Fermi's second-order acceleration. A more efficient version, in better agreement with observations, was developed in the late 1970s (Bell, 1978 ; Blandford & Ostriker, 1978 ; Krymskii, 1977), now known as Fermi's first-order acceleration. Both processes are based on the scattering of CRs by magnetic turbulence, with particles gaining energy if they encounter the turbulence head-on and losing energy if they catch up to it.

- Second-order Fermi acceleration :

The idea is that charged particles interact with magnetised clouds present in the ISM and exchange energy with them. Therefore, magnetic fields play a crucial role in the acceleration, even if the magnetic force does no work⁴. In reality, temporal variations in the magnetic field

⁴ $\vec{F}_L \cdot \vec{v} = q(\vec{v} \times \vec{B}) \cdot \vec{v} = 0$

create electric fields⁵ that can transfer energy to the particles. These temporal variations in the magnetic field are due to the motion of the magnetised interstellar clouds. Assuming an isotropic direction of the particles within the cloud and an isotropic motion of the cloud in the ISM, one can obtain, by conservation laws :

$$\left\langle \frac{\Delta E}{E} \right\rangle = \frac{4}{3} \frac{V_{cl}^2}{v_{cr}^2 - V_{cl}^2} \simeq \frac{4}{3} \left(\frac{V_{cl}}{v_{cr}} \right)^2 \quad (3.8)$$

With V_{cl} and v_{cr} being the velocities of the cloud and the CR particles, respectively. By that equation, there is an average relative energy increase which results in particle acceleration.

The significant advantage of this process is that it naturally produces a power-law spectrum which is in accordance with observations in astrophysical sources or even in the ISM. The differential spectrum of energetic particles is $N(E) \propto \left(\frac{E}{E_0}\right)^{-x}$ with $x = \left(1 + \frac{\tau_{acc}}{\tau_{esc}}\right)$ where τ_{acc} and τ_{esc} represent the acceleration and escape times respectively.

However, this model has several issues. Firstly, the acceleration time is very long. The velocity V_{cl} in the ISM is on the order of a few 10 km/s, therefore $V_{cl}/v_{cr} \sim 10^{-4}$, and the energy gain per collision with the cloud is on the order of 10^{-8} . Moreover, the distance between clouds is on the order of parsecs, so it would take about $\sim 10^9$ years to triple the energy of a particle. Given that the typical age of CRs in the galaxy is about 10^7 years, this second-order Fermi mechanism cannot explain the observed CR energies. Another problem is related to low-energy particles. As they propagate through the ISM, they lose energy due to Coulomb interactions. Due to the low collision frequency between particles and clouds, the gain from this Fermi mechanism cannot compensate for the Coulomb losses. Thus, a source of particles with at least 200 MeV is required to solve that problem which is complicated especially for heavy ions. The last problem is that the spectral index of the power-law depends on τ_{acc} (which depends on the distance between clouds and their velocities) and τ_{esc} (which depends on diffusion conditions). Therefore, the slope of the power-law is not universal.

- First-order Fermi acceleration :

In contrast to the previous case, this acceleration occurs through a shock wave. The front of the shock creates a discontinuity in various physical properties of the medium, such as temperature, volume density, pressure, and velocity. After passing through the shock, the medium becomes compressed, heated, and slowed down. In a regular shock, the atoms in the medium collide with each other, causing the temperature to increase rapidly, and the overall atom velocity to decrease. However, in astrophysical shocks, it is a non-collisional shock and particles interact with the medium through electromagnetic fields. Therefore, there is a magnetic turbulence formed upstream and downstream of the shock, and it is assumed that the particle distribution becomes isotropic in each of these environments. Under these assumptions, we find an average first-order energy gain :

$$\left\langle \frac{\Delta E}{E} \right\rangle = \frac{4}{3} \frac{\Delta v}{v_{cr}} \quad (3.9)$$

Here, Δv represents the relative velocity of the upstream and downstream media of the shock. The ratio of the densities ρ after and before the shock is called the compression ratio, usually

⁵ by Maxwell-Faraday's law : $\nabla \times \vec{E} = -\delta \vec{B} / \delta t$

denoted as r . The previous equation can be written as :

$$\left\langle \frac{\Delta E}{E} \right\rangle = \frac{4}{3} \frac{r-1}{r} \frac{V_{sh}}{v_{cr}} \quad (3.10)$$

With V_{sh} the shock velocity. For an ideal monoatomic gas with an adiabatic index $\gamma_{IG} = 5/3$, when the sonic Mach number M_s tends to infinity, the compressibility ratio is always $r \simeq 4$.

The shock velocity is on the order of several 10^3 km/s, which is higher than that of the magnetised clouds. In this case, the energy gain is on the order of 10^{-2} and not 10^{-8} as in the second-order case. Furthermore, the typical time interval between two accelerating "collisions" is very small compared to the previous case. As a result, this first-order mechanism leads to an acceleration time on the order of a few weeks for GeV particles, which correspond to the majority of CRs. Another advantage is that shock wave acceleration produces a power-law spectrum with a universal index. The differential spectrum of energetic particles is $N(E) \propto (\frac{E}{E_0})^{-x}$ with $x = (r+2)/(r-1)$. Therefore, the slope only depends on the compression ratio r . In a strong shock ($M_s \geq 20$), the compression ratio $r = 4$ and thus, $x = 2$ and the spectrum follows E^{-2} , which closely matches observations.

First-order Fermi acceleration is most efficient at accelerating particles with moderate energies because extremely low-energy particles may not gain enough energy to become fully relativistic CRs, while extremely high-energy particles may not experience significant acceleration due to limited gyration within the shock region. Because of these limits, shock waves cannot accelerate particles to more than 10^{13} or 10^{14} eV (Lagage & Cesarsky, 1983).

The Hillas (2006) criterion on the Knee break, discussed in the previous section, can be invoked to estimate the maximum energy of a particle of atomic number Z at a SNR shock of size R_{sh} moving at a velocity v_{sh} , giving :

$$E_{\max} \sim \frac{Z}{3} \left(\frac{R_{sh}}{1 \text{ pc}} \right) \left(\frac{V_{sh}}{10^3 \text{ km.s}^{-1}} \right) \left(\frac{B_{up}}{1 \mu\text{G}} \right) \text{ TeV} \quad (3.11)$$

Where B_{up} is the value of the magnetic field upstream of the shock. The rate at which SNRs convert energy into CRs peaks when the shock radius is of the order of the pc or so, and the shock speed is several 10^3 km.s⁻¹. This implies that for an interstellar value of the magnetic field, the predicted maximum energy of protons falls short of the knee.

To go beyond that, it is necessary to increase the intensity of the magnetic field upstream of the shock. Cosmic ray currents, escaping from the shock, induce plasma instability and a magnetic field gradient leading to the Bell instability. This process causes the magnetic field lines to stretch and fold which leads to amplification of the magnetic field by one or two orders of magnitude near the shock, which may accelerate protons to 10^{17} eV and heavy ions, with charge Ze , to $Z \times 10^{17}$ eV (Bell & Lucek, 2001).

For accelerating CRs to high-energies above PeV, it's believed that sources beyond our galaxy become more influential. Jets from Active Galactic Nuclei (AGNs) and galaxy clusters are potential contributors. However, the exact origin of the highest-energy CRs, often referred to as Ultra-High-Energy Cosmic Rays (UHECRs), remains a subject of active research and debate.

Between the "knee" and the "ankle", spanning from about 10^{16} to 10^{18} eV, one hypothesis involves superbubbles, which are expanding regions of rarefied gas, often spanning hundreds of light-years. These superbubbles are fueled by series of supernova explosions and contain both primary shock waves from these supernovae and secondary shock waves generated by shock reflections and by intense supersonic turbulence. The acceleration process within these superbubbles operates in two stages : First-order and second-order Fermi accelerations. In this context, CRs gain additional time and space for Fermi acceleration, but there is an associated energy loss (adiabatic losses) during their propagation between successive SN shocks. The described process shares some similarities with second-order Fermi acceleration, as both involve interactions within a turbulent environment. However, it progresses more slowly than first-order Fermi acceleration, which directly occurs at shock fronts. Models are reviewed in Sect. 5.1 of Bykov et al. (2018).

Experimental evidence showing that superbubbles act as high-energy CR sources comes from the γ -ray observation of the active Cygnus X superbubble where freshly accelerated CRs have been found with energies approaching the knee, up to 150 TeV (Ackermann et al., 2012). Another piece of evidence comes from the CR abundances of heavy elements recorded between ^{26}Fe and ^{40}Zr with the Super-TIGER instrument (Murphy & Supertiger Collaboration, 2016). The measurements support a two-step model of CR origin in which the accelerated material is a mixture of $19^{+11}_{-6}\%$ nuclei from massive-star winds and SN ejecta and of 81% normal interstellar material with Solar-System abundances. This indicates that a significant fraction of CR acceleration occurs in OB associations (i.e. superbubbles) (Binns et al., 2019). Yet, another superbubble, the Orion-Eridanus one, which does not seem to play a role in either the initial acceleration or re-acceleration of CRs (Joubaud et al., 2019).

3.9 Galactic CR distribution

Cosmic rays traverse the Galaxy over approximately 100 million years. By calculating spallation reactions, we can determine that the amount of matter they pass through is $3 \times 10^{24} \text{ cm}^{-2}$ of gas column density. If we integrate the total amount of gas (H I , H_2 , etc.) across the thickness of the Galactic disk, we obtain a value between 0.1 and $1.4 \times 10^{21} \text{ cm}^{-2}$. This suggests that the particles have made hundreds of round trips between the disc and halo, or that they have traveled convoluted paths in the disc, in particular in the dense regions where their SNR sources are preferably located. The radio emissions of external galaxies indicate that they travel far from the disc rather than remaining strongly confined near the Galactic plane.

The flux and spectrum of CRs in the local ISM, within a few hundred of parsecs around the Sun, is relatively uniform (cf. Chap.6). Further away, the CR distribution varies with location.

Spiral arms

Spiral arms are distinguished by the velocity of the gas emission lines, which is determined by the velocity component projected along the line of sight. The Doppler effect is employed to pinpoint their positions. However, this approach fails when observing the Galactic center because the circular-shaped spiral arms have a velocity perpendicular to the direction of the observation.

Within the spiral arms, there exists a greater density of CR sources compared to the inter-arm regions. Furthermore, large-scale magnetic field lines tend to align with the spiral arms. Consequently, an anisotropic distribution of CRs is expected between these arms and the inter-arm regions. Moreover, the gas in the spiral arms is characterised by a higher degree of turbulence, so the CR diffusion length may be shorter within the spiral arms (cf. Chap.5). In γ -ray observations, the difference in CR flux between the arms and inter-arm regions seems relatively minor, typically hovering around 30% (Grenier et al., 2015).

On the other hand, spiral arms may affect the secondary to primary abundance ratios because the arms are not stationary features. At sufficiently low energies the CR age will be governed not by the diffusion time from the spiral arms, but by the time since the last spiral arm passage, which would be shorter and give less spallation products (Benjamin et al., 2016).

Towards the Galactic Halo

We expect the CR flux to decrease with altitude above and below the Galactic plane, but radio observations of edge-on galaxies show that CRs extend several kpc away from the plane of galaxies. Local measurements show that the flux indeed decreases by a factor of ~ 2 at a distance of 1 kpc (see Fig.6.4). Several models of CR propagation relate the CR scale height and the observed spectral break around 300 GV to a change in the propagation mode near and far from the Galactic plane. One such model is described in Evoli, Blasi, et al. (2018).

The issue of the radial gradient in CR flux

There is a significantly higher quantity of sources in the central regions of the Galaxy where star formation and thus supernovae are more prevalent, compared to the periphery. Consequently, it would be anticipated to observe more CRs in the central regions. However, the actual profile, as determined by γ rays, indicates that there is not even a factor of 2 difference in CR flux between the center and the edges.

In Fig. 3.12, various measurements of γ -ray emissivity⁶ have been conducted in different spiral arms and inter-arm regions, as indicated in the left panel. The γ -ray emissivity scales with the CR flux in the specific region (cf. Chap.4). In the right panel, the black dot at 8 kpc represents the average γ -ray emissivity of the local clouds (cf. Chap.6). The other coloured dots represent the ratio of each γ -ray emissivity measurement to the local one. There is not much difference between a spiral arm and an inter-arm region.

Additional data are presented in Fig.3.13. The red circles represent γ -ray emissivities analysed by Acero et al. (2016) at 2 GeV across the Galaxy. The blue squares are γ -ray emissivities per gas atom integrated over the 1-100 GeV range and analysed by Pothast et al. (2018). The green triangles represent the analyses by R. Yang et al. (2016) for γ -ray emissivities above 1 GeV using a conversion factor X_{CO} that changes with the Galactic radius. The points close to the Galactic center are taken from analysis of the entire Central Molecular Zone (CMZ) (Cassandjian, 2015) and from the analysis of the giant molecular complex Sagittarius B complex (Sgr-B2) (R.-z. Yang et al., 2015).

In both Figs. 3.12 and 3.13, the top curve represents the distribution of CR source density $Q_{src}(R)$ based on the pulsars' distribution $Q_{src}(R) \propto (R/R_\odot)^{1.9} \exp(-5(\frac{R-R_\odot}{R_\odot}))$ (model C from

⁶The γ -ray emissivity, q_γ , represents the rate at which γ -ray photons are emitted per gas atom in a specific unit of solid angle and energy interval and measured in $\gamma \text{ s}^{-1} \text{ sr}^{-1} \text{ eV}^{-1} (\text{H atom})^{-1}$

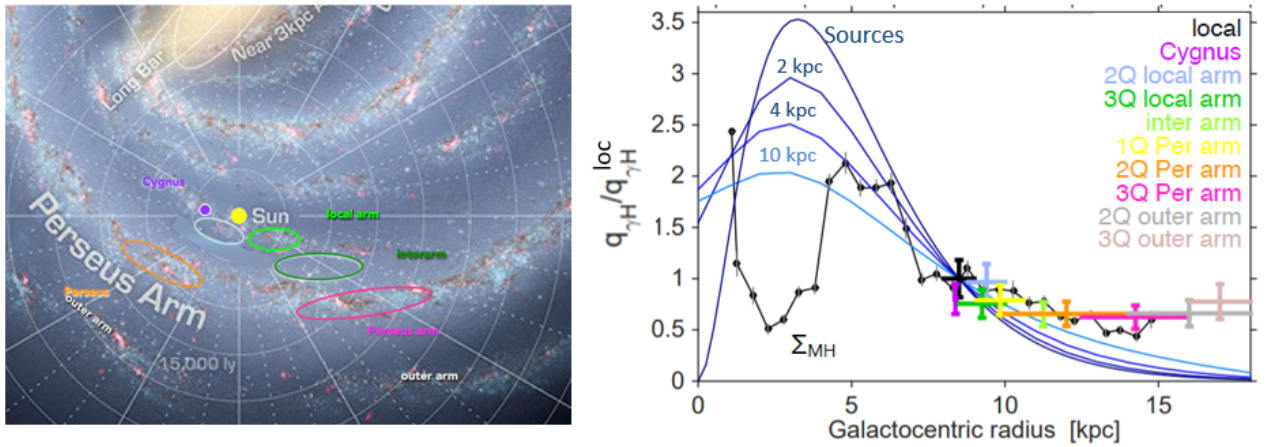


FIGURE 3.12 : A figure given by (Grenier et al., 2015). On the left are the areas of spiral arms and inter-arms in which γ -ray emissivity measurements were made. On the right is the ratio between these measurements and the average γ -ray emissivity of local clouds, given by the black point at 8 kpc, as a function of distance from the Galactic center. These emissivities are integrated above 400 MeV and are proxies for the CR densities. The curves, from top to bottom, represent the relative variations in CR source density (model C from Lorimer et al. (2006)) and in modelled CR density for several halo sizes modelled with GALPROP propagation code. The black curve shows the relative variation in gas surface mass density (Pineda et al., 2013). The errors include uncertainties in the *Fermi*-LAT satellite exposure and a 15% uncertainty in the derivation of N_{HI} column densities.

Lorimer et al. (2006)) . The other three curves are the proton density profile predicted by the GALPROP model for different halo sizes (Ackermann, Ajello, Atwood, et al., 2012).

Figure 3.14 represents a radial distribution of the spectral index of the hadronic emission obtained by the three analyses presented in Fig.3.13. This quantity is typically probed by secondary-to-primary CR ratios and most commonly the Boron to Carbon ratio (B/C), which is measured with high accuracy up to 1 TeV (cf. Chap.5). The plot shows a softening of the CR spectrum with Galactocentric distance, with a slope ranging from 2.6, at a distance of 3 kpc, to 2.9 in the external regions.

Near the Galactic center (< 5 kpc), the different results are not compatible between them and are less reliable in Fig.3.13 but also in Fig.3.14. One reason is due to a problem of separating components in the inner zone of the Galaxy. In this zone, a 1° pixel actually corresponds to a distance of 150 pc, which is the size of three giant molecular clouds. Therefore, the correct γ -ray emissivity cannot be attributed to each of these components. Moreover, if a source is not well separated, its γ -ray emissivity can be confused with that of the clouds (as exemplified by the pulsar separation problem near the Galactic center (Calore et al., 2014)). Another issue is the lack of a gas map in this inner zone of the Galaxy. In a single pixel, a mixture of HI and CO phases, and even dark gas (DNM) is found. Additionally, the lack of atomic HI phase is related to self-absorption as the 21 cm line traverses a large distance in the galaxy. For the molecular gas maps, the lack is related to the unknown X_{CO} ratio in these inner zones.

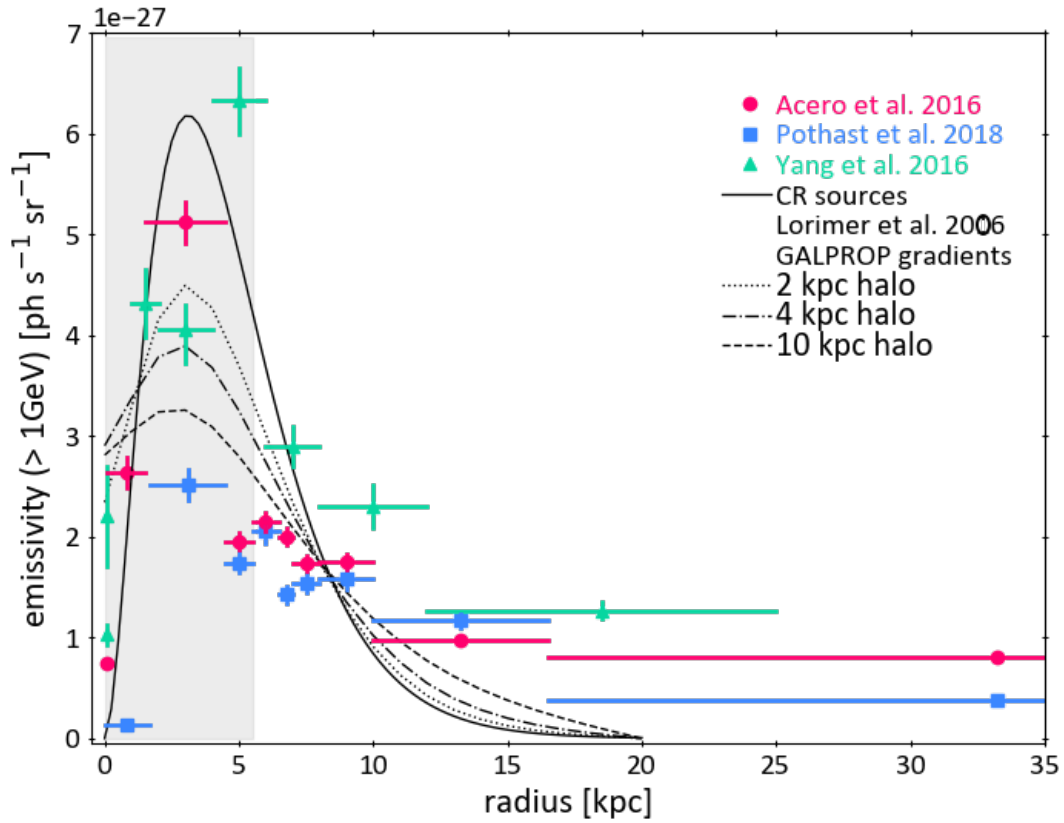


FIGURE 3.13 : Radial distribution of the γ -ray emissivity per H atom. The emissivity data are obtained by three different analyses by (Acero et al., 2016), (Pothast et al., 2018) and (R. Yang et al., 2016) represented by the red, blue and cyan symbols respectively. The curves, from top to bottom, represent the CR source density and modelled CR density for several halo sizes using GALPROP propagation code. Below 5 kpc, the grey rectangle represents the less reliable data.

In Figs.3.12 and 3.13, we can observe a small γ -ray emissivity difference when increasing the Galactic radius beyond the molecular region, indicating a small CR gradient between the center and outskirts of the Galaxy. However, the observed CR density does not align with the distribution of CR sources. Furthermore, for Galactocentric distances greater than 5 kpc, the predicted proton density gradient is steeper than the observed one. These discrepancies, referred to as "the CR gradient problem" has been known since the γ -ray surveys made by SAS-2 (Stecker & Jones, 1977), COS-B (Bloemen et al., 1986) and EGRET (A. W. Strong & Mattox, 1996).

The only way to have such a weak gradient is if the size of the CR halo exceeds 10 kpc. But a very thick halo is disfavored both by $^{10}\text{Be}/^9\text{Be}^7$ (A. W. Strong et al., 2007) and radio data (Bringmann et al., 2012).

To address the issue of the shallow CR gradient, one possible approach is to consider that the gas mass may be underestimated in the outer Galaxy, particularly the contribution from

⁷This ratio is explained in Chap.5

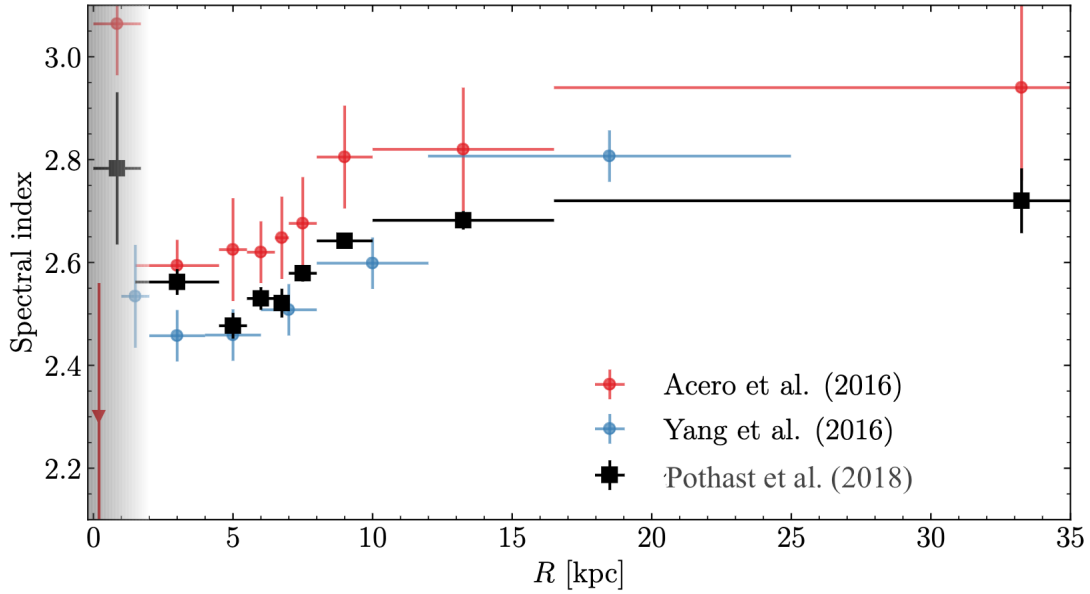


FIGURE 3.14 : A figure presented by Pothast et al. (2018) of spectral index of the hadronic emission for different Galactocentric rings. Different studies mentioned in the text are shown for comparison. Horizontal error bars indicate bin width in Galactic radius and vertical error bars are 68% credible intervals. The result associated to the first radial bin is less reliable and is therefore grayed out in the plot.

dark gas (DNM). Introducing more gas into the model would result in a lower estimated CR flux since the observed γ -ray intensity is fixed (cf. Chap.4). Another solution relates to the propagation of CRs. The curves obtained in Figs. 3.12 and 3.13 for different halo sizes assume a homogeneous and isotropic diffusion coefficient for CRs throughout the Galaxy. Conversely, one could consider that the propagation characteristics of CRs vary from one location to another in the Galaxy.

Regarding the spectral index, it is suggested that it becomes more challenging at low Galactocentric distances because of the gas associated with sources. In the Halo regions, there are fewer SNRs, and the sources are more distant from each other, resulting in less gas. Therefore, CRs must diffuse more to encounter more gas. Thus, the spectral gradient is attributed to : 1) source contamination, leading to a harder spectrum closer to the sources, 2) changes in the diffusion coefficient, and 3) strong advection in the central region.

I will present some previous studies that have attempted to find possible solutions to the problem of CR spatial and spectral gradients. In Fig. 3.15, the first plot represents γ -ray emissivity data at 2 GeV analysed by Acero et al. (2016). The second plot presents a radial distribution of cosmic proton density integrated beyond 10 GeV. The black dashed curve is the CR source profile deduced from the distribution of supernova remnants (SNR) (Green, 2015). The green curve is what GALPROP predicts with a uniform diffusion coefficient throughout the Galaxy for a halo size of 6 kpc. It is evident that this model does not reproduce the observable data.

Evoli et al. (2012) proposed a solution using the DRAGON numerical diffusion code. Their approach is based on the hypothesis that the CR diffusion coefficient is spatially correlated to

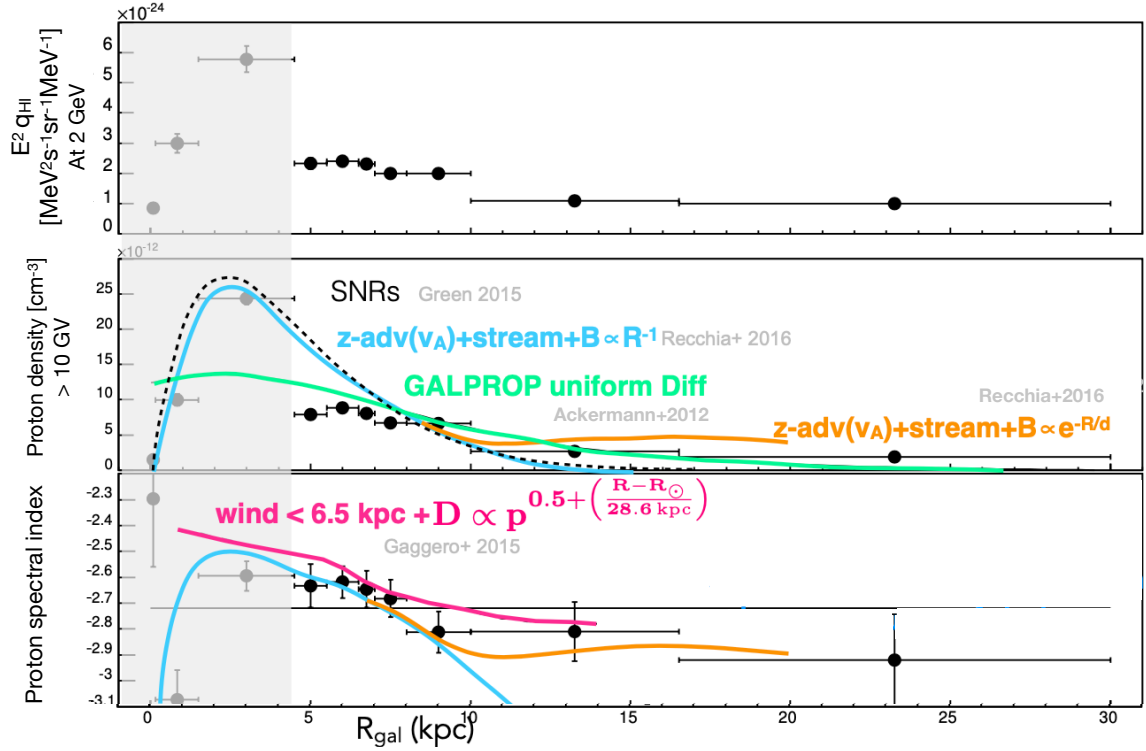


FIGURE 3.15 : The first plot is γ -ray emissivity data analysed by Acero et al. (2016). The second one is the distribution of proton density. The colored curves represent the different models and simulations proposed to reproduce the observable data. The black dashed curve is the distribution of the supernova remnants which represent the CR sources. The last plot represents the spectral index. The models are assigned the same color code as in the second plot. All data and models are plotted as a function of the Galactocentric distance. (courtesy of I. Grenier)

the source density, where star formation is stronger, and a higher turbulence level is expected. They state that $\kappa_{\perp} \propto Q_{src}^{0.85} \propto \kappa_{\parallel}^{-1}$, so the diffusion coefficient perpendicular to the magnetic field κ_{\perp} will be stronger in these turbulent zones near the sources, in contrast to what happens to the parallel coefficient κ_{\parallel} . Therefore, parallel diffusion becomes relevant only in the most external regions of the Galaxy, where the source density (and turbulence injection) is very small. The escape of cosmic rays from the most active regions is therefore faster, smoothing out their density throughout the Galaxy.

Gaggero et al. (2015) then proposed a phenomenological scenario using the DRAGON code. They assumed a high convective regime⁸ in the center and, outside, a diffusion with a coefficient that depends on the Galactocentric distance, as indicated by the magenta text in Fig.3.15. This approach allows for a good reproduction of both *Fermi*-LAT and local CR observables at both

⁸The convective regime is the transport of heat or energy where material moves in bulk. That bulk motion of a fluid (e.g., gas or plasma) is due to differences in temperature or density. It might occur in regions near massive stars or SNRs. It is a type of advection that is a more general term. Advection encompasses the transport of any property (not just heat) by the movement of the fluid. It might occur by the influence of gravitational forces, magnetic fields, or other large-scale phenomena.

low and mid Galactic latitudes, including the Galactic center, as shown by the magenta curve in the last plot of Fig.3.15.

The approaches presented by Evoli et al. (2012) and Gaggero et al. (2015) lack convincing physical motivation, and an alternative is proposed by Recchia et al. (2016). Building on the idea of Blasi et al. (2012) that below 100 GeV, particle transport at the Sun's location may be dominated by self-generated turbulence, Recchia et al. (2016) suggested that this could be the case throughout the Galaxy. They argued that both the gradient and the spectral shape can be explained by a non-linear CR transport mechanism : CRs excite Alfvén waves through streaming instability (cf. Chap.5) in the ionised Galactic halo and are advected with such waves at the Alfvén speed, v_A . This model is represented by the blue curves in Fig.3.15. Assuming that the background magnetic field drops exponentially at $R \geq 10$ kpc, they explained the data in the outer Galaxy. This scenario also fits well with the spectral slope of the CR spectrum as a function of R . These results are represented by the orange curves in Fig.3.15.

Until today, the problem of the spatial and spectral gradient of CRs remains unexplained, and several models have emerged in an attempt to interpret it.

Gas tracers : data and analyses

In Fig.4.1, we compare three maps of a given area of the sky, located between 140° to 231° in Galactic longitude and -38° to $+44^\circ$ in Galactic latitude : from left to right, the γ -ray map obtained by the *Fermi* Large Area Telescope (LAT) at energies over 1 GeV, the dust optical depth map τ_{353} inferred at 353 GHz from *Planck* and IRAS data, and the radio signal recorded at 408 MHz.

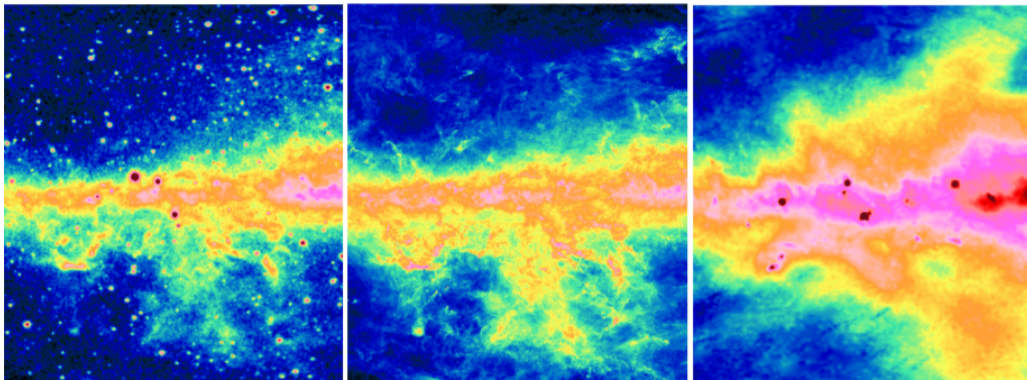


FIGURE 4.1 : Comparison of the γ -ray emission above 1 GeV (left), the dust optical depth at 353 GHz (middle), and the radio emission at 408 MHz (right) in the directions between 140° to 231° in Galactic longitude and -38° to $+44^\circ$ in Galactic latitude.

The *Fermi*-LAT map traces CR nuclei interacting with the interstellar gas along the line of sight whereas the dust map traces the column density of dust grains mixed with the same gas along the line of sight. The strong spatial correlation and the common structures found between these two maps indicate that they both trace, to first order, the total gas column density, N_H . The CR density and the dust-to-gas mass ratio and dust emissivity do not vary strongly from cloud to cloud (or they vary the same way, which is unlikely since dust and CRs are independent ISM components). Both maps can be used to trace the total gas, in all chemical and thermodynamical forms : atomic gas H I, dark neutral gas, and CO-bright molecular gas (Grenier et al., 2005 ; Planck Collaboration, Fermi Collaboration, et al., 2015).

The radio map differs from the other two. It mainly shows the synchrotron emission of primary cosmic leptons (electrons and positrons) and secondary leptons produced by hadronic

interactions between CR nuclei and the interstellar gas. The synchrotron emission is diffuse and the large difference between the radio map and the *Fermi*-LAT one, in Figure 4.1, stresses that the magnetic field is not uniform and/or that the distribution of leptons does not follow that of CR nuclei even though the two maps are produced by particles of comparable energies. It is difficult to recognise the clouds in the radio map therefore it cannot be used as a gas tracer.

4.1 Fermi-LAT

The Fermi Gamma-ray Space Telescope, often referred to simply as *Fermi*, is a NASA mission designed to study high-energy γ rays in the universe. It was launched on 11th of June 2008, and has provided significant insights into a wide range of astrophysical phenomena.

Fermi's primary objectives are to detect and study γ -ray sources, including γ -ray bursts, pulsars, active galactic nuclei (AGNs), and other high-energy phenomena. *Fermi* also contributes to the search for dark matter, as certain types of dark matter interactions might produce detectable γ -ray emissions. The mission aims to understand the origin of cosmic rays and their role in the universe. *Fermi* continues to operate and collect data, contributing to ongoing research in high-energy astrophysics. Its long-term mission has secured its place as one of the key observatories for studying the high-energy universe.

The Large Area Telescope (LAT) is the primary instrument on *Fermi* for high-energy γ -ray observations. It operates in the energy range from 20 MeV to about 1 TeV at a resolution of a few degrees at low energy, decreasing to about 0.1° at high energy. This resolution allows for precise localisation of γ -ray sources. The second instrument on board *Fermi* is the Gamma-ray Burst Monitor (GBM), dedicated to the study of transient phenomena between 8 keV and 40 MeV. In this work, the data we have used is provided by the LAT instrument.

4.1.1 The LAT in Space

Fermi is positioned in orbit around the Earth at an altitude of approximately 565 km, inclined at an angle of 25.6° onto the Equator. Following a thorough check-out and commissioning phase, the *Fermi* observatory commenced its regular scientific operations on August 13, 2008. The primary observing mode for *Fermi* involves a scanning technique, allowing the LAT to observe the entire sky approximately every two orbits, equivalent to around 3 hours. To accomplish this, the LAT alternates its boresight orientation during successive orbits, pointing towards $+50^\circ$ from the zenith direction and towards the orbit's pole on one orbit, followed by pointing -50° from the zenith on the subsequent orbit. The orbit of *Fermi* exhibits a precession period of roughly 53.5 days. The scanning strategy was modified after a malfunction in the rotation axis of one solar panel in 2018, but most of the sky is still surveyed every two orbits and the full sky is covered within a week (https://fermi.gsfc.nasa.gov/ssc/observations/types/post_anomaly/). On occasion, *Fermi* is operated in a pointing mode to investigate intriguing transient phenomena, and for some calibration runs.

4.1.2 Detector structure

The LAT, as designed by W. B. Atwood et al. (2009), is a wide-field γ -ray telescope based on the conversion of photons into e^-/e^+ pairs. It consists of a 4×4 matrix of towers, each housing a conversion-tracker module and a calorimetric module. Additionally, it includes an anticoincidence detector (ACD) covering the tracker to signal the passage of charged CRs), and a data acquisition (DAQ) system. Figure 4.2 illustrates the detector's configuration.

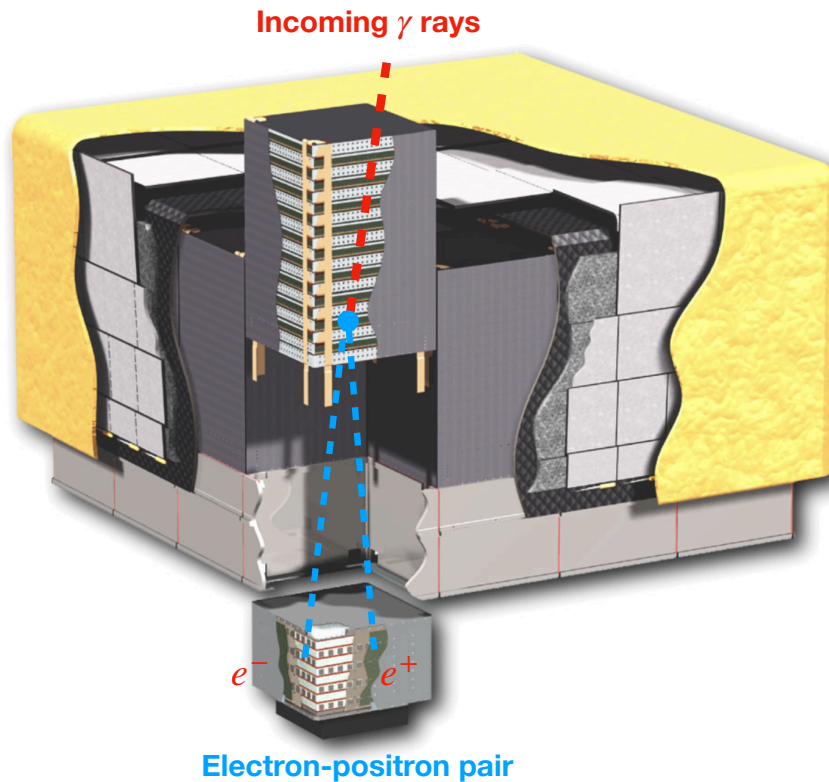


FIGURE 4.2 : Diagram of the LAT (W. B. Atwood et al., 2009). One tower is partially exploded to reveal the detector's structure. The real dimensions are $1.8 \text{ m} \times 1.8 \text{ m} \times 0.72 \text{ m}$.

To induce the conversion of high-energy photons into e^-/e^+ pairs, the conversion-tracker modules contain 16 sheets of tungsten ($Z=74$). They use two layers of silicon detectors between each sheet to track the trajectory of charged particles in the x and y directions. The last two layers do not contain tungsten sheets to precisely measure the entry point into the calorimeter. With a small height-to-width ratio of 0.4, the telescope's field of view is wide. It covers 2.4 sr and nearly all pair conversions pass through the calorimeter.

Each calorimetric module comprises 96 CsI crystals doped with thallium, arranged in 8 layers, providing a total depth of about 8.6 radiation lengths. The calorimeter measures the energy deposited by the electromagnetic shower generated by the initial e^-/e^+ pair. Photodiodes on both sides of the crystals collect the light signal, allowing each crystal to provide 3D information. This information includes two dimensions based on their position in the module's

matrix and a third dimension determined by measuring the signal asymmetry at each end.

The ACD consists of 89 plastic scintillator tiles arranged around the conversion/tracker modules. Its goal is to detect charged CRs entering the detector and, conversely, to prevent the rejection of certain events due to secondary charges created by high-energy photons. To achieve this, the signal from each tile is collected by photomultiplier tubes, and the spatial information of this signal is correlated with the signals from the tracker and calorimeter. Additionally, to protect against potential debris, the detector is shielded against micrometeorites.

For each tower, the tracker and calorimeter are connected by an electronic module that generates its own trigger. The signals from the various towers and the ACD are then collected by the DAQ system, which decides whether or not to initiate a trigger for the entire instrument. The trigger rate is approximately 2 to 3 kHz, and the rate of events transmitted to Earth is 500 Hz after an initial data filtering step performed by two on-board processors to reduce contamination from charged particles passing through the instrument.

4.1.3 Event reconstruction

After the data has been transmitted to the ground, the event analysis process can begin. This process involves several stages, starting with the initial filtering of potential γ -ray photon candidates, followed by the determination of their direction and energy. Additionally, these events are classified based on the quality of their reconstruction to minimise residual CR contamination and to allow performance selection according to the science goals. The entire analysis and filtering pipeline relies on Monte Carlo (MC) simulations of the instrument's performance.

MC simulation modelling

Before and after the telescope's launch, numerous MC simulations were conducted with dual purposes : event analysis and instrument performance assessment. These simulations were based on a tool specifically developed for the telescope, the GLAST LAT Event Analysis Machine, which made use of Geant-4 MC tools. The results were subsequently validated through an accelerator test campaign, during which a calibration module, consisting of two tracker/calorimeter towers, was exposed to photons (< 2.5 GeV), electrons (1-300 GeV), hadrons (π and p, ranging from a few GeV to 100 GeV), and ions (C and Xe, at 1.5 GeV/nucleon). These tests refined the detector's modelling and led to the selection of the Geant-4 interaction model that best reproduced the data.

Direction and energy reconstruction

After the conversion of the incident γ photon, e^- and e^+ leave activation signals in the silicon tracks of the tracker. Nearby signals are grouped into clusters characterised by a 3D position within the detector. These clusters are then combined to calculate the trajectory, taking into account the centroid and orientation of energy deposits in the calorimeter. The successive association of different clusters forms hypothetical trajectories, with the propagation between different detector layers calculated considering Compton scattering. The longest and straightest trajectory, corresponding to the highest-energy charged particle produced in the photon conversion, is retained as the best one. The clusters of signals composing it are marked as used, and

a new trajectory can be sought among the remaining clusters. Once individual trajectories are determined, interaction vertices are added to connect them in case of intersection.

The event's energy reconstruction is based on the energy deposited in each crystal of the calorimeter. Combining the different crystals provides information about the 3D energy distribution and an initial estimate of the total energy. The trajectory helps evaluate energy loss through the sides or the back of the calorimeter and through gaps between active volumes. At low energies, < 100 MeV, a significant fraction of the energy can be deposited in the tracker. Its contribution is added to that of the calorimeter, which is previously corrected to account for losses.

Event classification

Event classification allows for determining the best estimates of an event's direction and energy along with their corresponding uncertainties. A sequence of selection criteria and classification trees divides the data into different classes and generates associated probabilities. This classification significantly reduces CR background noise. Given the five-order-of-magnitude difference in trigger frequency between celestial photons and the much more numerous charged CRs, noise reduction is crucial. The primary tool for achieving this is the ACD coupled with trajectory estimations. Other parameters can also be used, such as event topology or the overall trajectory profile in the detector.

To address various scientific objectives, multiple event classes have been created, evolving over different data production cycles. The most recent one, called Pass8 (W. Atwood et al., 2013), includes classes like Transient, Source, Clean, with the purest being UltraCleanVeto for the strongest CR background rejection. Within the same class, events are further divided based on various criteria. The first criterion considers the location of the photon conversion in the detector, either in the front part of the tracker (Front) for better angular resolution than in the back part (Back). The Pass8 data version also includes three classes for the quality of photon direction reconstruction, ranging from the lowest, PSF0, to the highest, PSF3. Each of the four resolution classes has roughly the same number of total photons. Photons can also be sorted by energy reconstruction quality, from the lowest quality, EDISP0, to the highest, EDISP3.

4.1.4 Instrument response functions

The performance of *Fermi*-LAT has been accurately modelled through its instrumental response functions (IRFs). These functions provide a tool for analysing data after direction and energy reconstruction for different event classes.

The IRFs are defined by a general function R , dependent on the true energy E' and true direction p' of a photon. This general function is defined such that the differential number of photons in the reconstructed energy and direction space is the convolution of the source intensity with the response R :

$$\frac{dN(E, \vec{d}\vec{p}, t)}{dt d\vec{p} dE} = \int R(E, \vec{d}\vec{p} | E', \vec{d}\vec{p}'; t) \frac{dN(E', \vec{d}\vec{p}', t)}{dt d\vec{p}' dE' dS} \quad (4.1)$$

The function R can be factorised into three functions representing the effective sensitive area A , the angular resolution PSF , and the energy resolution D in addition to a temporal efficiency

$\epsilon(t)$:

$$R(E, d\vec{p}|E', d\vec{p}'; t) = \epsilon(t) A(E', d\vec{p}') PSF(d\vec{p}|E', d\vec{p}') D(E|E', d\vec{p}') \quad (4.2)$$

The factor $\epsilon(t)$ accounts for temporal variations such as a potential instrument degradation. The absence of consumables on board the LAT ensures a very stable performance, and continuous monitoring of bright constant sources verifies the constancy of the term $\epsilon(t)$ (Ajello et al., 2021). The IRFs are then :

- Effective area, $A(E', d\vec{p}')$, combining the true detector surface and the detection efficiency of a photon with true energy E' and true direction \vec{p}' ;
- Point spread function (PSF), $PSF(d\vec{p}|E', d\vec{p}')$, representing the probability density that a photon with true energy E' and true direction \vec{p}' has a reconstructed direction \vec{p} .
- Energy dispersion, $D(E|E', d\vec{p}')$, representing the probability density that a photon with true energy E' and true direction \vec{p}' has a reconstructed energy E .

The examples of performance metrics presented below correspond to the 'Source' event class used in the research presented in this thesis. This class offers a good compromise between effective area and CR rejection rate. It is commonly used in the analysis of point sources and of extended sources, with any residual contamination from isotropic CRs being easily manageable in γ -ray map analyses.

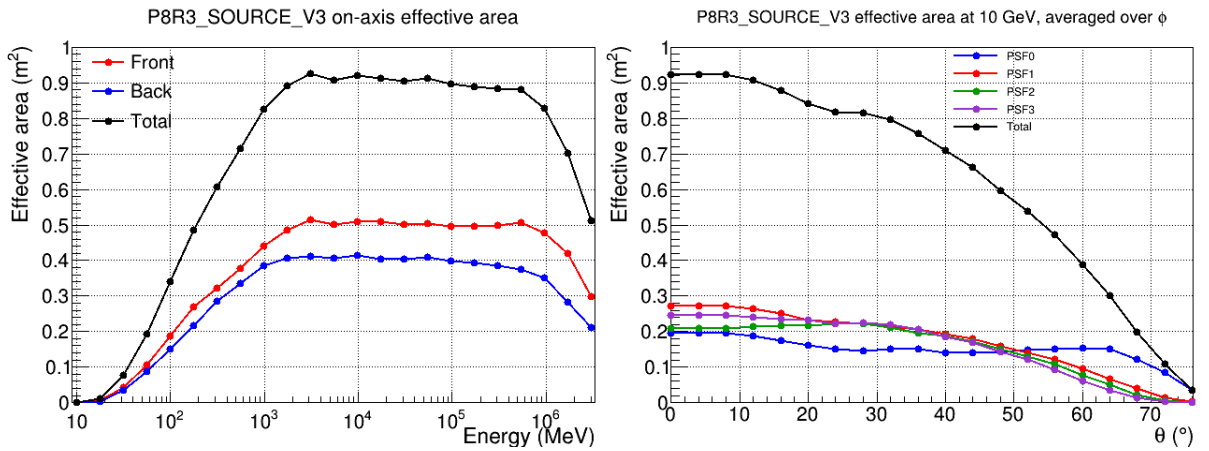


FIGURE 4.3 : Effective area as a function of energy for normally incident photons (*left panel*) and as a function of the angle of incidence for 10 GeV photons (*right panel*). The curves correspond to different locations of photon conversion in the tracker, or to different PSF types according to the labels.

Figure 4.3 illustrates the evolution of the effective area as a function of photon energy with a perpendicular incidence (*left panel*) and as a function of the 10 GeV photons' angle of incidence on the telescope (*right panel*). The integrated effective area over the telescope's field of view provides the acceptance.

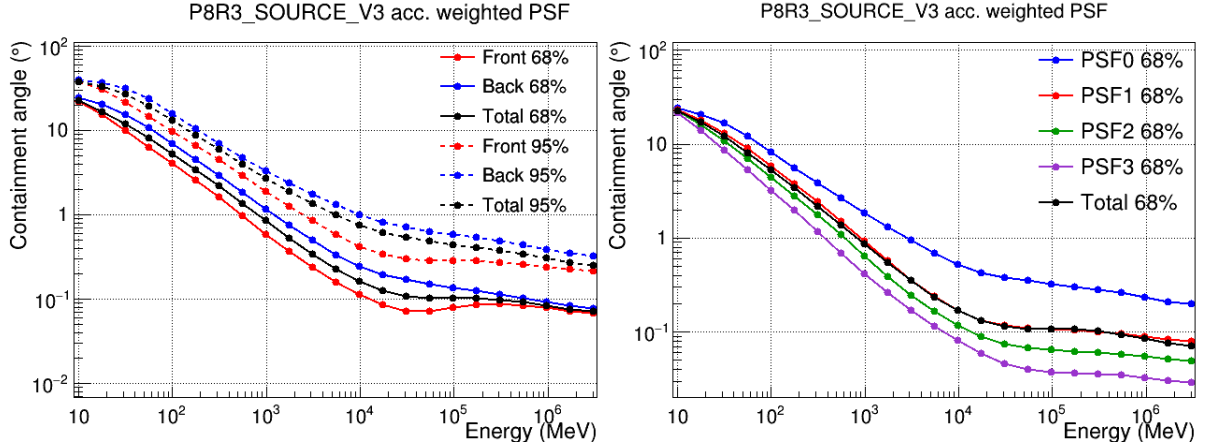


FIGURE 4.4 : Angular resolution as a function of energy. On the left panel, the 68% and 95% containment angles are shown based on the photon conversion location, and on the right panel, the 68% containment angle is presented for different event types.

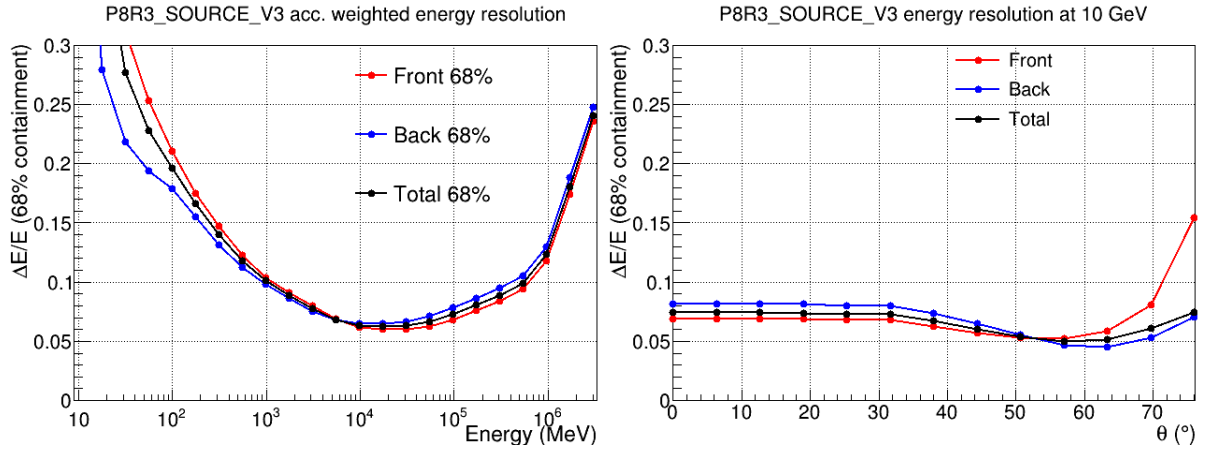


FIGURE 4.5 : 68% containment energy resolution as a function of incident photon energy (left) and as a function of incidence angle for 10 GeV photons (right). The curves represent different photon conversion locations : at the front of the detector (red), at the back (blue), and the total (black).

Figure 4.4 illustrates the evolution of the 68% and 95% containment angles for photons from a point source as a function of energy. The different event types (Front/Back/PSF0-3) are weighted by their respective acceptances. It is evident that the PSF strongly depends on energy due to Coulomb scattering of pairs in the tracker. The PSF typically exhibits a broader distribution tail than the ideal Gaussian case. In fact, it requires a sum of 3 or 4 Gaussians to fit the PSF profile. The PSF variation with the incidence angle in the field of view is minimal. Since the LAT observes the sky by regularly scanning it, the average PSF profile used in analyses must be calculated, taking into account the exposure time at different incidences during the period under consideration.

Figure 4.5 depicts the instrument's energy resolution, estimated as the acceptance weighted

68% containment half width of the reconstructed incoming photon energy. This resolution is better than 15% between 0.3 and 10^3 GeV and it is taken into account in our modelling.

4.1.5 Data likelihood analysis

Low photon counts, strong energy dependence of the angular resolution, and the overlap of point sources with diffuse emission necessitate the use of statistical tools for GeV sky studies. Here, I introduce the likelihood method developed since the 1980s based on Poisson statistics and its application with LAT data.

Let's consider a model describing the observations with a finite number of unknown parameters. $M(E', \vec{p}', t; \alpha_k) = \frac{dN_\gamma}{dt dS dE' d\Omega}$ represents the specific γ -ray intensity predicted by the model in different directions \vec{p}' of the sky and as a function of the true energy E' . The model includes unknown parameters $\{\alpha_k\}_{k=1, \dots, m}$ to be adjusted to the data. This intensity can be related to the photon count rate $\dot{\Lambda}$ obtained in the detector's phase space (reconstructed energy and direction E and \vec{p}) using the IRFs :

$$\dot{\Lambda}(\vec{p}, \{\alpha_k\}) = \int_{t_1}^{t_2} dt \int_{E_1}^{E_2} dE' \int_{\Omega} R(E, \vec{p} | E', \vec{p}'; t) M(E', \vec{p}', t; \{\alpha_k\}) d\vec{p}' \quad (4.3)$$

for a time interval $[t_1, t_2]$ and an energy band $[E_1, E_2]$ being observed.

Given the low count rate here, it is appropriate to use the Poisson distribution as proposed by (Cash, 1979) to compare the modelled and observed count maps. Thus, if the number of counts predicted by the model is Λ in a given direction, the probability of observing N counts will be :

$$f(n, \Lambda) = \frac{\Lambda^n}{n!} e^{-\Lambda} \quad (4.4)$$

The number of predicted photons can be compared to observations sampled on a grid in energy and incident direction. Because all pixels observed in a map are independent, the total likelihood is defined as the product of the probability densities of observing N_j photons in each pixel j :

$$\mathcal{L}(\{\alpha_k\}) = \prod_j f[N_j, \Lambda_j(\{\alpha_k\})] \quad (4.5)$$

Taking the logarithm, we obtain :

$$\ln \mathcal{L}(\{\alpha_k\}) = \sum_j N_j \log \Lambda_j(\{\alpha_k\}) - \sum_j \Lambda_j(\{\alpha_k\}) - \sum_j \log(N_j!) \quad (4.6)$$

The last term, which is a constant independent of the model, is discarded in the search for the maximum likelihood value. The penultimate term, representing the total number of predicted photons, can be denoted as Λ_{tot} . Thus, the set of parameters α_k that provides the best fit is

obtained by maximizing the logarithm of the likelihood as follows :

$$\ln \mathcal{L}(\{\alpha_k\}) = \sum_j N_j \log \Lambda_j(\{\alpha_k\}) - \Lambda_{tot}(\{\alpha_k\}) \quad (4.7)$$

This log-likelihood can be used to compare two models using the likelihood ratio test. Consider the model $M(\alpha_k, k = 1..m)$ and the simpler model $M_0(\alpha_k, k = 1..h)$, where $h > m$, and the parameters $\alpha_{k=1..h}$ are fixed at given values. In the null hypothesis where these parameters have their true values, Wilk's theorem (Wilks, 1938) states that the test statistic

$$TS = 2 (\ln \bar{\mathcal{L}} - \ln \bar{\mathcal{L}}_0) \quad (4.8)$$

where $\bar{\mathcal{L}}$ and $\bar{\mathcal{L}}_0$ are the maximum likelihood values obtained for models M and M_0 , respectively. The value of TS behaves asymptotically as a χ^2 distribution with $m-h$ degrees of freedom. A large value of TS indicates that model M better fits the data with a confidence level :

$$\text{c.l.} = \int_0^{TS} \chi_{m-h}^2(s) ds \quad (4.9)$$

The likelihood ratio can also be used when model M_0 is obtained by fixing certain parameters $\alpha_{k=1..m}$ of model M . This is, for example, the case when searching for a potential source above background noise. In this case, the source flux is imposed as zero in model M_0 . Neyman's lemma (Neyman & Pearson, 1933) shows that it is also possible to use the likelihood ratio to test how two different models compare with the same data, such as discriminating between two spectral models for a given source, like a power law and a blackbody spectrum.

4.2 Modelling γ rays

The γ -ray photons observed by *Fermi*-LAT are mainly produced by hadronic interactions of cosmic rays with the interstellar gas. The emission observed in the Fermi map shown in Fig.4.6 corresponds to the line-of-sight integral of the gas volume density multiplied by the volume density of cosmic rays as shown in Eq. 4.10.

$$I_\gamma \propto \int n_{gas} n_{CR} dL_{sight} \approx \bar{n}_{CR} \int n_{gas} dL_{sight} \quad (4.10)$$

Knowing the column density $N_H = \int n_{gas} dL_{sight}$ of a specific gas cloud in H at.cm^{-2} , we can obtain the γ -ray emissivity per gas atom, q_γ , which scales with the average CR density in that cloud if the CR density does not vary strongly inside the cloud. The strong spatial correlation observed between γ -ray maps and the dust optical depth, illustrated in Fig.4.1, and the large scales of potential CR gradients (of order a kpc) compared to the typical size of a cloud (tens of parsecs) have long supported this hypothesis when studying individual clouds (Grenier et al., 2015). The q_γ is defined as :

$$I_\gamma = q_\gamma N_H \quad (4.11)$$

where q_γ is measured in $\gamma \text{ s}^{-1} \text{ sr}^{-1} \text{ eV}^{-1} (\text{H atom})^{-1}$ while the intensity I_γ is in $\gamma \text{ cm}^{-2} \text{ s}^{-1} \text{ sr}^{-1} \text{ eV}^{-1}$.

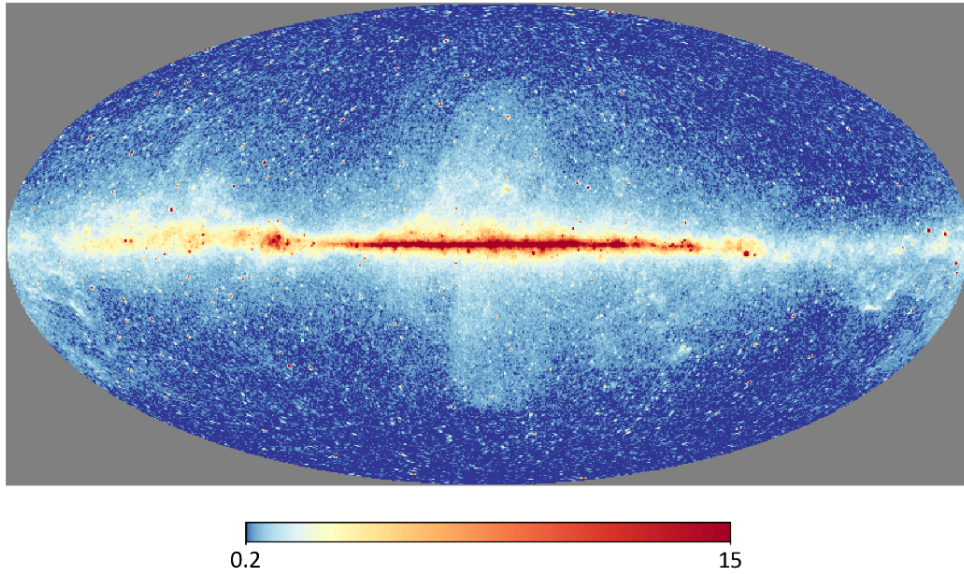


FIGURE 4.6 : Photon counts observed by *Fermi*-LAT for energy above 4 GeV in ten years of sky monitoring.

Earlier studies indicated that CRs radiating at 0.1–100 GeV have diffusion lengths much larger than typical cloud dimensions and that they propagate through the different gas phases. Therefore, the observed interstellar γ -ray intensity can be modelled, to first order, by a linear combination of the gas column densities, $N(l, b)$, present in the different phases of the different clouds seen along the lines of sight. The model also includes a contribution from the Galactic inverse-Compton (IC) intensity $I_{IC}(l, b, E)$ resulting from the up-scattering of CMB and interstellar infrared photons by CR leptons, as well as point sources of non-interstellar origin with individual flux spectra $S_j(E)$, the emission intensity from the Sun and the Moon I_{SM} , and an isotropic intensity $I_{iso}(E)$ that accounts for the extragalactic γ -ray background and for any residual cosmic rays misclassified as γ rays. The (E) refers to the energy and (l, b) are Galactic sky coordinates (longitude, latitude).

The predicted γ -ray photon counts in each (l, b) direction, is modelled in each energy band as :

$$\begin{aligned}
 N_\gamma(l, b, E) &= \sum_{i=gas} q_i(E) \tilde{N}_i(l, b) \\
 &+ q_{IC}(E) \tilde{I}_{IC}(l, b, E) \\
 &+ q_{iso}(E) \tilde{I}_{iso}(E) \\
 &+ q_{SM}(E) \tilde{I}_{SM}(l, b, E) \\
 &+ \sum_j q_{S_j}(E) \tilde{S}_j(E) \delta(l - l_j, b - b_j)
 \end{aligned} \tag{4.12}$$

where the term “gas” refers to the gas column densities in the different phases of clouds and in the different clouds in a given direction. They are multiplied by the respective hydrogen γ -ray

emissivities q_i .

The factors q_{IC} , q_{iso} , q_{SM} and q_{S_j} represent the re-normalisation factors associated with the predicted IC scattering (to allow for possible changes in the given region), the isotropic emission represented by a uniform intensity template, the Sun-Moon emission, and the γ sources. The gas emissivities and normalisation factors are obtained from a binned maximum-likelihood fit with Poisson statistics to the *Fermi*-LAT counts map. We denote by \tilde{I} and \tilde{S} the photon counts maps resulting from the convolution with the LAT response functions.

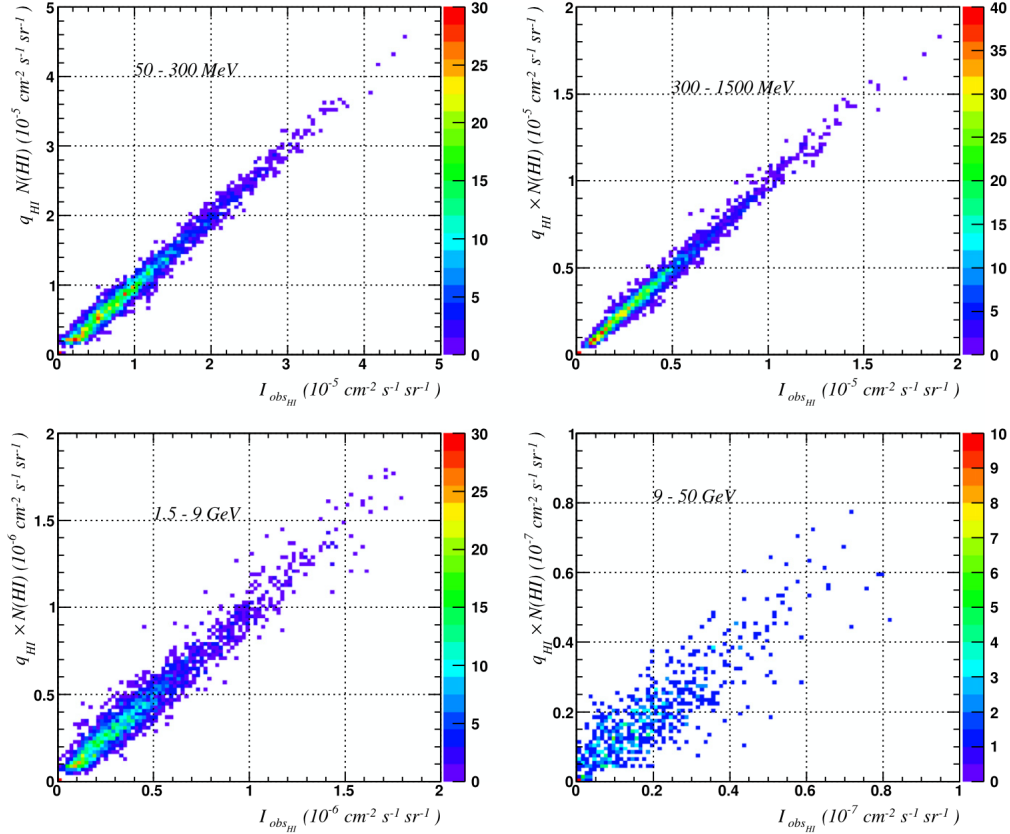


FIGURE 4.7 : Pixel-by-pixel correlation between the γ -ray intensity recorded in different energy bands and the N_{HI} column density at latitudes $10^\circ < |b| < 70^\circ$. The latter is multiplied by a standard γ -ray emissivity per gas atom to ease the comparison. (Casandjian, 2015)

In a specific study by (Casandjian, 2015), the observed quantity of γ -ray photons, as detected by *Fermi* at latitudes $10^\circ < |b| < 70^\circ$ and plotted on the horizontal axis of Figure 4.7, is directly compared to the intensity expected from the gas column density (on the vertical axis). Only photons seen toward the HI gas phase of the clouds have been used and contributions from other non-interstellar components such as point sources have been subtracted. The plots show a very strong correlation with the N_{HI} column densities measured at 21 cm. The correlation holds in different energy bands, even at 50 GeV. This correlation demonstrates that the model developed in eq. 4.12 produces a γ -ray intensity very close to reality. It is important to note that this analysis was conducted in 2015, utilising only seven years of *Fermi* data, so the high-

energy data was limited. Moreover, this study was applied far from the Galactic plane, resulting in minimal H_I self absorption along the line of sight.

4.3 Planck

The *Planck* satellite was launched by the European Space Agency (ESA) on 14th of May 2009 and its mission ended in 2013. It was orbiting the second Lagrange point of our Earth-Sun system, about 1.5 million km away. It was designed to observe the Cosmic Microwave Background (CMB) radiation and to study various aspects of the early universe with unprecedented precision. It could detect temperature differences of a few 10⁻⁶ degree Celsius. The major mirror was 1.5 m in diameter and was accompanied by two instruments : the Low Frequency Instrument (LFI), which operated between 30 and 70 GHz, and the High Frequency Instrument (HFI) between 100 and 857 GHz. The HFI had a resolution ranging from about 10 arcmin for the lowest frequencies to about 5 arcmin for the highest frequencies. The LFI had slightly poorer angular resolution <https://irsa.ipac.caltech.edu/Missions/planck.html>.

The observations at 353 GHz were crucial for studying the polarisation of both the CMB and the foreground cosmic dust thermal emission. The *Planck* satellite's study of cosmic dust polarisation at 353 GHz has provided valuable insights into the nature of dust and orientation of magnetic fields.

4.4 Modelling the dust optical depth

There are several different ways to observe the dust among which :

- observing its thermal emission. Grains are heated by the ultraviolet (UV) and optical radiation from stars. Large grains reach a thermal equilibrium by radiating in the IR with a peak emission around 100 – 200 μm in wavelength.
- measuring the reddening of stellar radiation as it is absorbed/scattered by dust grains along the path to Earth.
- observing emission lines produced by vibrations in polycyclic aromatic hydrocarbon molecules at IR wavelength between 3 and 20 μm , typically.

Frequencies in the far-infrared above 353 GHz are particularly useful for studying cosmic dust because the thermal emission is prominent in this range. Given the cold equilibrium temperature of the dust, which is close to 20 K on average (Planck Collaboration et al., 2014), the peak of the thermal emission occurs near 100–200 μm and has been observed by the *IRAS* satellite. Combining the spectral information from *Planck* and *IRAS* data, and modelling it with a modified blackbody spectral energy distribution, one can infer the dust optical depth. The thermal intensity of the dust radiation, $I_d(\nu)$, for a specific frequency ν is given by :

$$I_d(\nu) \propto \int \frac{M_d}{M_{\text{gas}}} n_{\text{gas}} B(T_d) \kappa_d(\nu) dL_{\text{sight}} \quad (4.13)$$

It is an integral over the line of sight of the dust mass M_d per unit gas mass M_{gas} , multiplied by the gas volume density n_{gas} which gives the dust quantity per unit volume. The ratio M_d/M_{gas} is considered to be fairly uniform in the local interstellar medium. The term $B(T_d)$ is the Planck blackbody law at the equilibrium temperature of the grains, and, since dust grains are not perfect blackbodies, this law is modified by an emissivity $\kappa_d(\nu)$ that depends on the grain material's ability to radiate at the specific frequency ν . The frequency dependence of $\kappa_d(\nu) \propto \nu^\beta$ is often taken as a power law.

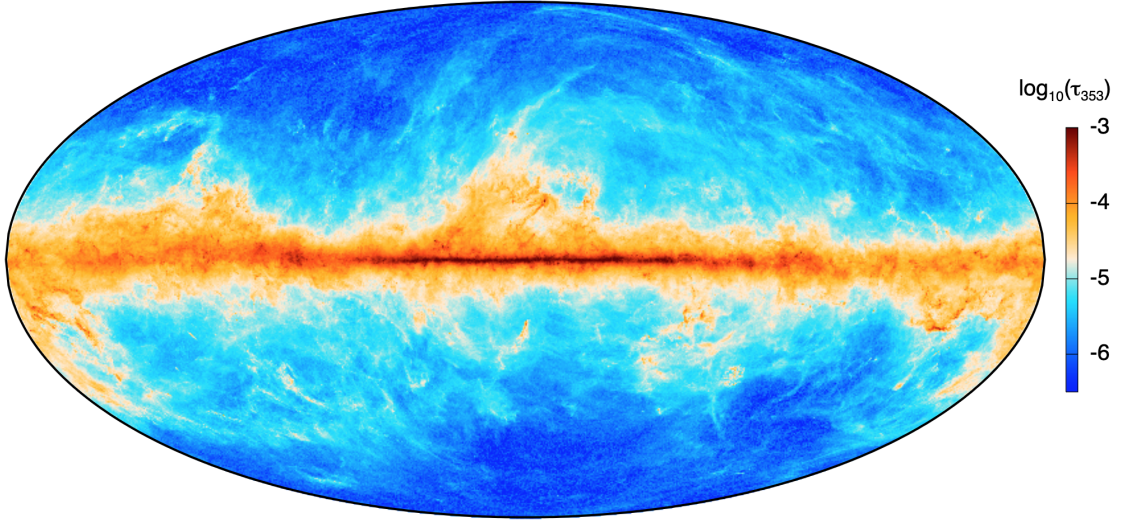


FIGURE 4.8 : Map of the dust optical depth τ_{353} at $5'$ resolution deduced at 353 GHz from the observations of the *Planck* and *IRAS* satellites. (Planck Collaboration et al., 2014)

The ratio of the observed intensity $I_d(\nu)$ over the black body one $B(T_d)$ represents the optical depth $\tau_\nu = I_d(\nu)/B(T_d)$ at a specific frequency ν . The sky map of the optical depth at 353 GHz is presented in Fig.4.8. This ratio makes it possible to follow changes in intensity due to variations in the amount of dust along the line of sight rather than caused by variations in the temperature, hence emissivity, of the grains.

Under the assumption of a uniform dust-to-gas mass ratio, M_d/M_{gas} , and a uniform emission coefficient per unit mass of the grains, the dust optical depth, τ , linearly scales with $\int n_{\text{gas}} dL_{\text{sight}}$, therefore with the total gas column density, N_H . Consequently, the $\tau_{353}(l, b)$ distribution can be modelled as a linear combination of the different gas contributions with free normalisations, y . These normalisations represent the average values of the dust opacity, τ_{353}/N_H , and are fitted to the data, as in Planck Collaboration, Fermi Collaboration, et al. (2015). A free isotropic term, y_{iso} , is added to the model to account for the residual noise and the uncertainty in the zero level of the dust maps (Casandjian et al., 2022; Planck Collaboration et al., 2014). The $\tau_{353}(l, b)$ model can be expressed as :

$$\tau_{353}(l, b) = \sum_{i=\text{gas}} y_i N_i(l, b) + y_{\text{iso}} \quad (4.14)$$

where the term ‘‘gas’’ refers to the gas column densities in the different phases of clouds and

in the different clouds in a given direction. They are multiplied by their respective opacities y_i . These fitted y_i parameters can probe opacity changes in the different interstellar gas phases.

4.5 The search for dark neutral gas

Figure 4.9a depicts the dust optical depth remaining after subtraction of the expected contributions from the atomic gas in the ISM. Regions of intense CO emission along the Galactic plane and towards nearby clouds have been discarded. Regions with no IRAS or CO information have been too. In parallel, Fig.4.9b shows the γ -ray intensity obtained after subtraction of all the γ -ray emissions produced in the H I and CO-bright phases of the ISM and of all non-interstellar components. By comparing the two maps, it becomes evident that they share the same pattern of excesses in corresponding regions.

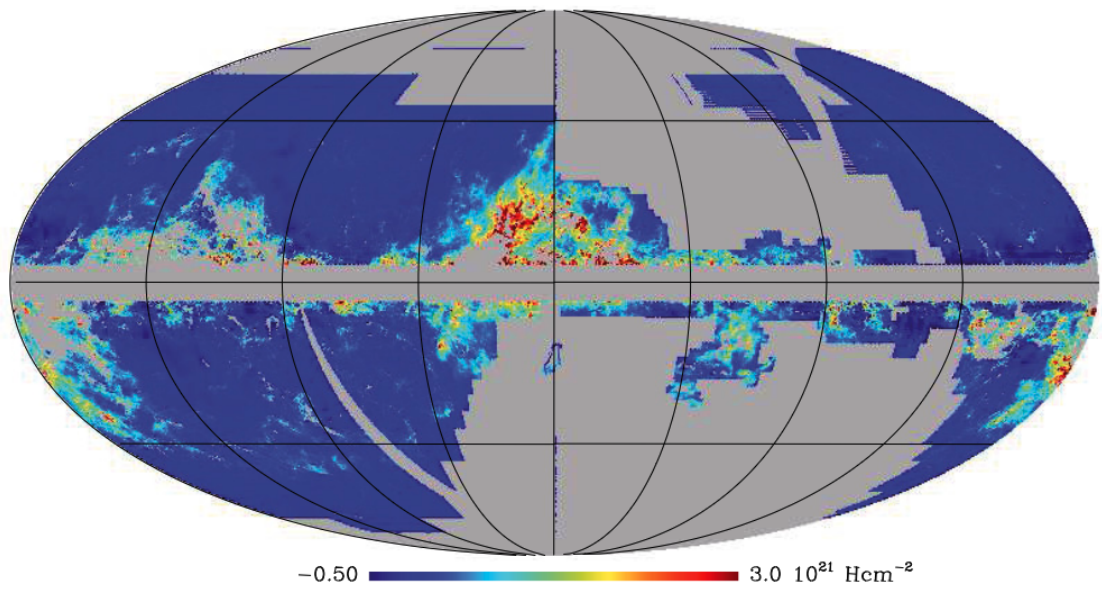
In the dust figure, the excesses correspond to dust mixed with undetectable gas and/or to variations in grain emissivity. In the γ -ray figure, the excess photons are produced by hadronic interactions of CRs with undetectable gas (because their energy spectrum is consistent with a hadronic origin), but they could also result from a local enhancement in CR flux. Since emission from hadronic interactions between CRs and dust grains is negligible, the spatial correlation between the dust and γ -ray excesses has a common origin in tracing the column density of undetectable gas (Grenier et al., 2005). The location of this gas with respect to the H I and CO distributions indicates that they trace the dark neutral medium, DNM, at the H I–H₂ transition (Grenier et al., 2005). Therefore, by jointly using the γ -ray and dust data, one can safely extract the amount of DNM and rule out other types of excesses due to local changes in CR flux or in dust emissivity. The extraction proceeds iteratively.

We first consider the DNM contribution of dust since it has a stronger signal-to-noise ratio than in γ rays. The model is generated by combining the column densities of gas from the visible phases in H I and CO. Then, we calculate the residual between the optical depth observation and the dust model, described in Eq.4.14.

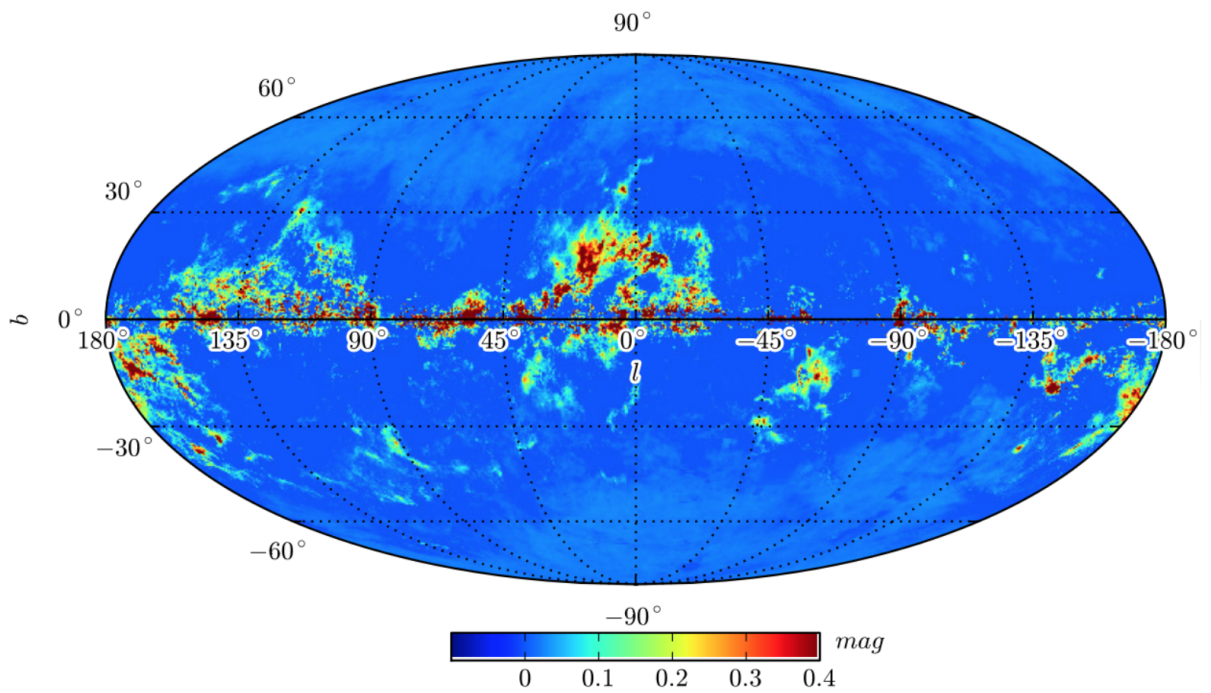
$$\tau^{res}(l, b) = \tau_{obs}(l, b) - \sum_{i=clouds} y_{HI,i} N_{HI,i}(l, b) - \sum_{i=clouds} y_{CO,i} W_i(CO) - y_{iso} \quad (4.15)$$

where "i" refers to the sum over different clouds along the line of sight. The y opacities obtained from the first iteration of the dust fit are overestimated because of the dark gas is missing in the model.

We then extract positive residuals in the τ^{res} map. Because of the noise around zero, a simple cut at $\tau^{res} > 0$ would induce an offset bias. Therefore, we have de-noised the residual maps using the multi-resolution (MR) support method implemented in the MR filter software (Starck & Pierre, 1998), considering a Gaussian noise estimated from the data itself. The DNM map obtained from the dust residuals, τ^{res} , is injected into the γ -ray model. We then generate the



(a) Map of the excess dust optical depth seen at 857 GHz after subtraction of the expected contributions from the atomic gas seen in H_I. The grey regions where no IRAS or CO data are available, or where intense CO emission is detected, have been greyed out (Planck Collaboration et al., 2011)



(b) Map of the γ -ray intensity obtained after subtraction of all the γ -ray emissions produced in the H_I and CO bright gas phases and other radiation components of non interstellar origin (Acero et al., 2016)

FIGURE 4.9

residual map between the observed and modelled photon counts, described in Eq.4.12.

$$\begin{aligned}
N_{\gamma}^{res}(l, b, E) &= N_{\gamma}(l, b, E) \\
&- \sum_{i=clouds} q_{HI,i}(E) \tilde{N}_{HI,i}(l, b) - \sum_{i=clouds} q_{DNM,i}(E) \tilde{\tau}_i^{res}(l, b) - \sum_{i=clouds} q_{CO,i}(E) \tilde{W}_i(CO) \\
&- q_{IC}(E) \tilde{I}_{IC}(l, b, E) - q_{iso}(E) \tilde{I}_{iso}(E) - q_{SM}(E) \tilde{I}_{SM}(l, b, E) \\
&- \sum_j q_{S_j}(E) \tilde{S}_j(E) \delta(l - l_j, b - b_j)
\end{aligned} \tag{4.16}$$

As for the dust residuals, we filter the positive excess in γ rays using the MR filter, but by considering a Poisson noise. The resulting map is then injected into the dust model for a second iteration of the dust fit to obtain improved γ opacities. When iterating both fits, the parameters γ and q rapidly converge to stable values. Two cycles are typically sufficient.

In order to transform the dust optical-depth residuals, $\tau^{res}(l, b)$, to gas column densities, $N_{H_{DNM}}$, we need to use the γ -ray information and to assume that the same CR flux permeates the atomic and DNM phases. This hypothesis is verified as we detect no spectral change in the γ -ray emissivity per gas atom in the HI, DNM, or CO phases. Any CR penetration problem into the dense gas would readily manifest itself as a spectral change in the low-energy part of the gas emissivity (Bustard & Zweibel, 2021 ; Schlickeiser et al., 2016). Under this assumption, the DNM gas column densities are calculated as

$$N_{H_{DNM}}^{Dust} = \frac{q_{DNM}}{q_{HI}} \tau^{res}(l, b) \tag{4.17}$$

and

$$N_{H_{DNM}}^{\gamma} = \frac{N_{\gamma}^{res}(l, b)}{q_{HI} A \Delta t \Delta \Omega} \tag{4.18}$$

The instrument parameters appearing in the denominator in this equation (the sensitive area A , exposure time Δt , and solid angle per pixel Ω) are due to the fact that the sky model and its emissivities is defined in γ -ray intensity, but the likelihood analysis is performed in photon counts, hence the convolution with the LAT response functions noted with a tilde in Eq. 4.12.

Cosmic-ray propagation

CRs are important for understanding the ISM. In galaxies like our Milky Way the energy density of CRs is roughly equivalent to that of magnetic fields, thermal gas and turbulent energy densities (Boulares & Cox, 1990; Hennebelle & Falgarone, 2012).

The CR energy density above 3 MeV/n is given by Cummings et al. (2016) :

$$\epsilon_{CR} = 0.83 - 1.02 \text{ MeV.m}^{-3} \quad (5.1)$$

For the magnetic field, Voyager 1 has measured a total magnetic field strength of $B_{\text{tot}} = 0.56 \pm 0.01$ nT (Burlaga et al., 2013) and therefore, the magnetic energy density $\epsilon_B = B_{\text{tot}}^2/2\mu_0$ is :

$$\epsilon_B = 0.8 \text{ MeV.m}^{-3} \left(\frac{B_{\text{tot}}}{0.56 \pm 0.01 \text{ nT}} \right)^2 \quad (5.2)$$

The local gas pressure at the cold atomic phase is $P/k_B = nT = 10^{3.58 \pm 0.175} \text{ K.cm}^{-3}$ (Jenkins & Tripp, 2011). Therefore, the energy density is :

$$\epsilon_{\text{Gas,CNM}} = 0.49_{-0.16}^{+0.24} \text{ MeV.m}^{-3} \quad (5.3)$$

Haud and Kalberla (2007) decomposed the 21-cm radio-lines of galactic HI gas into Gaussian profiles. They found that the mean width FWHM are 3.9 ± 0.6 , 11.8 ± 0.5 and 24.1 ± 0.6 for CNM, LNM and WNM respectively. According to $\text{FWHM} = 2\sqrt{2 \ln 2} \sigma_v \approx 2.35 \sigma_v$, we obtain the following turbulent energy densities $\epsilon_{\text{Turb}} = \frac{1}{2} \rho \sigma_v^2$:

$$\epsilon_{\text{Turb,CNM}} = 0.6 \text{ MeV.m}^{-3} \left(\frac{\sigma_v}{1.7 \pm 0.3 \text{ km.s}^{-1}} \right)^2 \left(\frac{n_{\text{HI}}}{30 \text{ cm}^{-3}} \right) \quad (5.4)$$

$$\epsilon_{\text{Turb,LNM}} = 0.5 \text{ MeV.m}^{-3} \left(\frac{\sigma_v}{5 \pm 0.2 \text{ km.s}^{-1}} \right)^2 \left(\frac{n_{\text{HI}}}{3 \text{ cm}^{-3}} \right) \quad (5.5)$$

$$\epsilon_{\text{Turb,WNM}} = 0.4 \text{ MeV.m}^{-3} \left(\frac{\sigma_v}{10.3 \pm 0.3 \text{ km.s}^{-1}} \right)^2 \left(\frac{n_{\text{HI}}}{0.5 \text{ cm}^{-3}} \right) \quad (5.6)$$

This energy equipartition suggests that these processes are coupled to each other (Hennebelle & Falgarone, 2012). Consequently, CRs affect the dynamics, energy balance, and various properties of the interstellar gas. This is crucial for galaxy evolution, including star formation, chemical composition changes, and the growth and maintenance of galactic magnetic fields (Zweibel, 2017). CRs originate from astrophysical sources such as supernova remnants (SNR), pulsars, and active galactic nuclei (AGN), where they are accelerated to high energies. After that, they travel through space in a complicated way (Amato & Blasi, 2018). This propagation is characterised by interactions with diverse components of the ISM including magnetic fields, plasma and gas.

5.1 Diffusion modes

In regions characterised by fast-moving hot gas, the primary mechanism governing CR transport is advection by thermal gas (Armillotta et al., 2021). CRs interact with the thermal gas through two distinct mechanisms :

- At relatively low energies, 2–10 MeV, CRs serve as an important source of collisional ionisation and heating of the interstellar gas.
- For higher-energy particles (few GeV), where the majority of CR energy density resides, they interact in a collisionless manner. This interaction is mediated by the ambient magnetic field and kinetic-scale waves and instabilities, forming the basis for the plasma physics associated with this coupling.

In cooler and denser gas regions marked by lower velocities, both extrinsic diffusion and streaming play significant roles in the cosmic-ray transport process (Armillotta et al., 2021).

As the CR energy increases, the gyroradius increases. When the gyroradius becomes significantly larger than the scale of magnetic fluctuations in the medium, the CR particles are less affected by these fluctuations and continue to follow the macroscopic magnetic field. This situation is represented in the middle diagram of Fig.5.1. Conversely, when the gyroradius is smaller than the scale of magnetic fluctuations, the particles respond by following these deviations from the large-scale field (as shown in the top diagram in Fig.5.1). When the gyroradius compares in size with the fluctuations, as shown in the bottom diagram in Fig.5.1, a resonance occurs, causing the CRs to closely track the fluctuations (Zweibel, 2013).

Early studies of CR coupling to the thermal gas focused on transport, which involves the diffusion of CR through fluctuating magnetic fields. However, in the late 1960s, researchers realised that these fluctuations could be generated by the CRs themselves through a kinetic instability. This discovery opened the door to a better understanding of the energy and momentum exchange processes between CR and the medium, with profound astrophysical implications.

The description of this energy and momentum exchange is explained by a set of fluid equations developed in the 1980s, known as "classical cosmic ray hydrodynamics" (CCRH). These equations allow the understanding of how CRs influence the surrounding medium, especially the turbulence. This type of CR transport is often referred to as nonlinear in nature. When one makes no assumptions about how these scattering waves are generated, it leads to a broader set

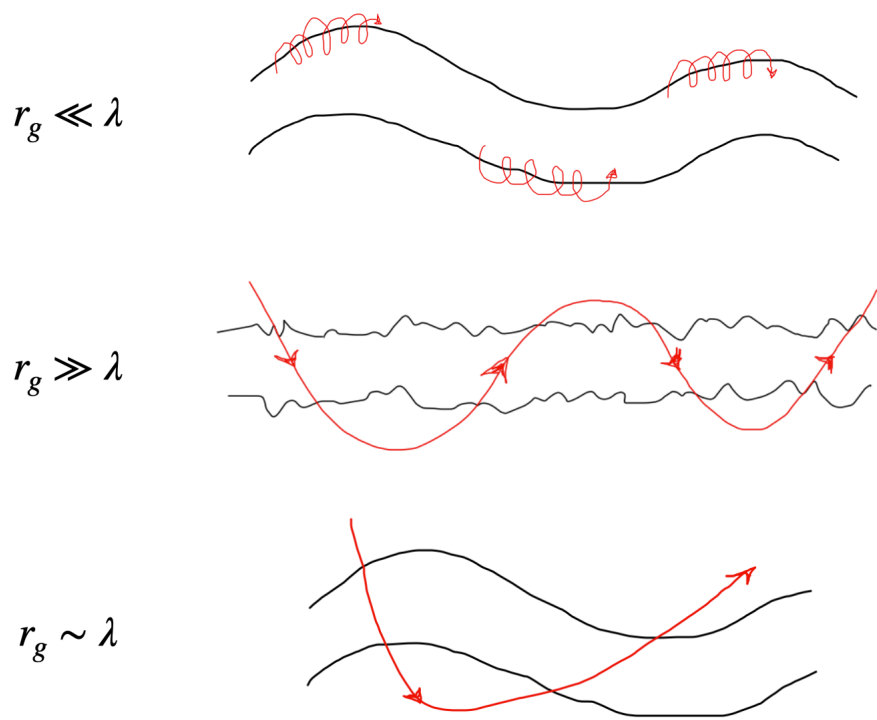


FIGURE 5.1 : Diagram representing the relationship between the CR gyroradius (r_g) in red and the scale of magnetic fluctuations (λ) in black. (Courtesy of Etienne Parizot)

of fluid equations called "generalised cosmic ray hydrodynamics" (GCRH). These equations provide a more complete framework for understanding the interactions between CRs and their environment (Zweibel, 2017).

Recent theoretical advances in CR research have primarily focused on delving into the non-linear aspects of CR interactions with their surrounding environment. As CRs propagate beyond their acceleration regions, their influence manifests in two principal forms. The mechanism that interests us is that CRs initiate the generation of hydromagnetic waves through streaming instabilities. These waves, in turn, affect the scattering properties of the ambient medium, impacting the energetic particle spectrum and its spatial distribution (Amato & Blasi, 2018). It is important to note that only CRs above a minimum momentum threshold, can effectively resonate with waves. This scattering process effectively reduces the speed at which CRs propagate through the medium. The presence of a gyroresonant instability, triggered by the streaming anisotropy of CRs, facilitates the exchange of energy and momentum between CRs and waves. In a steady state, the thermal background plasma must extract energy and momentum from the waves at the same rate at which they are added by CRs. This concept elucidates the collisionless nature of CR interactions with the thermal background (Zweibel, 2013).

Another noteworthy aspect is scattering induced by external turbulence, which involves the transfer of energy from the ISM turbulence to CRs. This process closely resembles second-order Fermi acceleration and serves as a substantial damping mechanism influencing the dynamics of interstellar turbulence.

An ongoing debate revolves around the origin of the magnetic fluctuations. It remains uncer-

tain whether they arise from Alfvén waves excited by the CRs themselves through the process known as resonant streaming instability (referred to as the "self-confinement" scenario) or if they stem from background turbulent fluctuations (the "extrinsic turbulence" scenario) driven by interstellar processes and cascading down from the injection scales, for instance from SNR.

Detailed spectral modeling offers support for self-confinement as the dominant mechanism for lower-energy CRs, while external turbulence appears to be more influential for very high-energy CRs (Armillaotta et al., 2022). Beyond the energy of 100 GeV, the population of CRs becomes insufficient to resonantly amplify the waves, leading to the failure of self-confinement (Zweibel, 2013).

The precise mechanisms through which magnetised turbulence influence CR acceleration and transport remain a subject of ongoing research. Recent theoretical advancements have provided insights into certain facets of these processes. This research often necessitates collaborative efforts among astronomers, plasma physicists, and other disciplines (Amato & Blasi, 2018).

5.2 Wave growth and damping rates

5.2.1 Growth rate of Alfvén waves

The interaction between CRs and the surrounding thermal gas is facilitated by the ambient magnetic field. CRs gyrate around the field lines and undergo scattering from magnetic fluctuations with sizes to their gyroradius. This scattering process results in a reduction in their collective propagation velocity. While very high-energy CRs are expected to be scattered by ISM-driven magnetohydrodynamics (MHD) turbulence, CRs observed in γ rays with *Fermi-LAT* are more likely scattering off self-generated Alfvén waves (R. Kulsrud & Pearce, 1969).

In the present work, we study GeV CRs so the dominant transport mode should be self-confinement via the streaming instability. CRs with a bulk drift speed greater than the Alfvén speed, $v_D > v_A$, can excite Alfvén waves through gyro-resonance and scatter off these waves as they propagate in the direction of decreasing CR density (Zweibel, 2017). The Alfvén speed used here is the ion one using the ion mass density, ρ_i , and the mean field strength, B_0 :

$$v_{A,0}^{\text{ion}} = \frac{B_0}{\sqrt{4\pi\rho_i}} \quad (5.7)$$

The growth rate of the Alfvén waves given by R. M. Kulsrud and Cesarsky (1971) is :

$$\Gamma_{\text{grow}}(k) = \pi^2 \left(\frac{\alpha - 3}{\alpha - 2} \right) \frac{Am_p \Omega_0}{\rho_i c} \Phi \left(p > \frac{ZeB}{kc} \right) \frac{v_D - v_{A,0}^{\text{ion}}}{v_{A,0}^{\text{ion}}} \quad (5.8)$$

for a CR nucleus with charge Ze , mass Am_p and flux $\Phi = \frac{dN}{dt dS d\Omega d^3p} \propto p^{-\alpha}$ with the power-law spectral index α in the range of interest. The flux is integrated in momentum above the threshold corresponding to the resonance $kr_L(p) = 1$ where r_L is the gyroradius, so the wavelength λ is equivalent to $2\pi r_L$. The term $\Omega_0 = \frac{ZeB}{Am_p c}$ notes the non-relativistic gyropulsation in the CGS system. The drift velocity v_D is the velocity of the frame where the CR distribution is isotropic.

For a specific CR species, denoted by j , with a velocity βc , the number volume density is :

$$n_j = \frac{4\pi}{\beta_j c} \Phi_j \quad (5.9)$$

By summing over CR species, one obtains :

$$\Gamma_{\text{grow}}(k) = \frac{\pi}{4} \left(\frac{v_D - v_A^{\text{ion}}}{v_A^{\text{ion}}} \right) \frac{1}{n_i} \sum_j \frac{\alpha_j - 3}{\alpha_j - 2} A_j \Omega_{0j} n_j \left(p > \frac{Z_j e B}{k c} \right) \quad (5.10)$$

To produce Alfvén waves, CRs should have a minimum momentum equal to $Z_j e B / k c$. Instead of integrating the CR volume density above this minimum momentum, we can integrate it for a rigidity \mathcal{R} above B/k . By eliminating the large-scale magnetic field strength term found in the Alfvén velocity and in the gyropulsation, one obtains :

$$\Gamma_{\text{grow}}(k) = \frac{\pi^{3/2}}{2} \frac{e}{c} (v_D - v_A^{\text{ion}}) \frac{1}{\sqrt{\rho_i}} \sum_j \frac{\alpha_j - 3}{\alpha_j - 2} Z_j n_j \left(\mathcal{R}_j > \frac{B}{k} \right) \quad (5.11)$$

The net drift with respect to the Alfvén wave frame ($v_D - v_A^{\text{ion}}$) can be written as a diffusive flux (Bustard & Zweibel, 2021 ; Jiang & Oh, 2018) :

$$v_D - v_A^{\text{ion}} = \kappa_{\parallel} \frac{\nabla \Phi_{\text{CR}}}{\Phi_{\text{CR}}} \quad (5.12)$$

with the diffusion coefficient κ_{\parallel} parallel to the mean B field. Introducing the characteristic length for a change in CR flux $\ell_{cr} = \Phi / \nabla \Phi$ (Hopkins et al., 2021), the growth rate becomes :

$$\Gamma_{\text{grow}}(k) = \frac{\pi^{3/2}}{2} \frac{e}{c} \frac{\kappa_{\parallel}}{\ell_{cr}} \frac{1}{\sqrt{\rho_i}} \sum_j \frac{\alpha_j - 3}{\alpha_j - 2} Z_j n_j \left(\mathcal{R}_j > \frac{B}{k} \right) \quad (5.13)$$

For CRs with energies of a few GeV and $(v_D / v_A - 1) \sim 1$, the growth time is a few 10^{10} s under average interstellar conditions (Zweibel, 2013). This value is long compared to the wave periods that are typically of order a year (3×10^7 s), justifying the weak damping approximation used to derive the growth rate. However, this value is short compared to typical macroscopic interstellar timescales, suggesting that the waves adjust quickly to local conditions. (Zweibel, 2013) shows that near the strong shocks that are responsible for CR acceleration, the CR flux is several orders of magnitude larger, making wave growth correspondingly faster. They also show that Γ_{grow} decreases rapidly with increasing particle energy. Above a certain energy, CRs will be unable to generate enough Alfvén waves to confine themselves, especially when important wave damping is present.

5.2.2 Damping modes

The attenuation in wave amplitudes and scattering rates can be attributed to wave damping processes that are influenced by the characteristics of the background MHD turbulence and the ambient plasma conditions. The predominant damping mechanisms traditionally studied in

the context of CR-induced waves are the ion-neutral damping and non-linear Landau damping. Their efficiency depend on the local ISM conditions. They both play pivotal roles in influencing the propagation of CRs, but in different environments (Armillotta et al., 2021). Other damping mechanisms are the turbulent damping and linear Landau damping.

5.2.2.1 Important notations

Before calculating damping formulas, we need to explore some important notations. Given the abundances in the ISM, we are going to limit the damping calculations to the hydrogen and helium atoms. For the atomic weights, the mass of helium can be written as $m_{\text{He}} = A_{\text{He}}m_{\text{HI}}$ with the mass number $A_{\text{He}} = 4$. It is not the case for the interstellar ions. In the WNM phase, the ions are mostly H^+ , so their mass $m_i = A_i m_{\text{HI}}$ with $A_i \sim 1$. While in the CNM phase, the ions are approximately half H^+ and half C^+ with $A_i \approx (A_{\text{H}} + A_{\text{C}})/2 = 6.5$. In fact, the equivalent ion mass gradually changes with the gas volume density and the C^+ fraction exceeds one half in the densest CNM clumps. The exact values of A_i are given by the simulations of Kim et al. (2023) as a function of gas density.

The abundance of a specific nucleon, x_n , is given relative to all H nucleons n_{Hn} . The number volume density of H nucleons in all gas phases is :

$$n_{\text{Hn}} = n_{\text{HI}} + n_{\text{HII}} + 2n_{\text{H}_2} \quad (5.14)$$

The number volume density of atomic hydrogen and helium are $n_{\text{HI}} = x_{\text{HI}}n_{\text{Hn}}$ and $n_{\text{He}} = x_{\text{He}}n_{\text{Hn}}$, respectively. The helium abundance x_{He} amounts to 0.085 from Asplund et al. (2009) or 0.01 from Kim et al. (2023). In our work, we chose the values given by Kim to be consistent with the use of his ISM model. Concerning the ions, the abundance is $x_i = (n_{\text{HII}} + n_{\text{CII}})/n_{\text{Hn}} = x_{\text{HII}} + x_{\text{CII}}$.

5.2.2.2 Ion-neutral damping

The initial damping mechanism to be examined was ion-neutral friction. It results from momentum transfer between ions and neutrals within partially ionised gas where neutrals are not magnetically bound (Armillotta et al., 2022).

Kulsrud formulation The majority of interstellar gas mass has less than 20% ionisation. Given that the collision frequency between ions and neutrals is significantly lower than the frequency of gyroresonant hydromagnetic waves, these Alfvén waves propagate through the plasma independently and experience damping due to neutral atoms at the rate $\Gamma_{\text{in,K69}}$ given by R. Kulsrud and Pearce (1969) :

$$\Gamma_{\text{in,K69}} = \frac{1}{2} \frac{n_n m_n}{m_n + m_i} \langle \sigma v \rangle_{\text{in}} \quad (5.15)$$

where n_n is the neutral number density, m_n is the mean mass of neutrals and m_i is the mean mass of ions. The ion-neutral momentum transfer rates $\langle \sigma v \rangle_{\text{in}}$ are given in table 2.1 of Draine (2011). They correspond to $\langle \sigma v \rangle_{\text{in}} = 3.25 \times 10^{-9} \text{ cm}^3 \text{ s}^{-1}$ for collisions between H and H^+ , $2.39 \times 10^{-9} \text{ cm}^3 \text{ s}^{-1}$ between H and C^+ and $1.42 \times 10^{-9} \text{ cm}^3 \text{ s}^{-1}$ between He and H^+ . The

ion-neutral damping for each interaction is :

$$\begin{aligned}\Gamma_{\text{H-H}^+} &= \frac{1}{2} \frac{n_{\text{HI}} m_{\text{HI}}}{(m_{\text{HI}} + m_{\text{HI}})} \langle \sigma v \rangle_{\text{H-H}^+} = \frac{n_{\text{HI}}}{4} \langle \sigma v \rangle_{\text{H-H}^+} \\ \Gamma_{\text{H-C}^+} &= \frac{1}{2} \frac{n_{\text{HI}} m_{\text{HI}}}{(m_{\text{HI}} + A_{\text{C}} m_{\text{HI}})} \langle \sigma v \rangle_{\text{H-C}^+} = \frac{n_{\text{HI}}}{2(1 + A_{\text{C}})} \langle \sigma v \rangle_{\text{H-C}^+} \\ \Gamma_{\text{He-H}^+} &= \frac{1}{2} \frac{(x_{\text{He}} n_{\text{Hn}})(A_{\text{He}} m_{\text{HI}})}{(A_{\text{He}} m_{\text{HI}} + m_{\text{HI}})} \langle \sigma v \rangle_{\text{He-H}^+} = \frac{x_{\text{He}} n_{\text{Hn}} A_{\text{He}}}{2(A_{\text{He}} + 1)} \langle \sigma v \rangle_{\text{He-H}^+}\end{aligned}$$

By summing these three main collisions and replacing n_{Hn} by $n_{\text{HI}}/x_{\text{HI}}$:

$$\Gamma_{\text{in,K69}} = \frac{n_{\text{HI}}}{2} \left[\frac{1}{2} \langle \sigma v \rangle_{\text{H-H}^+} + \frac{1}{1 + A_{\text{C}}} \langle \sigma v \rangle_{\text{H-C}^+} + \left(\frac{x_{\text{He}}}{x_{\text{HI}}} \right) \frac{A_{\text{He}}}{1 + A_{\text{He}}} \langle \sigma v \rangle_{\text{He-H}^+} \right] \quad (5.16)$$

If we replace the mass numbers A_n by their values (4 for A_{He} and 12 for A_{C}) and we use $x_{\text{He}} = 0.1$ and $x_{\text{HI}} \approx 1$, we obtain :

$$\Gamma_{\text{H-C}^+} = \frac{n_{\text{HI}}}{26} \langle \sigma v \rangle_{\text{H-C}^+} = 0.11 \times \Gamma_{\text{H-H}^+} \quad \Gamma_{\text{He-H}^+} = \frac{n_{\text{HI}}}{2} \frac{4}{5} \frac{x_{\text{He}}}{x_{\text{HI}}} \langle \sigma v \rangle_{\text{He-H}^+} = 0.07 \times \Gamma_{\text{H-H}^+}$$

In that case, the final equation for ion-neutral damping will be :

$$\Gamma_{\text{in,K69}} = \Gamma_{\text{H-H}^+} + \Gamma_{\text{H-C}^+} + \Gamma_{\text{He-H}^+} = 1.18 \times \Gamma_{\text{H-H}^+} = 0.96 \times 10^{-9} n_{\text{HI}} \quad (5.17)$$

This formulation does not depend on the gas temperature.

Soler formulation Momentum transfer between ions and neutral atoms of hydrogen or helium, all at the same equilibrium temperature T , results in the damping rate as :

$$\Gamma_{\text{in}} = \frac{\alpha_{\text{i,H}} + \alpha_{\text{i,He}}}{2\rho_{\text{i}}} \quad (5.18)$$

Where ρ_{i} is the ion mass density and equals to $\rho_{\text{i}} = n_{\text{i}} m_{\text{i}} = x_{\text{i}} n_{\text{Hn}} A_{\text{i}} m_{\text{HI}}$. The expression of the friction coefficient α_{iX} for collisions involving neutrals in the approximation of small velocity drift (Braginskii, 1965 ; Draine, 1986) has been taken from eq. 7 of Soler et al. (2016) :

$$\alpha_{\text{iX}} = \frac{4}{3} n_{\text{i}} n_{\text{X}} \sigma_{\text{iX}} \sqrt{\frac{8}{\pi} m_{\text{iX}} k_{\text{B}} T} \quad (5.19)$$

here, $X \in [\text{H}, \text{He}]$ stands for the neutral species, n_{i} and n_{X} are the ion and species number density respectively and m_{iX} is the ion-species reduced mass described as :

$$m_{\text{iX}} = \frac{m_{\text{i}} m_{\text{X}}}{m_{\text{i}} + m_{\text{X}}} \quad (5.20)$$

Which gives two equations for the two neutral species $[\text{H}, \text{He}]$:

$$m_{\text{iH}} = \frac{A_{\text{i}} m_{\text{HI}}^2}{A_{\text{i}} m_{\text{HI}} + m_{\text{HI}}} = \frac{A_{\text{i}} m_{\text{HI}}}{A_{\text{i}} + 1} \quad m_{\text{iHe}} = \frac{A_{\text{i}} A_{\text{He}} m_{\text{HI}}^2}{A_{\text{i}} m_{\text{HI}} + A_{\text{He}} m_{\text{HI}}} = \frac{A_{\text{i}} A_{\text{He}} m_{\text{HI}}}{A_{\text{i}} + A_{\text{He}}}$$

Therefore, by replacing m_{iH} , m_{iHe} , $n_i = x_i n_{Hn}$ and $n_{He} = x_{He} n_{Hn}$ in Eq.5.19, it will be :

$$\alpha_{iH} = \frac{4}{3} (x_i n_{Hn} n_{HI}) \sigma_{iH} \sqrt{\frac{8}{\pi} \left(\frac{A_i m_{HI}}{A_i + 1} \right) k_B T} \quad \alpha_{iHe} = \frac{4}{3} (x_i x_{He} n_{Hn}^2) \sigma_{iHe} \sqrt{\frac{8}{\pi} \left(\frac{A_i A_{He} m_{HI}}{A_i + A_{He}} \right) k_B T}$$

and finally, σ_{iX} corresponds to the ion-neutral momentum-transfer cross section for which Soler uses $\sigma_{iH} = 10^{-14} \text{ cm}^2$ and $\sigma_{iHe} = 3 \times 10^{-15} \text{ cm}^2$ from Vranjes and Krstic (2013). Draine (2011) has a discussion on this in section 2.5. After replacing n_{Hn} by n_{HI}/x_{HI} , the Eq.5.18 is :

$$\Gamma_{in,S16} = \frac{4}{3} \sqrt{\frac{2}{\pi} \frac{k_B T}{A_i m_H}} n_{HI} \left[\sigma_{iH} \sqrt{\frac{1}{A_i + 1}} + \frac{x_{He}}{x_{HI}} \sigma_{iHe} \sqrt{\frac{A_{He}}{A_i + A_{He}}} \right] \quad (5.21)$$

Hopkins formulation Hopkins et al. (2021) proposed (in eq.A1) an approximation for Γ_{in} to avoid calculating it directly. With the ion abundance x_i , this approximation is :

$$\Gamma_{in,H21} \simeq 10^{-9} \text{ s}^{-1} \left(\frac{T}{1000 \text{ K}} \right)^{1/2} \left(\frac{\rho_{tot}}{10^{-24} \text{ g cm}^{-3}} \right) (1 - x_i) \quad (5.22)$$

with the total mass density $\rho_{tot} = (1 + A_{He} x_{He} + A_C x_{CI}) m_{HI} n_{Hn}$.

5.2.2.3 Non-linear Landau damping

There is another damping mechanism that operates in fully ionised medium with a low density gas. It is the nonlinear Landau damping. The Landau resonance occurs when the velocity of a charged particle matches the phase velocity of a plasma wave which can lead to energy exchange between the charged particle and the wave. When Alfvén waves are present and their frequencies and wavelengths match the velocities and gyroradii of charged particles, the Landau resonance can lead to energy transfer from the waves to the particles, thereby damping the waves. Nonlinear Landau damping occurs when thermal ions have a Landau resonance with the beat wave formed by the interaction of two Alfvén waves (Armillotta et al., 2022). For CR generated waves the damping rate is given by R. M. Kulsrud (2005) and Armillotta et al. (2022) :

$$\Gamma_{nll} = 0.3 \Omega \frac{v_{t,i}}{c} \left(\frac{\delta B}{B} \right)^2 = 0.3 \frac{v_{t,i}}{c} v_p^2 \kappa_{||} \quad (5.23)$$

where c is the light speed and $\Omega = \Omega_0/\gamma_L(p)$ is the relativistic cyclotron frequency, with Ω_0 the classical cyclotron frequency and γ_L the Lorentz factor of CRs with momentum p . The ion thermal velocity is $v_{t,i}$ and $\delta B/B$ is the magnetic fluctuation at the resonant scale. In the last equivalence, v_p is the cosmic proton velocity and $\kappa_{||}$ is the diffusion coefficient parallel to the mean magnetic field.

Volk and McKenzie (1981) calculated the non-linear Landau damping rate $\Gamma_{nll,\pm}$ with the Alfvén-wave energy $e_{A,\pm}$. This wave energy corresponds to a wave propagating in the $\pm \vec{B}/|B|$ magnetic field direction. Hopkins et al. (2021) obtained an "effective" non-linear damping rate

$\langle \Gamma_{\text{nl}} \rangle \simeq \Gamma_{\text{nl}}(\langle e_{A,\pm} \rangle)$, which becomes :

$$\langle \Gamma_{\text{nl}} \rangle = \left[\frac{(\gamma_{cr} - 1) \pi^{1/2}}{8} \left(\frac{c_s v_A}{r_L \ell_{cr}} \right) \left(\frac{e_{cr}}{e_B} \right) \right]^{1/2} \quad (5.24)$$

where e_{cr} and e_B are the energy volume density of CRs and magnetic field respectively. The Larmor radius is r_L , the characteristic CR gradient scale length is ℓ_{cr} , the adiabatic factor is $\gamma_{cr} = 4/3$ for relativistic CRs and v_A the Alfvén speed. The sound speed c_s is given by $c_s^2 = (\gamma_{IG} - 1) \sigma_{turb}^2$ with $\gamma_{IG} = 5/3$ for an ideal monoatomic gas.

5.2.2.4 Turbulent damping

Turbulent damping is a notable mechanism of damping found in astrophysical plasmas. This phenomenon arises from the shearing apart of Alfvén waves as they propagate through anisotropic eddies in a turbulent background magnetic field. The turbulent damping was first mentioned in Yan and Lazarian (2002) and later studied by Farmer and Goldreich (2004) for trans-Alfvénic turbulence and by Lazarian (2016) in various turbulence regimes for more general astrophysical applications. For strong MHD turbulence, a critical balance is reached between the turbulent motion perpendicular to the local magnetic field and the wave-like motion along the field when the eddy turnover time is equal to the wave period (Goldreich & Sridhar, 1995) :

$$\frac{x_{\perp}}{u_x} = \frac{x_{\parallel}}{v_A} \quad (5.25)$$

where x_{\perp} and x_{\parallel} are the respective length scales of the eddy perpendicular and parallel to the local magnetic field, and u_x is the turbulent velocity resulting from the cascade at scale x_{\perp} . The turbulent damping rate is determined by the eddy turnover rate $\Gamma_{turb} = u_x/x_{\perp}$ at scale x_{\perp} . The effective rate depends on the super- or sub-Alfvénic character of the MHD turbulence (Lazarian, 2016) and is given by equations 14 and 16 of S. Xu and Lazarian (2022), respectively.

5.2.2.5 Linear Landau damping

This damping is closely related to the turbulent one. It represents the damping of oblique waves whose electric fields interact with the gas via Landau resonance. This happens when the propagation angle of the Alfvén waves relative to the local magnetic field is changing owing to turbulent motions (Zweibel, 2017). It scales with the local turbulent cascade time in exactly the same manner as Γ_{turb} , but with a different pre-factor. Following Zweibel (2017), we can write :

$$\Gamma_{LL} = \frac{\sqrt{\pi}}{4} \frac{c_s}{v_A} \Gamma_{turb} \quad (5.26)$$

where c_s is the speed of sound in the gas and v_A is the Alfvénic speed.

In Chap.8, the interstellar clouds we will be investigating exist in the neutral atomic phase (WNM, LNM, and CNM). That is why, we will focus on ion-neutral damping, which is the most dominant in these interstellar conditions, by a factor of 10^2 or even 10^3 .

5.3 Diffusion models

5.3.1 Leaky box model

The Leaky Box model, proposed by Cowsik et al. (1967), has long been a prominent framework to interpret the propagation of CRs within our Galaxy. This model was conceived to elucidate various intriguing observations. First, it aimed to account for the hardening of primary CR nuclei spectra in the 1-50 GeV/nucleon range as their atomic number (Z) increases. Additionally, it sought to address the decrease in energy of the secondary to primary ratios. The Leaky Box model represented a substantial improvement over the older "slab" model, which was prevalent at the time. The slab model assumed that all CRs cross a fixed ISM thickness during their journey from their source to Earth. While this model provided reasonable explanations for the production of secondary light elements (Li, Be, B) through spallation of medium elements (C, N, O), it failed to explain the abundance of heavier nuclei. If all CRs had indeed passed through the same average grammage, these heavier nuclei would have been significantly depleted. In contrast, the Leaky Box model posits that CRs experience an exponential distribution of path lengths during their journey. Consequently, numerous particles have traversed much shorter paths than the average (Jones et al., 1990).

In this model, CRs are postulated to originate from specific sources within the Galaxy and subsequently propagate through the ISM. It is assumed that the magnetic field confines CRs to the Galactic disk, and they can escape this confinement through a process called "leakage." Moreover, the model incorporates the idea that CRs undergo energy losses due to interactions with the ISM and can potentially be reaccelerated by shocks occurring within the ISM. The inner confinement box, surrounding the source, is presumed to have an energy-dependent lifetime, whereas the outer box, corresponding to the ISM, is assumed to be independent of the CRs energy (Gabici et al., 2019).

5.3.1.1 CRs in the Galactic disk

The total energy from CRs within the Galactic disk can be roughly estimated as $W_{cr} \approx 10^{55}$ erg. To maintain a steady state, Galactic sources must inject CRs into the galaxy at a rate of $P_{cr} \sim W_{cr}/\tau_{res}$. Here, τ_{res} signifies the residence time of CRs within the disk, where the CR sources are primarily situated. The estimation of the residence time τ_{res} is closely linked to distinctive patterns found in the chemical composition of CRs. This includes the notable excess of light elements (Li, Be, and B), as well as sub-iron elements (Sc, Ti, V, Cr, and Mn). This unusual composition can be explained by the fact that these elements are mainly secondary CRs, produced through spallation reactions between primary CR nuclei and the ISM.

By using known spallation cross-sections and CR secondary-to-primary ratios, such as the B/C ratio, it is possible to deduce that GeV CRs must accumulate a grammage of approximately $X \approx 5 \text{ g.cm}^{-2}$ (Zweibel, 2017) during their residence in the disk. Given the typical density of the interstellar medium $n_{ISM} \sim 1 \text{ cm}^{-3}$, this translates to a residence time within the Galactic disk, τ_{res} , on the order of a few 10^6 yr. Using the estimate of the residence time in the disk, it is feasible to calculate the CR power of the Galaxy, which is approximately $P_{CR} \sim 10^{41} \text{ erg.s}^{-1}$ (A. Strong et al., 2010). This suggests that a supernova explosion with a rate of 3 per century ($0.03 \text{ yr} \times 10^{51} \text{ erg} \approx 10^{42} \text{ erg.s}^{-1}$) could potentially provide the necessary energy for CR acceleration.

The residence time of CRs corresponds to a path traveled by the particles, roughly equivalent to $\lambda = \tau_{\text{res}} c \sim 1$ Mpc. This significantly exceeds both the radius and thickness of the disk. To reconcile these numbers, it is plausible to assume that CR motion within the disk is diffusive.

5.3.1.2 Radioactive clocks

Another significant constraint on CR propagation within the Galaxy emerges from the examination of unstable secondary particles, such as the radioactive isotope ^{10}Be . This isotope proves to be particularly suitable for these investigations because its decay time, $\tau(^{10}\text{Be}) \sim 1.4 \times 10^6$ yr, is of the same order as the CR residence time in the disk, τ_{res} .

During CR spallation reactions in the disk, ^{10}Be is generated together with stable Be isotopes. The decay of ^{10}Be implies an observed $^{10}\text{Be}/\text{Be}$ ratio that is lower than the production ratio by a factor of $\approx \tau(^{10}\text{Be})/\tau_{\text{esc}}$, where τ_{esc} is the CR escape time from the Galaxy. The measured $^{10}\text{Be}/\text{Be}$ ratio suggests that $\tau_{\text{esc}} \sim (10 - 20) \times 10^6$ yr, a duration significantly longer than the residence time of CRs in the disk, τ_{res} .

This apparent inconsistency is resolved by postulating that CRs are diffusively confined within a magnetised Galactic halo, which encompasses a much larger volume than the disk. Spallation reactions are significantly reduced while CRs reside in the low-density medium of the halo. The grammage is mostly accumulated by CRs during repeated transits through the thin gaseous Galactic disk.

5.3.1.3 Secondary-to-primary ratio

Considering a source rate $Q_a(E)$ for a specific species a , the equilibrium rate is :

$$Q_a(E) = \frac{N_a(E)}{\tau_c(E)} + \frac{N_a(E)}{\tau_{\text{esc}}(E)} \quad (5.27)$$

Where $\tau_c(E)$ denotes the catastrophic loss timescale by fragmentation or annihilation and $\tau_{\text{esc}}(E)$ is the escape timescale. $N_a(E)$ represents the quantity of species a injected at the source. Consider a CR species denoted as s , which is entirely secondary in origin (for instance, boron), and is primarily generated in spallation reactions involving a heavier CR species p , which is predominantly primary (e.g., carbon). The production rate of species s can be expressed as follows :

$$Q_s(E) = N_p(E) n_{\text{ISM}} \sigma_{p \rightarrow s}(E) v(E) \quad (5.28)$$

Where n_{ISM} represents the ISM gas density, $\sigma_{p \rightarrow s}(E)$ the production cross-section of s , and $v(E)$ the velocity of CRs. Supposing that secondary particles can annihilate to a tertiary particle t :

$$\frac{N_s(E)}{\tau_c(E)} = N_s(E) n_{\text{ISM}} \sigma_{s \rightarrow t}(E) v(E) \quad (5.29)$$

The Eq.5.28 can therefore be written as :

$$N_p(E) n_{\text{ISM}} \sigma_{p \rightarrow s}(E) v(E) = N_s(E) [n_{\text{ISM}} \sigma_{s \rightarrow t}(E) v(E) + \tau_{\text{esc}}^{-1}(E)] \quad (5.30)$$

Thus, the ratio of secondary to primary is :

$$\frac{N_s(E)}{N_p(E)} = \frac{\sigma_{p \rightarrow s}(E)}{\sigma_{s \rightarrow t}(E) + X^{-1}(E)} \quad (5.31)$$

With the "grammage" $X(E) = n_{\text{ISM}} v(E) \tau_{\text{esc}}(E)$. The secondary-to-primary ratio is therefore directly proportional to the "grammage" and to the escape time $N_s/N_p \propto X \propto \tau_{\text{esc}}$. Within the box, the "grammage" is accumulated over a time period $\tau_{\text{esc}} \sim H^2/\kappa$ where H and κ are respectively the thickness of the halo and the diffusion coefficient. Consequently, the secondary-to-primary ratio is inversely proportional to the diffusion coefficient $N_s/N_p \propto \kappa^{-1}$.

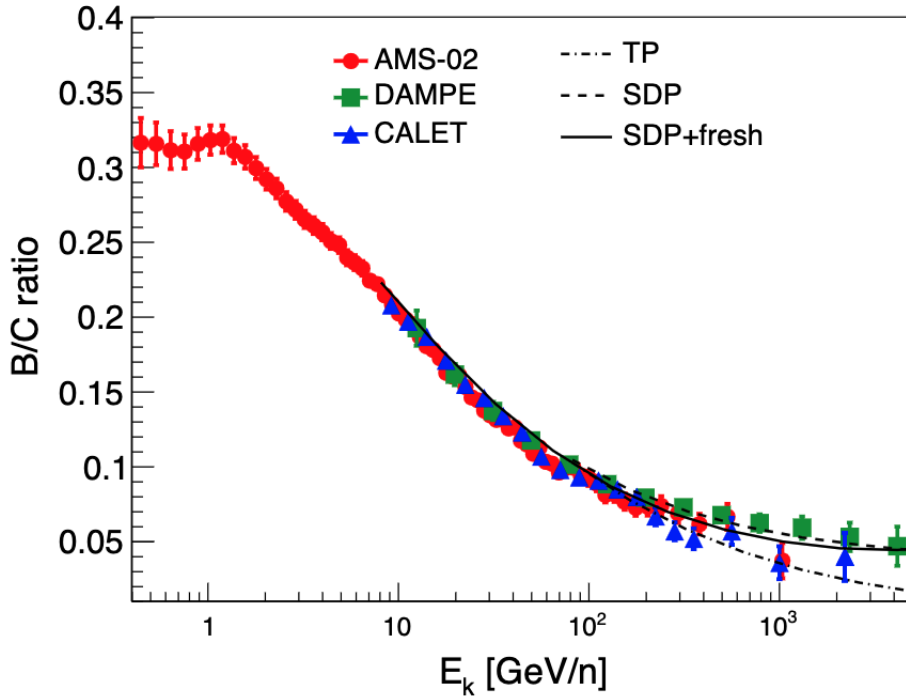


FIGURE 5.2 : Simulation by (Luo et al., 2023) in black curves compared to different data measurements by AMS-02, DAMPE and CALET.

Observations show that the secondary-to-primary ratio has a roughly power-law decrease according to $N_s/N_p \propto E^{-\delta}$ which means that the diffusion coefficient is $\kappa(E) \propto E^\delta$. Observations show that CRs are produced at the sources with a specific spectrum index but arrive on Earth with another one because of the diffusion. Best-fit parameters from various analyses of CR and γ -ray data for rigidity at a few GV suggest values of $\delta \sim 0.3 - 0.6$ and $\kappa \sim 10^{28} - 10^{29} \text{ cm}^2 \text{ s}^{-1}$ (A. W. Strong et al., 2007). The measurements of AMS-02 show that the B/C ratio exhibits a spectral index of -0.333 ± 0.014 (stat) ± 0.005 (syst) between the rigidity 65 GV and 2.6 TeV (Aguilar et al., 2016).

Figure 5.2 shows the B/C ratio data obtained by AMS-02 (Aguilar et al., 2018), CALET (Adriani et al., 2022) and DAMPE (Dampe Collaboration, 2022). The black curves are obtained by the simulation of Luo et al. (2023) using DRAGON and supposing a double structure of the halo. The inner one near the disk has a high level of turbulence and a low diffusion coefficient

because of the proximity of numerous SNRs. The outer one is characterised by a larger diffusion coefficient. Their result fits well the data, but according to the calculations of Armillotta et al. (2022) for self-confinement of CRs, the diffusion coefficient must be 10 to 100 times larger near the disk than in the halo.

5.3.1.4 Diffusion coefficient

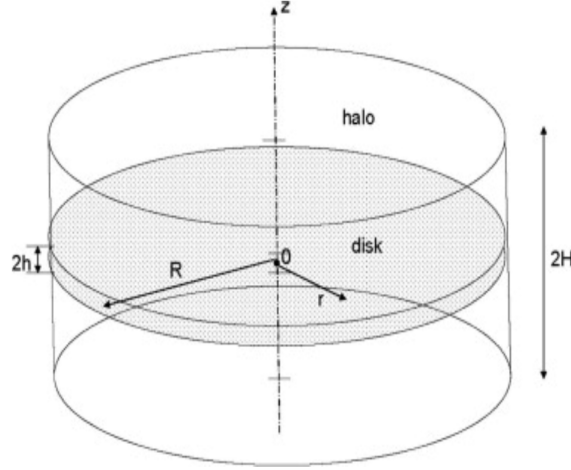


FIGURE 5.3 : Representation of the 2D Leaky Box model from Ptuskin (2012). It is characterised for having a disc region of $2h$ thickness and a magnetised halo region over and below the disc, with H the half-thickness

Let us consider a simple diffusive propagation with all CR sources in the disc of radius R_d and thickness $2h$. The sources are mainly due to SN remnants with an explosion rate R_{SN} per unit time. The Leaky box model contains a halo with a thickness H above and below the disk. The transport equation of a species a propagating in the box is :

$$\frac{\delta n_a(E, \vec{r}, t)}{\delta t} = \nabla[\kappa_a(E)\nabla n_a(E, \vec{r}, t)] - \Gamma_a^{sp} n_a(E, \vec{r}, t) + N_a(E)\delta(t - t_{\text{source}})\delta^3(\vec{r} - \vec{r}_{\text{source}}) \quad (5.32)$$

On the right hand side of the equation, the first term represents the diffusion, the second one is the spallation with spallation rate Γ^{sp} and the last one is the injection term.

To solve this transport equation we first put the boundary condition $n_a(E, z = \pm H) = 0$. We then consider the simpler case limited to protons, hence without spallation. If $H \ll R_d$, the CR density reaching Earth is :

$$n_{CR}(E) = \frac{N(E) R_{SN}}{2 H \pi R_d^2} \frac{H^2}{\kappa(E)} \quad (5.33)$$

where $H \pi R_d^2$ is the volume explored by the particles, $H^2/\kappa(E)$ is the diffusion time. This solution shows that the CR spectrum softens during propagation because the diffusion coefficient increases with energy.

5.3.1.5 Model limitations

The precise data collected by the AMS-02 experiment (Aguilar et al., 2016, 2018) challenges some of the historical results discussed above. We saw that primary CR fluxes are softened after propagation and should scale as $\Phi_p \propto R^{-\alpha-\delta}$ with α and δ the source and the diffusion spectral indexes, respectively. Secondary CRs should be even softer with $\Phi_s \propto R^{-\alpha-2\delta}$, so the secondary-to-primary ratio is expected to provide direct insights on the diffusion coefficient spectral index, $\Phi_s/\Phi_p \propto R^{-\delta}$. But, Batista et al. (2019) showed that this simplified scenario is questionable because inelastic collisions with ISM play an important role up the TeV domain. They cannot be neglected and imply that the spectral slope of the B/C ratio is not constant.

Furthermore, recent AMS-02 data (Aguilar et al., 2023) show that the fluxes of CR elements considered so far as pure primaries, such as S, Ne, Mg, and C, in fact include sizeable secondary components. Moreover, the secondary contribution to the "primary" flux depends on the odd or even Z number of the element. The carbon, always thought as a pure primary CR, is well described by the weighted sum of the primary oxygen flux and the secondary boron flux $\Phi_C = 0.84 \Phi_O + 0.67 \Phi_B$. In the carbon flux, the primary fraction goes from $80 \pm 1\%$ at 6 GV to $96 \pm 0.5\%$ at 2 TV. Therefore, one must consider the non-negligible secondary component of C when using the B/C ratios in CR propagation models.

5.3.2 Simulation models

It is really difficult to have full MHD simulations of the ISM combined with the interactions of CRs with Alfvén waves. An exact solution for the propagation of Galactic CRs can only be obtained by assuming severe simplifications like what was earlier done in the Slab and Leaky Box models. Another employed technique is the Monte Carlo method (Batista et al., 2019). This method is frequently used for ultra-high-energy CRs, but presents challenges when applied to Galactic CRs. This difficulty arises from the need to individually track a large number of particles to achieve small statistical errors and to account for the complex interactions within the entire network of nuclei. This computational demand makes it less practical for Galactic CR studies. Solving the propagation equations can be achieved through numerical simulations, such as GALPROP (A. W. Strong & Moskalenko, 1998), Usine (Maurin et al., 2001), DRAGON (Evoli et al., 2008), or PICARD (Kissmann, 2014). These models describe both CR transport and its implications concerning secondary particles and radiation (Amato & Blasi, 2018).

In the USINE package (Maurin et al., 2001), the propagation equation is solved in a semi-analytical way. This code handles partial derivatives related to spatial coordinates analytically (Webber et al., 1992), while those tied to energy coordinates are resolved through numerical integration. Its primary advantage lies in its speed compared to other existing propagation codes. However, it achieves this speed by requiring simplified problem formulations and geometries. The code is implemented in C++ and further technical details can be accessed at <https://dmaurin.gitlab.io/USINE/>.

The GALPROP code (A. W. Strong & Moskalenko, 1998) has been publicly available since the 1990s and remains one of the most widely used codes in the field [<https://galprop.stanford.edu/>]. It is primarily written in C++ with some incorporated FORTRAN-77 routines. New solvers of the transport equations have recently been implemented (Porter et al., 2022) and the code includes a 3D spatial density model for neutral and molecular hydrogen

which has been constructed from HI and CO line-survey data (Jóhannesson et al., 2018). The code also includes ionised gas and energy density distributions of the CMB, infrared, and radio radiation fields. A significant contribution from the GALPROP team is the detailed parametrisation of nuclear spallation cross-sections, which is frequently updated to enhance the accuracy. Various CR source distributions in the Galactic disc are available. The code can calculate steady-state solutions as well as follow fluctuations from ensemble of discrete sources in space and time (Porter et al., 2022). To ensure the convergence of the simulation, the time-integration steps are crucial. Very small time-steps can lead to simulations lasting for years. That is why the control of time-steps is managed through the configuration file.

More recently, the DRAGON (Diffusion of cosmic RAYs in Galaxy modelizatiON) team [www.dragonproject.org] has introduced a new propagation code (Evoli et al., 2008). It resembles GALPROP, but was designed to offer more flexibility. It enables anisotropic propagation, incorporates 3D spatial structures, and provides options for customising cross sections, magnetic-field details, and gas and source distributions. The code is primarily written in C++, with supplementary FORTRAN routines available for nuclear interactions. DRAGON has facilitated innovative studies, including the analysis of lepton spectra within spatial arm structures for source distribution, investigations into the origin of antiprotons related to dark matter, studies of CR gradients with anisotropic diffusion, and the production of neutrino and γ -ray emissions at very high energies. The most recent release of DRAGON, known as DRAGON2 (Evoli, Gaggero, et al., 2018), continues to evolve, aiming to comprehensively address the intricate processes associated with Galactic CRs and the secondary emissions generated during their propagation across a wide energy spectrum.

The latest publicly available code is PICARD (Kissmann, 2014), which was introduced around 2013 [<https://astro-staff.uibk.ac.at/~kissmrbu/Picard.html>]. PICARD aims for high resolutions while maintaining reasonable computational demands. It accomplishes this using fully 3D implementations and accounting for anisotropic diffusion. Similar to DRAGON, PICARD incorporates standard time-step sizes within the code. These time steps are progressively reduced until the smallest one is reached, which should accurately reflect the characteristic time scale of the specific problem under consideration.

Figure 5.4 shows different values obtained for the average isotropic CR diffusion coefficient using the DRAGON2, GALPROP, and USINE codes to explain the available direct and indirect CR data. Whereas the codes converge on the energy dependence of the diffusion coefficient, they diverge on its absolute value.

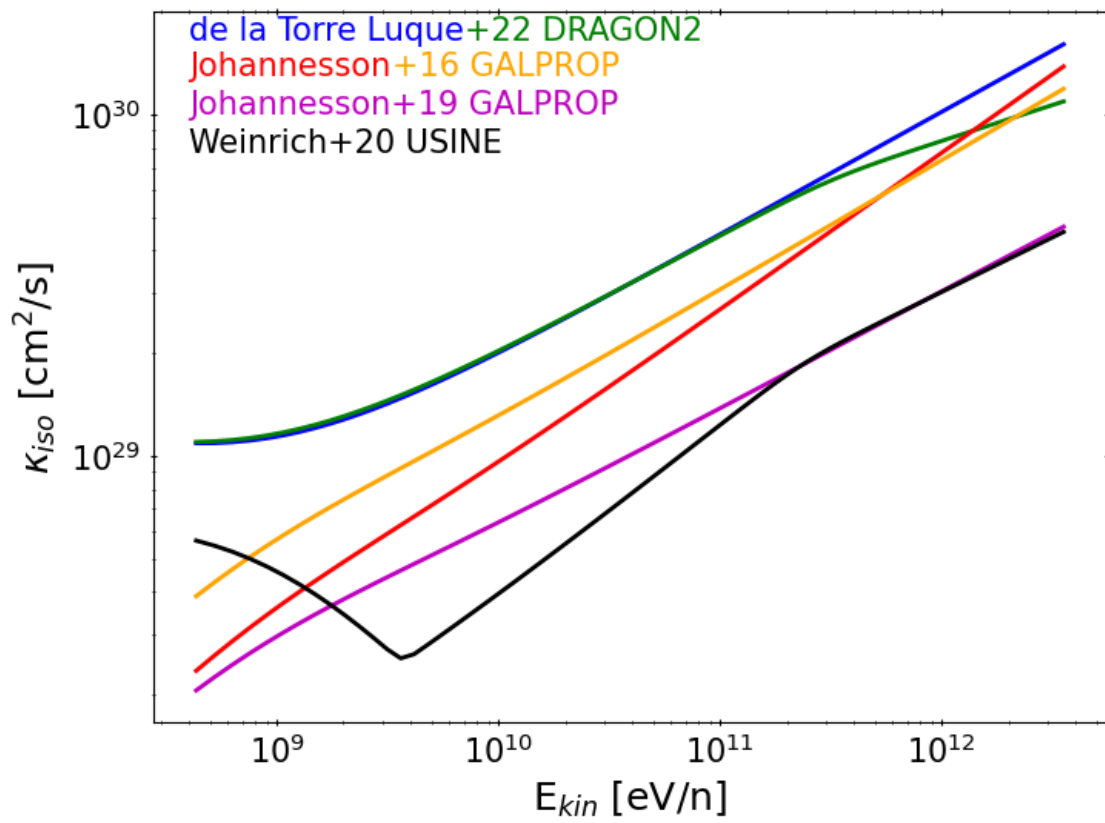


FIGURE 5.4 : Different fits of the diffusion coefficient values obtained by the different simulations using DRAGON2, GALPROP and USINE. (Nuñez-Castiñeyra et al., 2022)

γ -ray emissivities in local clouds

The Solar System is located within the Local Bubble represented by a polygon at the center of Fig.6.1. This bubble, formed by several supernova explosions, is located within a wide low-density gas valley, delimited by two walls of massive atomic and molecular clouds.

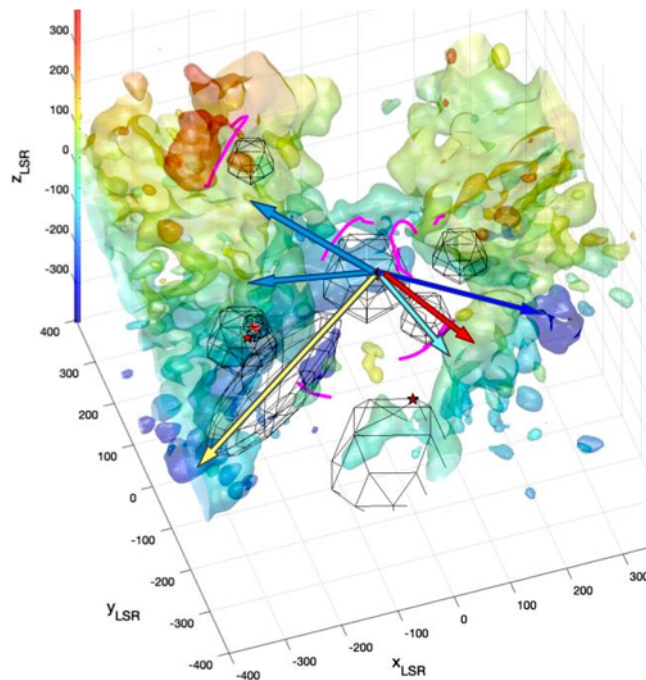
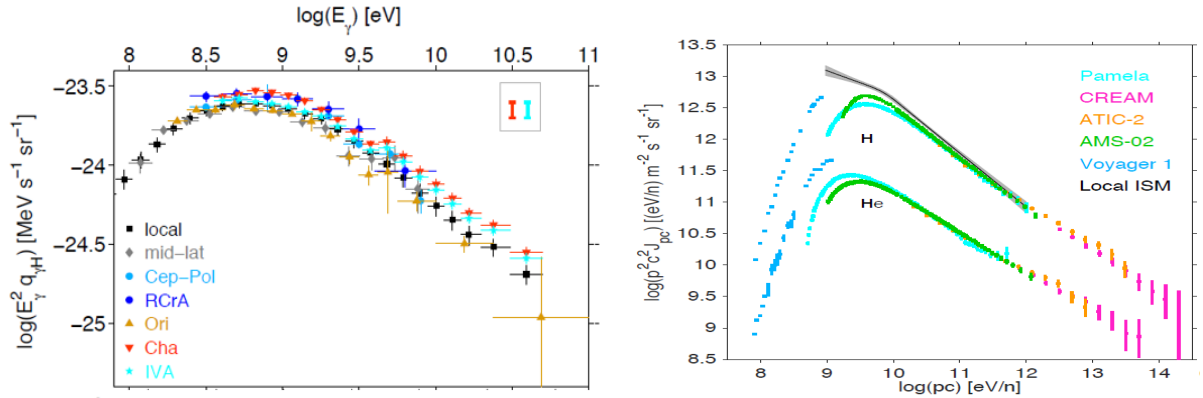


FIGURE 6.1 : 3D gas distribution at few hundreds of parsec around the Solar System. The central polygon is the Local Bubble in which the Solar System is located. The colored Oz axis gives the altitude relative to the Galactic plane. The coloured arrows represent the directions where γ -ray emissivity measurements have been made in nearby clouds. (Grenier et al., 2015)

Different nearby clouds have been studied in γ rays in a variety of directions depicted by the coloured arrows in Fig.6.1. By measuring the H I column density in each of these local clouds,

γ -ray emissivities per gas nucleon have been estimated according to Eq.4.11. Some of these γ -ray emissivities are shown in Fig.6.2a. It is noticed that the emissivity spectra in these clouds have the same shape and almost the same value. The black spectrum represents the average of emissivity found in the H I gas between 10° and 70° in Galactic latitude and is called the Local Interstellar Spectrum, q_{LIS} (Casandjian, 2015). From these observations, one can conclude that there is a fairly large spatial and spectral uniformity in the distribution of CR nuclei over a few hundred parsecs around the Solar System.



- (a) The γ -ray emissivity multiplied by the square of the photon energy as a function of the γ -ray energy. The coloured curves relate to different nearby cloud complexes (Grenier et al., 2015). The black curve is the average γ -ray emissivity, q_{LIS} , found for the atomic gas between 10° and 70° in Galactic latitude (Casandjian, 2015).
- (b) The spectral intensity of cosmic protons and alphas, multiplied by the momentum squared, as a function of momentum per nucleon. The different colors represent data from different particle detectors. The black curve is obtained from the average emissivity q_{LIS} and its $\pm 1\sigma$ dispersion is plotted in grey. (Grenier et al., 2015)

FIGURE 6.2

Using the cross sections of hadronic p-p interactions (Kamae et al., 2006), interstellar atom abundances, and corrections factors for heavier nucleus-nucleus interactions (Mori, 2009), the q_{LIS} emissivity can be translated into a CR spectral intensity as a function of particle momentum per nucleon. The result is represented in Fig.6.2b by the black curve and its $\pm 1\sigma$ dispersion in grey. This allows to compare the direct observations of the cosmic proton flux in the Solar System with the indirect observations a few hundred parsecs away. There is a great similarity between the two spectra at high energies, where the solar modulation is negligible. At low energies, the spectrum obtained by direct observations is strongly attenuated by solar modulation. It suggests that the CR flux reaching the Sun is consistent with the flux penetrating the local clouds. This comparison is more discussed in the next chapter.

Since the previous plots, γ -ray emissivity measurements in the Orion-Eridanus superbubble have been added (Joubaud et al., 2020). Updated plots are shown in Fig.6.3. It is important to note that they all have been derived using the same analysis methodology, including DNM extraction. We can see that numerous clouds exhibit emissivities close to the average q_{LIS} . The small differences can be due to uncertainties in the derived H I gas mass, but several start to show more significant deviations (Chamaeleon, Eridanus West, and Eridu). The small Eridu filamentary cloud located just outside the Orion-Eridanus superbubble stands out at the firmest

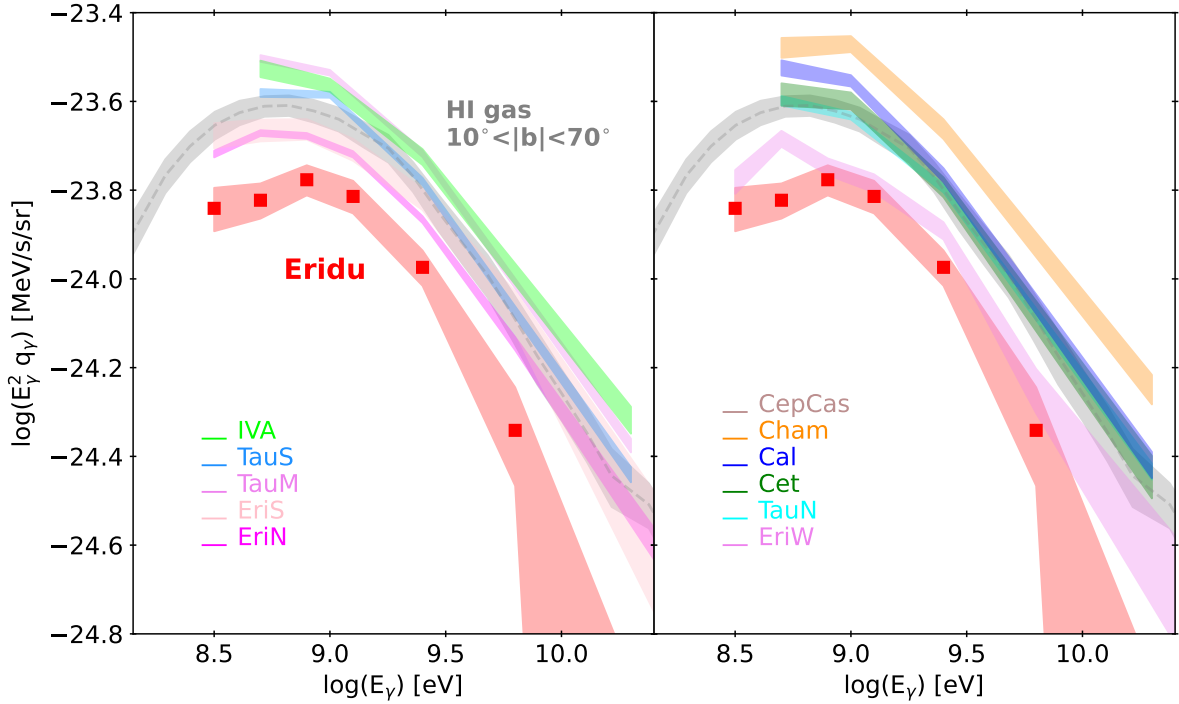


FIGURE 6.3 : γ -ray emissivity spectra multiplied by the square of the photon energy in a selection of nearby clouds. The grey band shows the average γ -ray emissivity, q_{LIS} , found for the atomic gas between 10° and 70° in Galactic latitude (Casandjian, 2015).

case of CR deficit, with a 34% deficit compared to the local average, which cannot be attributed to gas mass estimate problems. The lowest possible HI gas mass still yields an emissivity (hence CR flux) 25% below the local average (Joubaud et al., 2020).

Figure 6.4 compares the integrated γ -ray emissivity in the 0.4-10 GeV band of local clouds as a function of their height above or below the Galactic plane. The two curves represent two different models of CR propagation in the ISM. Even today, no model is conclusive. The grey rectangle represents the $\pm 1\sigma$ dispersion in γ -ray emissivity around the mean emissivity found below 300 pc. We can see that the Eridu cloud, at an altitude between 200 and 250 pc, stands as an outlier. In the next chapter, we will compare the CR flux in Eridu to that in our Solar System.

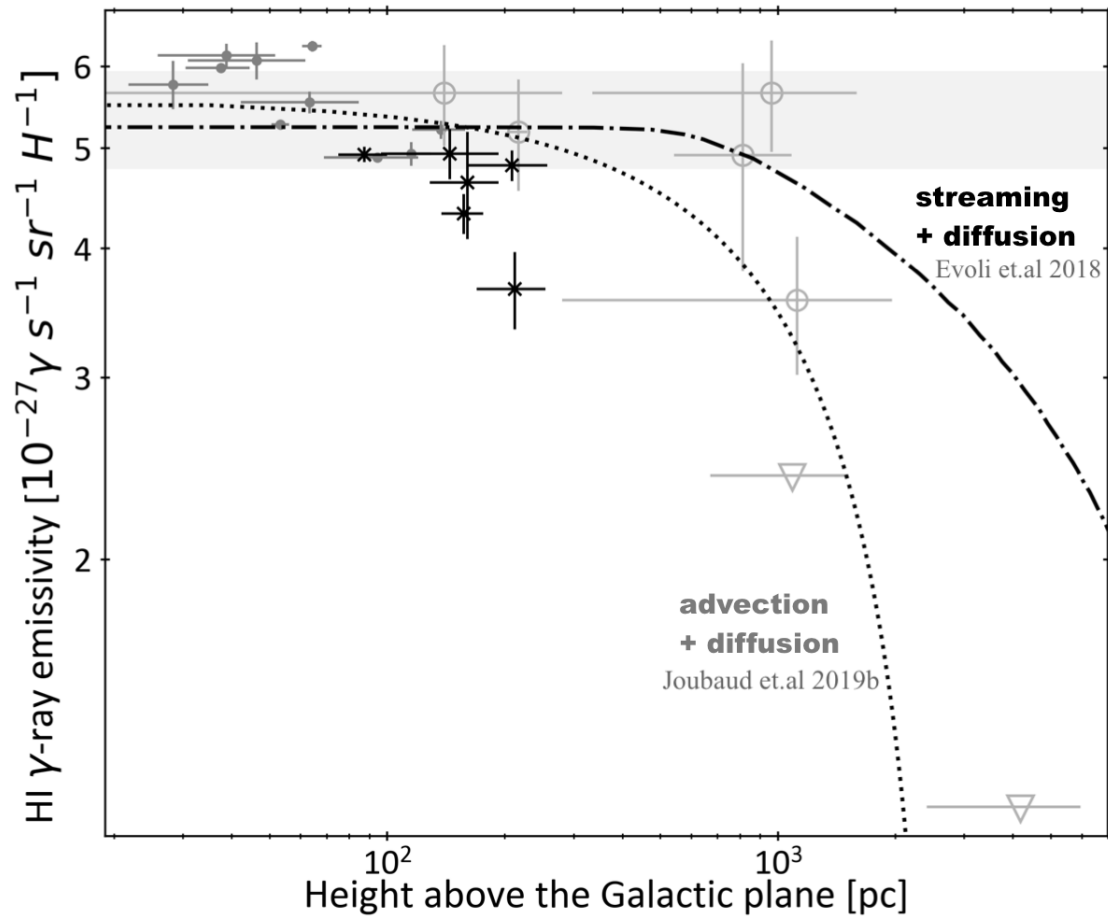


FIGURE 6.4 : The γ -ray emissivity of atomic clouds as a function of their absolute altitude with respect to the Galactic plane. The two curves represent the decline expected from two CR propagation models. The grey rectangle represents the $\pm 1\sigma$ dispersion of γ -ray emissivities obtained around the mean emissivity calculated at altitudes less than 300 pc. (Joubaud et al., 2020)

The CR flux in Eridu and near the Solar System

7.1 The Eridu cloud

The Eridu cloud is often called the Eridu cirrus because it is a very diffuse and elongated cloud with a filamentary structure. It lies outside the edge of the Orion-Eridanus superbubble, at a distance of 200 or 300 pc from the Sun, which we have investigated again in the present work. As mentioned above, the cloud exhibits a puzzingly low γ -ray emissivity compared to the local average and compared to the standard emissivity found in the neighbouring shell of the Orion-Eridanus superbubble (Joubaud et al., 2020).

Eridu is composed of pure atomic H I gas. There is no evidence of molecular gas inside the cirrus. The H I column density ranges between 1×10^{21} and $5 \times 10^{21} \text{ cm}^{-2}$ along the core of the cloud. We will show in this work that the volume densities do not exceed 10 cm^{-3} along the core.

Figure 7.1 shows the H I column density map of Eridu cirrus (delimited by the magenta contour) and part of the shell of the Orion-Eridanus superbubble (in brown contour). The orientation of the magnetic field in the plane of the sky, B_{sky} , inferred from dust polarisation, is shown as black lines. It can be observed that the cirrus magnetic field lines do not follow those of the superbubble, nor those of the low-latitude Galactic field which are parallel to Galactic plane. The field lines in Eridu appear to be inclined with respect to the Galactic plane and to point at 45° from the Galactic south pole.

Leike et al. (2020) used stellar data from the *Gaia*-DR2, ALLWISE, PANSTARRS and 2MASS surveys to model dust extinction and generate a 3D map of dust clouds within approximately 400 pc from the Sun, achieving a spatial resolution of 2 pc. The precise positions of stars provide accurate constraints on the distances to well defined clouds and their dust densities.

Figure 7.2 presents cuts of the 3D dust distribution within 20-pc-wide intervals, covering distances from 150 to 350 pc. The shape of the Orion-Eridanus shell can be recognised near 200 pc in the upper part of the figures, at latitudes around -50° . The general shape and position of the Eridu cloud is much less certain. No dust excess is seen in its direction up to ~ 250 pc. An inclined excess appears at larger distances that could relate to the cirrus at distances of 270-330

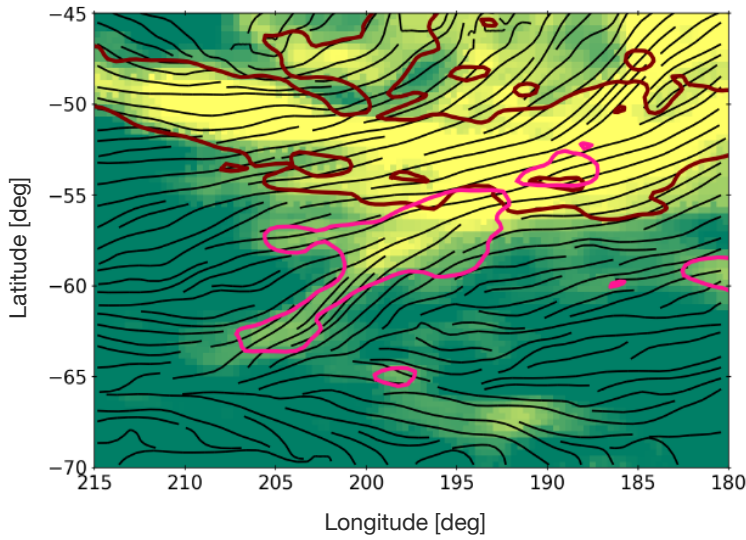


Figure 7.1 : Silhouette of the Eridu cirrus in magenta and the edge of the Orion-Eridanus superbubble in brown. The column density N_{HI} increases from green to yellow. The black curves show the orientation of the B_{sky} field inferred from dust polarisation measurements. (Joubaud et al., 2020)

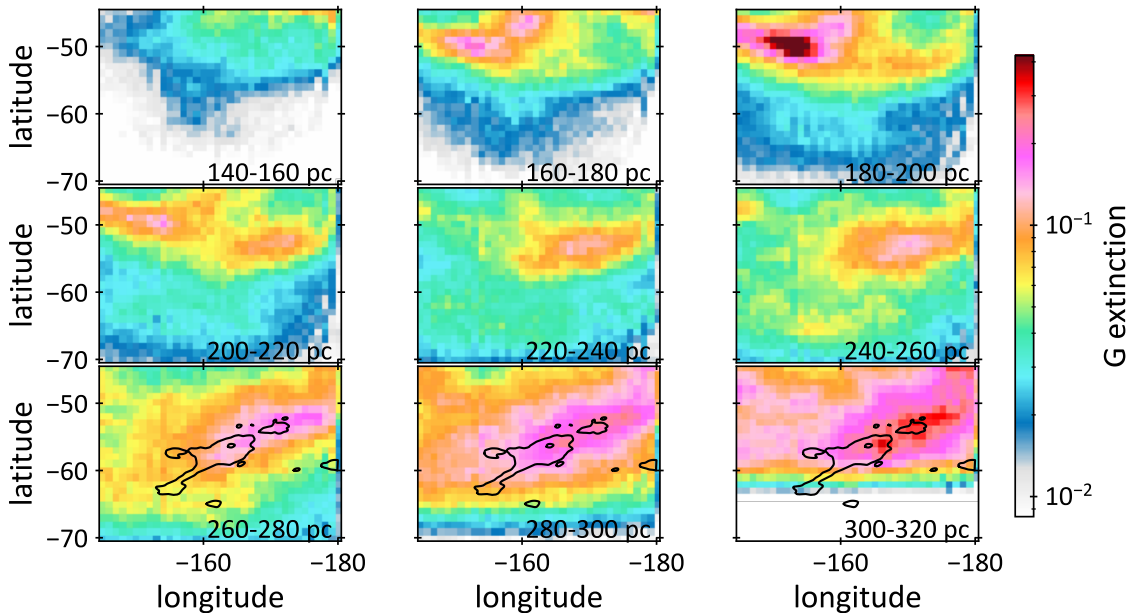


FIGURE 7.2 : Maps showing the integrated G-band extinction optical depth within 20 pc-wide intervals in distance from the Sun, directed towards the Orion-Eridanus region. They are based on data derived from the 3D distribution presented by Leike et al. (2020). The dust cloud which extends predominantly horizontally at a galactic latitude of approximately -50° and spans distances ranging from 160 to 260 pc corresponds to the boundary of the Orion-Eridanus superbubble. The black contours outline the Eridu HI cloud. The distance ranges are indicated in each map. (Kamal Youssef & Grenier, 2024)

pc, but an extension of the 3D cube to larger distances would greatly tighten this estimate.

7.2 The CR flux in Eridu

Figure 6.4 shows that nearly all the local clouds have a γ -ray emissivity compatible with the mean one and its $\pm 1\sigma$ dispersion, except for the Eridu cloud at a height around 200 pc. This cirrus shows a remarkable loss of γ -ray emissivity compared to the other clouds. Given that the observed γ -ray intensity scales as $I_\gamma = \int n_{\text{cr}} n_{\text{gas}} dL_{\text{sight}}$, an increase in gas volume density corresponds to a decrease in CR flux in the cloud. The minimum H I column densities in the cloud can be obtained by considering that the gas is optically thin to H I radiation, but, in this case, the γ -ray emissivity estimate in Eridu still remains 25% below the local average one. Therefore, this loss cannot be explained by an uncertainty in the H I gas mass.

Moreover, it is unlikely that the loss relate to the penetration of CRs into the cloud. That is because Eridu has a lower gas column density compared to more massive local clouds that exhibit a larger γ -ray emissivity. The particles probed with the *Fermi*-LAT observations have energies above a few GeV and should be able to penetrate and diffuse through the cloud without any problem (Everett & Zweibel, 2011). These authors have studied the evolution of the CR pressure within a diffuse cloud, where the gas and magnetic field conditions are similar to those found in the Eridu cirrus. They found that the Alfvén wave pressure increases by nearly two orders of magnitude at the cloud’s periphery due to the growth of the streaming instability which considerably reduces the CR velocity in the cloud. But the particle density at 1 GeV/nucleon only decreased by about 5% within the cloud and higher energy particles would be even less affected even though they used a gas density of 100 cm^{-3} that is ten times larger than those in Eridu. Consequently, a drop of 34% would necessitate a magnetic field intensity significantly larger than that indicated by the Planck polarisation in the Eridu cloud (Joubaud et al., 2020).

Another potential explanation for the CR loss relates to the magnetic field orientation of the cirrus that points towards the Galactic south pole. CRs propagate more easily along the field lines than perpendicular to them. It is possible that the magnetic configuration of the cirrus directs the CRs towards the Galactic pole. We have further investigated this possibility in the present work.

Before seeking the cause of the CR loss in Eridu, we have examined how the spectrum of cosmic nuclei (primarily protons and alphas) deduced from the γ -ray measurements compares with the spectrum measured near/in the Solar System.

7.3 A loss of cosmic rays ?

We aim to compare direct CR observations near the Solar System with the γ -ray emissivity of local clouds and, in particular, of the Eridu cloud in order to investigate the origin of its CR deficit. To calculate the γ -ray emissivity to be expected from the Solar System CR spectra, we need the hadronic cross-sections at the desired interval of energy.

7.3.1 CR flux in the Solar System

Low-energy CRs encounter difficulty penetrating the Solar System due to the magnetic structure of the heliosphere and of the expanding solar wind. Through the study of plasma physics, solar magnetic fields, and solar winds, several models have been developed to demodulate the

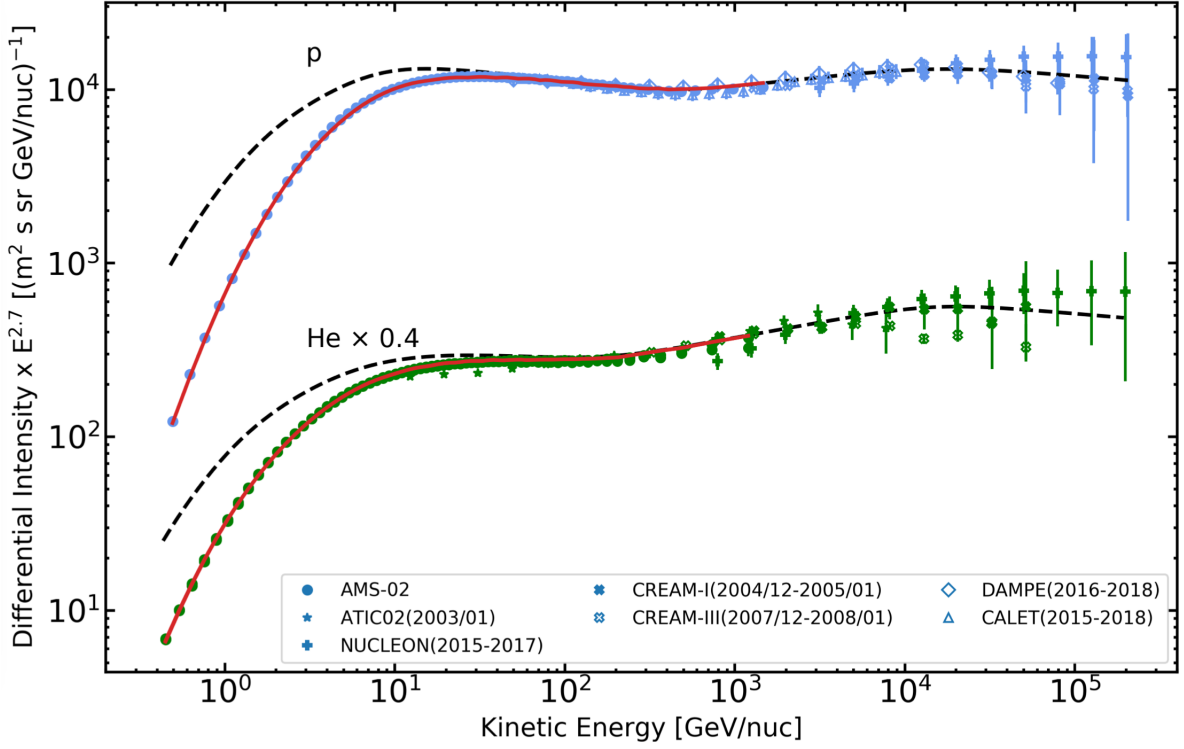


FIGURE 7.3 : The demodulated proton and He spectra (black dashed lines) in comparison with available data. The red lines show the modelled spectra for the modulation levels that correspond to the periods of data taking. (Boschini et al., 2020)

solar wind's effect on the incident flux of CRs. These models have allowed to connect the unmodulated CR spectra directly measured at high energies with the low-energy spectra captured by the Voyager probes just outside the heliosphere. One of these models has been developed by Boschini et al. (2020). Figure 7.3 shows the comparison between the Boschini model (demodulated in black and modulated in red) and the high-energy CR data obtained by different particle detectors for the proton and helium spectra. The Boschini model also matches the Voyager data at low energy as shown in Fig.7.4. The open circles in the proton and helium spectra are updated Voyager 1 data posted on the NASA page¹.

We note $R = pc/Ze$ the rigidity of CRs based on their momentum p , atomic number Z , c the speed of light, and e the elementary electron charge. The Boschini et al. (2020) code (HelMod) provides CR intensity spectra in rigidity :

$$J_R[m^{-2}s^{-1}sr^{-1}V^{-1}] = \frac{dN_{CR}}{dS dt d\Omega dR} \quad (7.1)$$

Where dS , dt , $d\Omega$ and dR are the elements of surface, time, solid angle, and rigidity in Volts. Using the total relativistic energy of the particle $E = mc^2 + E_k = \sqrt{(pc)^2 + (mc^2)^2}$, we establi-

¹<https://voyager.gsfc.nasa.gov/spectra.html>

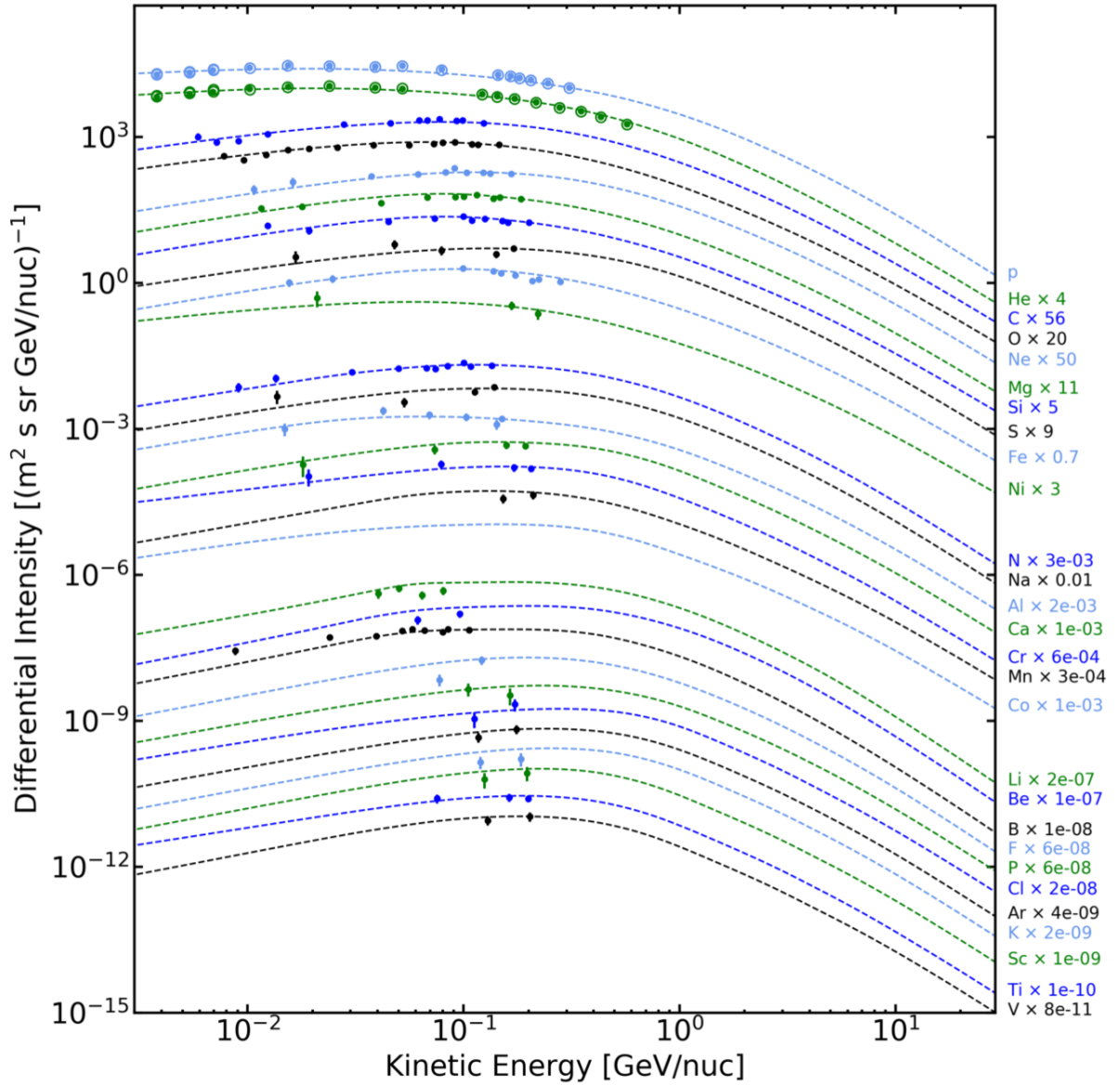


FIGURE 7.4 : The Boschini model, in dashed lines, compared to the Voyager 1 data, in filled circles (Cummings et al., 2016). Updated Voyager 1 data are also shown for H and He, in open circles, taken from 1st of September 2012 to 13th of November 2019. The elements are sorted by approximate amount of primary contribution : first group is mostly primary, second one with significant primary contribution, and third one is mostly secondary. (Boschini et al., 2020)

shed a connection between rigidity R and the kinetic energy E_k of the particle :

$$\frac{dR}{dE_k} = \frac{E}{Z^2 e^2 R} \quad (7.2)$$

Through the transformation shown in eq.7.2, we have computed the intensity of CRs as a func-

tion of the kinetic energy of incident particles, J_{E_k} :

$$J_{E_k} [m^{-2} s^{-1} sr^{-1} eV^{-1}] = \frac{J_R}{Ze} \left[1 + \frac{m^2 c^4}{Z^2 e^2 R^2} \right]^{1/2} \quad (7.3)$$

The volume density of CRs with velocity βc is obtained by :

$$n_{cr}(E_k) = \frac{dN_{cr}}{dV dE_k} = \frac{4\pi}{\beta c} J_{E_k} \quad (7.4)$$

We have used the CR spectra provided for nuclei up to $Z = 28$.

7.3.2 Cross sections

The cross-sections for hadronic interactions of cosmic nuclei with interstellar gas are provided by several models. In this thesis I have used and compared the Kamae parametrisation published in Kamae et al. (2006), the Kachelrieß matrices based on the QGSJET-II-04m simulations (Kachelrieß et al., 2019), and the matrices obtained with the FLUKA simulation by Mazziotta et al. (2016).

Kamae et al. provided cross sections up to 512 TeV and Kachelrieß and Ostapchenko (2012) advise to use his QGSJET-II-04m model for energies above 30 GeV and not below 12.5 GeV. Given that the γ -ray emissivity measurements typically probe CRs with energies between 1 and 500 GeV, we need to combine the Kamae cross sections with the QGSJET-II-04m ones.

7.3.2.1 Kamae vs Kachelrieß

Kamae et al. calibrated their model using data available in 2006, while Kachelrieß et al. used the new LHC data, especially from the LHCf, LHCb, and NA61 experiments. The Kachelrieß et al. model does not extend to very low energies, being limited to 3 GeV and 1.27 GeV for the proton and helium kinetic energy respectively.

Following the advices by Kachelrieß and Ostapchenko (2012), we have restricted the use of the QGSJET matrices to kinetic energies above 30 GeV/n. In contrast, the Kamae et al. model can reach down to 0.49 GeV for the proton, which is useful for our calculations. A detailed comparison between the two codes is presented in Table 7.1.

The cross sections σ , in mbarn, obtained by these two codes are in the form of :

$$\frac{\Delta\sigma(E_k, E_\gamma)}{\Delta\log(E_\gamma)} = \sigma(E_k) \frac{dN_\gamma}{d(\log E_\gamma)} \quad (7.5)$$

They represent the cross-section as a function of the CR kinetic energy, multiplied by the probability of emitting a photon at each γ -ray energy. For the calculation of the γ -ray emissivity, we perform the following transformation :

$$\sigma(E_k) \frac{dN_\gamma}{dE_\gamma} = \frac{\sigma(E_k)}{E_\gamma} \frac{dN_\gamma}{d(\log E_\gamma)} \quad \text{in [mbarn /eV]} \quad (7.6)$$

	Kamae	Kachelriess
year of publication	2006	2019
Based on LHC data	No	Yes
Incident particles	p	p, He, Fe, C, Al
Target particles	p	p, He (for incident p and He), C (for incident p)
Secondary particles	γ, e^-, e^+ $\nu_e, \bar{\nu}_e, \nu_\mu, \bar{\nu}_\mu$	γ, e^-, e^+ $\nu_e, \bar{\nu}_e, \nu_\mu, \bar{\nu}_\mu$ $p\bar{p}, n\bar{n}$
Kinetic energy range of the incident particles	0.49 GeV – 512 TeV	p : 3 GeV – $4 \cdot 10^{20}$ eV He : 1.27 GeV – $4 \cdot 10^{20}$ eV Others : 1 TeV – $2 \cdot 10^{18}$ eV

TABLE 7.1 : Comparison between the cross sections of the hadronic interactions between CRs and the interstellar gas, obtained by the Kamae and Kachelrieß codes.

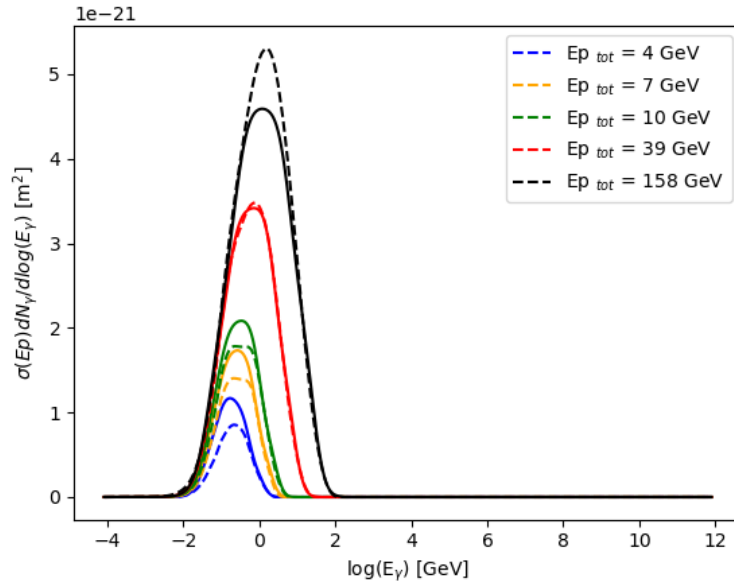


FIGURE 7.5 : Comparison of the cross-sections provided by the parametrisation of Kamae et al. (solid lines) and those obtained by QGSJET's model (dashed lines) as a function of the γ photon energy.

The cross-sections obtained by the parametrisation of Kamae et al., σ_{Kamae} , and the QGSJET one obtained by the code of Kachelrieß et al., σ_{QGSJET} , are shown in Fig.7.5 as solid and dashed lines respectively. At low total proton energy, the peak of σ_{Kamae} exceeds that of Kachelrieß, but it is the opposite at high energy.

I would like to note that the parameters published in Table 3 of Kamae et al. (2006) were not all correct. The correct ones are presented in Fig.7.6.

TABLE 3
PARAMETERS DESCRIBING GAMMA-RAY SPECTRA FOR ARBITRARY PROTON ENERGY

Parameter	Formulae as Functions of the Proton Kinetic Energy ($y = \log T_p$) in TeV
Nondiffraction, eq. (6)	
a_0	$-0.51187(y + 3.3) + 7.6179(y + 3.3)^2 - 2.1332(y + 3.3)^3 + 0.22184(y + 3.3)^4$
a_1	$-(1.2592 \times 10^{-5}) + (1.4439 \times 10^{-5}) \exp(-0.29360(y + 3.4)) + (5.9363 \times 10^{-5})/(y + 4.1485) + (2.2640 \times 10^{-6})y - (3.3723 \times 10^{-7})y^2$
a_2	$-(174.83 + 152.78) \log [1.5682(y + 3.4)] - 808.74/(y + 4.6157)$ Parentheses to remove
a_3	$0.81177 + 0.56385y + 0.0040031y^2 - 0.0057658y^3 + 0.00012057y^4$
a_4	$0.68631(y + 3.32) + 10.145(y + 3.32)^2 - 4.6176(y + 3.32)^3 + 0.86824(y + 3.32)^4 - 0.053741(y + 3.32)^5$
a_5	$+(9.0466 \times 10^{-7}) + (1.4539 \times 10^{-6}) \log [0.015204(y + 3.4)] + (1.3253 \times 10^{-4})/(y + 4.7171)^2 - (4.1228 \times 10^{-7})y + (2.2036 \times 10^{-7})y^2$
a_6	$-(339.45 + 618.73) \log [0.31595(y + 3.9)] + 250.20/(y + 4.4395)^2$ Parentheses to remove
a_7	$-35.105 + 36.167y - 9.3575y^2 + 0.33717y^3$
a_8	$0.17554 + 0.37300y - 0.014938y^2 + 0.0032314y^3 + 0.0025579y^4$
$r(y)$	$3.05 \exp(-107\{(y + 3.25)/[1 + 8.08(y + 3.25)]\}^2)$ for $T_p \leq 1.95$ GeV, 1.01 for $T_p > 1.95$ GeV
Diffraction, eq. (9) ^a	
b_0	$60.142 \tanh [-0.37555(y + 2.2)] - 5.9564(y + 0.59913)^2 + 6.0162 \times 10^{-3}(y + 9.4773)^4$
b_1	$35.322 + 3.8026 \tanh [-2.5979(y + 1.9)] - 2.1870 \times 10^{-4}(y + 369.13)^2$ -2.4979
b_2	$-15.732 - 0.082064 \tanh [-1.9621(y + 2.1)] + 2.3355 \times 10^{-4}(y + 252.43)^2$
b_3	$-0.086827 + 0.37646 \exp(-0.53053\{(y + 1.0444)/[1.0 + 0.27437(y + 1.0444)]\}^2)$
b_4	$2.5982 + 0.39131(y + 2.95)^2 - 0.0049693(y + 2.95)^4 + 0.94131 \exp(-24.347[y + 2.45 - 0.19717(y + 2.45)^2]^2)$
b_5	$0.11198 - 0.64582y + 0.16114y^2 + 2.2853 \exp(-0.0032432\{(y - 0.83562)/[1.0 + 0.33933(y - 0.83562)]\}^2)$
b_6	$1.7843 + 0.91914y + 0.050118y^2 + 0.038096y^3 - 0.027334y^4 - 0.0035556y^5 + 0.0025742y^6$
b_7	$-0.19870 - 0.071003y + 0.019328y^2 - 0.28321 \times \exp(-6.0516(y + 1.8441)^2)$
$\Delta(1232)$, eq. (12)	
c_0	$2.4316 \exp(-69.484\{(y + 3.1301)/[1.0 + 1.24921(y + 3.1301)]\}^2) - 6.3003 - 9.5349y + 0.38121y^2$ 0.14921
c_1	$56.872 + 40.627y + 7.7528y^2$
c_2	$-5.4918 - 6.7872 \tanh [4.7128(y + 2.1)] + 0.68048y$
c_3	$-0.36414 + 0.039777y$
c_4	$-0.72807 - 0.48828y - 0.092876y^2$
res(1600), eq. (12) ^b	
d_0	$3.2433 \exp(-57.133\{(y + 2.9507)/[1.0 + 1.2912(y + 2.9507)]\}^2) - 1.0640 - 0.43925y$
d_1	$16.901 + 5.9539y - 2.1257y^2 - 0.92057y^3$
d_2	$-6.6638 - 7.5010 \tanh [30.322(y + 2.1)] + 0.54662y$
d_3	$-1.50648 - 0.87211y - 0.17097y^2$
d_4	$0.42795 + 0.55136y + 0.20707y^2 + 0.027552y^3$

^a $b_0, \dots, b_3 = 0$ for $T_p < 5.52$ GeV

^b Parameters c_0, \dots, c_4 replaced with d_0, \dots, d_4 .

FIGURE 7.6 : Correction of the parameters provided by Kamae et al. for the $p+p \rightarrow \gamma$ interaction, presented in Table 3 of Kamae et al. (2006).

7.3.2.2 Cross-calibrating and combining cross-sections

To obtain cross-sections at low energy, it is necessary to use the σ_{Kamae} parametrisation. They must, however, first be adjusted to match the values of σ_{QGSJET} to align with the latest LHC data. The Kamae et al. parametrisation addresses the proton-proton (p-p) interaction yielding γ photons :

$$p_{CR} + p_{ISM} \longrightarrow \pi^0 \longrightarrow 2\gamma \quad (7.7)$$

We calculated the mean σ_{Kamae} to σ_{QGSJET} ratio over the 30 – 100 GeV/n of CR proton kinetic energy. We have then created a new matrix of p-p cross-section with the rescaled σ_{Kamae} one from 0.49 to 30 GeV/n and the QGSJET p-p matrix above 30 GeV/n.

For CRs heavier than protons, we have noticed that the QGSJET cross-sections, when expressed per nucleon-nucleon interaction and in kinetic energy per nucleon, closely followed the p-p one in shape and values. We have therefore applied the same method to scale σ_{Kamae} to the seven different interactions given by the QGSJET matrices. The results of the final combinations are presented in Fig.7.7.

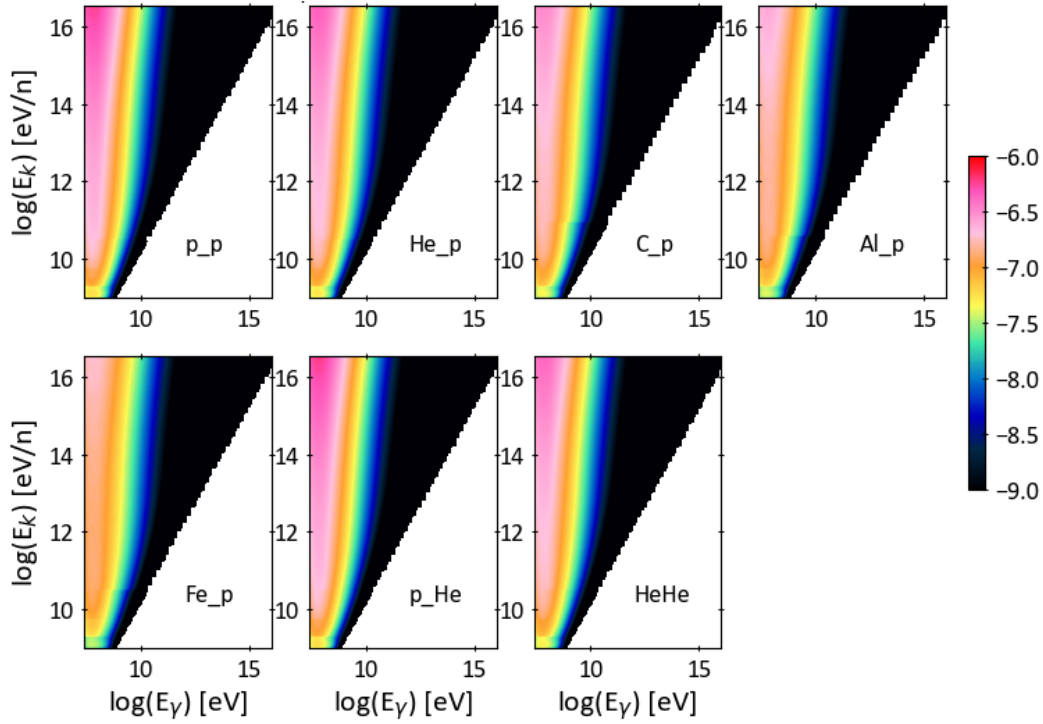


FIGURE 7.7 : $\log(d\sigma/dE_\gamma/N_{nuc})$ in mb/eV from the combination of Kamae et al. (2006) and Kachelrieß et al. (2019) cross-sections for different hadronic interactions of cosmic nuclei with interstellar gas.

7.3.2.3 Calibration of different interactions

Before the publication of the cross-sections by Kachelrieß et al. in 2019, coefficients known as the Mori factors (Mori, 2009) were used to estimate the cross-sections of various interactions based on the p-p one. The problem is that the Mori factors were produced for a given value of E_{k_p} , so they don't vary with energy.

Using the QGSJET matrices for the seven interactions presented in Fig.7.7, we can infer the cross-sections for all the other CR nuclei interacting with interstellar hydrogen and helium. To do so, we have interpolated the combined cross-sections, Kamae+QGSJET, with respect to $\log(A)$ where A is the mass number of the incident CR nucleus. The results for the 30 interactions are shown in Fig.7.8.

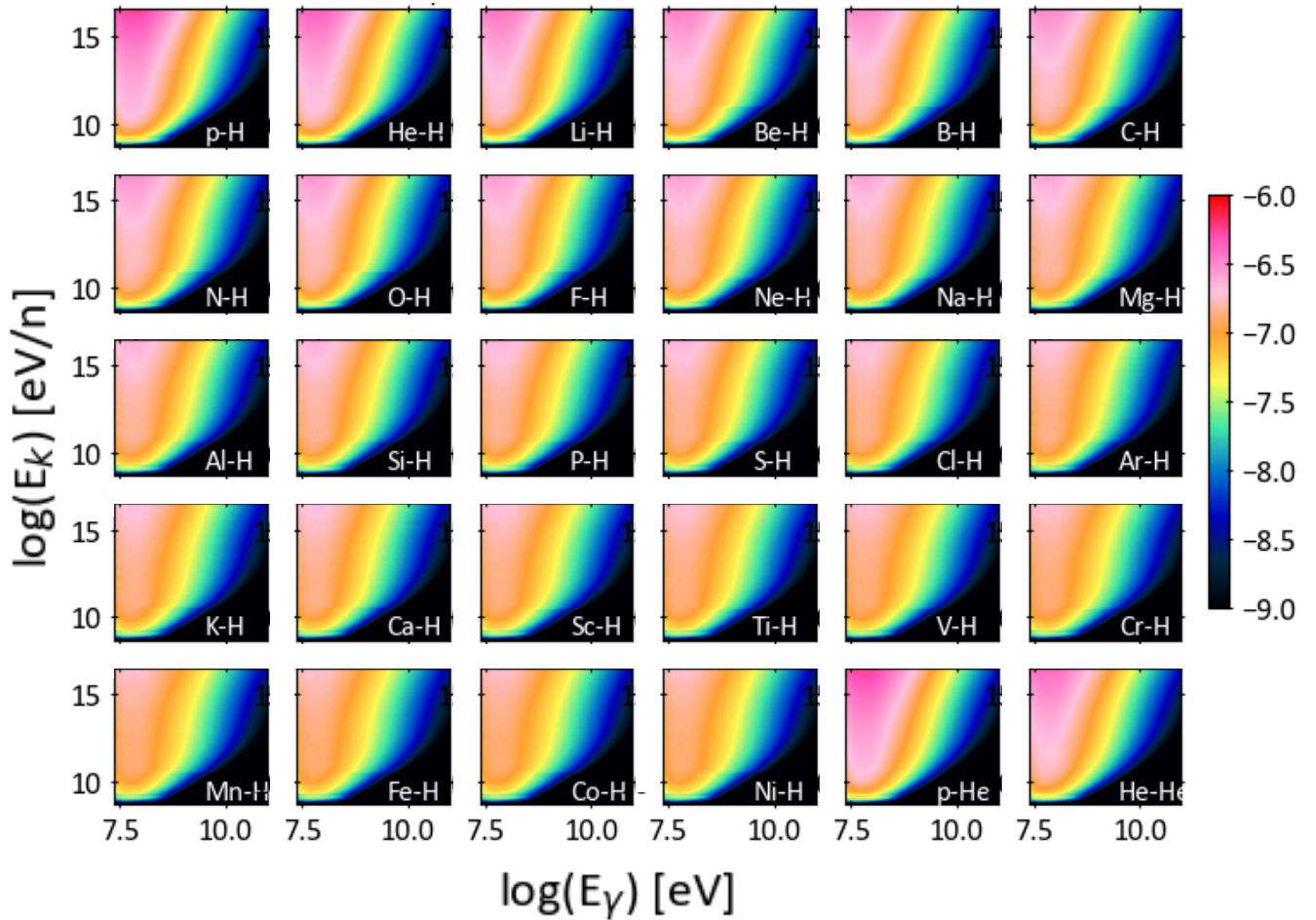


FIGURE 7.8 : $\log(d\sigma/dE_\gamma/N_{nuc})$ in mb/eV from the combination of Kamae et al. (2006) and Kachelrieß et al. (2019) cross-sections for different hadronic interactions of cosmic nuclei with interstellar gas.

It is also essential to consider the abundance of elements in the interstellar medium. The logarithmic abundance of an element is defined relative to hydrogen, in volumetric density, as

$\log_{10}(n_X/n_H) + 12$. The abundance of helium is 10.93 ± 0.01 (Asplund et al., 2009) corresponding to a density ratio $n_{He}/n_H = 8.51 \pm 0.093 \%$.

7.3.3 γ -ray emissivity

To calculate the γ -ray emissivity, it is first necessary to compute the Q_γ source function. We assume that the cloud has a volumetric gas density n_H and is permeated by a CR flux at the velocity β_{CRC} . Therefore, the γ -ray source function is given by :

$$Q_\gamma = \frac{dN_\gamma}{dV dt dE_\gamma} = n_H c \int_{E_k > E_\gamma}^{\infty} \beta_{CR}(E_k) n_{CR}(E_k) \left[\sigma(E_k) \frac{dN_\gamma}{dE_\gamma} \right] dE_k \quad (7.8)$$

The isotropic γ -ray emissivity per gas atom is equal to :

$$q_\gamma(E_\gamma) = \frac{Q_\gamma}{4\pi n_H} \quad [\gamma s^{-1} sr^{-1} eV^{-1}] \quad (7.9)$$

The results are published in the paper presented in the next section.

7.4 First Paper (2021)

In the first article, presented in this section, we compare the CR nuclear spectra obtained from various demodulation models. We also present the different models of cosmic electron demodulation, because these particles contribute to bremsstrahlung radiation to the γ -ray emissivity at low γ -ray energies.

We then obtain two different γ -ray emissivity curves using two distinct cross-sections : the combined Kamae+QGSJET one and the Fluka one. We conclude unfortunately that the present uncertainty associated with these cross-sections prevents us from deciding whether the low CR flux pervading the Eridu cirrus is consistent or not with the flux reaching the Sun.

Cosmic-ray variations in the solar neighbourhood

Isabelle A. Grenier,^{a,*} François R. Kamal Youssef^a and M. Nicola Mazziotta^b

^aUniversité de Paris and Université Paris Saclay, CEA, CNRS, AIM,
CEA Saclay, F-91190 Gif-sur-Yvette, France

^bIstituto Nazionale di Fisica Nucleare, Sezione di Bari,
via Orabona 4, I-70125 Bari, Italy
E-mail: isabelle.grenier@cea.fr, francois.kamalyoussef@cea.fr,
Marionicola.Mazziotta@ba.infn.it

The γ radiation produced in cosmic-ray and gas interactions has been used to probe the local cosmic-ray spectrum in several clouds to distances of about 1 kpc around the Sun. Early measurements made with Fermi LAT data were found in good agreement with the proton and helium cosmic-ray spectra reaching the Solar System, given the 10-15% uncertainty in target gas mass that is inherent to H α line observations. The local cosmic-ray uniformity has recently been challenged by the finding of a significant loss of particles in the nearby Eridu cirrus. We have revisited the γ -ray emissivity spectrum one would expect per gas nucleon from hadronic and bremsstrahlung emission using the latest cosmic-ray spectra inferred near the Sun, outside the heliosphere. We have also used improved photon production spectra in nucleus-nucleus interactions. We find that, because of the current uncertainty in the γ -ray yield per nuclear interaction, one cannot conclude whether the average cosmic-ray spectrum measured within ~ 1 kpc from the Sun is comparable or superior to that inferred just outside the Solar System, nor whether the low cosmic-ray flux pervading the Eridu cirrus is consistent or not with the flux reaching the Sun. The Eridu cirrus and the Sun both lie in a hollow valley of the local interstellar medium. We show that the cosmic-ray flux in Eridu is about half that observed in two other more massive clouds that flank the valley.

37th International Cosmic Ray Conference (ICRC 2021)
July 12th – 23rd, 2021
Online – Berlin, Germany

*Presenter

Most of the Galactic interstellar γ rays observed by Fermi LAT in the 10^8 - 10^{11} eV band originate from nuclear interactions between cosmic rays (CR) and interstellar gas. Below 300 MeV, electron bremsstrahlung radiation also contributes to the gas emission, but is difficult to separate because of source confusion given the LAT angular resolution at low energy. Above 300 MeV, the γ -ray emissivity spectra obtained per gas nucleon in different nearby clouds show a rather uniform distribution. The sample shows less than 30% variations in amplitude and the same spectrum across the γ -ray band (see Figure 4a of [1]). Those measurements were made in clouds within a few hundred parsecs from the Sun and at low altitude in the disc ($|z| \lesssim 100$ pc). They were made in the atomic phase of the gas where the mass threaded by CR can be directly estimated, unlike in the molecular phase. Yet residual systematic uncertainties due to self absorption of the H I lines in the densest atomic parts can limit the interpretation of amplitude variations in γ -ray emissivity. Claims of significant CR variations in flux or spectrum in the local interstellar medium (ISM), [e.g. 2, 3], have severely overlooked interstellar complications (cloud confusion along sightlines, non uniform conversions of CO line intensities to H₂ column densities, masses of optically-thick H I and CO-dark H₂, severe non-linearities in the use of dust optical depths to trace the total gas, etc). The CR homogeneity near the Sun was, however, significantly challenged by the study of the light Eridu H I cirrus, at a height of 200–250 pc below the Galactic plane, which presents a 34% lower γ -ray emissivity, but similar spectrum, than the local ISM average [4]. This emissivity is at variance with the dispersion seen among other nearby clouds and with the CR flux decline expected towards the halo (see Figure 13 of [4]). The emissivity of the Eridu cirrus was compared to the average [15] found in the atomic gas at latitudes $10^\circ \leq |b| \leq 70^\circ$ which span distances to typically 1 kpc. Here we compare the Eridu emissivity to more local measurements, i.e. to the local interstellar spectra (LIS) of CR incident on the heliosphere, and to emissivities in specific clouds that outline the contrasted structure of the local ISM.

1. Hadronic and bremsstrahlung cross sections

The γ -ray yields produced by inelastic interactions between different CR and gas nuclei have been calculated with the FLUKA simulation package [5] and, alternatively, with a combination of the QGSJET-II-04m model [6] and of the "Kamae" parametrisation for p-H interactions [7]. We refer to these calculations as 'FLUKA' and 'K+QGSJET', respectively. The FLUKA simulation has been benchmarked with a large set of experimental data collected in accelerator experiments and it notably includes prompt pion production as well as secondary production from short-lived particles in the nuclear interaction. We have produced cross sections for the main p-H, p-He, He-H, and He-He interactions. The results of the QGSJET-II-04m model have been tuned to LHCf, LHCb, and NA61 data at kinetic energies of tens to hundreds of GeV. Following [8], we have restricted the use of the QGSJET matrices provided in [6] to kinetic energies $E_k > 30$ GeV per nucleon and we have scaled the Kamae matrix to the QGSJET ones in the $30 \leq E_k \leq 100$ GeV/n range. To extend the QGSJET matrices at lower energies for CRs heavier than protons, we have exploited the fact that these cross-sections, when expressed per nucleon-nucleon interaction and in kinetic energy per nucleon, closely follow the p-H one in shape and values. The resulting nuclear enhancement factors vary with both the nucleon and photon energies. They agree to better than 10% with the Mori DMPJET-3 estimates [9] in the 10-1000 GeV/n range for 1 GeV photons. The agreement degrades

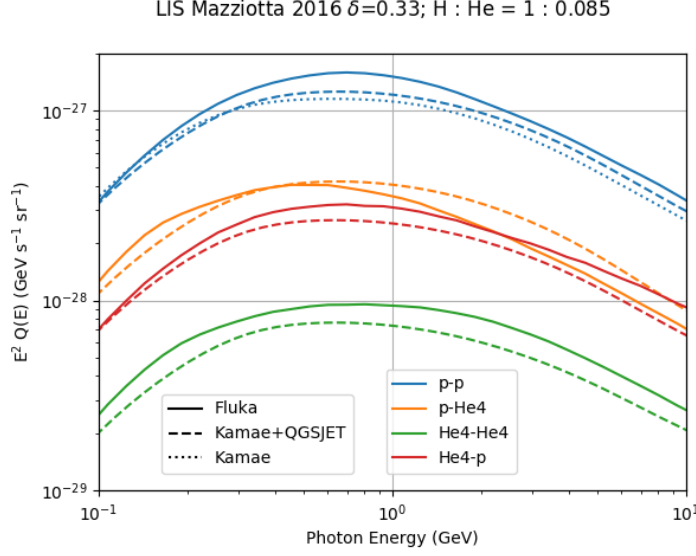


Figure 1: Comparison of the γ -ray yields obtained for the main p-H, p-He, He-H, and He-He interactions with the FLUKA and K+QGSJET cross-sections assuming the same input CR spectra from [5].

at higher photon energies. [6] provides cross sections for the main p-H, p-He, He-H, He-He, C-H, Al-H, and Fe-H interactions. Since we have solar-demodulated CR spectra for all nuclei with charge number $Z \leq 28$, we have interpolated this set of cross sections (per nucleon-nucleon interaction and in kinetic energy per nucleon) to produce matrices for the missing interactions. The FLUKA calculations were run .

Figure 1 compares the γ -ray yield obtained for the four main p-H, p-He, He-H, and He-He interactions with the FLUKA and K+QGSJET sets of cross-sections, assuming the same input CR spectra from [5]. The maximum deviations reach 26%, 38%, 21%, and 34%, respectively. The higher yield from FLUKA may stem from secondary pion production from the decay of heavier mesons, such as η , produced at intermediate energy in the interaction. Whereas the average multiplicity primarily follows the number of nucleon-nucleon interactions in the collision, non-linear effects occur near the π^0 production threshold. They are visible in Figure 1, in particular for the p-He interaction.

For the bremsstrahlung cross section, we have followed the formulation of [11] for electron kinetic energies above 2 MeV, interpolating the ϕ_1 and ϕ_2 functions for hydrogen and helium atoms from [12, table II, Hartree-Fock solution for He] onto our grid of electron and γ -ray energies. We have used the Schiff formula for heavier atoms and set the minimum Fano-Sauter value to the cross section when the emerging γ -ray energy approaches the incident electron kinetic energy.

We have restricted the choice of target gas nuclei to hydrogen and helium for hadronic production and to H, He, C, N, O, Ne, Mg, Si, S, Fe, and Ni for bremsstrahlung radiation since those gas components, with local interstellar abundances from [13], dominate the γ -ray yield.

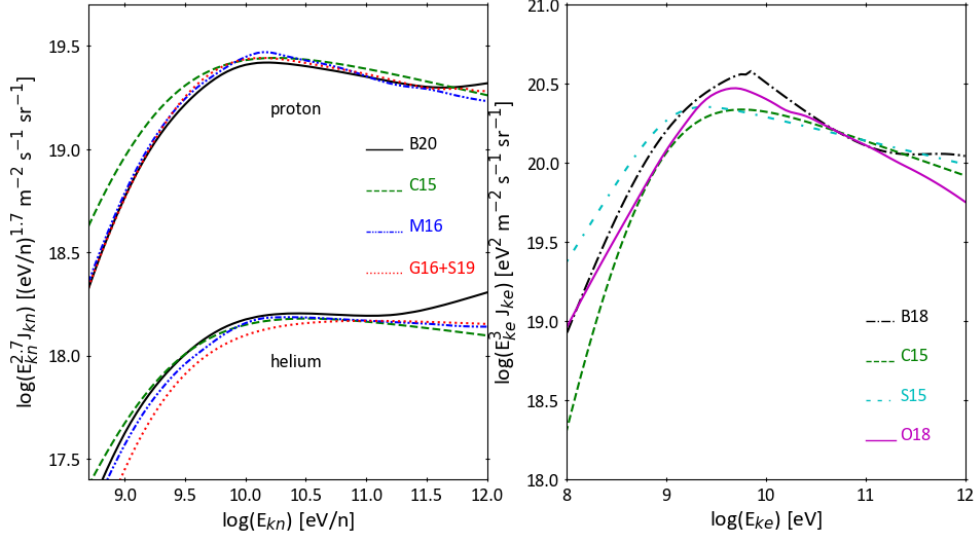


Figure 2: Comparison of the local interstellar spectra (LIS), incident on the heliopause, inferred for CR protons and helium (*left*, from [5, 10, 15–17]) and for all CR electrons (*right*, from [15, 19–21]).

2. Cosmic-ray spectra near the Sun

The heliospheric propagation of CRs leads to a marked flux reduction below ~ 50 GV in rigidity. The LIS, incident on the heliopause, have been measured aboard Voyager 1 and 2 at kinetic energies ≤ 700 MeV/n for nuclei and ≤ 74 MeV for electrons [14]. At higher energy, they have been inferred from direct particle data taken inside the Solar System, using either the force-field approximation for solar demodulation with a time-dependent potential [e.g. 15, 16], or solving the Parker transport equation in a time variable configuration of the heliosphere [e.g. 10, 17, 21]. LIS estimates have thus been obtained by purely demodulating the Solar-System data [e.g. 16, 17], by combining solar demodulation and the γ -ray emissivity of the gas in nearby interstellar clouds [15], or by combining solar demodulation and more distant information on CR propagation in the Galaxy (γ -ray and radio maps, secondary to primary spallation ratios, antiprotons, etc) [e.g. 5, 10, 21].

The γ -ray emissivity of the interstellar gas is best measured in the 0.05–30 GeV range. Figure 2 shows that the proton and helium spectra compare well in the 1–300 GeV/n band that contributes most of these γ rays. The hardening break confirmed by CALET near 200–300 GeV/n [18] was modelled only in the ‘B20’ curve shown from [10] in this set. At lower energies, the proton spectra differ by less than 12% if we discard the low-energy part of the Casandjian (2015) spectrum which was not constrained by Voyager data like the others. The difference in helium is more pronounced as it varies from 45% down to 10% and up again to 20% with increasing energy across the band. The comparison in Figure 2 shows that the addition of indirect information on propagated CRs in the Galaxy does not strongly affect the result, the latter being largely driven by Solar-System data and solar demodulation.

The all-electron spectrum is more uncertain, in particular at energies below 1 GeV which are most relevant for Fermi LAT observations, even if we take into account that the two most extreme

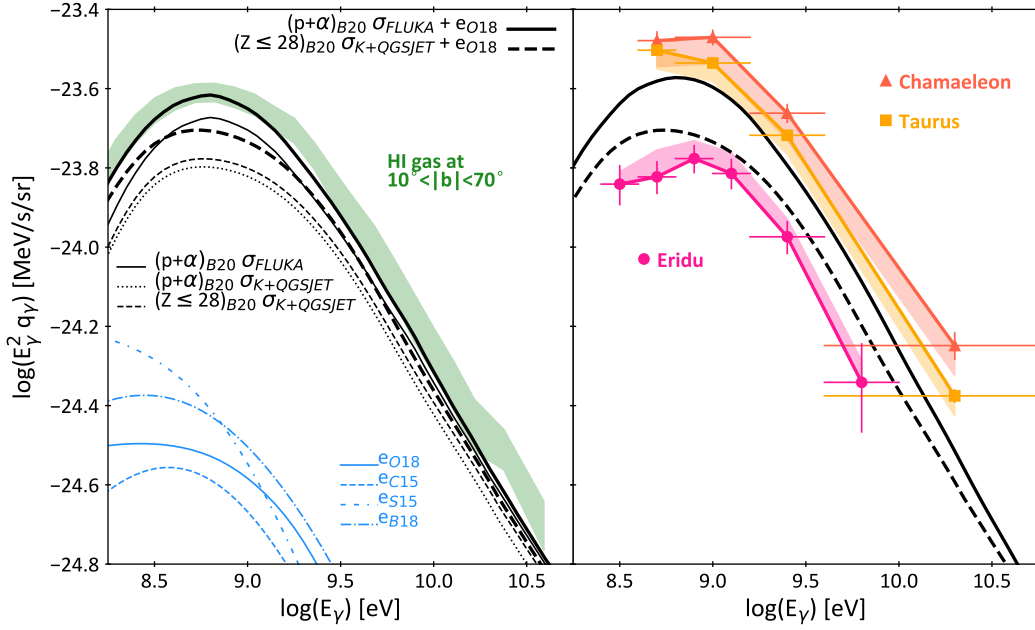


Figure 3: Emissivity spectra per gas nucleon for hadronic (thin black), bremsstrahlung (thin blue), and total (thick) emission, using the FLUKA (solid) and 'K+QGSJET' (dashed) cross sections. The emissivities are calculated for the CR spectra found near the Solar System (LIS) in nuclei (from [10]) and all electrons (from [19]). See Figure 2 for the other electron references. The emissivities are compared with the average found in the atomic gas within ~ 1 kpc from the Sun (left plot, shaded green, from [15]) and in the nearby clouds of Eridu, Taurus, and Chamaeleon (right plot, from [4, 22, 23]). The shaded area for the 1-kpc average on the left corresponds to the statistical error. For the other three clouds on the right, statistical uncertainties are given as error bars and the impact of systematic uncertainties in the HI mass as shaded areas.

spectra at low energy were not constrained by Voyager data. Indirect information plays an important role to constrain the spectrum at intermediate energies as spectra brighter than the Orlando (2018) one in the 1-10 GeV band are disfavoured by the radio and γ -ray maps [19].

3. The cosmic-ray deficit in the Eridu cirrus

Figure 3 shows the γ -ray emissivities one would expect in nearby clouds if the CR spectra pervading them were the same as the LIS reaching the heliophere. For the total emissivity, we took the input CR spectra from [10] for nuclei and [19] for all electrons. The choice of the proton and helium spectra from [5] would yield a 10% larger emissivity. We have used the 'K+QGSJET' cross section to illustrate the $\sim 5\%$ gain in hadronic emissivity if one includes interactions with CR nuclei heavier than helium (see Figure 3, left). We have also used the FLUKA simulation to check that interactions with interstellar C, N, O, Ne, Mg, and Si atoms only contribute 0.2% to the hadronic emissivity on hydrogen and helium.

The average emissivity measured with the LAT in the atomic gas lying within about 1 kpc around the Sun (at $10^\circ \leq |b| \leq 70^\circ$) assumes a low HI spin temperature of 140 K to partially correct for the self absorption of the gas to the HI line radiation [15]. Figure 3 (left) illustrates that

the current uncertainty in the γ -ray yield per nuclear interaction makes it impossible to conclude whether the average CR spectrum measured in a 1-kpc-wide region around the Sun is comparable or $\sim 25\%$ superior to that passing the Solar System. It also shows that the bremsstrahlung radiation represents at least 15% of the total emission at energies near 1 GeV in this region.

Figure 3 (right) compares the low γ -ray emissivity found in the Eridu cirrus with measurements in two specific nearby clouds on the one hand, and with the range of expectations from the LIS near the Solar System on the other hand. The emissivity measurements have been obtained in the atomic phase of the clouds, at comparable linear resolutions of 0.3-1 pc, with the same tracers to map all gas phases, including the dark one, and the same method to model the spatial and spectral distributions of γ rays observed by the LAT. The emissivity measurement relies on the spatial correlation between the γ rays and the gas column densities in the H I-bright phase. The Eridu cirrus is located 200-300 pc away from the Sun and at a height of 200-250 pc below the Galactic plane [4]. It shares with the Sun a common location in a long, rather hollow valley of the local ISM that is surrounded by denser, star forming, molecular clouds. In order to compare Eridu with other nearby clouds, we have selected two regions along the valley rim and toward the same valley sector, namely the Chamaeleon complex and the main cloud of the Taurus complex. They respectively lie at distances of $(183 \pm 3_{stat} \pm 9_{syst})$ pc and $(141 \pm 2_{stat} \pm 7_{syst})$ pc from the Sun and at heights of ~ 50 pc and ~ 40 pc below the Galactic plane [24]. Figure 3 shows the marked difference observed in γ -ray emissivity between the light atomic cirrus of Eridu and the more massive molecular clouds flanking the valley. Given the statistical and systematic uncertainties shown in Figure 3, the emissivity difference reflects a significant difference in CR flux between clouds that are only 200 to 300 pc away from each other.

The CR flux in the Eridu cirrus appears to be half lower than in the nearby massive clouds. Gas mass uncertainties cannot account for this large difference. The Eridu emissivity cannot exceed the upper limit of the shaded area which corresponds to optically thin H I gas, hence to the very minimum amount of H I gas present in the cloud. Conversely, adding hidden H I gas to the Chamaeleon and Taurus clouds would reduce their emissivities in an energy-independent way. The shaded areas show the magnitude of the effect when changing the cloud H I optical thickness from the optimum value to a much thicker case. One could further add opaque H I clumps and diffuse CO-dark H₂ gas, but this dark phase has a different spatial distribution than the H I-bright one and it is mapped and included in the analyses as a separate gas component. So is the CO-bright molecular phase. The emissivity of the H I-bright gas is therefore not affected by the presence of the denser gas phases, whether dark or bright, as long as their spatial distributions can be resolved and distinguished. This is the case for the Chamaeleon and Taurus clouds [22, 23]. Doubling the H I-bright gas mass of the Chamaeleon and Taurus clouds to reconcile their emissivities with that of Eridu is therefore implausible.

Because of the uncertainty in γ -ray yield per nuclear interaction, it is unfortunately impossible at this stage to conclude whether the CR flux reaching the Solar System is close to that of Eridu as both lie in a low-density valley where the large-scale magnetic field is more ordered than in the denser and clumpier clouds surrounding the valley, or whether the CR flux near the Sun compares well with that in the massive clouds and the deficit towards Eridu is specific to its magnetic configuration and/or height off the plane. As seen in dust polarisation toward this sector, the magnetic field in the local valley is mostly parallel to the Galactic disc whereas the filamentary

cirrus of Eridu stretches along a different magnetic tube that is highly inclined (at $\sim 45^\circ$) toward the South Galactic pole and halo [4]. The alignment between gas filaments and magnetic-field lines is frequent in this type of cirrus [25], but assessing whether or not such a configuration favours a fast CR diffusion along the filament requires detailed parsec-scale models. As argued in [4] and by Bustard & Zweibel at this conference, the difference between the CR flux in the filamentary Eridu cirrus and the clumpier and denser Chamaeleon and Taurus clouds is unlikely due to hampered CR penetration into the multi-phase gas, especially at the energies above a few GeV that are sampled by the LAT data. Moreover, the light Eridu cirrus is much less dense than the Chamaeleon and Taurus clouds where we see CR in γ rays deep into the dense molecular parts with the same energy spectrum as in the atomic envelopes. This set of clouds therefore offers an excellent test bed to study CR transport in different types of clouds and over short distance scales of 200 or 300 pc.

Acknowledgements: we acknowledge the financial support by the Institut Universitaire de France and LabEx UnivEarthS (ANR-10-LABX-0023 and ANR-18-IDEX-0001) for this work.

References

- [1] Grenier I. A., Black J. H., Strong A. W., 2015, ARA&A, 53, 199
- [2] Yang R.-zhi., de Oña Wilhelmi E., Aharonian F., 2014, A&A, 566, A142
- [3] Neronov A., Malyshev D., Semikoz D. V., 2017, A&A, 606, A22
- [4] Joubaud T., et al., 2020, A&A, 635, A96
- [5] Mazziotta M. N., Cerutti F., Ferrari A., Gaggero D., Loparco F., Sala P. R., 2016, APh, 81, 21
- [6] Kachelrieß M., Moskalenko I. V., Ostapchenko S., 2019, CoPhC, 245, 106846
- [7] Kamae T., Karlsson N., Mizuno T., Abe T., Koi T., 2006, ApJ, 647, 692
- [8] Kachelrieß M., Ostapchenko S., 2012, PhRvD, 86, 043004
- [9] Mori M., 2009, APh, 31, 341
- [10] Boschini M. J., et al., 2020, ApJS, 250, 27
- [11] Strong A. W., Moskalenko I. V., Reimer O., 2000, ApJ, 537, 763
- [12] Blumenthal G. R., Gould R. J., 1970, RvMP, 42, 237
- [13] Asplund M., Grevesse N., Sauval A. J., Scott P., 2009, ARA&A, 47, 481
- [14] Stone E. C., Cummings A. C., Heikkilä B. C., Lal N., 2019, NatAs, 3, 1013
- [15] Casandjian J.-M., 2015, ApJ, 806, 240
- [16] Ghelfi A., Barao F., Derome L., Maurin D., 2016, A&A, 591, A94
- [17] Shen Z.-N., Qin G., Zuo P., Wei F., 2019, ApJ, 887, 132

- [18] Adriani, O., Akaike, Y., Asano, K., et al. 2019, PRL, 122, 181102.
- [19] Orlando E., 2018, MNRAS, 475, 2724
- [20] Strong A., Fermi-LAT Collaboration, 2015, ICRC, 34, 506
- [21] Boschini M. J., et al., 2018, ApJ, 854, 94
- [22] Planck Collaboration, Fermi Collaboration, et al., 2015, A&A, 582, A31
- [23] Remy Q., Grenier I. A., Marshall D. J., Casandjian J. M., 2017, A&A, 601, A78
- [24] Zucker C., et al., 2019, ApJ, 879, 125
- [25] Clark S. E., Hensley B. S., 2019, ApJ, 887, 136

CRs in Reticulum vs Eridu

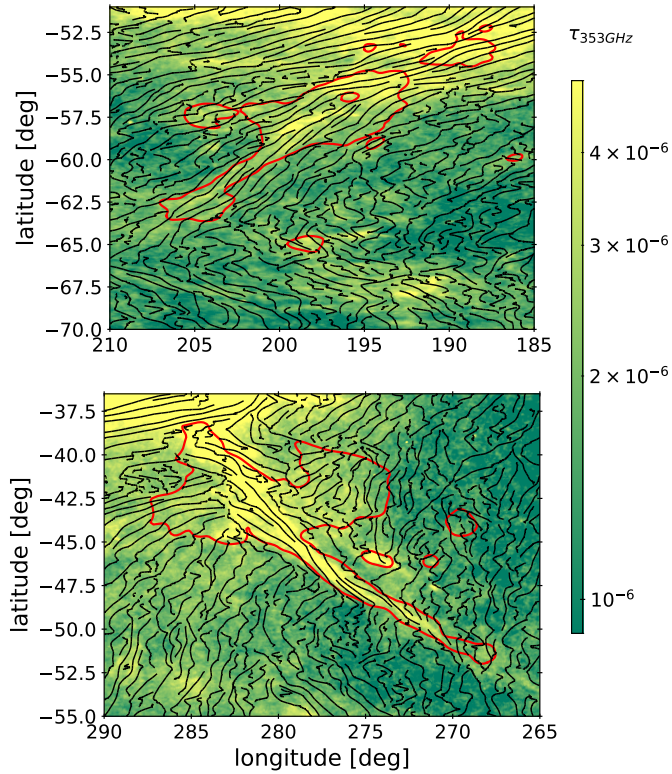


Figure 8.1 : Dust optical depth τ_{353} at 353 GHz in Galactic coordinates toward the Eridu (top) and Reticulum (bottom) filaments. The black lines give the orientation of the plane-of-the-sky B_{sky} magnetic field inferred from the dust polarisation observations at 353 GHz with *Planck* at an angular resolution of 14' (FWHM). The red contours delineate the filaments at HI gas column densities of $3 \times 10^{20} \text{ cm}^{-2}$ and $1.2 \times 10^{20} \text{ cm}^{-2}$, respectively. (Kamal Youssef & Grenier, 2024)

In order to study the reason for a change in CR flux in the Eridu cloud, we decided to study another filament, called Reticulum, with gaseous and magnetic characteristics comparable to those of Eridu. In this chapter, we aim to first measure the γ -ray emissivity spectrum per gas nucleon in the Reticulum filament and to compare it with the average one in the local ISM q_{LIS} and with the low emissivity spectrum in the Eridu cloud. We then aim to compare the inter-

stellar properties of both clouds in order to search for possible differences in CR propagation properties.

8.1 General characteristics of Reticulum

The Reticulum cloud is an atomic filamentary cloud that lies at the edge of the Local Valley. Figure 8.1 shows that Reticulum, in the bottom plot, is inclined with respect to the Galactic plane, like Eridu. Both clouds point towards the South halo and have magnetic field lines well-ordered and aligned with the filament axis.

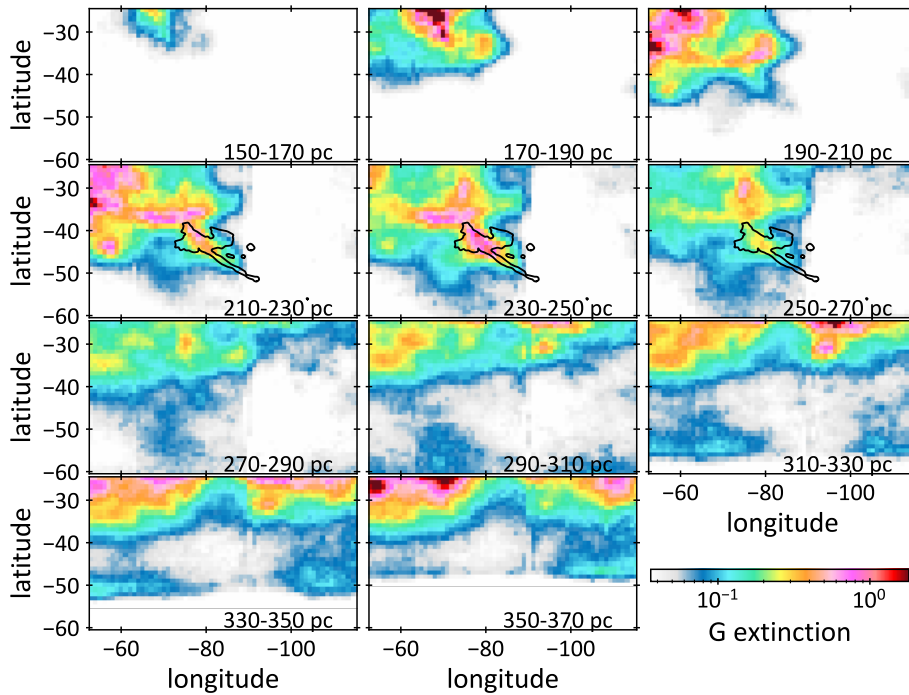


FIGURE 8.2 : Maps of the G-band extinction optical depth integrated over 20 pc-wide intervals in distance from the Sun across the analysis region. The data come from the 3D distribution of Leike et al. (2020). The distance ranges are labelled in each map. The black contours delineate the Reticulum H I cloud. (Kamal Youssef & Grenier, 2024)

As for Eridu, we have used the model of dust extinction by Leike et al. (2020) to estimate the distance to the Reticulum cloud. Figure 8.2 presents cuts of the 3D dust distribution within 20-pc-wide intervals, covering distances from 150 to 350 pc. The general shape and position of the Reticulum cloud can be distinguished in the dust distribution at a distance of 240 ± 30 pc.

According to Eq.4.11, we need to measure the gas column densities in the different phases of the Reticulum cloud in order to estimate the γ -ray emissivity per gas nucleon and therefore the CR flux pervading the cloud.

8.2 Gas estimates

8.2.1 H I gas phase

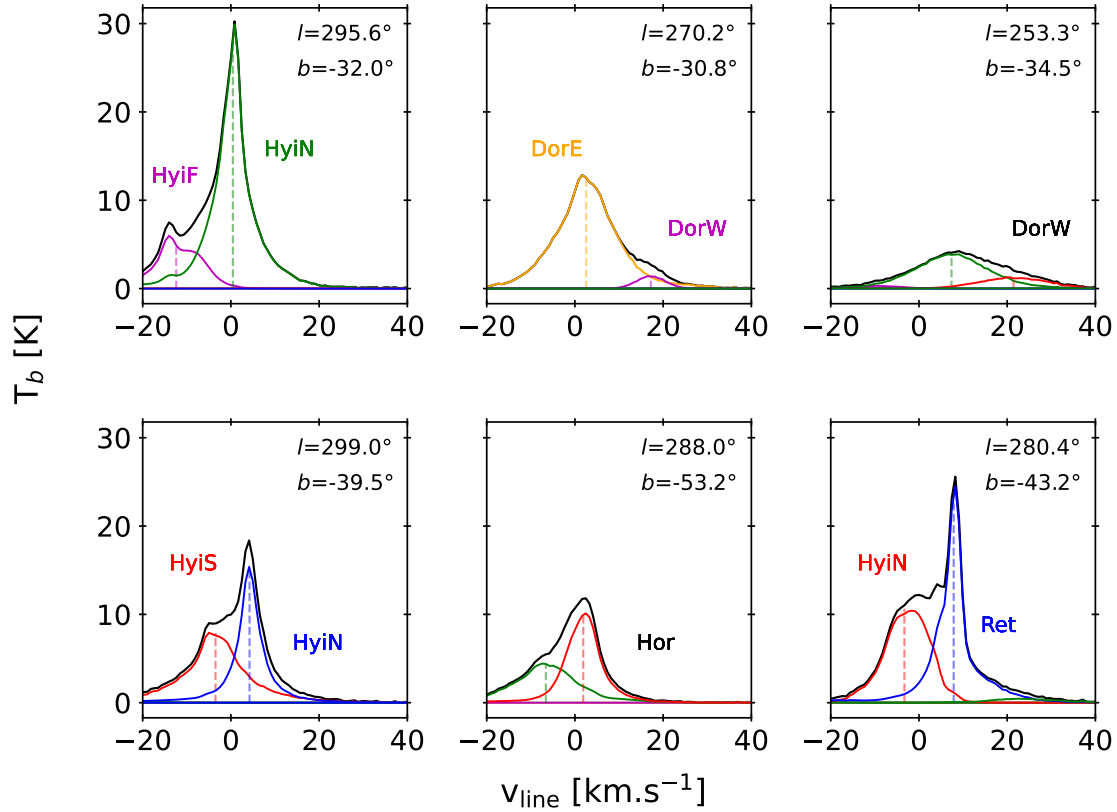


FIGURE 8.3 : H I GASS spectra, in brightness temperature, T_b , measured toward different directions indicated in the plots. The black curve represents the original data. The pointed lines indicate the central velocity and temperature of the individual lines that contribute to a cloud.

Since Reticulum is an atomic filamentary cloud, we collected the H I GASS III data in the analysis area extending from 251.5° to 302.5° in Galactic longitude and from -54.5° to -30.5° in Galactic latitude. Then, we decomposed the H I spectra into sets of individual lines based on the spatial and velocity distributions. Each set corresponds to a nearby cloud complex in the analysis region. Examples of individual lines are shown in Fig.8.3. We have named these clouds according to the constellation in their direction, therefore as Reticulum (Ret), Far Hydrus (HyiF), North Hydrus (HyiN), South Hydrus (HyiS), East Dorado (DorE), West Dorado (DorW), and Horologium (Hor).

To calculate the column density map of each cloud, the lines in the measured H I spectrum are fitted with pseudo-Voigt profiles. Each profile combines a Gaussian and a Lorentzian with the

same velocity centroid, width, and height, and a relative weight that spans the interval from 0 (pure Gaussian) to 1 (pure Lorentzian). We have then used the distribution of line centroids in velocity and space to separate the lines between different clouds. To preserve the total H I intensity observed in each direction, the small positive and negative residuals between the observed and modelled spectra have been distributed between the lines in proportion to the height of each line at each velocity. Examples of different cloud H I profiles are represented by the colored curves in Fig.8.3. Finally, we have integrated each line profile to add its contribution to the N_{HI} map of the relevant cloud. This method is explained in details in Planck Collaboration, Fermi Collaboration, et al. (2015). The final integration has been done for several values of the spin temperature to correct the resulting column density for the H I optical depth. We have produced N_{HI} maps for a set of uniform spin temperatures, T_{S} , of 100, 125, 150, 200, 300, 400, 500, 600, 700 and 800 K and also for the optically thin case.

8.2.2 Molecular phase

We did not find observations of CO emission lines towards the analysis region. *Planck* has not detected any CO intensity up to 1 K km/s in this region. That means that the Reticulum gas is not dense enough to form detectable amounts of CO molecules.

In order to search for any dark gas undetected by the H I observation, we have applied the method described in Sec.4.5. As shown in Fig.8.4, we have used the *Fermi*-LAT γ rays and the *Planck* optical depth τ_{353} at 353 GHz. Both observation maps are shown in the first row. In the second row, we show the best-fit γ -ray and dust models obtained by combining the gas contributions of the different clouds, point sources, and background maps, following eqs.4.14 and 4.12.

The residual maps between observations and best-fit models are plotted in the third row when the models included only the atomic gas (no DNM). We can see the same distribution of positive residuals in both maps, which indicates the presence of additional DNM gas.

We have found significant DNM gas only in the North Hydrus and Reticulum clouds. Therefore, we removed all excess fluctuations in the other regions. The cleaned DNM maps are shown in the last row.

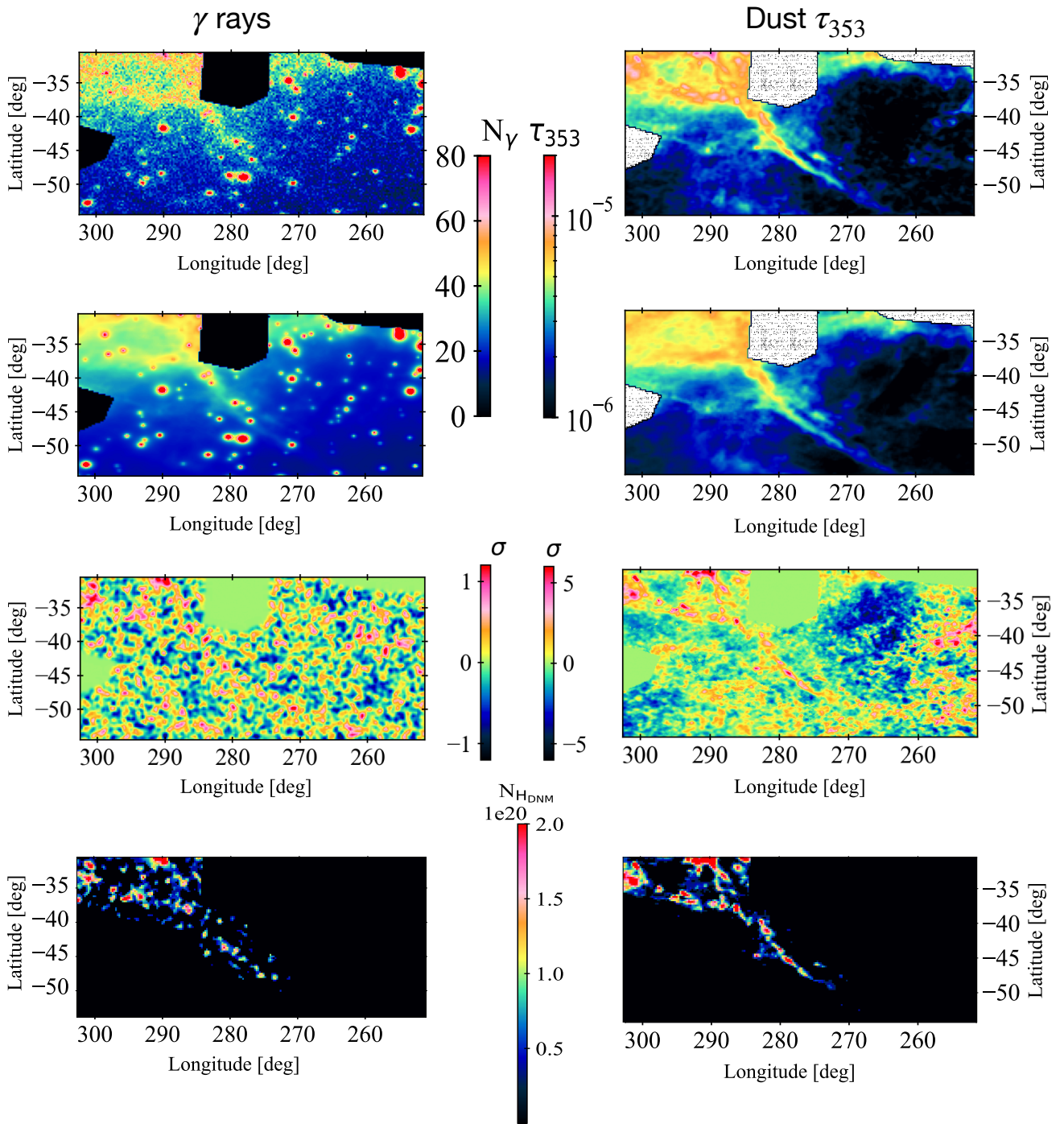


FIGURE 8.4 : The γ -ray map is on the left and the dust one on the right. The observations by *Fermi*-Lat and *Planck* are shown in the first row. The second one represents our best-fit models. The residual maps between observations and best-fit models (without DNM) are plotted in the third row. The DNM maps are shown in the last row.

8.3 Second Paper (2023)

The second paper is separated into two parts. The first concerns the results on the γ -ray emissivity of the two main clouds of the analysis region, Reticulum and North Hydrus. We compare them to the local average emissivity and to that in the Eridu cloud. The γ -ray emissivities of the other clouds found in the analysis region are shown in Sec.9. We have found that the γ -ray emissivity in Reticulum and North Hydrus is compatible with the average one, q_{LIS} . That implies that the CR flux in Eridu is lower than the flux in Reticulum even though they both have the same interstellar characteristics and magnetic field orientation.

In the second part of the paper, we explore the propagation properties of GeV CRs in both the Reticulum and Eridu filaments to search for a potential difference between them. We focused on the gas densities in the clouds as the ion-neutral damping of the MHD turbulence might differ. We have also estimated the diffusion coefficient parallel to the magnetic field one expects in the steady-state framework of self-generated Alfvén waves where the wave growth rate is balanced by the damping rate. We have then inferred magnetic-field strengths along the core of both filaments from dust polarisation data. We have finally compared the level of turbulence in gas motions and in magnetic-field orientation along both clouds. Puzzingly, we have found no notable difference between the properties of the two clouds that could shed light on the CR flux difference. All these investigations were conducted at a scale of ≈ 1 pc.

Cosmic-ray diffusion in two local filamentary clouds

F.R. Kamal Youssef¹ and I. A. Grenier¹

Université Paris Cité and Université Paris-Saclay, CEA, CNRS, AIM, F-91190 Gif-sur-Yvette, France
e-mail: francois.kamalyoussef@cea.fr
e-mail: isabelle.grenier@cea.fr, <https://orcid.org/0000-0003-3274-674X>

December 2, 2023

ABSTRACT

Context. Hadronic interactions between cosmic rays (CRs) and interstellar gas have been probed in γ rays across the Galaxy. A fairly uniform CR distribution is observed to a few hundred parsecs from the Sun, except in the Eridu cloud which shows an unexplained 30–50% deficit in GeV to TeV CR flux.

Aims. To explore the origin of this deficit, we have studied the Reticulum cloud that shares notable traits with Eridu: a comparable distance in the low-density region of the Local Valley and a filamentary structure of atomic hydrogen extending along a bundle of ordered magnetic-field lines that are steeply inclined to the Galactic plane.

Methods. We have measured the γ -ray emissivity per gas nucleon in the Reticulum cloud in the 0.16 to 63 GeV energy band using 14 years of *Fermi*-LAT data. We have also derived interstellar properties that are important for CR propagation in both the Eridu and Reticulum clouds, at the same parsec scale.

Results. The γ -ray emissivity in the Reticulum cloud is fully consistent with the average spectrum measured in the solar neighbourhood, but this emissivity, hence CR flux, is 1.57 ± 0.09 times larger than in Eridu across the whole energy band. The difference cannot be attributed to uncertainties in gas mass. Yet, the two clouds are similar in many respects: in magnetic-field strengths of a few micro-Gauss in the plane of the sky; in approximate equilibrium between magnetic and thermal pressures; in turbulent velocities and sonic Mach numbers; in magnetic-field order with a dispersion in orientation lower than 10° – 15° over large zones. The gas in Reticulum is colder and denser than in Eridu, but we find similar parallel diffusion coefficients around a few times $10^{28} \text{ cm}^2 \text{ s}^{-1}$ in both clouds if CRs with rigidity larger than 1 GV are dispersed by resonant, self-excited Alfvén waves that are damped by ion-neutral interactions.

Conclusions. The loss of CRs in Eridu remains unexplained, but these two clouds provide important test cases to further study how magnetic turbulence, line tangling, and ion-neutral damping regulate the diffusion of streaming CRs in the dominant gas phase of the interstellar medium.

Key words. Gamma rays: ISM – ISM: clouds – ISM: cosmic rays – ISM: magnetic field – Cosmic rays: propagation – Cosmic rays: diffusion coefficient

1. Introduction

The Sun is located in a valley of low gas density surrounded by two walls of dense molecular clouds (see Fig. 2 of Leike et al. 2020). Part of the valley, out to ~ 150 pc or ~ 250 pc depending on the direction, corresponds to the Local Bubble (see Fig. 1 of Pellegrini et al. 2020), but the elongated valley extends further away along opposite directions roughly parallel to the local spiral arm. The γ -ray intensity produced by the interaction of cosmic rays (CRs) with the interstellar gas and radiation fields present inside and around the valley has been recorded at energies above 30 MeV by the Large Area Telescope (LAT) on board the *Fermi* Gamma-Ray Space Telescope. Since the hadronic contribution to this γ -ray intensity gathers the integral along the lines of sight of the product of the CR and gas volume densities, one can use the γ -ray map of nearby clouds to probe the CR flux in different locations and in different types of environments in the valley or along its borders (Lebrun et al. 1982). This method requires an accurate measurement of the gas mass of a cloud.

In the warm atomic phase of the clouds, often referred to as the Warm Neutral Medium (WNM), one can directly infer the gas mass from the observation of the H α 21 cm lines (e.g. Dickey et al. 2000; Heiles & Troland 2003). In the denser, cold atomic phase of the clouds, where the H α brightness temperature probes the excitation (spin) temperature of the gas rather than the col-

umn density, the lines must be corrected for partial self absorption in order to estimate the gas mass (Murray et al. 2015, and references therein). This cold atomic phase, referred to as the Cold Neutral Medium (CNM), is ubiquitous, but it generally contributes only 5 to 28% of the total atomic mass (Murray et al. 2018, 2020). H $_2$ molecules radiate inefficiently in the cold conditions of molecular clouds, so one must rely on surrogate observations such as the rotational lines of ^{12}CO and its isotopologues in order to quantify the H $_2$ mass. This is only possible where the abundance and excitation temperature of CO molecules are large enough. Environmental variations of the X_{CO} conversion factor between the $^{12}\text{CO}(1-0)$ line intensity and the H $_2$ column density have been studied theoretically and observationally (Bolatto et al. 2013; Gong et al. 2018; Remy et al. 2017, and references therein), but the variations are too large and too uncertain to reliably use the CO data to measure the CR flux in the dense molecular phase of clouds.

Complementary information can be obtained from the thermal emission of large dust grains mixed with the gas. The emission is observed at sub-millimeter and infrared wavelengths (Planck Collaboration et al. 2014a,b). Dust grains and CRs are both tracers of the total gas, in all chemical and thermodynamical forms (Grenier et al. 2005; Planck Collaboration et al. 2015b). The γ rays reveal the gas mass convolved by the ambient CR flux

whereas the dust optical depth shows the gas mass convolved by the ambient dust-to-gas mass ratio and by the ambient grain emissivity. Both the CR and dust properties vary from place to place, but the spatial correlation between the two tracers in a given cloud can be used to trace the dark gas that escapes H_I and CO line observations (Grenier et al. 2005). This Dark Neutral Medium (DNM) accumulates at the H_I-H₂ transition in the clouds (Liszt et al. 2019). It is not seen in H_I or CO emission because of self-absorption in the dense H_I clumps and because CO molecules are efficiently photo-dissociated or too weakly excited in the diffuse H₂ gas.

Given the uncertainty in gas mass estimates in the dark and molecular phases of clouds, one can only infer the CR spectrum with adequate precision in the atomic phase. The analysis exploits the spatial correlation between the γ -ray intensity and H_I column density (N_{HI}). It requires maps of the other phases to avoid biasing the γ -ray emissivity, q_{HI} , obtained per gas nucleon in the atomic phase (Planck Collaboration et al. 2015b). Emissivity spectra are typically obtained at energies above a few hundred MeV to take advantage of the better angular resolution of the LAT in order to resolve the clouds and their different phases.

Such emissivity measurements have been performed in different clouds of the local interstellar medium (ISM) (e.g. Abdo et al. 2010; Ackermann et al. 2012a; Planck Collaboration et al. 2015b; Casandjian 2015; Tibaldo et al. 2015; Remy et al. 2017; Joubaud et al. 2019) and across the Milky Way (e.g. Ackermann et al. 2013; Acero et al. 2016). The local emissivity spectra appear to be often consistent with the local average, $q_{\text{LIS}}(E)$, that has been obtained for the whole atomic gas seen at Galactic latitudes ranging between 7° and 70° (Casandjian 2015). Such a consistency implies that the CR flux is rather uniform within a few hundred parsecs from the Sun (Grenier et al. 2015).

At variance with this uniformity, a significantly lower γ -ray emissivity spectrum has been found in a nearby cloud named Eridu. The spectrum is 34% lower than the q_{LIS} average (Joubaud et al. 2020). The deviation is statistically significant (14 σ) and there is no confusion with other clouds along the lines of sight. The deviation cannot be attributed to uncertainties in the H_I mass since the minimum amount of gas inferred from the H_I lines (optically thin case) gives an upper limit to the emissivity that is still 25% below q_{LIS} . More CRs would outshine the observed γ rays. The γ -ray analysis has probed CRs with energies above several GeV. Their penetration in the cloud is likely unhampered given the modest column densities ($1\text{--}5 \times 10^{20} \text{ cm}^{-2}$) and low volume densities (around 7 cm^{-3}) of the diffuse gas (Joubaud et al. 2019). The Eridu cloud therefore appears to be pervaded by a $\sim 30\%$ lower CR flux, but with the same particle energy distribution as in the local ISM.

The Eridu cloud is a diffuse, atomic, and filamentary cirrus. It is located outside the edge of the Orion-Eridanus superbubble, at high Galactic latitudes around -50° and at an altitude of about 200–250 pc below the Galactic plane (Joubaud et al. 2019). Figure 1 shows that the filament is inclined with respect to the Galactic plane and the dust polarisation data at 353 GHz from *Planck* (Planck Collaboration et al. 2015a) shows that the filament extends along a bundle of well-ordered magnetic-field lines, pointing within 45° of the South Galactic pole (see Fig. 10 of Joubaud et al. 2020).

Magnetic loops are pushed out of the Galactic disc by gas fountains. In order to investigate their impact on CR transport to the halo, we have searched for another filament with gaseous and magnetic characteristics comparable to those of Eridu. The

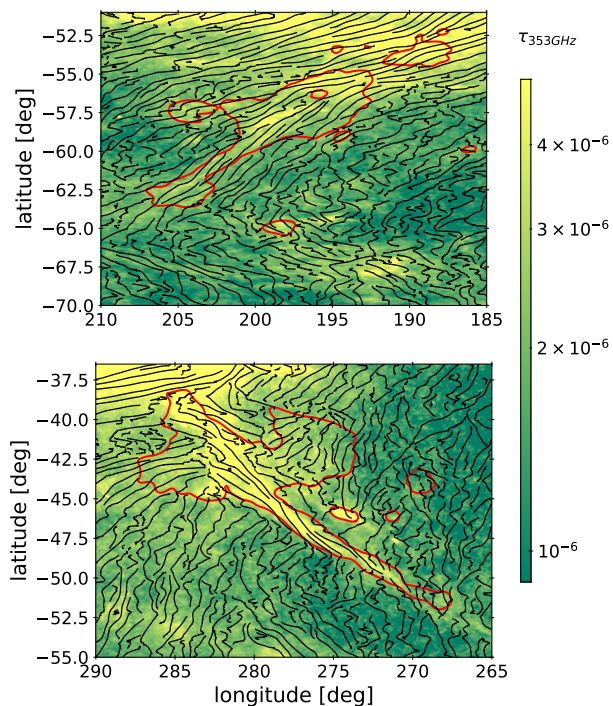


Fig. 1. Dust optical depth τ_{353} at 353 GHz in Galactic coordinates toward the Eridu (top) and Reticulum (bottom) filaments. The black lines give the orientation of the plane-of-the-sky B_{sky} magnetic field inferred from the dust polarisation observations at 353 GHz with *Planck* at an angular resolution of $14'$ (FWHM). The red contours delineate the filaments at H_I gas column densities of $3 \times 10^{20} \text{ cm}^{-2}$ and $1.2 \times 10^{20} \text{ cm}^{-2}$, respectively.

Reticulum cloud is also an atomic and filamentary cloud that lies at the edge of the local valley, at a distance we estimate to be about 240 pc (Appendix A). Figure 1 shows that, like Eridu, it is largely inclined with respect to the Galactic plane. It points towards the South halo and it has well-ordered magnetic field lines, aligned with the filament axis. We therefore aim to measure the γ -ray emissivity spectrum per gas nucleon in the Reticulum filament and to compare it with the average in the local ISM and with the emissivity spectrum in the Eridu cloud.

The paper is structured as follows: the data are presented in Sect. 2 and the models are described in Sect. 3. The results and the detection of dark gas are detailed in Sect. 4. The CR content of the clouds is discussed in Sects. 5.1 to 5.5.

2. Data

We have selected an analysis region around the Reticulum filament extending from $251:5$ to $302:5$ in Galactic longitude and from $-54:5$ to $-30:5$ in Galactic latitude, as shown in Fig. 2. We have masked regions with large column densities from the Large Magellanic Cloud (LMC) and Small Magellanic Cloud (SMC), and from the edge of the Gum Nebula.

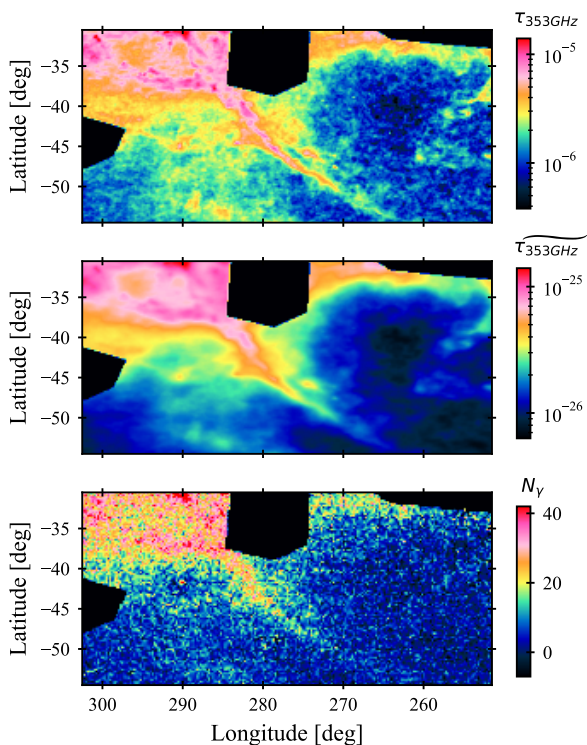


Fig. 2. Dust optical depth measured at 353 GHz from the *Planck* and *IRAS* data and displayed on a $10\cdot2\times7\cdot5$ grid at the angular resolution of *Planck* (top panel) and of *Fermi-LAT* (middle). The bottom panel shows the γ -ray photon counts produced by CR interactions with gas and recorded by *Fermi-LAT* in $0\cdot25\times0\cdot25$ bins in the 0.16–63 GeV energy band (other emissions of non-gaseous origin have been subtracted). Three zones have been excluded from the analysis region : the SMC on the left, LMC in the middle, and the edge of the Gum nebula on the upper right. The Reticulum cloud is the long filament crossing the region below the LMC.

2.1. Dust data

In order to trace the dust column density, we have used the all-sky map of the dust optical depth, τ_{353} , at 353 GHz (*Planck Collaboration et al. (2014a)*, updated by *Irfan et al. (2019)*). It was constructed at an angular resolution of $5'$ by modelling the intensity, I_ν , of the dust thermal emission recorded in frequency ν by *Planck* and the Infrared Astronomical Satellite (*IRAS*). The dust optical depth relates to the black-body intensity $B_\nu(T_d)$ for a dust temperature T_d and modified by a spectral index, β , according to $I_\nu = \tau_{353} B_\nu(T_d)(\nu/353 \text{ GHz})^\beta$. The dust opacity at 353 GHz is defined for a hydrogen column density N_H as the ratio τ_{353}/N_H .

Figure 2 shows the distribution of the dust optical depth in the analysis region at the original *Planck* resolution in the upper panel and at the angular resolution of *Fermi-LAT* for the 0.16–63 GeV band in the middle one.

2.2. Gamma-ray data

We have used fourteen years of *Fermi-LAT* Pass 8 P8R3 survey data for energies between 0.16 and 63 GeV (*Bruel et al. 2018*) and we have analysed the data in eight energy bands, bounded by $10^{2.2}$, $10^{2.4}$, $10^{2.6}$, $10^{2.8}$, $10^{3.0}$, $10^{3.2}$, $10^{3.6}$, $10^{4.0}$, and $10^{4.8}$ MeV.

The *Fermi-LAT* point-spread-function (PSF) strongly varies with energy. In order to retain sufficient photon statistics in this faint region and to preserve a good contrast in photon counts across small cloud structures, we have combined photons of different PSF types in each energy band. Photons are labelled from the worst (PSF0) to best (PSF3) quality in angle reconstruction. We have used PSF 3 in the three lowest-energy bands, PSF 2 and 3 in the next band, PSF 1 to 3 in the next two bands, and PSF 0 to 3 in the two highest energy bands. The 68% containment radius of the resulting PSF varies from $0\cdot9$ above 630 MeV to $1\cdot4$ at 250 MeV and to $2\cdot1$ at 160 MeV. The resulting photon map is shown in the lower panel of Fig. 2 where we have subtracted the point sources and the very smooth isotropic and inverse-Compton (IC) components to display the γ rays produced in the clouds.

In order to reduce the contamination of the photon data by residual CRs and by Earth atmospheric γ rays to less than 10%, we have applied tight selection criteria such as the SOURCE class and photon arrival directions within an energy-dependent and PSF-type-dependent angle varying from 90° to 105° from the Earth zenith, namely 90° in the first energy band, 100° in the second, and 105° at higher energies. We have used the associated instrument response functions P8R3_SOURCE_V3.

We have modelled the interstellar emission in a broader region than the analysis one in order to take into account the extent of the *Fermi-LAT* PSF. The 5° -wide peripheral band around the analysis perimeter corresponds to the PSF $>95\%$ containment radius for our selections. It is displayed in Fig. 3.

The positions and flux spectra of the γ -ray sources in the field are provided by the *Fermi-LAT* 4FGL-DR3 12-year source catalogue (*Abdollahi et al. 2022*). The analysis region and the 5° -wide peripheral band contain 220 point sources. Their flux spectra have been calculated with the spectral characteristics given in the catalogue.

The observation also includes IC γ rays produced by CR electrons up-scattering the interstellar radiation field in the Milky Way. This was modelled by GALPROP¹ and we have used the LRYusifovXCO5z6R30_Ts150_Rs8 model version (*Ackermann et al. 2012b*). The isotropic spectrum for the extragalactic and residual instrumental backgrounds is given by the *Fermi-LAT* science support center². We have used the isotropic spectrum provided for each PSF type of the SOURCE class.

2.3. Gas data

In order to map the neutral atomic hydrogen (HI) in the region, we have used the 21-cm Galactic All Sky Survey GASS III data (*Kalberla & Haud 2015*). The survey has an angular resolution of $16\cdot2$, a velocity resolution of 0.82 km/s in the local standard of rest, and an rms sensitivity of 57 mK. Lines in the analysis region span velocities from -125 to $+495$ km/s.

Following the method developed by *Planck Collaboration et al. (2015b)*, we have decomposed the HI spectra into sets of individual lines with Pseudo-Voigt profiles. Based on the (l, b, v) distribution of the fitted lines, we have identified seven nearby cloud complexes that are coherent in velocity and in position across the region. We have named these clouds according to the constellation in their direction, therefore as Reticulum (Ret), Far Hydrus (HyiF), North Hydrus (HyiN), South Hydrus (HyiS), East Dorado (DorE), West Dorado (DorW), and Horologium (Hor). They are displayed in Fig. 3 and they span velocities from

¹ <http://galprop.stanford.edu>

² <http://fermi.gsfc.nasa.gov/ssc/data/access/lat/BackgroundModels.html>

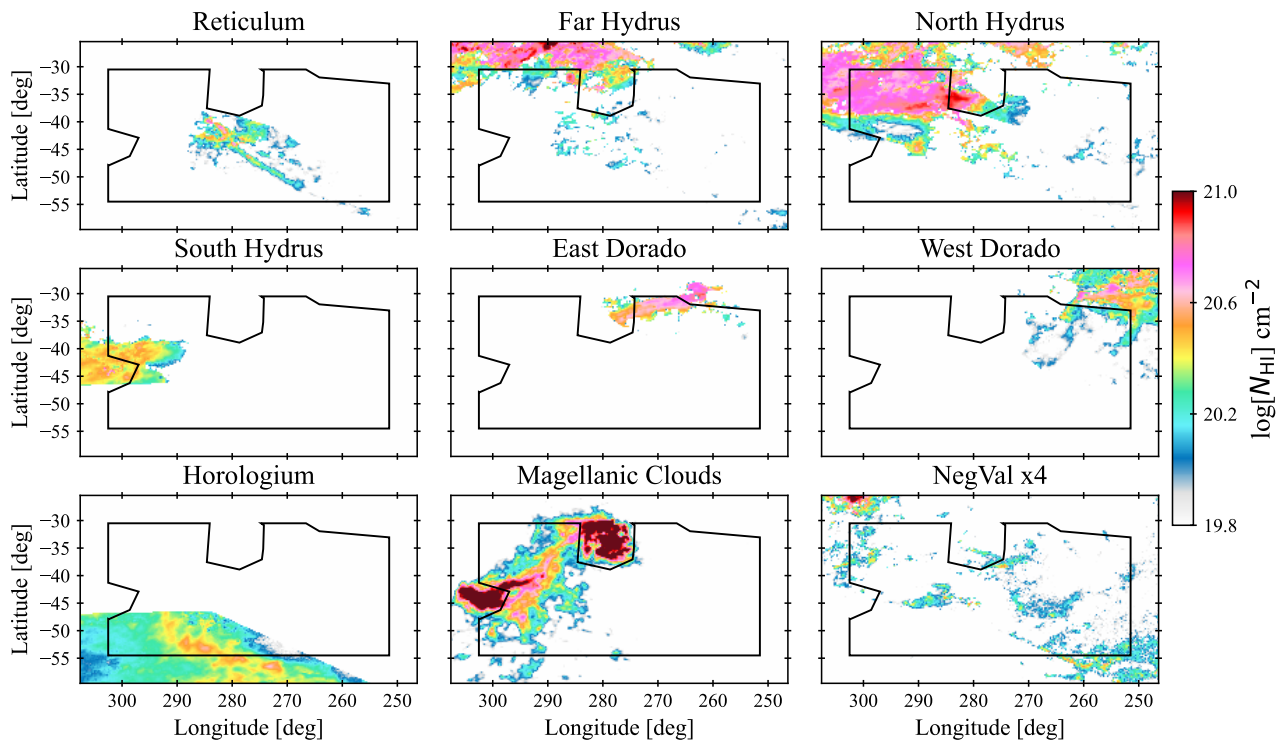


Fig. 3. N_{HI} column densities in the Reticulum (Ret), Far Hydrus (HyiF), North Hydrus (HyiN), South Hydrus (HyiS), East Dorado (DorE), West Dorado (DorW), Horologium (Hor), and Magellanic clouds for an H α at the optically thin case. The negative-velocity (NegVel) map gathers the faint H α lines below -8 km/s. Their column densities have been multiplied by 4 for display. The maps include a 5° -wide peripheral band around the analysis region (black perimeter) to account for the wings of the *Fermi*-LAT PSF in the γ -ray model.

3.3 to 20.6 km/s, -15.7 to -1.6 km/s, -0.8 to 13.2 km/s, -14.8 to 2.5 km/s, 2.5 to 4.9 km/s, 5.8 to 33.8 km/s, and -14.8 to 5.8 km/s, respectively. These clouds are local. Lines from the Magellanic clouds have been gathered in a single map. We have added a ninth component gathering the very weak lines found at velocities below -8 km/s.

We have produced N_{HI} column-density maps for each complex by integrating the fitted lines that have a central velocity within the chosen velocity interval for each (l, b) direction. This method corrects for potential line spill-over from one velocity interval (i.e. cloud) to the next. The line fits produce small residuals between the modelled and observed H α spectra. To preserve the total H α intensity, we have distributed these residuals among the fitted lines according to their relative strength in each velocity channel.

In order to correct the H α intensity for potential self absorption, we have produced the N_{HI} maps for a set of uniform spin temperatures, T_{S} , of 100, 125, 150, 200, 300, 400, 500, 600, 700, and 800 K and also for the optically thin case. Nguyen et al. (2018) have shown that a simple isothermal correction of the emission spectra with a uniform spin temperature can well reproduce the more precise N_{HI} column densities that are inferred from the combination of emission and absorption spectra. Given the wide range of potential spin temperatures we could not test individual temperatures for each cloud, but we have used the same temperature for all clouds and we have let it vary when modelling the dust and γ -ray data.

The nearby clouds in the region are mainly composed of atomic gas. We have looked for CO(1-0) emission at 115 GHz

towards them, but haven't found published observations in that area and *Planck* has detected no CO(1-0) intensity up to 1 K km/s in the region (Planck Collaboration et al. 2014c).

2.4. Cloud distances

Leike et al. (2020) have used the stellar data from the *Gaia*-DR2, ALLWISE, PANSTARRS, and 2MASS surveys to model the dust extinction and to reconstruct the 3D map of dust clouds within ~ 400 pc from the Sun with a spatial resolution of 2 pc. Distances to compact clouds and their dust densities are expected to be well constrained by the precise locations of the stars. We display in Figs. A.1 and A.3 cuts of the 3D dust distribution in 20-pc-wide intervals spanning distances from 150 to about 350 pc. The shapes and locations of the clouds isolated in the H α data in Fig. 3 can be roughly recognised in the dust distribution. We have also probed the dust distribution along lines of sight exhibiting large gas column densities in the different clouds (see Fig. A.2). From the dust and gas correspondence we infer average distances of 240 ± 30 pc, 220 ± 30 pc, 220 ± 30 pc, 170 ± 30 pc, 310 ± 30 pc, 340 ± 30 pc, and 280 ± 30 pc to the Reticulum, North Hydrus, South Hydrus, Far Hydrus, East Dorado, West Dorado, and Horologium clouds, respectively. The ± 30 pc uncertainty reflect the size of dust overdensities that can be isolated in the 3D dust cube.

We have applied the same method to revisit the distance to the Eridu cloud. The rim of the Orion-Eridanus superbubble is clearly detected at a distance around 200 pc in the dust 3D data. The Eridu cloud lies beyond this edge. Figure A.3 shows a sec-

ond dust front at a distance of 300 ± 30 pc with an inclination and extent in the sky that is compatible with that of the elongated Eridu cloud seen in H α . This distance places the cloud at an altitude of 260 pc below the Galactic plane, near the edge of the ~ 220 -pc thick H α layer of the local ISM (Nakanishi & Sofue 2016). A much larger distance would be disfavoured. The H α line velocities of the cloud are also typical of the local ISM and not of intermediate- or high-velocity clouds outside the disc. Extending the 3D dust analysis to larger distances than available in the Leike et al. (2020) cube would help confirm the distance to Eridu.

3. Models and analyses

The dust optical depth and the γ -ray intensity produced by CRs in the different clouds are strongly correlated. This is illustrated in Fig. 2 where the dust optical depth has been convolved by the *Fermi*-LAT angular resolution and non-gaseous emissions have been subtracted from the γ -ray data. The dust and γ rays both trace, to first order, the total gas column density N_{H} .

To detect neutral gas not observed in the H α data, we have used the fact that it is permeated by both CRs and dust grains. We have therefore extracted γ -ray and dust residuals between observation and the model expected from the N_{H} distribution. We have then used the spatial correlation between positive residuals found in dust and in γ rays to extract the additional gas column densities (see Sect 3.3). This additional gas corresponds to the DNM at the H-H $_2$ transition where the dense H α becomes optically thick to 21-cm line emission and CO emission is absent or too faint to trace the H $_2$ gas. The analysis results yield small amounts of dark gas in the Reticulum and North Hydrus clouds (see Sect. 4.2).

3.1. Dust model

Under the assumption of a uniform dust-to-gas mass ratio and a uniform mass emission coefficient of the grains within each cloud and gas phase, the dust optical depth linearly scales with the total gas column density N_{H} . The $\tau_{353}(l, b)$ distribution has therefore been modelled as a linear combination of the different gas contributions (N_{H} and $N_{\text{H}_{\text{DNM}}}$) with free normalisations, y , to be fitted to the data, as in Planck Collaboration et al. (2015b). A free isotropic term, y_{iso} , has been added to the model to account for the residual noise and the uncertainty in the zero level of the dust maps (Planck Collaboration et al. 2014a; Casandjian et al. 2022).

The $\tau_{353}(l, b)$ model can be expressed as :

$$\tau_{353}(l, b) = \sum_{i=1}^9 y_{\text{H}\alpha, i} N_{\text{H}\alpha, i}(l, b) + \sum_{i=1}^2 y_{\text{DNM}, i} N_{\text{H}\gamma}^{\text{DNM}, i}(l, b) + y_{\text{iso}} \quad (1)$$

where $N_{\text{H}\alpha, i}(l, b)$ denotes the nine N_{H} maps depicted in Fig. 3 and $N_{\text{H}\gamma}^{\text{DNM}, i}(l, b)$ stands for the column density in the two DNM components constructed from the γ -ray data (see Sect. 3.3).

The $y_{\text{H}\alpha, i}$ coefficients give the average values of the dust τ_{353}/N_{H} opacity in the different clouds. The $y_{\text{DNM}, i}$ parameters can probe opacity changes in the denser DNM phases.

We have degraded the optical-depth map from its original resolution of $5'$ down to $16/2'$ to match the resolution of the GASS H α survey.

The model parameters have been estimated using a least-square χ^2 minimisation. We expect the uncertainties of the model to exceed those of the dust map because of our assumption of

uniform grain distributions through the clouds and because of the limited capability of the H α data to trace the total gas. As we cannot precisely estimate the model uncertainties, we have set a fractional error of 11% that yields a reduced χ^2 value of one in the dust fit. This fraction is slightly larger than the 1% to 9% uncertainties in the τ_{353} values across this region.

3.2. Gamma-ray model

Earlier studies indicated that the Galactic CR radiating at 0.1–100 GeV have diffusion lengths much larger than typical cloud dimensions and that they propagate through the different gas phases. The observed interstellar γ -ray emission can therefore be modelled, to first order, by a linear combination of the gas column densities present in the different clouds seen along the lines of sight, in both the H α and DNM gas phases. The model also includes a contribution from the Galactic IC intensity, $I_{\text{IC}}(l, b, E)$, point sources of non-interstellar origin with individual flux spectra $S_j(E)$ and an isotropic intensity, $I_{\text{iso}}(E)$, to account for the extragalactic γ -ray background and for any residual cosmic rays misclassified as γ rays. We have verified that the soft emission from the Earth limb is not detected in the present energy range for the choice of maximum zenith angle. The γ -ray intensity, $I(l, b, E)$, in $\gamma \text{ cm}^{-2} \text{ s}^{-1} \text{ sr}^{-1} \text{ MeV}^{-1}$ in each (l, b) direction, is modelled in each energy band E as :

$$\begin{aligned} I(l, b, E) = & q_{\text{LIS}}(E) \times \left[\sum_{i=1}^9 q_{\text{H}\alpha, i}(E) N_{\text{H}\alpha, i}(l, b) \right] \\ & + q_{\text{LIS}}(E) \times \left[\sum_{i=1}^2 q_{\text{DNM}, i}(E) \tau_{353}^{\text{DNM}, i}(l, b) \right] \\ & + q_{\text{IC}}(E) I_{\text{IC}}(l, b, E) + q_{\text{iso}}(E) I_{\text{iso}}(E) \\ & + \sum_j q_{S_j}(E) S_j(E) \delta(l - l_j, b - b_j) \end{aligned} \quad (2)$$

where $N_{\text{H}\alpha, i}(l, b)$ denotes the H α column density map of each component and the extraction of the dust DNM $\tau_{353}^{\text{DNM}, i}$ maps is explained in Sect. 3.3. The q coefficients of the model are determined from fits to the *Fermi*-LAT data.

The $q_{\text{H}\alpha, i}$, q_{IC} , and q_{iso} parameters are simple normalization factors to account for possible deviations from the input spectra taken for the local gas γ -ray emissivity $q_{\text{LIS}}(E)$ and for the isotropic and IC intensities. The input q_{LIS} spectrum, in $\gamma \text{ s}^{-1} \text{ sr}^{-1} \text{ MeV}^{-1}$ per gas nucleon, was based on four years of LAT data and on the correlation found between the γ radiation and the N_{H} column densities derived from the Leiden-Argentine-Bonn (LAB) survey for a spin temperature of 140 K, at latitudes $10^\circ \leq |b| \leq 70^\circ$ (Casandjian 2015). The $q_{\text{H}\alpha, i}$ parameter in the model can therefore compensate for differences in the H α data (calibration, angular resolution, spin temperature) and for cloud-to-cloud variations in CR flux. These differences will affect the normalisations equally in all energy bands whereas a change in CR penetration inside a specific cloud will show as an energy-dependent correction, primarily a loss at energies below one GeV (Schlickeiser et al. 2016).

The source flux spectra $S_j(E)$ have been calculated with the spectral characteristics given in the 4FGL-DR3 catalogue. The $q_{S_j}(E)$ normalisations in the model allow for possible changes to these fluxes due to the longer exposure used here and to the use of a different interstellar background for source detection in the 4FGL-DR3 catalogue. The $q_{S_j}(E)$ normalisations of the sources inside the analysis region or in the peripheral band were fitted individually, except for those inside the SMC and LMC

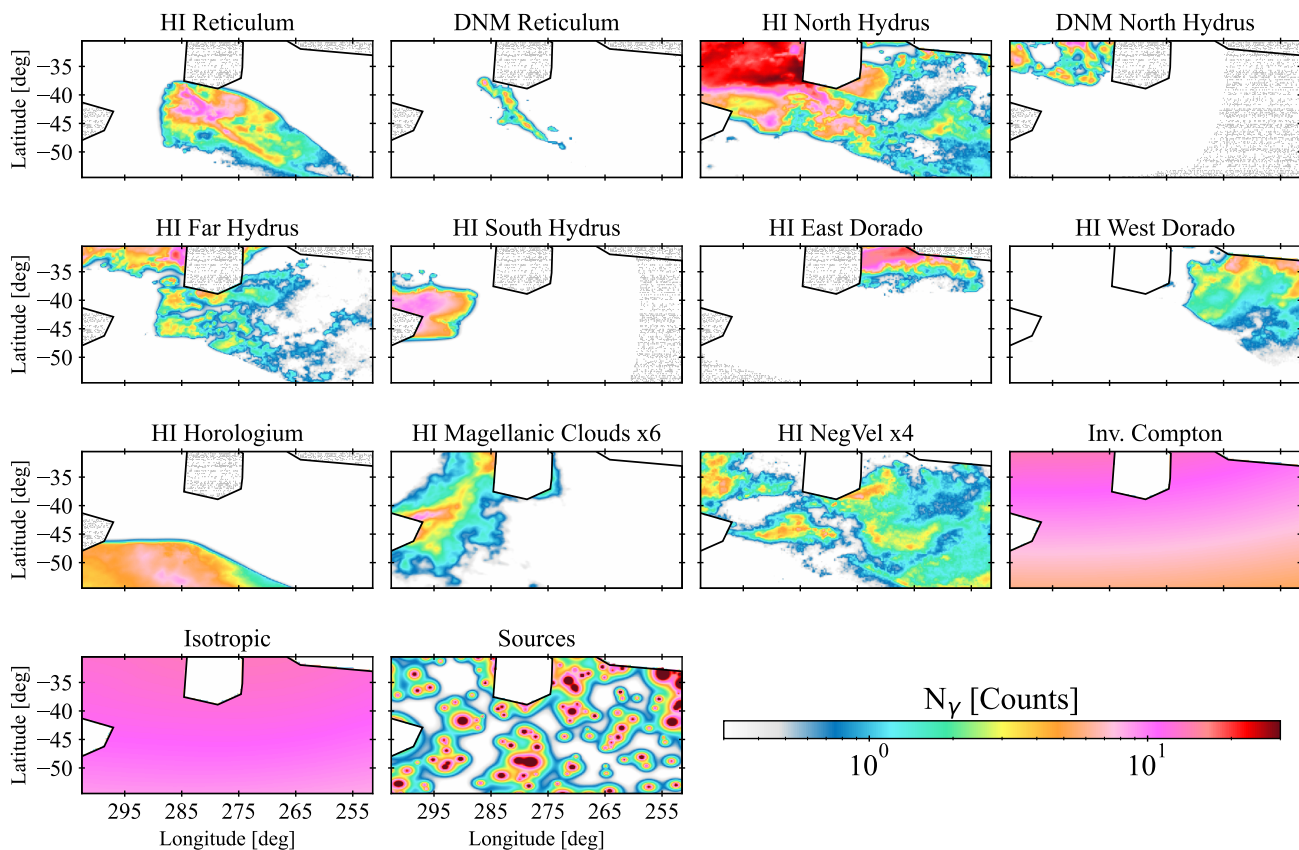


Fig. 4. Photon yields on a 0.25° -pixel grid from the main components of the γ -ray model in the 0.16–63 GeV band. The yields come from the N_{HI} column densities derived for the optically thin case in the different clouds, the dark-gas $N_{\text{H}_{\text{DNM}}}$ column densities derived from the dust optical depth, the isotropic background, the Galactic IC emission, and γ -ray point sources.

regions and those found in the lowest dust zones ($\tau_{353} < 3 \times 10^{-6}$), which were treated collectively in three separate sets with a single normalisation factor per set.

In order to compare the model with the LAT photon data in the different energy bands, we have multiplied each component map by the energy-dependent exposure and we have convolved it with the energy-dependent PSF and energy resolution. The convolution with the response functions was done for each PSF event type independently in small energy bands. We have also calculated the isotropic map for each PSF event type in the same small energy bands. We have then summed the photon count maps in energy and for the different combinations of PSF types to get the modelled count maps in the eight energy bands of the analysis for the same photon selection as in the data.

Figure 4 gives the photon yields that have been obtained in the entire energy band. It shows that the emission originating from the gas can be distinguished from the much smoother emission backgrounds and that the LAT angular resolution allows to separate the various clouds, as well as the different gas phases within the clouds. The distinct spatial distributions of the clouds and of their phases allow rather independent measurements of their individual γ -ray emissivities. On the contrary, we do not expect a firm separation of the isotropic and IC spectra across this region. We have used a binned maximum-likelihood with Poisson statistics to fit the model coefficients q to the LAT data in each of the eight energy bands and in the overall one.

3.3. Analysis iterations

In order to extract the DNM gas present in both the dust and γ -ray data, we have iteratively coupled the γ -ray and dust models. We have started by fitting independently the dust optical depth and the γ -ray data according to Eqs. 1 and 2 with only the HI maps as gaseous components and with ancillary (other than gas) components. We have then built maps of positive residuals (see how below) between the data (dust or γ rays) and the best-fit contributions of the model components. We have separated these excesses into two DNM maps according to their location, one in the Reticulum cloud and the other one in the North Hydrus area.

The next loops in the iterative process provide the DNM templates estimated from the dust to the γ -ray model (τ_{353}^{DNM} in Eq. 2) and conversely provide the DNM column density maps derived from the γ rays to the dust model ($N_{\text{H}}^{\text{DNM}}(l, b)$ in Eq. 1). We have repeated the iteration between the γ -ray and dust models until the log-likelihood of the fit to γ -ray data saturates.

The estimates of the q and γ model coefficients and of the DNM templates improve at each iteration since there is less and less need for the other components, in particular the HI ones, to compensate for the missing gas. They can still miss gas at some level because the DNM maps provided by the γ rays or dust emission have limitations (e.g., dust emissivity variations, limited γ -ray sensitivity).

Care must be taken in the extraction of the positive residuals because of the noise around zero. A simple cut at zero would induce an offset bias, so we have de-noised the residual maps using the multi-resolution support method implemented in the MR

filter software (Starck & Pierre 1998). For the dust residuals, we have used a multi-resolution thresholding filter, with six scales in the B-spline-wavelet transform (à trous algorithm), Gaussian noise and a $2\text{-}\sigma$ threshold to filter. For the γ -ray residuals, we have used the photon residual map obtained in the 0.16–63 GeV band and we have filtered it with six wavelet scales, Poisson noise, and a $2\text{-}\sigma$ threshold. The stability of the iterative analysis and the results of the dust and γ -ray fits are discussed in the following section.

4. Results

Before presenting the γ -ray emissivity spectra obtained in the Reticulum cloud in Sect. 4.4, we discuss how the fits to the γ -ray and dust data improve with optical depth corrections to the N_{HI} column densities (Sect. 4.1) and with the addition of DNM gas templates (Sect. 4.2). We also assess the robustness of the best-fit models with jackknife tests in Sect. 4.3.

4.1. H I optical depth correction

We don't know the exact level of H I opacity in the different clouds. It induces systematic uncertainties in the N_{HI} column densities, hence on the H I contributions to the γ -ray and dust models. Nguyen et al. (2019) showed that a uniform isothermal correction of the H I emission spectra across a cloud provides a good approximation to the more precise N_{HI} column densities determined from the combination of emission and absorption H I spectra. The difference on a pixel-by-pixel basis can reach 25%, but the mean difference between the two N_{HI} distributions is small ($\lesssim 1\%$) and the standard deviation is better than 10%. We have therefore produced the dust and γ -ray models for a wide range of optical depth corrections, from a rather optically thick case ($T_{\text{S}} = 100$ K) to the optically thin case which yields the minimum amount of gas in the cloud. Even though the spin temperature is uniform, the H I opacity correction depends on the H I temperature recorded in each direction and velocity channel, so it varies across the cloud and modifies the N_{HI} spatial distribution of a cloud.

Figure 5 shows that the goodness of the γ -ray fit (after the DNM iteration) significantly improves as we increase the H I spin temperature. The N_{HI} maps best match the spatial structure of the γ -ray flux emerging from the atomic gas for $T_{\text{S}} \gtrsim 300$ K, therefore for small H I opacities. Given the saturation of the log-likelihood ratio towards the optically thin case, we will present the analysis results obtained for this thin case in the rest of the paper, unless otherwise mentioned. The residual maps between the γ -ray data and best-fit model show that using the same T_{S} for all the clouds can reproduce the γ -ray data without any significantly deviant cloud.

As the spin temperature T_{S} increases, the optical depth correction and N_{HI} column densities decrease, and the γ -ray emissivity q_{HI} and dust opacity y_{HI} of the H I clouds increase. They do so respectively by 4–11% and 3–7% as the spin temperature rises over the entire range, from 100 K to optically thin conditions. H I optical depth corrections have therefore a small effect in this region because the clouds are not massive.

4.2. DNM detection

In order to check for the presence of DNM gas not traced by H I line intensities, we have first performed the dust and γ -ray fits with only the N_{HI} maps as gaseous components. The residuals

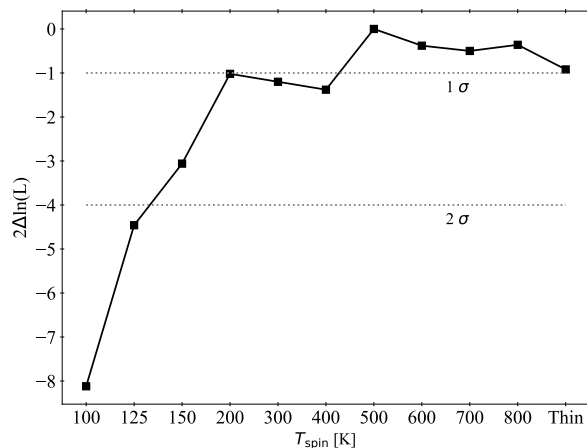


Fig. 5. Evolution of the log-likelihood ratio of the γ -ray fit in the 0.16–63 GeV band as a function of the H I spin temperature used to calculate the N_{HI} column densities in the clouds.

are displayed in the upper panels of Fig. 6. Positive residuals indicate that the data exceed the model predictions. Coincident excesses are seen in dust and in γ rays even though the two fits are independent. They cross the region in diagonal, from the North Hydrus cloud (upper left corner) down along the Reticulum filament. A coincident increase in CR density and in dust opacity is very improbable. Hadronic CR interactions with dust grains produce undetectable γ -ray emission (Grenier et al. 2005), so this correlated excess is likely due to additional gas. The distribution of positive γ -ray excesses along the Reticulum cloud is sparse, but the large extent of negative (blue) excesses across the whole analysis region indicates that the γ -ray fit has unduly pushed the H I emissivities of the clouds upward to compensate for some missing gas.

The DNM gas column density is built by correlating and filtering the excess dust and γ -ray signals in the iteration between both model fits (see Sect. 3.3). We have built separate DNM maps for the North Hydrus and Reticulum clouds. Adding them improves the fits quality (see the middle maps of Fig. 6). A log-likelihood ratio increase by 161 between the γ -ray fits with and without the DNM templates implies a very significant DNM detection. The spectrum of the γ -ray emission associated with both DNM components is consistent with that found in the H I gas phase over the whole energy range (see below). This gives further support to a gaseous origin of the γ -ray emission in the DNM structures.

Positive residuals remain in the final dust fit, even after the addition of the DNM maps. Those in spatial coincidence with the DNM phase are partially due to the non-linear increase in dust opacity as the gas density rises towards the dense molecular phase (Remy et al. 2017). They also result from the limited γ -ray photon statistics that limit the residual filtering precision to provide a DNM template to the dust fit. The negative and positive residuals seen at longitudes $l < 270^\circ$ reflect difficulties in separating the dust emission from other sub-mm emissions and also difficulties in determining its optical depth in these very faint zones (Planck Collaboration et al. 2014a; Irfan et al. 2019, and references therein). These regions were excluded from the DNM analysis.

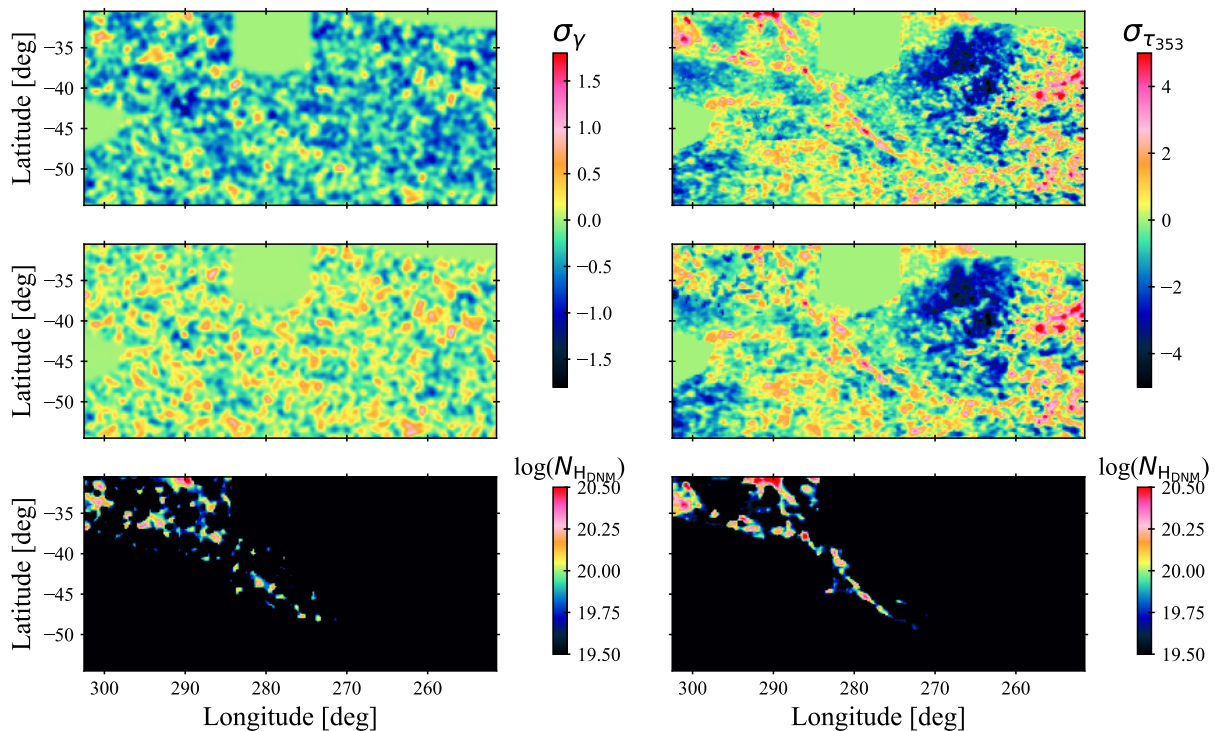


Fig. 6. Residual maps (data minus best-fit model, in sigma units) in γ -ray counts in the 0.16–63 GeV band (σ_γ) and in dust optical depth ($\sigma_{\tau_{353}}$), obtained when including different sets of gaseous components in the models: without (*top*) and with (*middle*) the DNM components in addition to the H I templates. The $N_{\text{H, DNM}}$ column-density maps (*bottom*) extracted from the γ -ray residuals (*left*) and from dust residuals (*right*) are shown in the bottom row. The models are derived for an H I at the optically thin case.

4.3. Best fits and jackknife tests

525 The best dust and γ -ray fits with the models described by Eqs. 1 and 2 include the nine H I and two DNM maps for the gaseous components. Table 1 gives the best-fit coefficients obtained for the H I and DNM phases of the main Reticulum and North Hydrus clouds. The results found for the other small local clouds will be discussed in a subsequent paper (their emissivity spectra are rather close to the q_{LIS} expectation). We focus here on the Reticulum filament to compare it with the Eridu one and we include the emissivity measurement in the North Hydrus cloud as it partially overlaps the northern end of Reticulum. The γ -ray emissivities are given in each of the eight energy bands and for the whole 0.16–63 GeV band.

530 The final iteration of the dust and γ -ray fits leads to the residual maps presented in the middle panels of Fig. 6. The γ -ray residuals are small and randomly distributed, so our linear model provides an excellent statistical fit to the γ -ray data in the 0.16–63 GeV energy band across the whole region. The same conclusion is reached in the eight separate energy bands that are not shown here.

545 The statistical errors on the best-fit coefficients are inferred from the information matrix of the fits (Strong 1985). They include the correlation between parameters. They are generally small (2–9% for the H I gas γ -ray emissivities, 15% and 10% for DNM emissivities for Ret and HyiN, 13% for q_{IC} , 9% for q_{iso} , 0.4–1.3% for the H I dust opacities, 8% and 3% for $y_{\text{DNM, Ret}}$ and $y_{\text{DNM, HyiN}}$ and 2% for y_{iso}) because the clouds are spatially well resolved in the analysis and because tight correlations exist between the gas, dust and γ -ray maps (see Fig. 2).

555 We have also checked the magnitude of potential systematic uncertainties due to the linear-combination approximation underlying the models. In order to evaluate the impact of possible spatial changes in the model parameters and/or in the mean level of H I self absorption, we have repeated the last iteration of the dust and γ -ray fits a thousand times over random subsets of the analysis region, each time masking out 20% of the pixels with 1-degree-wide randomly selected squares. In γ rays, the jackknife tests have been performed for the total 0.16–63 GeV energy band and for each of the eight bands. Figure 7 shows the distribution obtained for the best-fit coefficients relating to the Reticulum and North Hydrus clouds and to the large-scale IC and isotropic components. The Gaussian-like distributions indicate that the emissivities and opacities presented in Table 1 are statistically stable and not driven by subset regions in each cloud complex. The standard deviations found in the jackknife distributions amount to 1–6% for the H I gas γ -ray emissivities, 9% and 4% for DNM emissivities for Ret and HyiN, 8% for q_{IC} , 5% for q_{iso} , 0.6–3% for the H I dust opacities, 12% and 3% for $y_{\text{DNM, Ret}}$ and $y_{\text{DNM, HyiN}}$ and 4% for y_{iso} . Both statistical errors (1σ) and systematic uncertainties (jackknife standard deviations) are given in Table 1. We have quadratically added them to construct the final uncertainties on the q and y coefficients.

570 Figure 8 shows the stability with γ -ray energy of the best-fit coefficients relating to the Reticulum and North Hydrus clouds and to the IC and isotropic intensities. We find no significant deviation with respect to the average coefficient fitted for the entire energy band (dashed lines). This implies that the H I and DNM gas emissivity spectra in the two clouds have the same shape

Table 1. The first part of the table gives the best-fit dust opacities obtained in the HI and DNM phases of the Reticulum and North Hydrus clouds, as well as the isotropic term. The second part of the table lists the best-fit γ -ray emissivities obtained per gas nucleon in the HI and DNM phases of the same clouds, in eight energy bands and in the overall 0.16–63 GeV band. The first uncertainties are statistical (1σ) and the second give the standard deviations obtained in the jackknife fits.

$\gamma_{\text{HI Ret}}$ [10^{-27} cm^2]	$\gamma_{\text{DNM Ret}}$ [10^{-27} cm^2]	$\gamma_{\text{HI HyiN}}$ [10^{-27} cm^2]	$\gamma_{\text{DNM HyiN}}$ [10^{-27} cm^2]	γ_{iso} [10^{-7}]
$8.91 \pm 0.07 \pm 0.12$	$5.05 \pm 0.40 \pm 0.58$	$8.68 \pm 0.03 \pm 0.05$	$14.90 \pm 0.42 \pm 0.44$	$2.79 \pm 0.06 \pm 0.12$

Energy Band [MeV]	$q_{\text{HI Ret}}$	$q_{\text{DNM Ret}}$ [10^{26} cm^{-2}]	$q_{\text{HI HyiN}}$	$q_{\text{DNM HyiN}}$ [10^{26} cm^{-2}]
$10^{2.2} - 10^{2.4}$	$1.56 \pm 0.23 \pm 0.09$	$0.21 \pm 1.22 \pm 0.28$	$1.17 \pm 0.15 \pm 0.04$	$0.78 \pm 0.52 \pm 0.18$
$10^{2.4} - 10^{2.6}$	$1.27 \pm 0.13 \pm 0.07$	$0.74 \pm 0.61 \pm 0.26$	$1.10 \pm 0.08 \pm 0.03$	$0.61 \pm 0.26 \pm 0.09$
$10^{2.6} - 10^{2.8}$	$0.98 \pm 0.10 \pm 0.06$	$0.85 \pm 0.41 \pm 0.20$	$1.02 \pm 0.06 \pm 0.02$	$0.65 \pm 0.17 \pm 0.06$
$10^{2.8} - 10^{3.0}$	$1.16 \pm 0.08 \pm 0.04$	$0.85 \pm 0.29 \pm 0.12$	$1.04 \pm 0.04 \pm 0.02$	$0.77 \pm 0.12 \pm 0.04$
$10^{3.0} - 10^{3.2}$	$0.98 \pm 0.07 \pm 0.04$	$0.85 \pm 0.27 \pm 0.14$	$1.03 \pm 0.04 \pm 0.01$	$0.64 \pm 0.11 \pm 0.05$
$10^{3.2} - 10^{3.6}$	$0.98 \pm 0.07 \pm 0.04$	$1.46 \pm 0.26 \pm 0.11$	$1.00 \pm 0.04 \pm 0.02$	$0.70 \pm 0.11 \pm 0.04$
$10^{3.6} - 10^{4.0}$	$1.02 \pm 0.16 \pm 0.09$	$1.20 \pm 0.55 \pm 0.32$	$1.12 \pm 0.09 \pm 0.03$	$0.98 \pm 0.23 \pm 0.09$
$10^{4.0} - 10^{4.8}$	$0.93 \pm 0.38 \pm 0.18$	$0.05 \pm 1.14 \pm 0.25$	$1.13 \pm 0.21 \pm 0.06$	$1.18 \pm 0.55 \pm 0.17$
$10^{2.2} - 10^{4.8}$	$1.11 \pm 0.04 \pm 0.03$	$0.99 \pm 0.15 \pm 0.09$	$1.05 \pm 0.02 \pm 0.01$	$0.75 \pm 0.07 \pm 0.03$

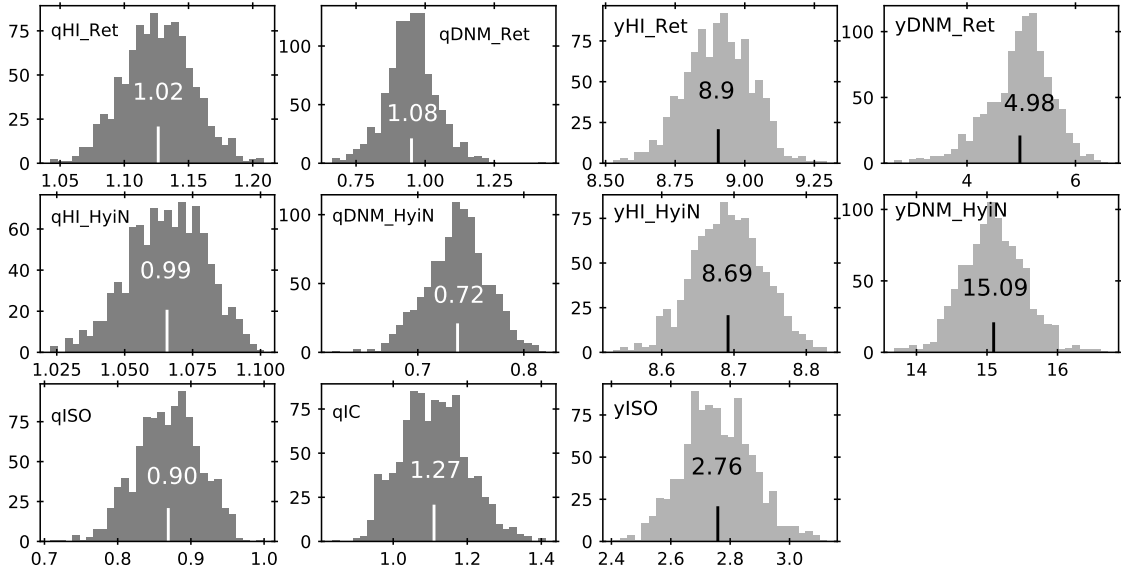


Fig. 7. Distributions of the best-fit coefficients obtained in the thousand jackknife fits to the 0.16–63 GeV γ -ray data (two left columns) and dust data (two right columns) for the optically-thin HI case. The vertical lines and overlaid numbers give the mean values of the distributions. The units are 10^{26} cm^{-2} for q_{DNM} , 10^{-27} cm^2 for γ_{HI} and γ_{DNM} , and 10^{-7} for γ_{iso} . $q_{\text{HI},i}$, q_{IC} and q_{iso} are dimensionless normalisation factors.

as the average $q_{\text{LIS}}(E)$ spectrum measured in the local ISM. We further discuss their relative normalisation with respect to q_{LIS} in the next section.

585 Figure 8 and the value of the relative intensity ratio $q_{\text{IC}} = 1.18 \pm 0.15$ in the whole energy band further show that the IC spectrum detected in these directions of the sky is fully con-

sistent in shape and in intensity with the GALPROP prediction based on the complex evolution of the interstellar radiation field and of the CR lepton spectra across the Milky Way. The isotropic spectrum found in this small region of the sky is also close to the larger-scale estimate obtained between 10° and 60°

590

in latitude³. The relative intensity ratio is $q_{\text{iso}} = 0.84 \pm 0.08$ in the 0.16–63 GeV energy band. The interstellar foregrounds are faint enough to separate the IC and isotropic components despite rather similar spatial distributions across the analysis region (see Fig. 3).

Planck Collaboration et al. (2014a) and Remy et al. (2017) have found marked gradients in dust opacity across the sky. These variations reflect a systematic opacity increase as the gas becomes denser and the grains evolve in size and chemistry (Remy et al. 2017; Ysard et al. 2019, and references therein). Diffuse atomic cirrus at high latitudes exhibit low opacities around a mean value of $(7.0 \pm 2.0) \times 10^{-27} \text{ cm}^2$ (Planck Collaboration et al. 2014a) or $(7.1 \pm 0.6) \times 10^{-27} \text{ cm}^2$ (Planck Collaboration et al. 2014b)) whereas larger values ranging from 10×10^{-27} to $16 \times 10^{-27} \text{ cm}^2$ are found in the denser atomic envelopes of nearby clouds (Remy et al. 2017), and values from 15×10^{-27} to $17 \times 10^{-27} \text{ cm}^2$ characterise the DNM phase (Planck Collaboration et al. 2015b; Remy et al. 2017; Joubaud et al. 2020). Dust opacities further increase in the dense, CO-bright, molecular phase, reaching values as high as $60 \times 10^{-27} \text{ cm}^2$ (Remy et al. 2017). The dust opacities we have found in the H I phase of the Reticulum and North Hydrus clouds are consistent with this trend. They are close to the low diffuse cirrus values and, in particular, to the dust opacity of $(6.4 \pm 0.1) \times 10^{-27} \text{ cm}^2$ measured in the Eridu filament (Joubaud et al. 2020). The dust opacity we have found in the DNM phase of the North Hydrus cloud fully agrees with other estimates. We caution the reader that the unusually low γ_{DNM} value found for the Reticulum cloud may not be reliable because of the difficulty discussed in Sect. 4.2 to fully extract the $N_{\text{H, DNM}}$ column density along Reticulum from the γ -ray data. The final dust residual map in Fig. 6 shows a leftover positive excess along the Reticulum filament. Taking this excess into account would increase the γ_{DNM} value.

4.4. Cosmic rays in the Reticulum and Eridu filaments

Figure 9 compares the γ -ray emissivity spectrum we have found per gas atom in the Reticulum filament to that in the similar filament of Eridu and in the more massive North Hydrus cloud. We also compare it to the average q_{LIS} spectrum measured in the local ISM, at latitudes between 10° and 70° across the sky (Casandjian 2015). We compare them for the spin temperatures that best fitted their respective γ -ray data, therefore at $T_{\text{S}} = 100 \text{ K}$ for Eridu, 140 K for q_{LIS} , and for optically thin H I for Reticulum and North Hydrus. The results indicate that the CR population that permeates the H I and DNM phases of the Reticulum and North Hydrus clouds has the same energy distribution and same flux as the average population in the local ISM. This population applies to the 100-150-pc-long sector subtended by the Reticulum and North Hydrus clouds along the rim of the Local Valley. As expected for the low N_{HI} column densities characterising these clouds, we find no significant spectral deviation at low energies that would mark a loss or concentration of CRs when penetrating into the denser DNM clumps (Schlickeiser et al. 2016; Bustard & Zweibel 2021).

Figure 9 illustrates that the CR flux in the Reticulum filament is 1.57 ± 0.09 times that pervading the similar Eridu filament. This discrepancy decreases to 1.51 ± 0.09 if we compare them for the same H I spin temperature of 100 K , to 1.38 ± 0.08 if we assume them both optically thin. The minimum ratio is 1.32 ± 0.08 if Eridu is optically thin and Reticulum thicker with $T_{\text{S}} = 100 \text{ K}$, a case yielding a worse γ -ray fit to the data for both clouds. The

loss mechanism that affects CRs in Eridu should be energy independent to preserve the same emissivity spectral shape in the three clouds across the entire energy band.

H_α hydrogen recombination line emission has been recorded along the Reticulum cloud in the Southern H α Sky Survey Atlas (Gaustad et al. 2001), suggesting that the cloud be a cooling filament or cooling shell surrounded by recombining warm ionised gas. The cross correlation between dust and γ rays detects any gas in addition to the H I gas, regardless of its chemical or ionisation state. The inferred DNM column densities are dominated by the dense CNM and diffuse H_2 , but they also include the much more dilute ionised gas. The γ -ray emissivity we have obtained in the cloud H I phase is therefore not strongly biased by untraced ionised gas surrounding it. As a further check, we have used the H_α map reprocessed by Finkbeiner (2003) as an additional gas template into the dust and γ -ray fits, even though the H_α emission measure does not scale with the N_{H} column density, but it integrates the product of the electron and ion densities along the line of sight, $\text{EM}_\alpha \propto \int_{\text{LOS}} n_e n_{\text{H}^+} dl$. With this crude additional template, the Reticulum γ -ray emissivity remains consistent with the local-ISM q_{LIS} average and is still 1.51 ± 0.11 times larger than in Eridu over the whole energy band for the choice of best fitting spin temperatures.

Assuming the same CR flux pervades the recombining and neutral hydrogen, the γ -ray signal related to the H_α template yields N_{H^+} column densities around 10^{19} cm^{-2} in Reticulum, an order of magnitude below those in the neutral phase. Column densities of the Galactic warm ionised medium, integrated to the Reticulum distance, are also an order of magnitude below the N_{HI} ones and would not spatially correlate with the H I clouds to impact the values of the q_{HI} emissivities (Gaensler et al. 2008).

5. Discussion

The Reticulum and Eridu clouds are both light and filamentary clouds, with ordered magnetic fields on a few parsec scale, and a large inclination with respect to the Galactic plane. Yet, the first has $57 \pm 9\%$ more CRs than the second. In the next sections, we try to characterise the dynamical and magnetic states of those clouds which can influence CR transport, namely the diffusion coefficient in the self-confinement, streaming mode on the one hand, and the dispersion in velocity and in magnetic bending on the other hand. In order to constrain these transport modes we derive the gas volume density and the B_{sky} magnetic-field strength from observations.

5.1. Gas densities in the atomic phase

Given the elongated aspect of the Reticulum and Eridu filaments, we have used two different assumptions for the cloud geometry, namely a cylindrical fiber or a shell seen edge on, in order to bracket its unknown depth along the line-of-sight (LOS) and to estimate the H I gas volume density, n_{HI} . In the fiber-like configuration, the LOS depth is close to the observed width in the plane of the sky. In order to estimate the latter, we have used the Gaussian FWHM widths of the N_{HI} column-density profiles observed along cuts perpendicular to the filament axis. Figure 10 shows the eight and seven cuts respectively chosen along the Reticulum and Eridu filaments. The resulting depths are shown in the middle panel of Fig. 11 with an uncertainty reflecting that in cloud distance. The mean depth and rms dispersion are $5.0 \pm 0.6 \text{ pc}$ in Reticulum and $10.5 \pm 1.0 \text{ pc}$ in Eridu. In the shell shaped configuration, the LOS depth is closer to half the chord length through

³ <http://fermi.gsfc.nasa.gov/ssc/data/access/lat/BackgroundModels.html>

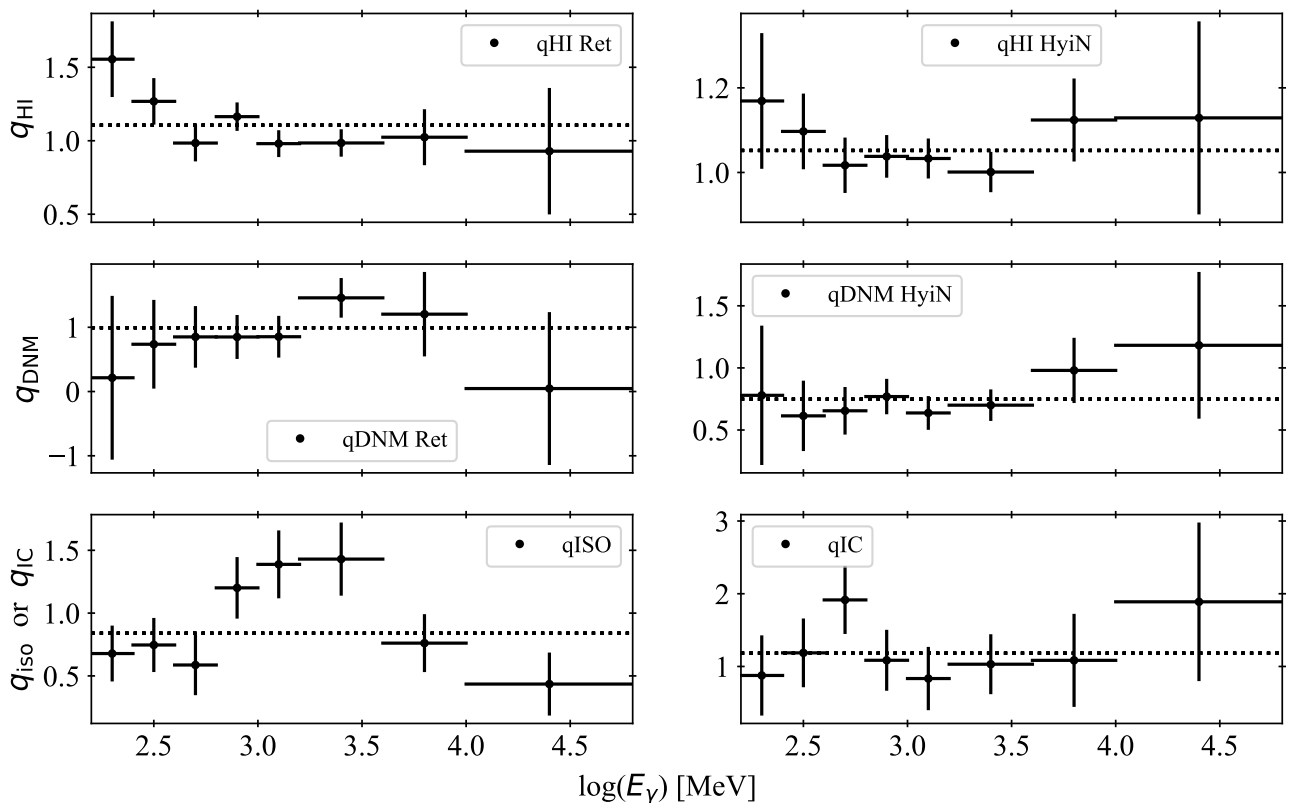


Fig. 8. Spectral evolution, relative to the local interstellar spectrum q_{LIS} , of the γ -ray emissivities found for the HI and DNM phases of the Reticulum and North Hydrus clouds (top and middle panels). Spectral evolution of the isotropic and IC intensities found in the region relative to the input spectra (bottom panel). $q_{\text{DNM}}/q_{\text{LIS}}$ is given in 10^{26} cm^{-2} . The results are shown for the optically thin HI case. The error bars combine the statistical and systematic uncertainties.

the thick shell. Given the mean widths measured above and assuming a shell radius of curvature of about 100 pc, we estimate the LOS depths to roughly be 20 pc for Reticulum and 30 pc for Eridu. These limits are represented as triangles in the middle plot of Fig. 11. They provide reasonable upper limits to the cloud depth.

We have derived the mean gas volume density in a 1-degree-wide square around the peak of each N_{HI} profile cutting perpendicularly through the Reticulum and Eridu filaments. The results are shown in the bottom plot of Fig. 11. The shell-like geometry provides approximate lower limits to the gas densities.

Figure 11 illustrates that the larger N_{HI} column densities recorded in the Eridu filament are likely due to longer LOS depths and that the Reticulum filament has denser substructures than Eridu. In both geometries, the density estimates along Reticulum are typical of the CNM and they are consistent with the detection of similar $N_{\text{H,DNM}}$ column densities in the DNM. For both geometries, the Eridu volume densities are more typical of the unstable lukewarm neutral medium (LNM) that transitions between the stable WNM and CNM phases. They indicate that CNM clumps are likely present inside both clouds, but should be more numerous and densely packed in Reticulum than in Eridu.

5.2. Self-confined diffusion

The ambient magnetic field mediates the collisionless interaction between CRs and the thermal gas. CRs stream along magnetic field lines and scatter off small-scale magnetic fluctuations with sizes close to their gyroradius, thereby reducing their effective propagation speed. Whereas very high energy CRs are likely scattered by interstellar magnetohydrodynamic (MHD) turbulence, the lower-energy CRs that we sample here in γ rays are more likely scattering off Alfvén waves that are excited by the CRs themselves via the resonant streaming instability (Kulsrud & Pearce 1969). In this self-confinement scenario, CRs with a bulk drift speed v_D greater than the ion Alfvénic speed $v_A^{\text{ion}} = B/\sqrt{4\pi\rho_i}$ can excite Alfvén waves with the growth rate (Kulsrud & Cesarsky 1971) :

$$\Gamma_{\text{grow}}(k) = \frac{\pi^{3/2}}{2} \frac{e}{c} (v_D - v_A^{\text{ion}}) \frac{1}{\sqrt{\rho_i}} \sum_j \frac{\alpha_j - 3}{\alpha_j - 2} Z_j n_j(\mathcal{R}_j > \frac{B}{k}) \quad (3)$$

where ρ_i notes the mass density of interstellar gas ions, B is the mean field strength, and we add the contributions of different CR nuclei with charge $Z_j e$, rigidity \mathcal{R}_j , and volume number density spectrum $n_j(\mathcal{R})$ with a power-law spectral index α_j in the range of interest. The CR density is integrated in rigidity above the threshold corresponding to the resonance condition $\mathcal{R}_j = B/k$. We have considered the CR spectra with $Z_j \leq 28$ incident on the heliopause (Boschini et al. 2020), which correspond to the q_{LIS}

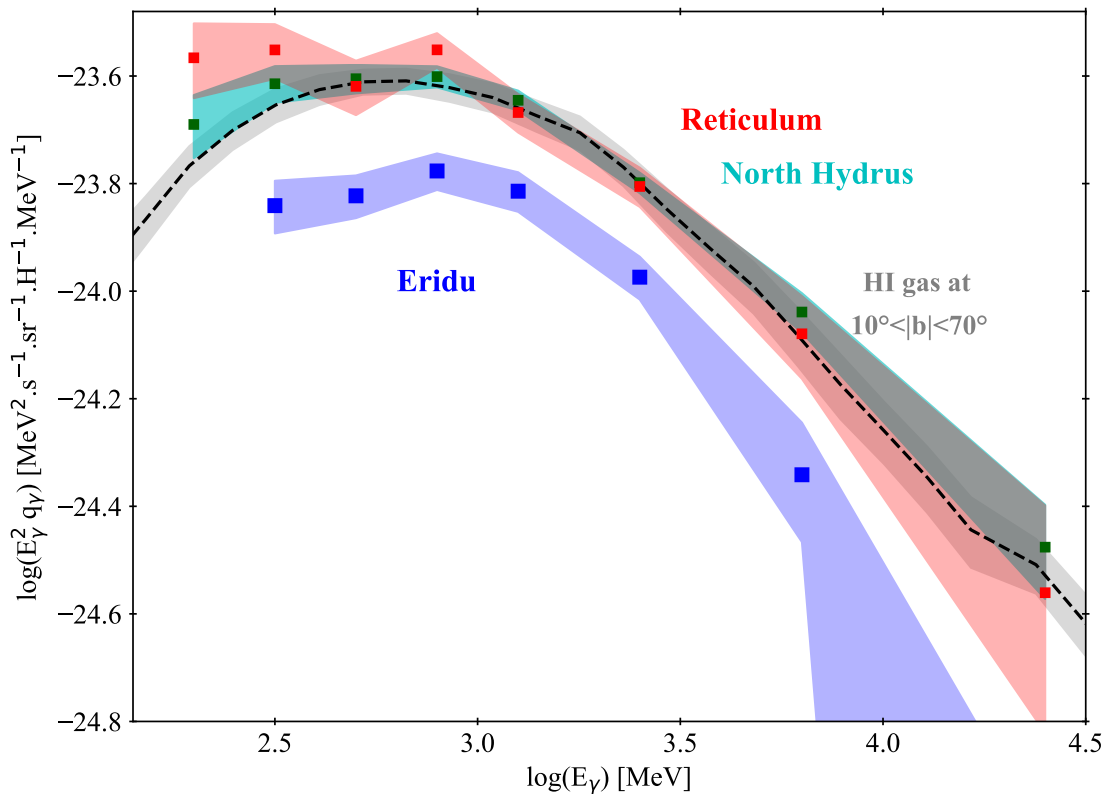


Fig. 9. Spectral evolution of the γ -ray emissivities per gas nucleon in the Eridu (blue), Reticulum (red), and North Hydrus (cyan) clouds. The grey curve gives the average q_{LIS} emissivity measured at latitudes $10^\circ \leq |b| \leq 70^\circ$ (Casandjian 2015). The emissivities are shown for the HI optical-depth correction that best fits the γ -ray data ($T_s = 100$ K for Eridu, 140 K for q_{LIS} , and optically thin for the others). The shaded bands include the statistical and systematic uncertainties.

emissivity discussed above. We have integrated the spectra over 1 GV in rigidity and fitted the α_j spectral indices in the 1–20 GV range that contributes most to the growth rate.

The net drift with respect to the Alfvén wave frame ($v_D - v_A^{\text{ion}}$) can be written as a diffusive flux (Jiang & Oh 2018; Bustard & Zweibel 2021) :

$$v_D - v_A^{\text{ion}} = \frac{\kappa_{\parallel}}{\ell_{\text{cr}}} \quad (4)$$

with the characteristic length for a change in CR flux, ℓ_{cr} , and the diffusion coefficient κ_{\parallel} parallel to the mean B field.

Wave amplitudes and scattering rates are reduced by wave damping processes that depend on the properties of the background MHD turbulence and on ambient plasma conditions. The main damping mechanism in the neutral gas phases that we have probed in γ rays is the ion-neutral one. Following Hopkins et al. (2021) and Xu & Lazarian (2022), we have checked that the linear Landau, nonlinear Landau, and turbulent damping rates are two to three orders of magnitude smaller than the ion-neutral one in the typical environments of the Reticulum and Eridu clouds.

Momentum exchange between the ions and hydrogen or helium neutral atoms, all with the same equilibrium temperature T , leads to the damping rate given by Soler et al. (2016) :

$$\Gamma_{\text{in,S16}} = \sqrt{\frac{32 k_B T}{9\pi A_i m_{\text{H}}}} n_{\text{HI}} \left[\sigma_{\text{iH}} \sqrt{\frac{1}{1 + A_i}} + \sigma_{\text{iHe}} \frac{x_{\text{He}}}{x_{\text{HI}}} \sqrt{\frac{A_{\text{He}}}{A_i + A_{\text{He}}}} \right]$$

Article number, page 12 of 25

$$(5)$$

where k_B is the Boltzmann constant, m_{H} is the H atom mass, x_{HI} and x_{He} are the neutral hydrogen and helium abundance by number, relative to the total number of hydrogen nucleons, and $A_{\text{He}}=4$ is the atomic weight of helium. The ion-neutral momentum-transfer cross sections are $\sigma_{\text{iH}} = 10^{-14} \text{ cm}^2$ and $\sigma_{\text{iHe}} = 3 \times 10^{-15} \text{ cm}^2$ from Vranjes & Krstić (2013).

The ion abundance, x_i , and mean ion atomic weight, A_i , vary with the gas state (Draine 2011). The predominant form of ions gradually varies from H^+ in the WNM to about half H^+ and half C^+ in the CNM and their abundance decreases by two orders of magnitude, down from about 2% in the WNM. We have used the heating, cooling, chemistry, and ionisation model of Kim et al. (2023) to calculate the equilibrium gas temperature T , ion abundance x_i , and average ion weight A_i as a function of the gas densities observed in the neutral phase (n_{HI}) and for the local interstellar conditions ($x_{\text{He}} = 0.1$, $x_{\text{C}} = 1.6 \times 10^{-4}$ in the gas phase, solar metallicity, primary CR ionisation rate of $2 \times 10^{-16} \text{ s}^{-1}$, and local FUV intensity). This allowed us to estimate the damping rates of Alfvén waves in different points along both clouds.

Another formalism for ion-neutral damping is given by Kulsrud & Pearce (1969) :

$$\Gamma_{\text{in,K69}} = \frac{1}{2} \frac{n_n m_n}{m_n + m_i} \langle \sigma v \rangle_{\text{in}} \quad (6)$$

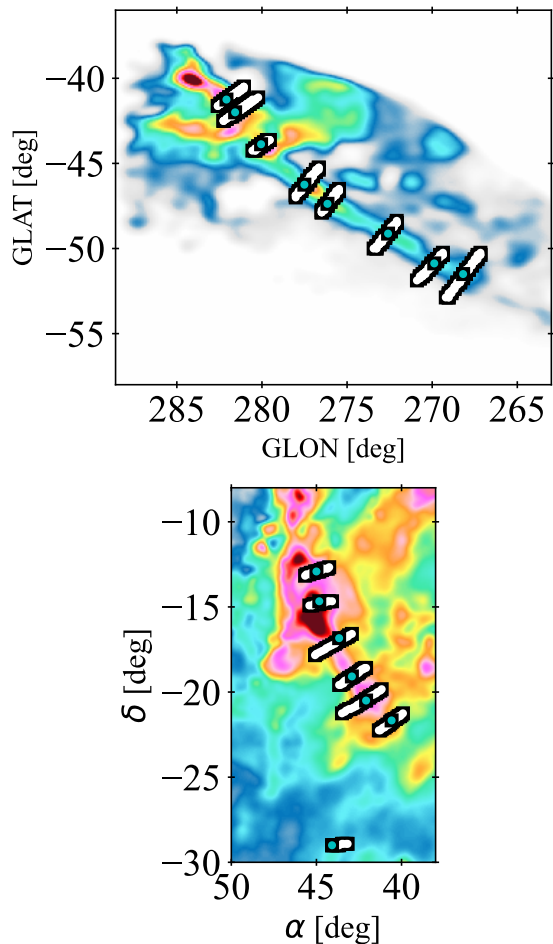


Fig. 10. N_{HI} maps of the Reticulum (top) and Eridu (bottom) filaments, smoothed by a Gaussian kernel of 0.3° and 0.2° , respectively, to highlight the cloud edges. The white lines show the perpendicular cuts used to estimate the cloud widths. The cyan squares show $1^\circ \times 1^\circ$ squares adopted to estimate gas volume densities, B_{sky} field strengths and parallel diffusion coefficients κ_{\parallel} along the filament core.

where n_n is the neutral number density, m_n is the mean mass of neutrals, and $m_i = A_i m_{\text{H}}$ is the mean mass of ions. The ion-neutral momentum transfer rates are $\langle \sigma v \rangle_{\text{in}} = 3.25 \times 10^{-9} \text{ cm}^3 \text{ s}^{-1}$ for collisions between H and H^+ , $2.39 \times 10^{-9} \text{ cm}^3 \text{ s}^{-1}$ between H and C^+ , and $1.42 \times 10^{-9} \text{ cm}^3 \text{ s}^{-1}$ between He and H^+ (from Table 2.1 of [Draine \(2011\)](#)). This formulation does not depend on the gas temperature.

We have adopted the [Soler et al. \(2016\)](#) damping rate as the baseline for this work. Assuming a uniform LOS depth equal to the mean value of the estimates shown in Fig. 11 in each geometry, we find rather uniform damping rates close to $6 \times 10^{-9} \text{ s}^{-1}$ across both clouds, in both geometries. We note that the two damping rate formulations yield comparable rates across the clouds in the shell geometry, but the [Kulsrud & Pearce \(1969\)](#) one yields a few times larger rates than the [Soler et al. \(2016\)](#) ones in the denser fiber geometry (one to three times larger along Eridu and one to five times larger along Reticulum). This difference is due to the drop in temperature and increase in ion atomic weight in the denser fiber gas in Eq. 5.

A quasi-steady state is reached when the growth rate Γ_{grow} of the gyro-resonant waves is balanced by the damping rate Γ_{in} ,

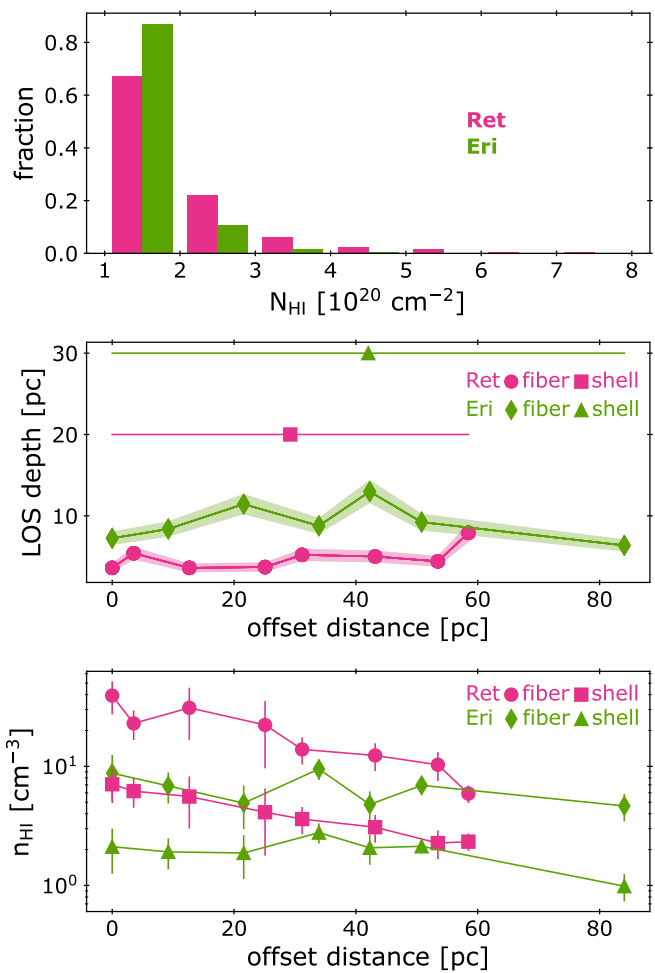


Fig. 11. Distributions of HI column densities (top), LOS depths (middle), and mean HI volume densities (bottom) in the Reticulum (magenta) and Eridu (green) clouds. The offset distance is the separation between a $1^\circ \times 1^\circ$ square along a filament and the first one (of largest latitude or declination). The different symbols refer to the fiber-like or shell-like cloud geometry. The LOS depth shading is due to the distance uncertainty whereas the data points and error bars in volume density respectively give the mean value in each ~ 5 pc-wide square and the rms dispersion at 0.5 – 0.7 pc scale within each square.

giving a parallel diffusion coefficient:

$$\kappa_{\parallel} = \frac{2}{\pi^{3/2}} \frac{c}{e} \Gamma_{\text{in}} \ell_{\text{cr}} \frac{\sqrt{\rho_i}}{\sum_j \left(\frac{\alpha_j - 3}{\alpha_j - 2} \right) Z_j n_j (\mathcal{R}_j > \frac{B}{k})} \propto T^{1/2} x_i^{1/2} n_{\text{HI}}^{3/2} \ell_{\text{cr}} \quad (7)$$

We note that the diffusion coefficient does not depend on the mean magnetic field strength under this steady-state assumption. The distance that separates the Reticulum and Eridu filaments ranges from 170 pc to 270 pc given their respective length and distance uncertainty to the Sun. They are also about 150 pc away from other clouds exhibiting γ -ray emissivities close to the average q_{LIS} . Given the 30–60% change in CR flux between Eridu and the other clouds, we have adopted $\ell_{\text{cr}} = 200$ pc as a typical CR gradient length scale for the particle energies probed with the LAT.

Figure 12 presents maps of the parallel diffusion coefficient obtained for both clouds when using a uniform LOS depth across the whole cloud (the mean one in the fiber configuration or the upper limit in the shell geometry). We have also relaxed the uniformity of the LOS depth by calculating the diffusion coefficient

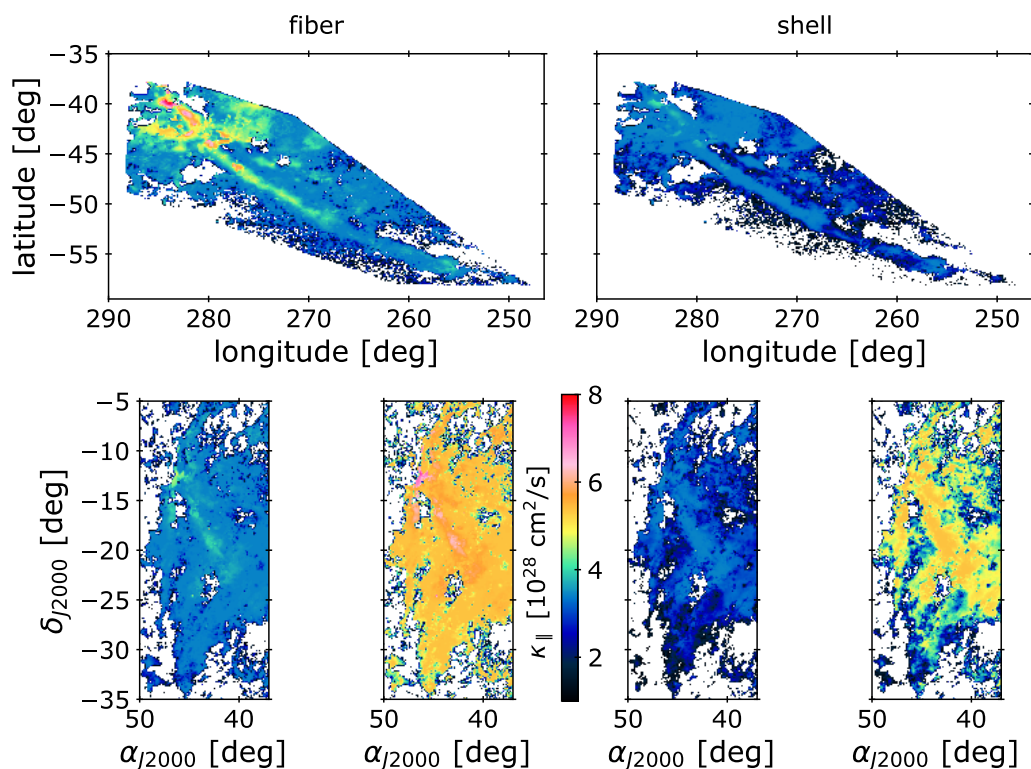


Fig. 12. Parallel diffusion coefficients obtained for the Reticulum (top) and Eridu (bottom) clouds in the fiber (left) and shell (right) geometries, assuming the damping rate of Eq. 5 and a uniform LOS depth equal to the shell one or to the average of the fiber ones. For each geometry, the Eridu plots show κ_{\parallel} values for the same CR flux exciting the Alfvén waves as in Reticulum (left) or for the reduced CR flux corresponding to the cloud lower γ -ray emissivity (right).

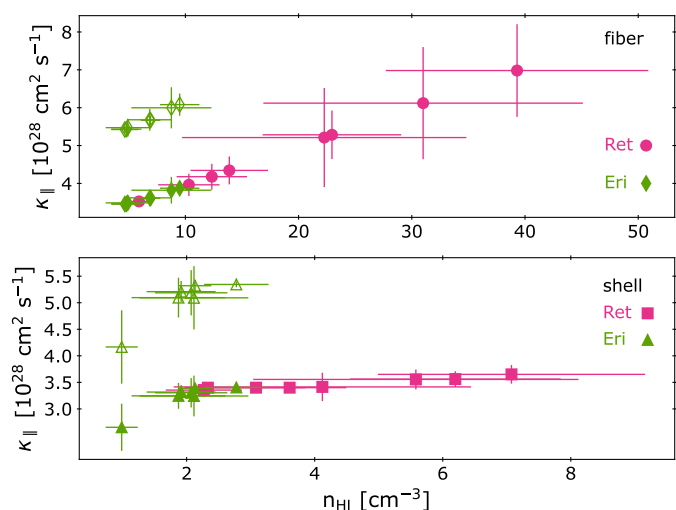


Fig. 13. Estimates of the parallel diffusion coefficient in the $1^{\circ} \times 1^{\circ}$ squares chosen along the core of the Reticulum (magenta) and Eridu (green) filaments, for the fiber (top) and shell (bottom) geometries, for the same CR flux pervading the two clouds (filled symbols) and for the reduced CR flux in Eridu (open symbols). The data points and error bars respectively give the mean value in each ~ 5 pc-wide square and the rms dispersion at 0.5–0.7 pc scale within each square. Note the different n_{HI} and κ_{\parallel} scales for each geometry.

istic CR gradient scale length ℓ_{cr} of 200 pc, we find κ_{\parallel} values that typically range from 3×10^{28} to 8×10^{28} $\text{cm}^2 \text{s}^{-1}$ across the Reticulum cloud in both geometries. They are closer to 3×10^{28} or 4×10^{28} $\text{cm}^2 \text{s}^{-1}$ for Eridu because of its lower contrast in gas column density. The maps show that the diffusion coefficient does not vary substantially as the gas density increases from the cloud envelopes to the cores because the drop in wave excitation is tempered by the loss in ion abundance and the damping rise is tempered by the drop in gas temperature and increase in ion mass. The overall variation from edge to core is of the order two to three. We stress that these κ_{\parallel} estimates sample the cloud properties at parsec scales rather than at the micro-parsec scales of gyroresonance, so in-situ variations may well be much more severe.

Figure 12 illustrates that, when using the same CR flux to excite Alfvén waves in the Reticulum and Eridu clouds, both filaments exhibit very similar diffusion properties over most of their area in each of the fiber or shell configurations. Figure 13 shows the evolution of the diffusion coefficient in the 1° -wide squares sampling the core of the filaments. The larger κ_{\parallel} values pertaining to Reticulum in Fig. 13 correspond to the densest cores where CRs can flow more rapidly due to the enhanced damping. In the self-confinement theory, CRs trap themselves by amplifying magnetic fluctuations through the streaming instability, so fewer CRs have a lower scattering efficiency. The CR flux reduction in Eridu with respect to Reticulum leads to an increase in diffusion length, an increase by the flux ratio of 1.57 ± 0.09 . Taking this reduction into account, Fig. 12 shows that CRs should diffuse at about the same speed in the densest parts of Eridu and Reticulum, but twice as fast at the periphery of Eridu than in the envelope of Reticulum, in both geometries.

in each of the $1^{\circ} \times 1^{\circ}$ squares chosen along both filaments, with the locally-derived fiber LOS depth estimate in each square. The results are shown in Tables B.1 and B.2 and as a function of the mean H I gas density in each square in Fig. 13. For a character-

The diffusivity difference between the two clouds is, however, too small and the uncertainties too large to relate the loss of CRs in Eridu to different self-confinement efficiencies.

CRs transfer energy to the magnetic fluctuations if they have an anisotropic distribution with a degree of anisotropy larger than v_A^{ion}/c , thus if their mass drift velocity v_D along the mean magnetic field exceeds v_A^{ion} (Kulsrud & Pearce 1969). If the CRs are well scattered, there is a direct relationship between their anisotropy and spatial density gradient (Zweibel 2013), so a possible cause for a difference in CR flux inside Eridu and Reticulum may originate outside the clouds, in different CR gradients in their immediate environment (different ℓ_{cr} values). Both clouds lie near the dense walls of the Local Valley, but Eridu stands in the vicinity of the Orion-Eridanus superbubble where steep CR gradients are possible even though we have found no evidence for fresh acceleration or re-acceleration of CRs in the compressed outer rim of the superbubble (Joubaud et al. 2020). Steeper gradients would, however, excite more streaming instabilities and decrease the diffusion coefficient rather than increase it compared to Reticulum. On the other hand, Reticulum may be a cooling fragment of an old (supernova remnant?) shell with steep CR gradients to efficiently confine the particles in the shell, but a local boost of the wave growth rate inside this cloud is hard to reconcile with the fact that its CR flux matches that found in other local clouds with different histories and environments. Future studies of 3D gradients in γ -ray emissivity in the local ISM will shed light on potential ℓ_{cr} variations.

We note that κ_{\parallel} linearly scales with ℓ_{cr} . This is the reason why the present estimates drastically differ from those found by Armillotta et al. (2021) for the same gas density. They find very smooth CR densities in the CNM with about two orders of magnitude larger gradient scale lengths in their simulations (Lucia Armillotta, private communication).

The κ_{\parallel} values found in these individual clouds compare well with the range of recent estimates obtained for the entire Milky Way for isotropic diffusion, which vary from 4×10^{28} to $20 \times 10^{28} \text{ cm}^2 \text{ s}^{-1}$ for 10 GeV/n CRs (Jóhannesson et al. 2016, 2019; Weinrich et al. 2020; De La Torre Luque et al. 2022). We stress that the choice of 200 pc for the ℓ_{cr} gradient scale was set prior to the κ_{\parallel} calculations and was driven by the 3D separation between clouds exhibiting different γ -ray emissivities. It was not tuned to match Milky Way values. The latter are based on direct measurements of CR nuclear spectra measured inside and near the heliosphere (by Voyager, ACE-CRIS, HEAO-3, CREAM, AMS-02, and PAMELA) and on different propagation codes to model spallation reactions (namely GALPROP, USINE, and DRAGON-2). The different estimates vary by a factor five even though the models merely try to constrain an isotropic, homogeneous, environment-independent coefficient in the Galaxy. The convergence with the values presented in Fig. 12 and 13 therefore brings important new insight as our estimates apply to individual clouds instead of the whole Galaxy, they exploit detailed ISM data and ISM physics rather than uncertain 3D gas maps of the Milky Way, and they use different CR information (the overall number density instead of secondary to primary spectral ratios).

The turbulent wandering of magnetic-field lines has been proposed to regulate the diffusion of streaming CRs in super-Alfvénic turbulence (Xu & Lazarian 2022, and references therein). Scattering by magnetosonic waves in a compressible medium has also been invoked (Sampson et al. 2023, and references therein). We have therefore explored the turbulence level in gas velocity and in B_{sky} orientation, and we have estimated the sonic and Alfvén Mach numbers of the turbulence, the for-

mer indicating the plasma compressibility and the latter gauging the magnetic stiffness against tanglement and its impact on the $\kappa_{\perp}/\kappa_{\parallel}$ ratio.

5.3. Velocity dispersion and sonic Mach numbers

We have taken advantage of the pseudo-Voigt decomposition of the H α spectra used for the cloud separation to follow LOS velocity changes in the main line of a cloud across the structure. We have mapped the σ_v line widths of the main line across Eridu (top panel, left) and Reticulum (bottom panel, upper) in Fig. 14, respectively. We have also mapped the position-to-position velocity dispersion at the smallest scale resolved by the GASS using a two-point structure function in LOS velocity:

$$S_v(\mathbf{x}, \delta) = \sqrt{\frac{1}{N} \sum_{i=1}^N [v_{\text{LOS}}(\mathbf{x}) - v_{\text{LOS}}(\mathbf{x} + \delta_i)]^2} \quad (8)$$

where the velocity dispersion compares the line central velocity in a given direction \mathbf{x} and in a displaced direction $v(\mathbf{x} + \delta_i)$. The average is taken over displaced directions spanning an annulus $\delta/2 \leq \delta_i \leq 3\delta/2$ around the \mathbf{x} direction, with δ equal to the effective GASS FWHM angular resolution of $16''.2$ (Kalberla et al. 2010). The resulting S_v maps are shown for the Reticulum and Eridu clouds in the top panel, right and bottom panel, lower plots of Fig. 14 respectively.

Figure 14 shows that the line width and velocity dispersion values decrease from the cloud edges to the cores of both clouds, as expected from CNM regions. The σ_v line widths are commensurate with the thermal broadening expected from the temperature map inferred in the previous section. The velocity resolution of GASS and the uncertainty in the modelled gas temperature do not allow the rms measure of turbulent velocities to be extracted beyond the thermal broadening. The σ_v line widths therefore provide upper limits to the turbulent motions along the lines of sight. On the other hand, because of the average over the δ ring, the S_v structure function is closer to a lower limit to the turbulent motions along the line of sight. Both S_v and σ_v are one-dimensional measures of the turbulent velocity field.

Figure 14 indicates that the dispersion in the velocity field of the Eridu cloud is about twice larger than in the more compact Reticulum filament (both in S_v and σ_v). We have calculated the sonic Mach numbers of the turbulence in the $1^\circ \times 1^\circ$ squares sampling the core of each filament in the case of isotropic turbulence ($\delta v_{3D}^2 = 3\delta v_{1D}^2$). Figure 15 shows that these estimates are consistent with the distribution of Mach numbers obtained in cold CNM clumps by Heiles & Troland (2003) when comparing the H α line width with the thermal broadening inferred from spin temperatures. Figure 15 indicates that the turbulence is mildly supersonic along both Eridu and Reticulum in the fiber configuration and trans-sonic in the warmer shell geometry. The Mach numbers compare well in both clouds and the turbulence appears to be moderately compressible in both of them.

5.4. Dispersion in the B_{sky} magnetic field orientation

In order to study the complexity of the magnetic field lines in the Reticulum and Eridu clouds we have used the dust polarisation data recorded by *Planck* at 353 GHz. We have degraded the original $4''.8$ resolution to an angular resolution of $14''$ (FWHM) in order to increase the signal to noise ratio. The data come from the third public data release (PR3) which is described in the *Planck*

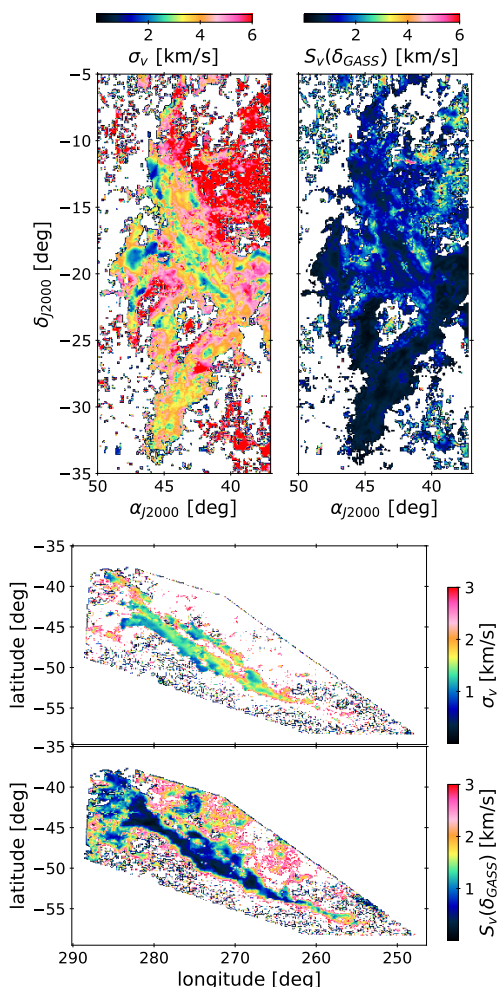


Fig. 14. Maps of the velocity line width, σ_v , and of the velocity dispersion function, $S_v(\delta_{GASS})$, of the main H α emission line across the Eridu (top) and Reticulum (bottom) clouds. Note the different colour scale for each cloud.

2018 Release Explanatory Supplement⁴. The Q and U Stokes parameters provided in the Planck database are defined with respect to the Galactic coordinates, but in a direction opposite to the IAU convention along the longitude axis, so we define the polarisation angle:

$$\psi_{IAU} = \frac{1}{2} \arctan(-U, Q) \quad (9)$$

ψ is zero at the North Galactic pole and it follows the IAU convention by increasing counter-clockwise with increasing longitude. The $\arctan(\sin, \cos)$ is the arc-tangent function that solves the π ambiguity taking into account the sign of the cosine.

The nearby Reticulum and Eridu clouds are the dominant dust clouds along their respective lines of sight, so the dust polarisation measurements give us access to the magnetic field in the plane of the sky, B_{sky} , in those clouds. In order to quantify the regularity of the B_{sky} direction, we have used the polarisation angle dispersion function (Planck Collaboration et al. 2015a):

$$S_\psi(\mathbf{x}, \delta) = \sqrt{\frac{1}{N} \sum_{i=1}^N [\psi(\mathbf{x}) - \psi(\mathbf{x} + \delta_i)]^2} \quad (10)$$

⁴ <http://wiki.cosmos.esa.int/planck-legacy-archive>

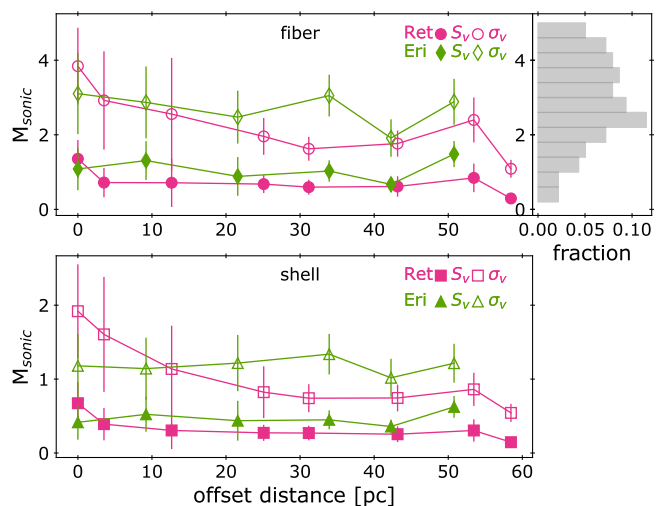


Fig. 15. Sonic Mach numbers of turbulent motions in the $1^\circ \times 1^\circ$ squares chosen along the Eridu (green) and Reticulum (magenta) filaments, in the fiber (top) and shell (bottom) geometries, assuming isotropic turbulence and using the S_v dispersion function (dark filled symbols) or the σ_v line width (light open symbols) to trace the one-dimensional turbulent velocity dispersion. The data points and error bars respectively give the mean value in each ~ 5 pc-wide square and the rms dispersion at 0.5–0.7 pc scale within each square. The histogram shows the Mach number distribution in cold CNM clumps from Heiles & Troland (2003)

where $\Delta\psi_{xi} = \psi(\mathbf{x}) - \psi(\mathbf{x} + \delta_i)$ is the difference between the polarisation angle in a given direction \mathbf{x} and in a displaced direction $\mathbf{x} + \delta_i$. In practice, we have calculated $\Delta\psi_{xi}$ from the Stokes parameters as (Planck Collaboration et al. 2015a):

$$\Delta\psi_{xi} = \frac{1}{2} \arctan(Q_i U_x - Q_x U_i, Q_i Q_x + U_i U_x) \quad (11)$$

where the x and i indices stand for the central and displaced directions, respectively. The average in S_ψ is taken over displaced directions spanning an annulus around the \mathbf{x} direction with an inner radius $\delta/2$ and an outer radius $3\delta/2$. We have taken 15' for the δ lag.

The S_ψ dispersion values range from 0° for a well ordered B_{sky} magnetic field to $S_\psi = 90^\circ$ for a disordered one. When the polarisation signal is dominated by noise, S_ψ converges to $\pi/\sqrt{12} (\approx 52^\circ)$. The results on the B_{sky} field orientation and on its dispersion are displayed as field lines in Fig. 1, as ψ angle maps in Fig. 16, and as S_ψ angle dispersion maps in Fig. 17.

Atomic filamentary clouds have mean magnetic fields often aligned with the filament axis (Clark et al. 2014; Clark & Hensley 2019) whereas the field orientation turns to perpendicular or to disorder in the dense molecular parts (Soler et al. 2013; Planck Collaboration et al. 2016a). The atomic Eridu and Reticulum clouds follow the expected trend. Figures 1, 16, and 17 jointly show that the B_{sky} magnetic field is well ordered along the axis of both filaments, with a stable direction along nearly their whole length and with a dispersion lower than 10° on a 1-pc scale over large parts of the filament extent. Moreover, these ordered fields are almost perpendicular to the orientation of the Galactic magnetic field inferred in the solar neighbourhood from dust polarisation in local clouds (Planck Collaboration et al. 2016b) or by the field draping around the heliosphere (Zirnstein et al. 2016).

The Reticulum field appears to be slightly more ordered in its dense part than in Eridu, likely because of the compression that originally formed the compact fiber or shell. The dispersion in field orientation appears to be rather uniform across the whole

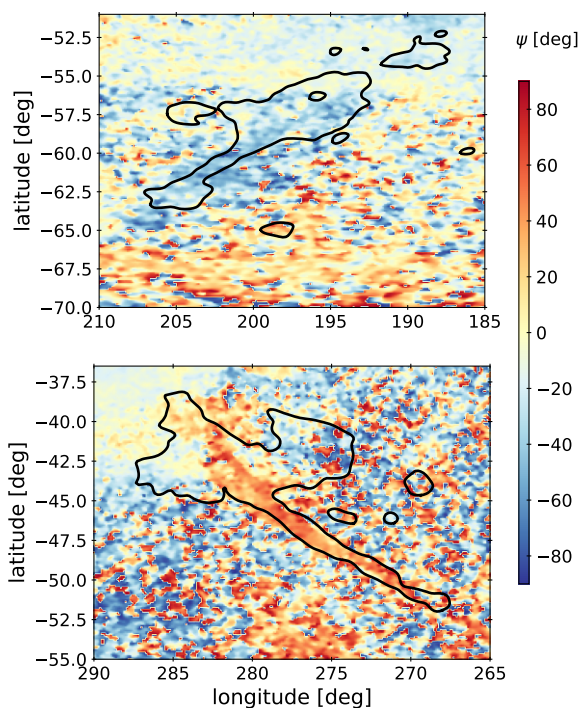


Fig. 16. Map of the polarisation angle ψ at 353 GHz with 14' resolution in the Eridu (top) and Reticulum (bottom) clouds. The angle gives the orientation of the B_{sky} field. The black contours delineate the filaments at HI column densities of $3 \times 10^{20} \text{ cm}^{-2}$ and $1.2 \times 10^{20} \text{ cm}^{-2}$, respectively.

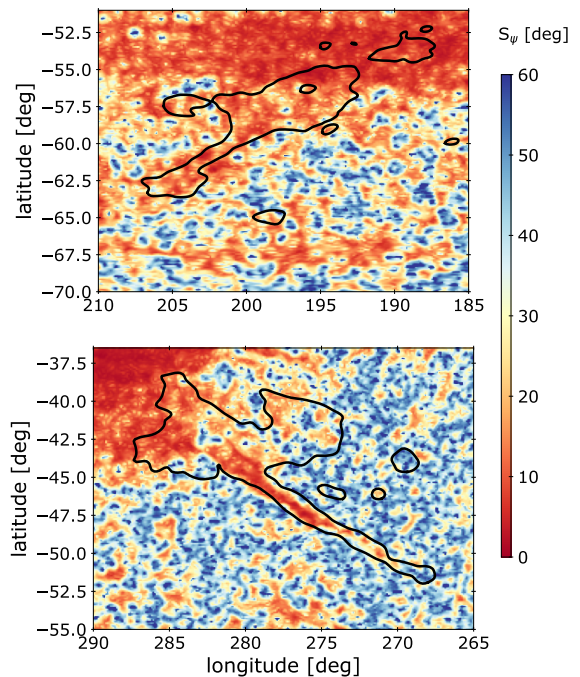


Fig. 17. Map of the polarisation angle dispersion function S_ψ at 353 GHz with 14' resolution and for lag $\delta=15'$ in the Eridu (top) and Reticulum (bottom) clouds. The black contours delineate the filaments at HI gas column densities of $3 \times 10^{20} \text{ cm}^{-2}$ and $1.2 \times 10^{20} \text{ cm}^{-2}$, respectively.

of Eridu and is a little more contrasted between the filament axis and edges of Reticulum. The parsec-scale data does not, however, suggest that CRs have slowed down in Reticulum because of a much more tangled field. To the contrary, compared to Eridu, they should stream along more ordered fields over a large fraction of the filament length.

5.5. Magnetic-field strength

The total magnetic field is composed of a mean component, \mathbf{B}_0 , and a small fluctuating one, $|\delta\mathbf{B}| \ll |\mathbf{B}_0|$, so that the magnetic energy density is $\frac{B^2}{8\pi} = \frac{1}{8\pi}[B_0^2 + \delta B^2 + 2\delta\mathbf{B} \cdot \mathbf{B}_0]$. To infer the mean field strength from dust polarisation, the Davis-Chandrasekhar-Fermi (DCF) method assumes that isotropic turbulent motions initiate incompressible, transverse, Alfvén waves ($\delta\mathbf{B} \cdot \mathbf{B}_0 = 0$) in the frozen field (Davis 1951; Chandrasekhar & Fermi 1953). They also assume that the kinetic energy of the turbulence is equal to the fluctuating magnetic energy density, and that the dispersion in polarisation angle ψ traces the dispersion in magnetic-field orientation. From the equipartition condition, $\frac{1}{2}\rho\delta v^2 = \frac{\delta B^2}{8\pi}$ and from $S_\psi \approx \delta B/B_0$ one obtains:

$$B_{\text{sky}}^{\text{DCF}} = f \sqrt{4\pi\rho} \frac{\delta v}{S_\psi} \quad (12)$$

where the f correction factor varies with authors between 0.3 and 0.7, for instance $f = 1/\sqrt{3}$ for isotropic turbulence (Chandrasekhar & Fermi 1953). Other values are reviewed by Skalidis & Tassis (2021, Sect. 2.2.3). We have adopted their $f = 0.5$ recommendation for this work.

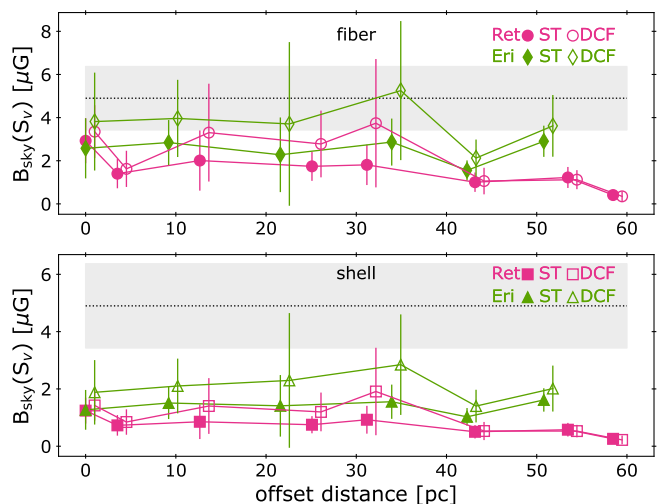


Fig. 18. Plane-of-sky magnetic-field strengths in the $1^\circ \times 1^\circ$ squares chosen along the Reticulum (magenta) and Eridu (green) filaments, in the fiber (top) and shell (bottom) geometries, using the S_ν dispersion function in the ST (dark filled symbols) or DCF method (light open symbols). The data points and error bars respectively give the mean value in each ~ 5 pc-wide square and the rms dispersion at 0.5–0.7 pc scale within each square. The offset distance of the DCF data points has been slightly displaced for clarity. The grey area shows the mean CNM B_{sky} value from Heiles & Troland (2005) assuming $B_{\text{sky}}^2 = \frac{2}{3}B^2$.

The DCF method tends to overestimate the actual field strength because of line-of-sight and beam averaging and be-

cause it overlooks the strong anisotropy in ISM turbulence and the role of non-Alfvénic (compressible) modes in the cross-term $\delta\mathbf{B}\cdot\mathbf{B}_0 \neq 0$ (Skalidis & Tassis 2021). To include the compressible modes, these authors propose an alternative formulation that agrees within 20-30% with MHD simulation data:

$$B_{\text{sky}}^{\text{ST}} = \sqrt{2\pi\rho} \frac{\delta v}{\sqrt{S_\psi}} \quad (13)$$

We have applied both methods to calculate the plane-of-sky magnetic-field strengths in the 1° -wide squares chosen along the Reticulum and Eridu filaments, with the velocity dispersion function S_ν as a proxy for the turbulent velocity δv . The results are shown in Fig. 18 and in Tables B.1 and B.2. Following the discussion by Skalidis & Tassis (2021), the $B_{\text{sky}}^{\text{ST}}$ and $B_{\text{sky}}^{\text{DCF}}$ estimates likely bracket the true B_{sky} value, the latter being about 40% (50%) larger than the former in the case of Reticulum (Eridu). We have also calculated upper limits to B_{sky} using the σ_ν line width as an upper limit to the turbulent velocity. The results are provided in Tables B.1 and B.2. They are about three times larger than the S_ν -based estimates for each method.

Figure 18 shows that the B_{sky} field strength is rather uniform along the core of each cloud and that it is about one and a half larger along Eridu than along Reticulum: around 3.1 (1.7) μG for Eridu and 1.9 (0.9) μG for Reticulum in the fiber (shell) configuration if we use the S_ν velocity dispersion to trace the turbulent motions. Three times larger upper limits to the fields are found when using the line width instead. The difference between Eridu and Reticulum does not depend much on the cloud geometry, but one should keep in mind that the magnetic-field component along the line of sight may significantly differ in both clouds. Figure 18 also illustrates that the B_{sky} strengths in Eridu and Reticulum compare reasonably with the median total field $B_{\text{tot}} = 6 \pm 1.8 \mu\text{G}$ inferred from Zeeman splitting of H α lines and Monte Carlo simulations (Heiles & Troland 2005) if one assumes $B_{\text{sky}}^2 = (2/3) B^2$ for a random field orientation with respect to the line of sight (Heiles & Troland 2005).

We cannot estimate whether the MHD turbulence is super-Alfvénic or not since both B_{sky} derivations assume equipartition between the fluctuating kinetic and magnetic energy densities, whether the latter is dominated by $\delta B^2/8\pi$ in the case of incompressible turbulence (DCF) or by $\delta B B/4\pi$ when compressible modes are present (ST). In both cases, the Alfvén Mach numbers will be close to one. We can, however, estimate the gas magnetization level from the squared ratio of the sound to Alfvén speed, c_s^2/v_A^2 (Soler et al. 2013), which is close to the gas to magnetic pressure ratio. To derive the Alfvén velocity of the total gas, we have assumed $B^2 = (3/2)B_{\text{sky}}^2$ and the ST formulation for B_{sky} . Figure 19 shows the normalised distributions of the ratios found in the 1° -wide squares sampling the gas along the core of both filaments. If we use the $B_{\text{sky}}(S_\nu)$ estimate, the gas and magnetic pressures compare well across both clouds in their fiber geometry and the gas pressure slightly exceeds the magnetic one in the shell configuration. The magnetization is skewed to values below one (i.e. to dominant magnetic pressure) when using the $B_{\text{sky}}(\sigma_\nu)$ upper limits to the field, but not severely, so equivalent gas and magnetic pressures may prevail over large parts of the clouds. Therefore, whether in terms of B_{sky} orientation dispersion or in magnetic stiffness against turbulent gas motions, we find no important difference on parsec scale between the two clouds that would suggest more magnetic-field tangling and slower CR diffusion in one of them.

6. Conclusions

We have compared the CR flux in the atomic phase of two nearby clouds that have many properties in common. They are both elongated filaments, crossing the same hollow sector of the Local interstellar Valley, at comparable distances from the Sun. They are both threaded by ordered magnetic fields, mostly aligned with the filament long axis, largely inclined with respect to the Galactic plane, and with magnetic pressures of the same order as the thermal ones. Yet, we have found that the γ -ray emissivity per gas nucleon in one cloud, Reticulum, is 1.57 ± 0.09 times larger than in the other cloud, Eridu, over the whole energy range of analysis, from 0.16 to 63 GeV. The difference cannot be attributed to uncertainties in gas mass since the correlation between the dust and γ -ray data allows an efficient detection of any additional gas that is not traced by H α line emission (as we have found in Reticulum) and the γ -ray contribution of this additional gas is included in the model. Furthermore, we cannot reduce the CR flux ratio below 1.32 ± 0.08 when allowing for strong differences in H α spin temperature between the two clouds, even at the expense of a worse γ -ray fit.

Beyond characterising the global magnetic orientation and average field strength of a few microGauss in the clouds, we have studied turbulence characteristics at a parsec scale that might hint at different environmental conditions for particle diffusion, namely the dispersion in gas velocity and magnetic-field orientation, the sonic Mach numbers (compressibility), and the magnetization level (magnetic stiffness against gas turbulent motions). We have found that the two clouds compare well on all these aspects. The only notable difference is that the core of the Reticulum cloud has collapsed (or been compressed) to larger densities typical of the CNM and DNM phases whereas as a large fraction of the more diffuse gas in Eridu may be transitioning through the unstable, lukewarm phase. MHD simulations will help study the level of magnetic-field tangling and stretching in the different atomic and DNM gas phases, or in shell compression behind a slow shock, in order to search for changes that might impact the collective drift of the CR population (Xu & Lazarian 2022; Sampson et al. 2023).

If the 1 – 500 GeV/n CRs we have probed in γ rays primarily scatter off MHD waves they have excited by the streaming instability, one would expect a stronger damping in the denser Reticulum cloud, but we have shown that the difference in expected steady-state diffusion coefficient between the two clouds is small (less than a factor of two) because the increase in diffusion length with the ambient gas density is moderated by the corresponding drop in temperature and ionisation fraction. We have, however, probed the cloud properties at a parsec scale whereas the growth and damping of the relevant MHD waves occur at wavelengths of a few micro-parsecs where the interstellar gas properties cannot be explored. The damping rates we have estimated indicate that the Alfvén waves or magnetic eddies propagating along the field lines should dissipate over typical lengths of tens to hundreds of micro-parsecs ($L \approx v_A^{\text{ion}}/\Gamma_{\text{in}}$, Spangler et al. 2011). The median of their distribution is twice as large in Eridu as in Reticulum. The dissipation lengths correspond to proton gyroradii for energies in the ~ 0.01 to ~ 1 TeV band, with a median energy three times larger in Eridu than in Reticulum. The waves must be constantly replenished or we would observe a change in spectral slope in the γ -ray emissivity spectra in the ~ 1 to ~ 100 GeV band as the higher-energy particles would leak out more rapidly. The fact that we have found a change in CR flux, but not in spectrum, in the two clouds is therefore an important constraint.

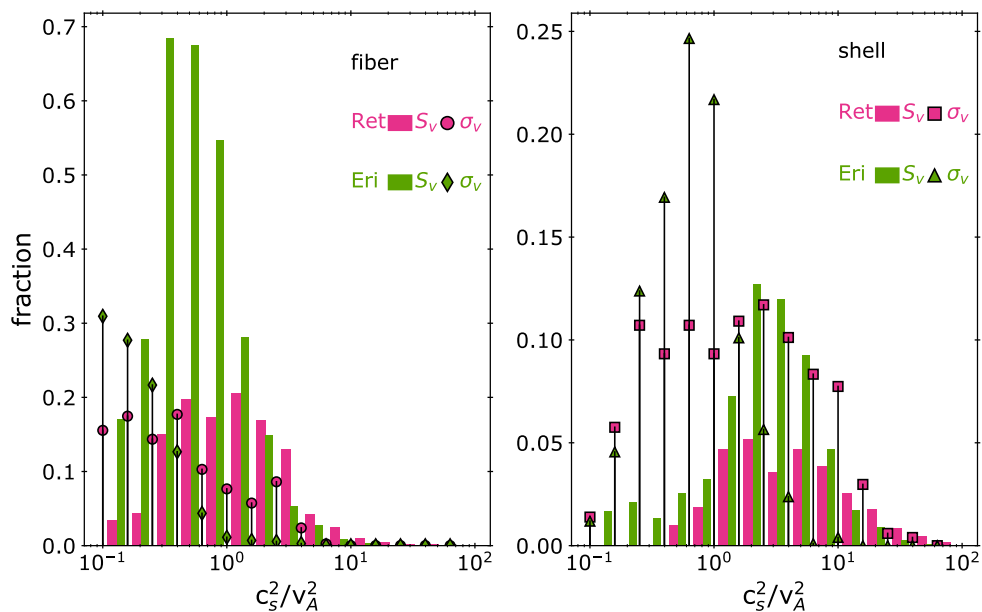


Fig. 19. Histograms of the gas magnetization levels in the $1^\circ \times 1^\circ$ squares chosen along the Eridu (green) and Reticulum (magenta) filaments, for each geometry, and using the S_v velocity dispersion (filled bars) or the σ_v line width (markers) in the ST formulation to infer B_{sky} and the total magnetic-field strength.

On the other hand, the wave growth rate in each cloud relates to the degree of CR velocity anisotropy or, equivalently, to the steepness of the CR spatial density gradient (Zweibel 2013) which could differ in the vicinity of the clouds (different ℓ_{cr}). The *Fermi*-LAT data can help advance this aspect to enlighten why these two similar clouds are pervaded by different CR fluxes.

Acknowledgements. We thank Jeong-Gyu Kim for sharing his interstellar model for the solar neighbourhood conditions, Lucia Armillotta for sharing information from her work, and we thank the members of the Interstellar Institute (I2) CNRS International Research Network for enlightening discussions. We acknowledge the financial support by the LabEx UnivEarthS (ANR-10-LABX-0023 and ANR-18-IDEX-0001) for this work. The *Fermi* LAT Collaboration acknowledges generous ongoing support from a number of agencies and institutes that have supported both the development and the operation of the LAT as well as scientific data analysis. These include the National Aeronautics and Space Administration and the Department of Energy in the United States, the Commissariat à l’Énergie Atomique and the Centre National de la Recherche Scientifique / Institut National de Physique Nucléaire et de Physique des Particules in France, the Agenzia Spaziale Italiana and the Istituto Nazionale di Fisica Nucleare in Italy, the Ministry of Education, Culture, Sports, Science and Technology (MEXT), High Energy Accelerator Research Organization (KEK) and Japan Aerospace Exploration Agency (JAXA) in Japan, and the K. A. Wallenberg Foundation, the Swedish Research Council and the Swedish National Space Board in Sweden. Additional support for science analysis during the operations phase is gratefully acknowledged from the Istituto Nazionale di Astrofisica in Italy and the Centre National d’Études Spatiales in France.

References

Abdo, A. A., Ackermann, M., Ajello, M., et al. 2010, *ApJ*, 710, 133
 Abdollahi, S., Acero, F., Baldini, L., et al. 2022, *ApJS*, 260, 53
 Acero, F., Ackermann, M., Ajello, M., et al. 2016, *ApJS*, 223, 26
 Ackermann, M., Ajello, M., Allafort, A., et al. 2012a, *ApJ*, 756, 4
 Ackermann, M., Ajello, M., Atwood, W. B., et al. 2012b, *ApJ*, 750, 3
 Ackermann, M., Ajello, M., Baldini, L., et al. 2013, *ApJ*, 772, 154
 Armillotta, L., Ostriker, E. C., & Jiang, Y.-F. 2021, *ApJ*, 922, 11
 Bolatto, A. D., Wolfire, M., & Leroy, A. K. 2013, *ARA&A*, 51, 207
 Boschini, M. J., Della Torre, S., Gervasi, M., et al. 2020, *ApJS*, 250, 27
 Bruel, P., Burnett, T. H., Digel, S. W., et al. 2018, *arXiv e-prints*, arXiv:1810.11394
 Bustard, C. & Zweibel, E. G. 2021, *ApJ*, 913, 106
 Casandjian, J.-M. 2015, *ApJ*, 806, 240

Casandjian, J.-M., Ballet, J., Grenier, I., & Remy, Q. 2022, *ApJ*, 940, 116
 Chandrasekhar, S. & Fermi, E. 1953, *ApJ*, 118, 113
 Clark, S. E. & Hensley, B. S. 2019, *ApJ*, 887, 136
 Clark, S. E., Peek, J. E. G., & Putman, M. E. 2014, *The Astrophysical Journal*, 789, 82
 Davis, L. 1951, *Physical Review*, 81, 890
 De La Torre Luque, P., Mazziotta, M. N., Ferrari, A., et al. 2022, *J. Cosmology Astropart. Phys.*, 2022, 008
 Dickey, J. M., Mebold, U., Stanimirovic, S., & Staveley-Smith, L. 2000, *ApJ*, 536, 756
 Draine, B. T. 2011, *Physics of the Interstellar and Intergalactic Medium*
 Finkbeiner, D. P. 2003, *ApJS*, 146, 407
 Gaensler, B. M., Madsen, G. J., Chatterjee, S., & Mao, S. A. 2008, *PASA*, 25, 184
 Gaustad, J. E., McCullough, P. R., Rosing, W., & Van Buren, D. 2001, *PASP*, 113, 1326
 Gong, M., Ostriker, E. C., & Kim, C.-G. 2018, *ApJ*, 858, 16
 Grenier, I. A., Black, J. H., & Strong, A. W. 2015, *ARA&A*, 53, 199
 Grenier, I. A., Casandjian, J.-M., & Terrier, R. 2005, *Science*, 307, 1292
 Heiles, C. & Troland, T. H. 2003, *ApJ*, 586, 1067
 Heiles, C. & Troland, T. H. 2005, *ApJ*, 624, 773
 Hopkins, P. F., Squire, J., Chan, T. K., et al. 2021, *MNRAS*, 501, 4184
 Irfan, M. O., Bobin, J., Miville-Deschênes, M.-A., & Grenier, I. 2019, *A&A*, 623, A21
 Jiang, Y.-F. & Oh, S. P. 2018, *ApJ*, 854, 5
 Jóhannesson, G., Porter, T. A., & Moskalenko, I. V. 2019, *ApJ*, 879, 91
 Jóhannesson, G., Ruiz de Austri, R., Vincent, A. C., et al. 2016, *ApJ*, 824, 16
 Joubaud, T., Grenier, I. A., Ballet, J., & Soler, J. D. 2019, *A&A*, 631, A52
 Joubaud, T., Grenier, I. A., Casandjian, J. M., Tolksdorf, T., & Schlickeiser, R. 2020, *A&A*, 635, A96
 Kalberla, P. M. W. & Haud, U. 2015, *A&A*, 578, A78
 Kalberla, P. M. W., McClure-Griffiths, N. M., Pisano, D. J., et al. 2010, *A&A*, 521, A17
 Kim, J.-G., Gong, M., Kim, C.-G., & Ostriker, E. C. 2023, *ApJS*, 264, 10
 Kulsrud, R. & Pearce, W. P. 1969, *ApJ*, 156, 445
 Kulsrud, R. M. & Cesarsky, C. J. 1971, *Astrophys. Lett.*, 8, 189
 Lebrun, F., Paul, J. A., Bignami, G. F., et al. 1982, *A&A*, 107, 390
 Leike, R. H., Glatzle, M., & EnBlin, T. A. 2020, *A&A*, 639, A138
 Liszt, H., Gerin, M., & Grenier, I. 2019, *A&A*, 627, A95
 Murray, C. E., Peek, J. E. G., & Kim, C.-G. 2020, *ApJ*, 899, 15
 Murray, C. E., Stanimirović, S., Goss, W. M., et al. 2015, *ApJ*, 804, 89
 Murray, C. E., Stanimirović, S., Goss, W. M., et al. 2018, *ApJS*, 238, 14
 Nakanishi, H. & Sofue, Y. 2016, *PASJ*, 68, 5
 Nguyen, H., Dawson, J. R., Lee, M.-Y., et al. 2019, *ApJ*, 880, 141
 Nguyen, H., Dawson, J. R., Miville-Deschênes, M. A., et al. 2018, *ApJ*, 862, 49
 Pelgrims, V., Ferrière, K., Boulanger, F., Lallement, R., & Montier, L. 2020, *A&A*, 636, A17

- Planck Collaboration, Abergel, A., Ade, P. A. R., et al. 2014a, A&A, 571, A11
- 1270 Planck Collaboration, Abergel, A., Ade, P. A. R., et al. 2014b, A&A, 566, A55
- Planck Collaboration, Ade, P. A. R., Aghanim, N., et al. 2015a, A&A, 576, A104
- Planck Collaboration, Ade, P. A. R., Aghanim, N., et al. 2014c, A&A, 571, A13
- Planck Collaboration, Ade, P. A. R., Aghanim, N., et al. 2016a, A&A, 586, A138
- Planck Collaboration, Aghanim, N., Alves, M. I. R., et al. 2016b, A&A, 596, A105
- 1275 Planck Collaboration, Fermi Collaboration, Ade, P. A. R., et al. 2015b, A&A, 582, A31
- Remy, Q., Grenier, I. A., Marshall, D. J., & Casandjian, J. M. 2017, A&A, 601, A78
- Sampson, M. L., Beattie, J. R., Krumholz, M. R., et al. 2023, MNRAS, 519, 1503
- 1280 Schlickeiser, R., Caglar, M., & Lazarian, A. 2016, ApJ, 824, 89
- Skalidis, R. & Tassis, K. 2021, A&A, 647, A186
- Soler, J. D., Hennebelle, P., Martin, P. G., et al. 2013, ApJ, 774, 128
- Soler, R., Terradas, J., Oliver, R., & Ballester, J. L. 2016, A&A, 592, A28
- Spangler, S. R., Savage, A. H., & Redfield, S. 2011, in American Institute of
- 1285 Physics Conference Series, Vol. 1366, Partially Ionized Plasmas Throughout the Cosmos-Proceedings of the 2010 Huntsville Workshop, ed. V. Florinski, J. Heerikhuisen, G. P. Zank, & D. L. Gallagher, 97–106
- Starck, J. L. & Pierre, M. 1998, A&AS, 128, 397
- Strong, A. W. 1985, A&A, 150, 273
- 1290 Tibaldo, L., Digel, S. W., Casandjian, J. M., et al. 2015, ApJ, 807, 161
- Vranjes, J. & Krstic, P. S. 2013, A&A, 554, A22
- Weinrich, N., Génolini, Y., Boudaud, M., Derome, L., & Maurin, D. 2020, A&A, 639, A131
- Xu, S. & Lazarian, A. 2022, ApJ, 927, 94
- 1295 Ysard, N., Koehler, M., Jimenez-Serra, I., Jones, A. P., & Verstraete, L. 2019, A&A, 631, A88
- Zirnstein, E. J., Heerikhuisen, J., Funsten, H. O., et al. 2016, ApJ, 818, L18
- Zweibel, E. G. 2013, Physics of Plasmas, 20, 055501

Appendix A: Distance estimates to the nearby clouds

We have used the 3D dust distribution reconstructed from stellar surveys by [Leike et al. \(2020\)](#) out to distances of about 400 pc from the Sun to place constraints on the distance to different cloud complexes seen in the analysis region. Figure [A.1](#) displays the dust extinction in the G band in contiguous 20-pc-wide intervals. The lack of dust information at latitudes below about 50° for the three most distant intervals is due to the limited size of the 3D data cube perpendicular to the Galactic plane (± 270 pc). In addition to those maps, one can plot the extinction profile as a function of distance along sightlines of large N_{HI} column density in each cloud. Examples are shown in [Fig. A.2](#) when probing directions along the Reticulum filament. We have used the peaks found in the dust profiles and the correspondence in shape found between atomic clouds in [Fig. 3](#) and dust clouds in [Fig. A.1](#) to estimate the cloud distances that are given in [Sect. A](#).

We have repeated the analysis to revisit the distance to the Eridu cloud. The latter, being rather diffuse, is more difficult to identify in the dust data, but [Fig. A.3](#) suggests that it lies at about 300 pc from the Sun, beyond the edge of the Orion-Eridanus superbubble that is clearly detected at closer distances around 200 pc as the long arc crossing the maps horizontally at latitudes around -50° .

Appendix B: ISM properties in the 1° -wide squares along the cloud filaments

Tables [B.1](#) and [B.2](#) list the mean value and rms dispersion of the interstellar properties found in the $1^\circ \times 1^\circ$ squares that are depicted in [Fig. 10](#) and that span the length of the Reticulum and Eridu filaments, along their core. The properties include the LOS depth, the N_{HI} column density and n_{HI} volume density in the atomic gas, the HI velocity dispersion in the plane of the sky (S_v) and along the line of sight (σ_v line width), the gas temperature T and the abundance (x_{ion}) and atomic weight (A_{ion}) of ions inferred from the gas density and the [Kim et al. \(2023\)](#) model, the B_{sky} magnetic-field strengths estimated according to [Eqs. 12](#) and [13](#) with the S_v velocity dispersion or σ_v line width as a proxy for the turbulent velocity δv , the sonic Mach numbers M_S of the turbulence for the same options in δv , the Alfvénic Mach numbers M_A of the MHD turbulence inferred with the ST and DCF methods, the ion-neutral damping rate according to [Eq. 5](#), and the steady-state κ_{\parallel} diffusion coefficient for self-confinement with the CR flux reaching the heliosphere in the 1–20 GV rigidity range.

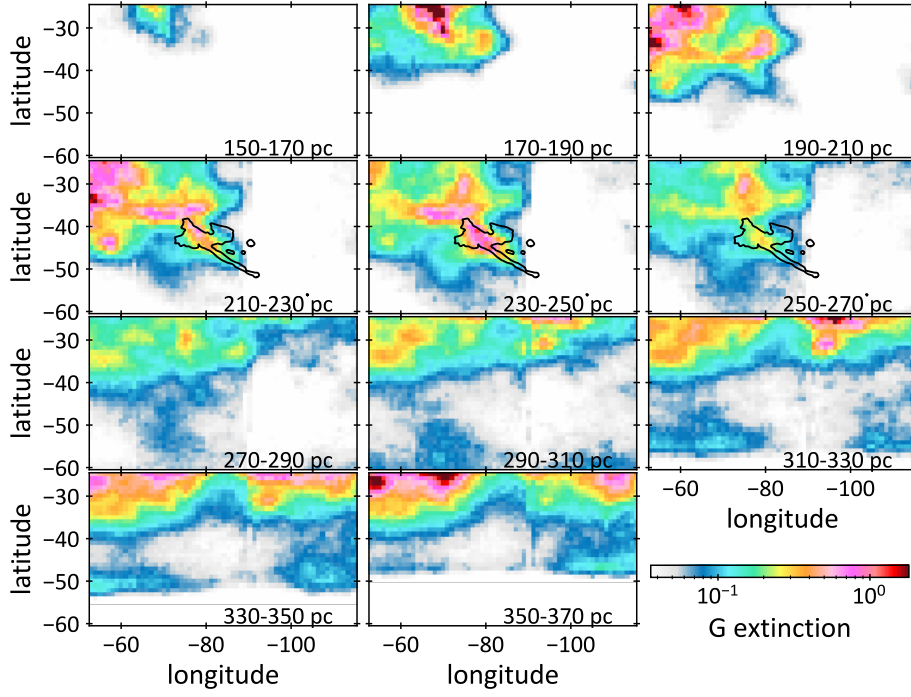


Fig. A.1. Maps of the G-band extinction optical depth integrated over 20 pc-wide intervals in distance from the Sun across the analysis region. The data come from the 3D distribution of [Leike et al. \(2020\)](#). The distance ranges are labelled in each map. The black contours delineate the Reticulum HI cloud as in [Fig. 1](#).

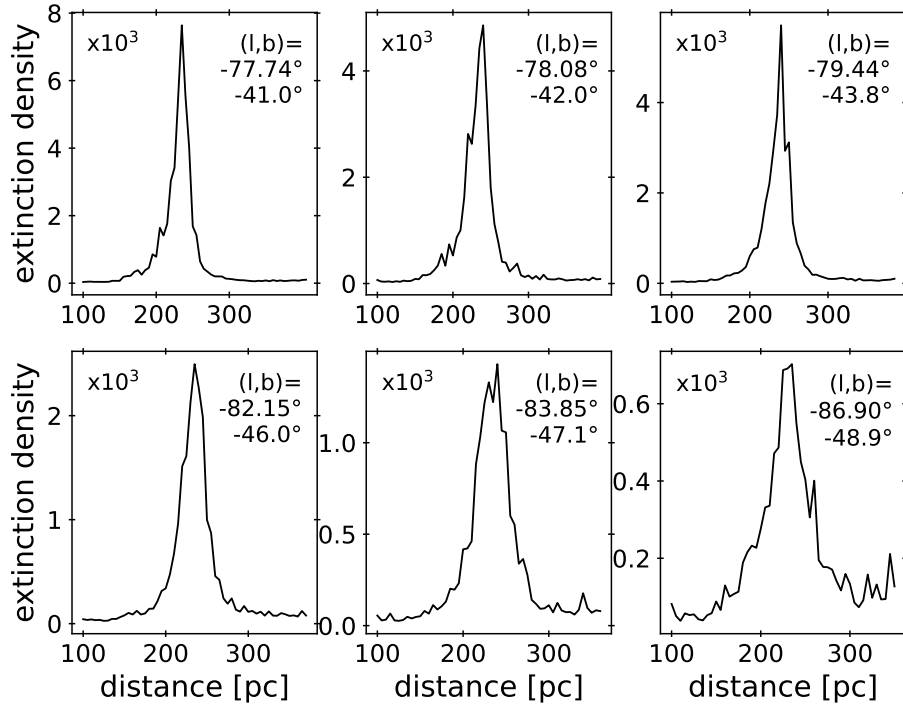


Fig. A.2. Dust extinction density profiles as a function of radial distance from the Sun for selected lines of sight along the Reticulum filament. The data come from the 3D distribution of [Leike et al. \(2020\)](#).

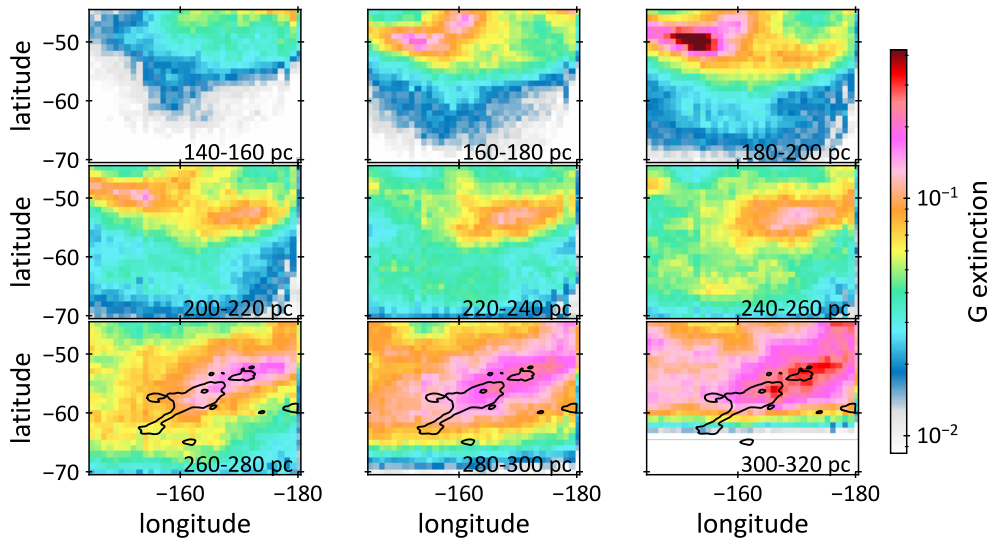


Fig. A.3. Maps of the G-band extinction optical depth integrated over 20 pc-wide intervals in distance from the Sun, toward the Orion-Eridanus region. The data come from the 3D distribution of [Leike et al. \(2020\)](#). The dust cloud that spans the region nearly horizontally around $b = 50^\circ$ and at distances between 160 and 260 pc marks the rim of the Orion-Eridanus superbubble. At larger distances, the black contours delineate the Eridu H I cloud as in [Fig. 1](#). The distance ranges are labelled in each map.

Table B.1. ISM properties along the Reticulum filament, for the fiber (regular font) or shell (bold font) geometry. The values and errors respectively give the mean value in each ~ 5 pc-wide square and the rms dispersion at 0.5–0.7 pc scale within each square.

Square center	LON [deg]	282.09	281.58	280.05	277.51	276.15	272.59	269.88	268.18
	LAT [deg]	-41.25	-42.0	-43.88	-46.25	-47.38	-49.12	-50.88	-51.5
N_{HI} [10^{20} cm $^{-2}$]		4.4	3.8	3.4	2.5	2.2	1.9	1.4	1.4
LOS depth [pc]		3.6 ± 0.5	5.4 ± 0.7	3.6 ± 0.4	3.7 ± 0.5	5.2 ± 0.6	5.0 ± 0.6	4.4 ± 0.6	7.9 ± 1.0
		20.0 ± 2.5							
n_{HI} [cm $^{-3}$]		39 ± 11	23 ± 6	31 ± 14	22 ± 13	14 ± 3	12 ± 3	10 ± 3	6 ± 1
		7 ± 2	6 ± 2	6 ± 3	4 ± 2	4 ± 1	3 ± 0.8	2 ± 0.5	2 ± 0.4
S_V [km s $^{-1}$]		0.78	0.48	0.48	0.52	0.49	0.55	0.81	0.37
σ_V [km s $^{-1}$]		2.2	1.9	1.7	1.4	1.3	1.5	2.3	1.4
S_ψ [deg]		19.95	24.44	10.73	14.9	11.8	28.74	35.62	42.91
T [K]		106	143	130	194	220	238	290	502
		503	517	843	1581	1193	1457	2322	2044
x_{ion} [10^{-4}]		4.2	6.3	5.6	8.9	10.5	11.5	14.2	24.3
		23.2	24.6	35.3	59.2	48.4	56.9	82.8	74.8
A_{ion}		5.6	4.0	4.8	3.8	2.9	2.7	2.4	1.7
		1.9	1.8	1.7	1.5	1.4	1.3	1.2	1.2
$B_{\text{sky}}^{\text{DCF}}(S_V)$ [μG]		3.9 ± 1.5	1.7 ± 0.9	3.6 ± 2.3	3.2 ± 1.8	3.9 ± 2.8	1.2 ± 0.7	1.1 ± 0.4	0.4 ± 0.2
		1.7 ± 0.7	0.9 ± 0.5	1.5 ± 1.0	1.4 ± 0.8	2.0 ± 1.4	0.6 ± 0.4	0.5 ± 0.2	0.2 ± 0.1
$B_{\text{sky}}^{\text{DCF}}(\sigma_V)$ [μG]		10.1 ± 4.2	6.8 ± 3.7	12.7 ± 6.1	9.2 ± 6.5	10.9 ± 8.4	3.2 ± 1.6	3.3 ± 1.2	1.2 ± 0.4
		4.3 ± 1.8	3.5 ± 1.9	5.4 ± 2.6	3.9 ± 2.8	5.6 ± 4.3	1.6 ± 0.8	1.6 ± 0.6	0.8 ± 0.2
$B_{\text{sky}}^{\text{ST}}(S_V)$ [μG]		3.2 ± 1.2	1.4 ± 0.7	2.1 ± 1.4	1.9 ± 0.7	1.9 ± 0.9	1.1 ± 0.5	1.2 ± 0.4	0.4 ± 0.2
		1.3 ± 0.5	0.7 ± 0.4	0.9 ± 0.6	0.8 ± 0.3	0.9 ± 0.5	0.5 ± 0.2	0.6 ± 0.2	0.3 ± 0.1
$B_{\text{sky}}^{\text{ST}}(\sigma_V)$ [μG]		8.6 ± 2.8	5.8 ± 2.7	7.6 ± 3.3	5.4 ± 2.6	5.1 ± 2.4	3.0 ± 0.9	3.5 ± 0.9	1.5 ± 0.3
		3.6 ± 1.2	3.0 ± 1.4	3.2 ± 1.4	2.3 ± 1.1	2.6 ± 1.2	1.5 ± 0.5	1.7 ± 0.4	0.9 ± 0.2
$\Gamma_{\text{in,S16}}$ [10^{-9} s $^{-1}$]		6.4	6.1	6.3	6.1	5.9	5.9	5.9	6.0
		6.0	6.0	6.0	6.0	6.1	6.1	6.1	6.2
κ_{\parallel} [10^{28} cm 2 s $^{-1}$]		6.9 ± 1.2	5.3 ± 0.6	6.2 ± 1.5	5.2 ± 1.3	4.4 ± 0.4	4.2 ± 0.3	4.0 ± 0.3	3.5 ± 0.07
		3.7 ± 0.2	3.6 ± 0.1	3.6 ± 0.2	3.4 ± 0.3	3.4 ± 0.08	3.4 ± 0.04	3.4 ± 0.1	3.4 ± 0.02
M_A^{DCF}		0.99 ± 0.31	1.21 ± 0.54	0.53 ± 0.22	0.74 ± 0.45	0.58 ± 0.46	1.42 ± 0.56	1.76 ± 0.53	2.12 ± 0.47
M_A^{ST}		1.17 ± 0.17	1.28 ± 0.27	0.85 ± 0.17	0.97 ± 0.31	0.85 ± 0.32	1.39 ± 0.28	1.56 ± 0.25	1.72 ± 0.2
$M_S(S_V)$		1.35 ± 0.49	0.72 ± 0.37	0.72 ± 0.63	0.68 ± 0.22	0.6 ± 0.18	0.62 ± 0.26	0.84 ± 0.36	0.29 ± 0.11
		0.67 ± 0.28	0.39 ± 0.21	0.31 ± 0.24	0.27 ± 0.1	0.27 ± 0.09	0.25 ± 0.1	0.3 ± 0.14	0.15 ± 0.05
$M_S(\sigma_V)$		3.83 ± 1.01	2.93 ± 1.3	2.57 ± 1.49	1.96 ± 0.48	1.63 ± 0.3	1.77 ± 0.33	2.39 ± 0.58	1.09 ± 0.22
		1.92 ± 0.63	1.6 ± 0.77	1.14 ± 0.58	0.82 ± 0.34	0.74 ± 0.18	0.74 ± 0.17	0.86 ± 0.22	0.54 ± 0.11

Table B.2. ISM properties along the Eridu filament, for the fiber (regular font) or shell (bold font) geometry. The values and errors respectively give the mean value in each ~ 5 pc-wide square and the rms dispersion at 0.5–0.7 pc scale within each square.

Square center	LON [deg]	194.05	196.73	199.49	203.1	205.33	206.79	224.21
	LAT [deg]	-56.77	-57.76	-59.73	-61.29	-62.52	-64.22	-62.46
$N_{\text{HI}} [10^{20} \text{ cm}^{-2}]$		2.0	1.8	1.7	2.6	1.9	2.0	0.9
LOS depth [pc]		8.1 ± 0.8	8.4 ± 0.8	11.4 ± 1.1	8.8 ± 0.9	16.1 ± 1.6	9.2 ± 0.9	6.7 ± 0.7
		30.0 ± 3.0						
$n_{\text{HI}} [\text{cm}^{-3}]$		9 ± 4	7 ± 2	5 ± 2	10 ± 1.7	5 ± 1	7 ± 1	5 ± 1
		2 ± 0.8	2 ± 0.5	2 ± 0.7	3 ± 0.5	2 ± 0.6	2 ± 0.2	1 ± 0.2
$S_V [\text{km s}^{-1}]$		1.11	1.49	1.27	1.0	1.01	1.7	0.47
$\sigma_V [\text{km s}^{-1}]$		3.2	3.3	3.7	3.0	2.8	3.3	3.4
$S_\psi [\text{deg}]$		11.62	14.32	18.15	9.41	15.05	19.01	
$T [\text{K}]$		488	440	789	295	1102	408	845
		2847	2867	3202	1592	2673	2317	5868
$x_{\text{ion}} [10^{-4}]$		22.2	21.4	34.6	14.6	45.3	20.1	36.9
		101.2	98.2	108.9	61.4	94.4	82.7	200.4
A_{ion}		2.0	1.9	1.6	2.3	1.5	1.9	1.5
		1.2	1.2	1.2	1.3	1.2	1.2	1.1
$B_{\text{sky}}^{\text{DCF}}(S_V) [\mu\text{G}]$		4.6 ± 2.8	4.9 ± 2.3	4.6 ± 5.4	6.4 ± 4.0	2.2 ± 0.8	4.1 ± 1.6	
		2.4 ± 1.5	2.6 ± 1.2	2.9 ± 3.3	3.4 ± 2.2	1.6 ± 0.6	2.3 ± 0.9	
$B_{\text{sky}}^{\text{DCF}}(\sigma_V) [\mu\text{G}]$		10.7 ± 4.6	9.0 ± 4.6	9.1 ± 5.5	15.4 ± 8.6	5.9 ± 2.2	7.1 ± 3.3	
		5.3 ± 2.3	4.8 ± 2.5	5.6 ± 3.4	8.4 ± 4.7	3.9 ± 1.5	4.0 ± 1.8	
$B_{\text{sky}}^{\text{ST}}(S_V) [\mu\text{G}]$		2.8 ± 1.5	3.2 ± 1.1	2.5 ± 2.0	3.1 ± 1.2	1.5 ± 0.4	3.1 ± 0.7	
		1.4 ± 0.8	1.7 ± 0.6	1.6 ± 1.2	1.7 ± 0.6	1.1 ± 0.3	1.7 ± 0.4	
$B_{\text{sky}}^{\text{ST}}(\sigma_V) [\mu\text{G}]$		7.3 ± 2.6	6.3 ± 2.4	6.0 ± 2.2	8.5 ± 2.5	4.4 ± 1.1	5.7 ± 1.5	
		3.6 ± 1.3	3.4 ± 1.3	3.7 ± 1.3	4.6 ± 1.4	2.9 ± 0.8	3.2 ± 0.8	
$\Gamma_{\text{in,S16}} [10^{-9} \text{ s}^{-1}]$		6.0	5.9	6.0	5.9	6.1	5.9	6.1
		5.9	6.0	5.9	6.2	6.0	6.2	4.9
$\kappa_{\parallel} [10^{28} \text{ cm}^2 \text{ s}^{-1}]$		3.7 ± 0.3	3.6 ± 0.3	3.5 ± 0.1	3.9 ± 0.2	3.4 ± 0.08	3.6 ± 0.07	3.4 ± 0.05
		3.3 ± 0.4	3.3 ± 0.3	3.3 ± 0.2	3.4 ± 0.03	3.3 ± 0.3	3.4 ± 0.06	2.7 ± 0.4
M_A^{DCF}		0.57 ± 0.19	0.71 ± 0.38	0.9 ± 0.7	0.46 ± 0.2	0.74 ± 0.25	0.94 ± 0.37	
M_A^{ST}		0.89 ± 0.14	0.97 ± 0.25	1.05 ± 0.4	0.79 ± 0.18	1.01 ± 0.17	1.13 ± 0.22	
$M_S(S_V)$		1.02 ± 0.53	1.3 ± 0.51	0.88 ± 0.5	1.03 ± 0.27	0.57 ± 0.14	1.48 ± 0.33	0.85 ± 0.16
		0.41 ± 0.23	0.52 ± 0.23	0.44 ± 0.26	0.45 ± 0.12	0.36 ± 0.08	0.62 ± 0.14	0.31 ± 0.03
$M_S(\sigma_V)$		2.93 ± 1.02	2.85 ± 0.97	2.47 ± 0.69	3.05 ± 0.54	1.64 ± 0.42	2.89 ± 0.6	1.7 ± 0.31
		1.18 ± 0.42	1.14 ± 0.42	1.22 ± 0.37	1.34 ± 0.27	1.02 ± 0.25	1.21 ± 0.25	0.61 ± 0.06

8.4 Complementary results : γ -ray point sources

In the Reticulum region, using the 4FGL-DR3 catalogue, we have found 220 γ -ray point sources where 140 are inside the analysis region, excluding the peripheral band. According to Abdollahi et al. (2020), we have calculated the flux of each source, $S(E)$, with the spectral characteristics.

I created four maps of sources. The first two concern sources located in the LMC and SMC regions, while the third map contains sources situated in the lowest dust zones, $\tau_{353} < 3 \times 10^{-6}$. In each of these three maps, the sources will be fitted collectively in the γ -ray model (Eq.4.12). The other 145 sources have been fitted individually. We have not fitted their spectral parameters, but only a correction factor, q_s , in each energy band in order to account for possible changes due to the longer exposure and to the use of a different interstellar background for source detection compared to the analysis of the 4FGL-DR3 catalogue.

Figure 8.5 shows the sources in the analysis region except for those present behind the SMC and LMC regions that have been masked out of the analysis. The sources found in low dust zones and treated collectively are represented by black circles while those treated individually are shown in black crosses. We have retained sources in the low dust regions for individual fits because they were variable and/or bright.

Nearly all the sources ended up having a flux correction factor around 1. We have found three sources with a factor $q > 2$ and two with $q < 0.4$. These sources are represented in Fig.8.5 by green squares and red circles, respectively. The position of these five sources in Galactic longitude and latitude, and their normalisation factors are presented in Table 8.1. The first three sources with upward correction factors are blazars. The flux change is likely due to variability between the 12 years of data considered for the 4FGL-DR3 catalogue and the 14 years of data in our analysis. The first one was already known to be variable. The other two are much fainter objects. The last two sources of Table 8.1 are faint (6.2σ and 5.6σ) and unidentified in the 4FGL-DR3 catalogue. Their flux is now consistent with zero. Even when excluding the lowest energy band and applying a γ -ray fit in 7 energy bands between 0.25-63 GeV, we obtain a negligible emissivity of 0.03 ± 0.38 for the last source. Their disappearance in the present analysis is due to the detection of DNM gas in the Reticulum and North Hydrus clouds.

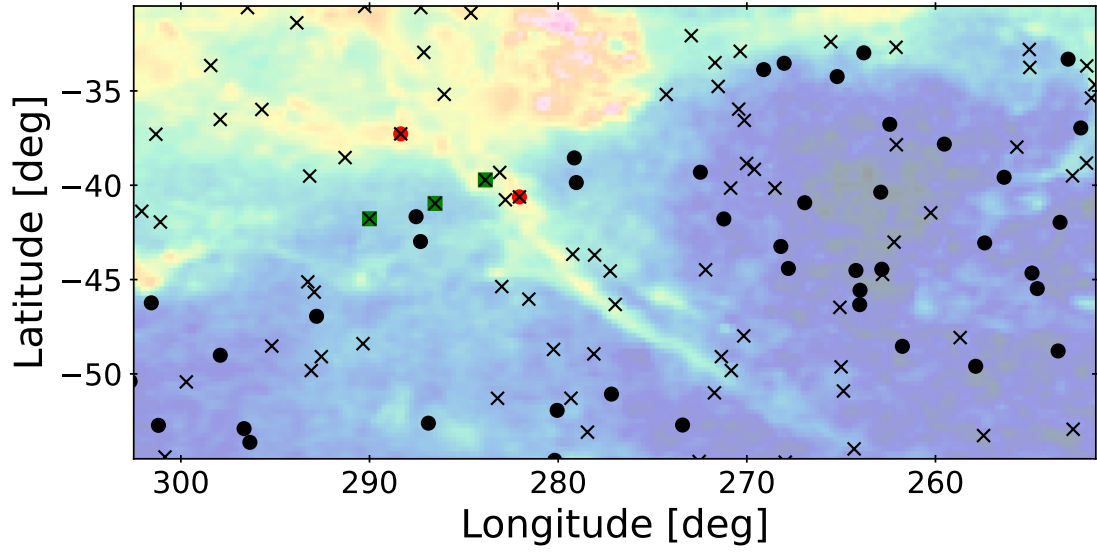


FIGURE 8.5 : Optical depth map at 353 GHz, τ_{353} with all the sources of the analysis region except those in the LMC-SMC zones. The sources fitted collectively are represented by black circles and those fitted individually are shown as black crosses. The red circles represent sources that we do not confirm in the present analysis. The green squares show sources that have a higher average flux over 14 years of data than in the 12-year 4FGL-DR3 catalogue.

Source name	Longitude [deg]	Latitude [deg]	$q \pm dq_{\text{stat}}$
J0301.6-7155	290.00	- 41.78	3.91 ± 0.10
J0331.8-7040	286.53	- 40.96	2.13 ± 0.75
J0358.0-6946	283.86	- 39.72	2.28 ± 0.34
J0358.7-7403	288.35	- 37.28	0.38 ± 0.18
J0357.7-6808	282.05	- 40.62	0.00 ± 0.42 0.03 ± 0.38

TABLE 8.1 : Location and normalisation factors for five specific sources. The last row contains two values. The first one is by doing the γ -ray fits in 8 energy bands in the range 0.16-63 GeV while the second one is for 7 bands between 0.25-63 GeV.

Conclusions and perspectives

Our Solar System resides in a Local Bubble, itself located in a Local Valley of low gas density compared to the surroundings where dense local clouds are present. Figure 9.1 illustrates the 3D distribution of gas around the Solar System (SS), which is symbolised by the red star in the middle of the plot. The colors indicate the height relative to the Galactic plane : red is above, while blue is below the plane. In the valley, the large-scale magnetic field is likely more ordered than in the denser clouds surrounding the valley. Two possible directions have been measured for this large-scale magnetic field as shown by the two lines in the figure, one from the dust polarisation in the local ISM, the other closer to the Sun from the magnetic-field wrapping around the heliosphere.

Since the launch of the *Fermi* observatory, scientists have measured precise γ -ray emissivities in local clouds at hundreds of parsecs around the Solar System, relying on the radiation emitted by hadronic interactions between CRs and the ISM. Most of clouds emissivities are consistent between each other and compatible with the average one, q_{LIS} , calculated in the H I gas between 10° and 70° in Galactic latitude. In 2019, Joubaud et al. (2020) serendipitously noticed that one cloud exhibited a lower γ -ray emissivity compared to the other clouds. This cloud is called Eridu and is located outside the edge of the Orion-Eridanus bubble (see Fig.6.1) at an altitude of 200 pc below the Galactic plane and at a distance of 300 ± 30 pc from the Sun. It is composed of purely H I gas and optically thin to H I line radiation, so the uncertainties in the gas mass are small. Furthermore, given the gas column densities found in that cloud, there is no penetration problem for CRs, especially for the chosen energy range. Therefore, one can concluded that there is a deficit of CRs in Eridu compared to all the other local clouds previously studied.

Eridu and the Sun are both located in the Local Valley. They may be connected by the large-scale magnetic field (see Fig.6). Therefore, we have compared the flux of CRs penetrating this cloud with that measured inside the Solar System and just outside the heliosphere. To do that, we have used the effective cross-sections of hadronic interactions provided by the Kamae parameterisation (Kamae et al., 2006), the Kachelrieß matrices based on the QGSJET-II-04m simulations (Kachelrieß et al., 2019), and the matrices obtained from the FLUKA simulation (Mazziotta et al., 2016). First, we find that bremsstrahlung emission accounts for at least 15% of the total emission in the 1-kpc-wide region around the Sun for energies below a GeV. Second, we found a difference of 30.3 ± 4.3 % between the different cross-sections in the 0.25–10 GeV energy range making it impossible to conclude whether the average CR spectrum measured in

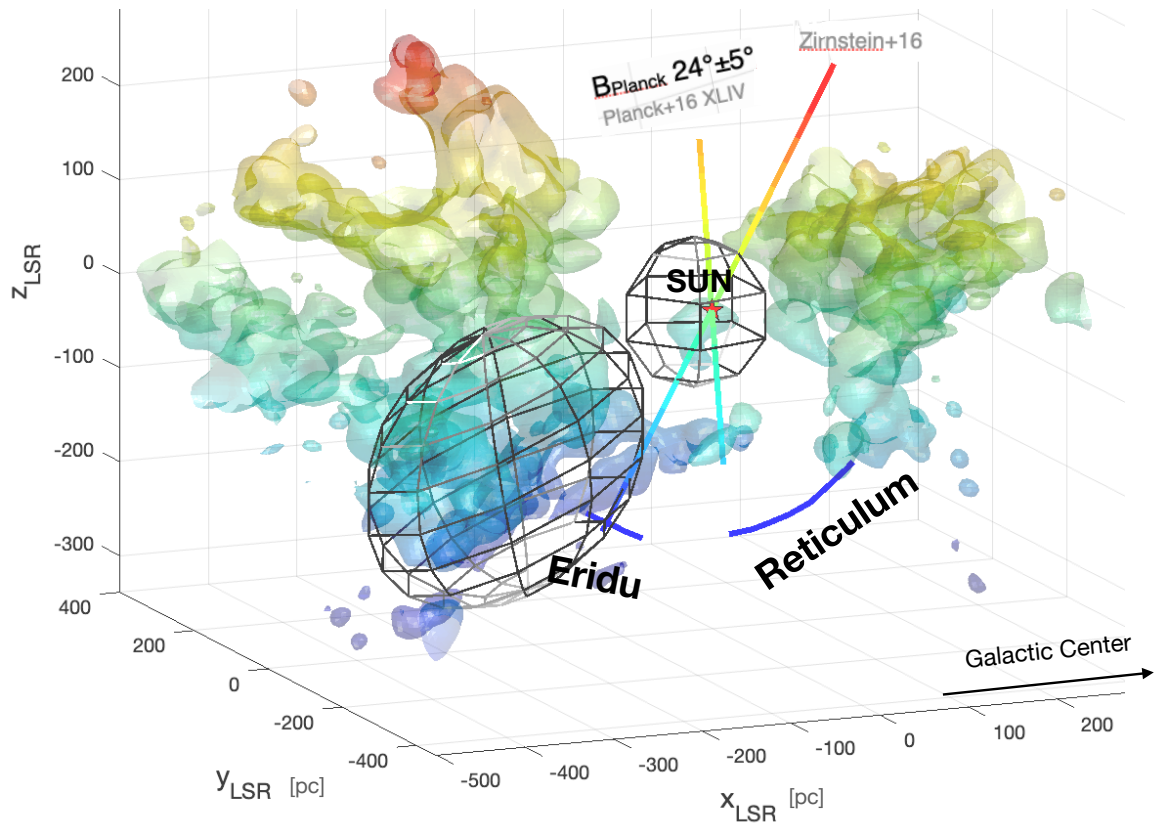


FIGURE 9.1 : A 3D gas distribution around the Solar System represented by the red star. The data are obtained by Lallement et al. (2019). Red and blue colors represent respectively the local clouds above and below the Galactic plane. Two possible directions of the magnetic-field in the valley are represented by the two oblique lines. The middle sphere is the local bubble around the Solar System and the second one is the Orion-Eridanus superbubble.

local clouds around the Sun is comparable or $\sim 25\%$ superior to that passing the Solar System. Moreover, we cannot determine whether the CR flux reaching the Solar System is close to that of Eridu or if Eridu indeed has a deficit of CR flux. More experiments should be conducted, especially with low-energy accelerators (below TeV), to firmly establish the cross sections of hadronic interactions, at least for low-Z nuclei. The present cross-sections well match the high-energy LHC data, but the uncertainties at low energies prevent us from studying GeV CRs, which represent an important component in the Galaxy.

In order to try and understand the change in CR flux within Eridu, we have explored another filament, Reticulum, which shares similar characteristics with Eridu. Reticulum is located at the rim of the local valley, as indicated in Fig.6.1, at a distance ranging between 170 pc and 270 pc from Eridu given their lengths. Both filaments are inclined with respect to the Galactic plane and have well-ordered magnetic field lines aligned with the filament axis. However, we

have found that the γ -ray emissivity per gas nucleon, and consequently the CR flux, in Eridu is 1.57 ± 0.09 times lower than that in Reticulum. By varying the H α optical thickness of the clouds, the smallest difference we can find between the two filaments becomes $32 \pm 8\%$. Therefore, Eridu remains distinct with a significant deficit in CR flux.

Through the 21 cm H α spectral lines from the analysis region, we have identified 6 other atomic clouds : 3 in the Hydrus constellation, 2 in Dorado and 1 in Horologium. They are all different in space, velocity and shape which allowed us to fit them individually in order to extract dust opacity and γ -ray emissivity for each one of them. The γ -ray emissivities are presented in Fig.9.2. We can see that Reticulum, North Hydrus, South Hydrus and East Dorado have a γ -ray emissivity compatible with the average q_{LIS} in the energies between 0.16 GeV and 63 GeV. The Far Hydrus and West Dorado have a relatively lower γ -ray emissivity, but that is because they are not well detected at the edge of the γ -ray fit region. According to Fig.3 in the second paper (see Sec.8.3), we can see that the major parts of the clouds are outside the analysis region. The low γ -ray emissivity of Horologium should also be revisited because Figure 8.3 shows that there is another component towards the Horologium line of sight that we have not separated in two components because the clouds extended much further out of the Reticulum analysis region. Because the present analysis region only partially encompassed those clouds, a detailed study of the Horologium, Far Hydrus and West Dorado should be done with a better gas velocity component separation to re-investigate their relatively low γ -ray emissivities. The Horologium is of particular interest because of the large height of the cloud with respect to the Galactic plane, similar to Eridu.

By combining the energy integral of the γ -ray emissivities we have obtained in this work with those previously found in other local clouds, we can plot how the emissivity in the 0.4–10 GeV energy band evolves as a function of absolute height above the Galactic plane, up to 300 pc, in Fig. 9.3. If we add the emissivities found by Tibaldo et al. (2015) in intermediate-velocity H α clouds at altitudes around 1 kpc, and upper limits to high-velocity H α clouds, we obtain the larger scale trend shown Fig.9.4.

Figure 9.3 shows a systematic decrease by a factor nearly two in emissivity over only 300 pc of altitude. Eridu stands as the lowest γ -ray emissivity cloud below 300 pc and revisiting the emissivity values of West Doradus and Horologium as well as adding other low-altitude clouds to this trend would be extremely useful to investigate how the emissivity gradient compares with model predictions for the CR halo. Those models are reviewed by Dogiel et al. (2020). The emissivity decline is at variance with the two models shown in Fig.6.4 or with the large halo size of 5_{-2}^{+3} kpc recently inferred from AMS-02 data (Weinrich et al., 2020). The vertical distribution of CRs and the existence of a break near 200–300 GeV/n in their spectra are important complementary facets of how advection and diffusion compete in CR propagation, hence of how advection by the local Galactic wind (Schlickeiser et al., 2014) and self-generated turbulence (which locks the particles in Alfvénic advection) on the one hand, and diffusion by ISM disk turbulence cascades on the other hand influence particle transport and set the halo size. The transition from neutral to ionised gas plays a crucial role in the CR vertical gradient, especially at the energies below the break that are probed in γ rays (Dogiel et al., 2020).

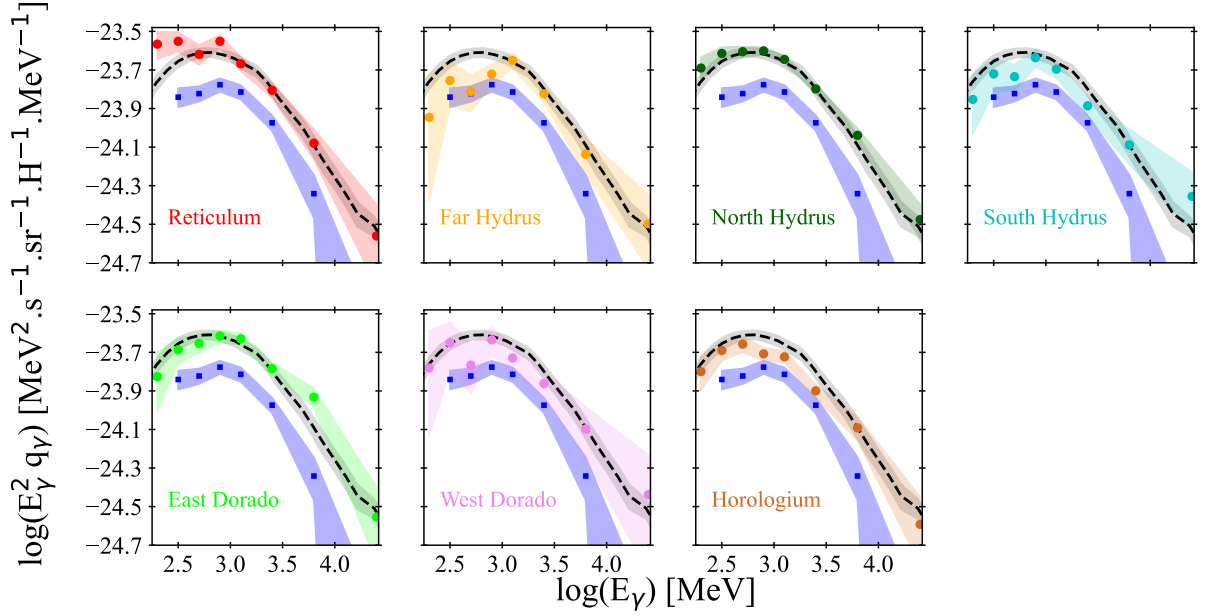


FIGURE 9.2 : Spectral evolution of the γ -ray emissivities per gas nucleon in the Eridu cloud (blue) and the different clouds found in the analysis region. The grey curve gives the average q_{LIS} emissivity measured at latitudes $10^\circ \leq |b| \leq 70^\circ$ (Casandjian, 2015). The emissivities are shown for the HI optical-depth correction that best fits the γ -ray data ($T_{\text{S}} = 100$ K for Eridu, 140 K for q_{LIS} , and optically thin for the others). The shaded bands include the statistical and systematic uncertainties.

We have two filamentary clouds situated on either side of the Local Valley at comparable distances from the Sun. Both of them exhibit ordered magnetic fields aligned with the filament axis and inclined relative to the Galactic plane. They have similar gas column densities, but different CR fluxes in the energy range of 0.16-63 GeV. We have delved deeper into the differences between these two clouds to understand this flux change. First, we have found that both clouds have magnetic pressure of a similar magnitude as the thermal ones, and both have a B_{sky} strength on the order of a few microGauss. With two different assumptions about the filament geometry, we find that the denser gas in Reticulum is in the cold CNM phase (which is consistent with the detection of DNM gas in the cloud) whereas the more diffuse gas in Eridu is in the unstable LNM phase. MHD simulations should be conducted to study the level of magnetic-field tangling and stretching in the different atomic and molecular gas phases or behind a slow shock in shell compression to search for differences that might impact CR propagation.

Considering that GeV CRs scatter off Alfvén waves excited by streaming instabilities in the self-confinement scenario, we expect more damping in the denser Reticulum, implying a lower γ -ray emissivity than in Eridu. We have, however, found that the difference in κ_{\parallel} diffusion coefficient between the two filaments is small. CRs escape from both clouds at the same velocity. For a characteristic CR gradient scale length ℓ_{cr} of 200 pc, the κ_{\parallel} values that we find in these single clouds are compatible with the average measurements in the Milky Way (see Chapter 5). It is important to keep in mind that the growth and damping rates of Alfvén waves were

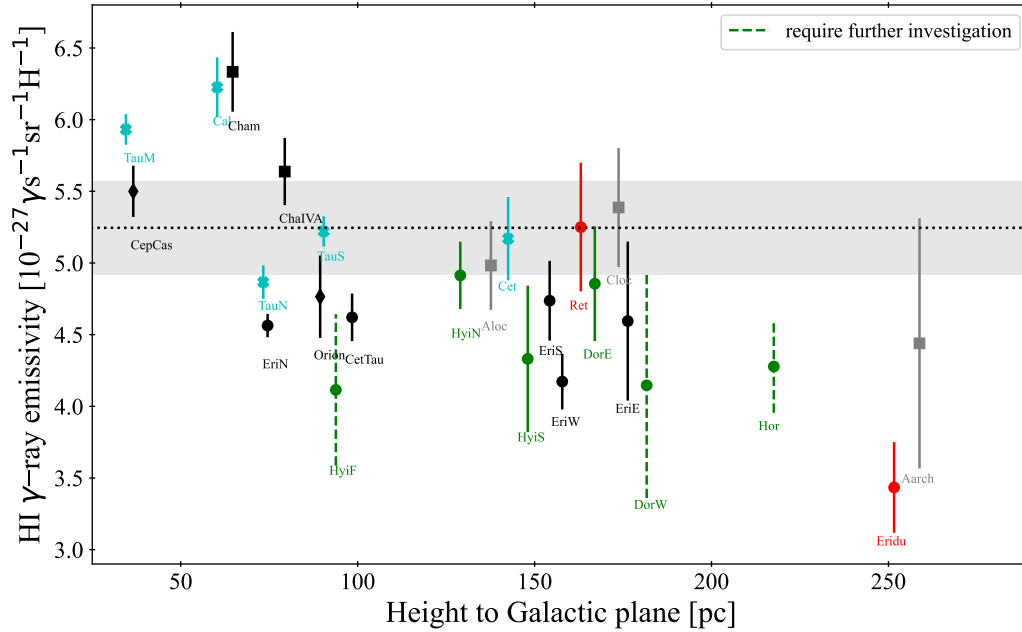


FIGURE 9.3 : γ -ray emissivities of HI clouds as a function of their absolute altitude with respect to the Galactic plane. The emissivity values in the 0.4–10 GeV band and statistical error bars are given for Reticulum and Eridu in red, the 6 clouds of the present analysis in green, the clouds studied by Remy et al. (2017b) in cyan, those by Tibaldo et al. (2015) in grey, those by Joubaud et al. (2019) as black circles, the Chamaelon and IVA from Planck Collaboration, Fermi Collaboration, et al. (2015) as black squares, and black diamonds for Cepheus-Cassiopeia from Abdo et al. (2010) and Orion from Ackermann, Ajello, Allafort, et al. (2012). The data points that require further investigation and confirmation are shown with dashed lines. The grey rectangle represents the average emissivity and $\pm 1\sigma$ uncertainty obtained by Casandjian (2015) in the local atomic ISM.

estimated on a parsec scale, while in reality, the important Alfvén waves are on the order of the particle gyroradius at micro-parsecs.

Atomic filamentary clouds are characterised by a magnetic field aligned with the filament’s axis, whereas this field becomes perpendicular or disordered in dense molecular regions. Reticulum contains clumps of molecular DNM gas, which is not the case for Eridu. The magnetic field may therefore be more tangled and reduce the collective velocity of CRs in the case of Reticulum. By studying the gas velocity dispersion, we found that turbulence is mildly supersonic along both clouds in the fiber geometry, and trans-sonic in the warmer shell geometry. This means that both clouds contain slightly compressible gas. Regarding the dispersion of the magnetic field orientation, Reticulum has a slightly more ordered field, which is expected since it is more compact than Eridu. On a parsec scale, we can conclude that magnetic field lines are not very tangled, which does not reduce the escape velocity of CRs in Reticulum. On the

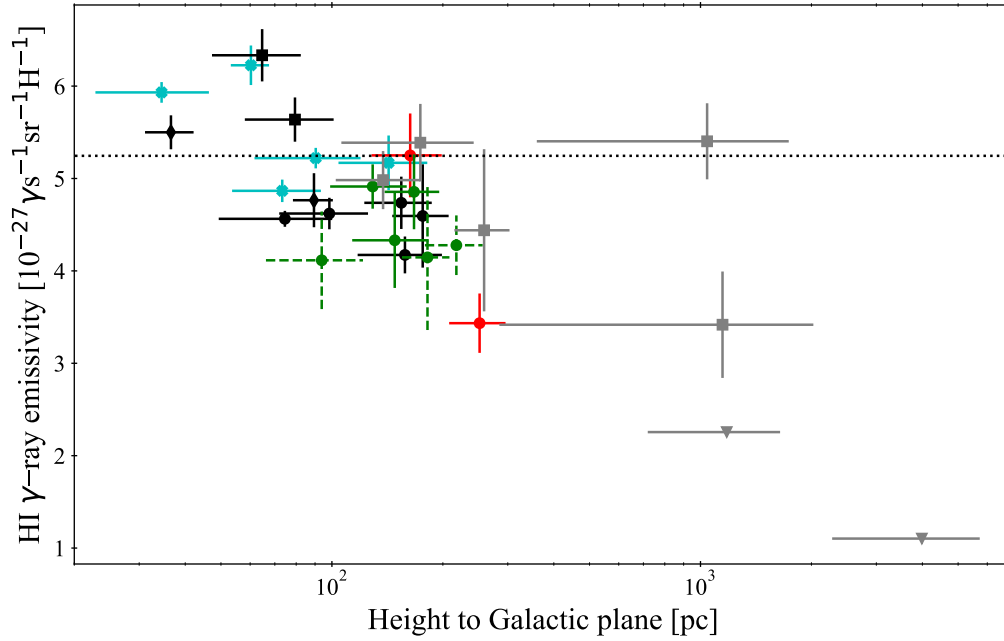


FIGURE 9.4 : The same as Fig.9.3 but adding more clouds at high altitude. The horizontal error bars are due to the distance uncertainties.

contrary, they stream along more ordered field lines, compared to Eridu, over a large fraction of the filament length.

Whether CRs are self-confined in the clouds or following tangled field lines driven by external turbulence, we find similar diffusion properties between Reticulum and Eridu. The 57% difference in γ -ray emissivity between both clouds remains therefore unexplained. Another aspect that should be examined is the environment of each filament. According to Zweibel (2013), the wave growth rate relates to the degree of CR velocity anisotropy, hence to the ambient CR density gradient, which could differ in the vicinity of both clouds.

In the end, I can say that we provide to the community two test cases to study CR propagation more profoundly, especially since there is a difference of six orders of magnitude between what we can infer in the cloud at big scale and what is actually happening at tiny scales where the CRs are reacting to turbulence.

Bibliographie

- Abdo, A. A., Ackermann, M., Ajello, M., Baldini, L., Ballet, J., Barbiellini, G., . . . Fermi/LAT Collaboration (2010, February). Fermi Observations of Cassiopeia and Cepheus : Diffuse Gamma-ray Emission in the Outer Galaxy. *ApJ*, 710(1), 133-149. doi: 10.1088/0004-637X/710/1/133
- Abdollahi, S., Acero, F., Ackermann, M., Ajello, M., Atwood, W. B., Axelsson, M., . . . Zaharijas, G. (2020, March). Fermi Large Area Telescope Fourth Source Catalog. *ApJ Supp.*, 247(1), 33. doi: 10.3847/1538-4365/ab6bcb
- Abeyssekara, A. U., Alfaro, R., Alvarez, C., Arceo, R., Arteaga-Velázquez, J. C., Avila Rojas, D., . . . IceCube Collaboration (2019, January). All-sky Measurement of the Anisotropy of Cosmic Rays at 10 TeV and Mapping of the Local Interstellar Magnetic Field. *ApJ*, 871(1), 96. doi: 10.3847/1538-4357/aaf5cc
- Acero, F., Ackermann, M., Ajello, M., Albert, A., Baldini, L., Ballet, J., . . . Zimmer, S. (2016, April). Development of the Model of Galactic Interstellar Emission for Standard Point-source Analysis of Fermi Large Area Telescope Data. *ApJ Supp.*, 223(2), 26. doi: 10.3847/0067-0049/223/2/26
- Ackermann, M., Ajello, M., Allafort, A., Baldini, L., Ballet, J., Barbiellini, G., . . . Bontemps, S. (2012, February). The cosmic-ray and gas content of the Cygnus region as measured in γ -rays by the Fermi Large Area Telescope. *A&A*, 538, A71. doi: 10.1051/0004-6361/201117539
- Ackermann, M., Ajello, M., Allafort, A., Baldini, L., Ballet, J., Bastieri, D., . . . Yang, Z. (2012, August). GeV Observations of Star-forming Galaxies with the Fermi Large Area Telescope. *ApJ*, 755(2), 164. doi: 10.1088/0004-637X/755/2/164
- Ackermann, M., Ajello, M., Atwood, W. B., Baldini, L., Ballet, J., Barbiellini, G., . . . Zimmer, S. (2012, May). Fermi-LAT Observations of the Diffuse γ -Ray Emission : Implications for Cosmic Rays and the Interstellar Medium. , 750(1), 3. doi: 10.1088/0004-637X/750/1/3
- Adriani, O., Akaike, Y., Asano, K., Asaoka, Y., Bagliesi, M. G., Berti, E., . . . Calet Collaboration (2019, May). Direct Measurement of the Cosmic-Ray Proton Spectrum from 50 GeV to 10 TeV with the Calorimetric Electron Telescope on the International Space Station. *Phys. Rev. Letters*, 122(18), 181102. doi: 10.1103/PhysRevLett.122.181102
- Adriani, O., Akaike, Y., Asano, K., Asaoka, Y., Bagliesi, M. G., Bigongiari, G., . . . Calet Collaboration (2017, November). Energy Spectrum of Cosmic-Ray Electron and

- Positron from 10 GeV to 3 TeV Observed with the Calorimetric Electron Telescope on the International Space Station. *Physical Review Letters*, 119(18), 181101. doi: 10.1103/PhysRevLett.119.181101
- Adriani, O., Akaike, Y., Asano, K., Asaoka, Y., Berti, E., Bigongiari, G., . . . Calet Collaboration (2022, December). Cosmic-Ray Boron Flux Measured from 8.4 GeV/n to 3.8 TeV/n with the Calorimetric Electron Telescope on the International Space Station. *Physical Review Letters*, 129(25), 251103. doi: 10.1103/PhysRevLett.129.251103
- Adriani, O., Barbarino, G. C., Bazilevskaya, G. A., Bellotti, R., Boezio, M., Bogomolov, E. A., . . . Zverev, V. G. (2009, April). An anomalous positron abundance in cosmic rays with energies 1.5-100GeV. *Nature*, 458(7238), 607-609. doi: 10.1038/nature07942
- Adriani, O., Barbarino, G. C., Bazilevskaya, G. A., Bellotti, R., Boezio, M., Bogomolov, E. A., . . . Zverev, V. G. (2011, April). PAMELA Measurements of Cosmic-Ray Proton and Helium Spectra. *Science*, 332(6025), 69. doi: 10.1126/science.1199172
- Adriani, O., Barbarino, G. C., Bazilevskaya, G. A., Bellotti, R., Boezio, M., Bogomolov, E. A., . . . Zverev, V. G. (2014, November). The PAMELA Mission : Heralding a new era in precision cosmic ray physics. *Physics Reports*, 544(4), 323-370. doi: 10.1016/j.physrep.2014.06.003
- Aguilar, M., Aisa, D., Alpat, B., Alvino, A., Ambrosi, G., Andeen, K., . . . AMS Collaboration (2014, November). Precision Measurement of the ($e^+ + e^-$) Flux in Primary Cosmic Rays from 0.5 GeV to 1 TeV with the Alpha Magnetic Spectrometer on the International Space Station. *Physical Review Letters*, 113(22), 221102. doi: 10.1103/PhysRevLett.113.221102
- Aguilar, M., Aisa, D., Alpat, B., Alvino, A., Ambrosi, G., Andeen, K., . . . AMS Collaboration (2015, May). Precision Measurement of the Proton Flux in Primary Cosmic Rays from Rigidity 1 GV to 1.8 TV with the Alpha Magnetic Spectrometer on the International Space Station. *Phys. Rev. Letters*, 114(17), 171103. doi: 10.1103/PhysRevLett.114.171103
- Aguilar, M., Ali Cavasonza, L., Alpat, B., Ambrosi, G., Arruda, L., Attig, N., . . . AMS Collaboration (2023, May). Properties of Cosmic-Ray Sulfur and Determination of the Composition of Primary Cosmic-Ray Carbon, Neon, Magnesium, and Sulfur : Ten-Year Results from the Alpha Magnetic Spectrometer. *Physical Review Letters*, 130(21), 211002. doi: 10.1103/PhysRevLett.130.211002
- Aguilar, M., Ali Cavasonza, L., Ambrosi, G., Arruda, L., Attig, N., Aupetit, S., . . . AMS Collaboration (2016, December). Precision Measurement of the Boron to Carbon Flux Ratio in Cosmic Rays from 1.9 GV to 2.6 TV with the Alpha Magnetic Spectrometer on the International Space Station. *Physical Review Letters*, 117(23), 231102. doi: 10.1103/PhysRevLett.117.231102
- Aguilar, M., Ali Cavasonza, L., Ambrosi, G., Arruda, L., Attig, N., Aupetit, S., . . . AMS Collaboration (2018, January). Observation of New Properties of Secondary Cosmic Rays Lithium, Beryllium, and Boron by the Alpha Magnetic Spectrometer on the International Space Station. *Physical Review Letters*, 120(2), 021101. doi: 10.1103/PhysRevLett.120.021101
- Aharonian, F., Akhperjanian, A. G., Anton, G., Barres de Almeida, U., Bazer-Bachi, A. R., Becherini, Y., . . . Zech, A. (2009, December). Probing the ATIC peak in the cosmic-

- ray electron spectrum with H.E.S.S. *A&A*, 508(2), 561-564. doi: 10.1051/0004-6361/200913323
- Aharonian, F. A. (2013, March). Gamma rays from supernova remnants. *Astroparticle Physics*, 43, 71-80. doi: 10.1016/j.astropartphys.2012.08.007
- Aharonian, F. A., Atoyan, A. M., & Voelk, H. J. (1995, February). High energy electrons and positrons in cosmic rays as an indicator of the existence of a nearby cosmic tevatron. *A&A*, 294, L41-L44.
- Ahn, H. S., Allison, P., Bagliesi, M. G., Beatty, J. J., Bigongiari, G., Childers, J. T., ... Zinn, S. Y. (2010, May). Discrepant Hardening Observed in Cosmic-ray Elemental Spectra. *ApJL*, 714(1), L89-L93. doi: 10.1088/2041-8205/714/1/L89
- Ahn, H. S., Allison, P. S., Bagliesi, M. G., Beatty, J. J., Bigongiari, G., Boyle, P. J., ... Zinn, S. Y. (2008, October). Measurements of cosmic-ray secondary nuclei at high energies with the first flight of the CREAM balloon-borne experiment. *Astroparticle Physics*, 30(3), 133-141. doi: 10.1016/j.astropartphys.2008.07.010
- Ajello, M., Atwood, W. B., Axelsson, M., Bagagli, R., Bagni, M., Baldini, L., ... Zaharijas, G. (2021, September). Fermi Large Area Telescope Performance after 10 Years of Operation. *ApJ Supp.*, 256(1), 12. doi: 10.3847/1538-4365/ac0ceb
- Alfvén, H. (1942, October). Existence of Electromagnetic-Hydrodynamic Waves. , 150(3805), 405-406. doi: 10.1038/150405d0
- Aloisio, R., & Blasi, P. (2013, July). Propagation of galactic cosmic rays in the presence of self-generated turbulence. *JCAP*, 2013(7), 001. doi: 10.1088/1475-7516/2013/07/001
- Amato, E., & Blasi, P. (2018, November). Cosmic ray transport in the Galaxy : A review. *Advances in Space Research*, 62(10), 2731-2749. doi: 10.1016/j.asr.2017.04.019
- An, Q., Asfandiyarov, R., Azzarello, P., Bernardini, P., Bi, X. J., Cai, M. S., ... Zimmer, S. (2019, September). Measurement of the cosmic ray proton spectrum from 40 GeV to 100 TeV with the DAMPE satellite. *Science Advances*, 5(9), eaax3793. doi: 10.1126/sciadv.aax3793
- Antoni, T., Apel, W., Badea, A., Bekk, K., Bercuci, A., Blümer, J., ... others (2005). Cascade measurements of energy spectra for elemental groups of cosmic rays : Results and open problems. *Astroparticle physics*, 24(1-2), 1–25.
- Armillotta, L., Ostriker, E. C., & Jiang, Y.-F. (2021, November). Cosmic-Ray Transport in Simulations of Star-forming Galactic Disks. *ApJ*, 922(1), 11. doi: 10.3847/1538-4357/ac1db2
- Armillotta, L., Ostriker, E. C., & Jiang, Y.-F. (2022, April). Cosmic-Ray Transport in Varying Galactic Environments. *ApJ*, 929(2), 170. doi: 10.3847/1538-4357/ac5fa9
- Asplund, M., Grevesse, N., Sauval, A. J., & Scott, P. (2009, September). The Chemical Composition of the Sun. *ARAAS*, 47(1), 481-522. doi: 10.1146/annurev.astro.46.060407.145222
- Atwood, W., Albert, A., Baldini, L., Tinivella, M., Bregeon, J., Pesce-Rollins, M., ... Zimmer, S. (2013, March). Pass 8 : Toward the Full Realization of the Fermi-LAT Scientific Potential. *arXiv e-prints*, arXiv :1303.3514. doi: 10.48550/arXiv.1303.3514
- Atwood, W. B., Abdo, A. A., Ackermann, M., Althouse, W., Anderson, B., Axelsson, M., ... Ziegler, M. (2009, June). The Large Area Telescope on the Fermi Gamma-Ray Space Telescope Mission. *ApJ*, 697(2), 1071-1102. doi: 10.1088/0004-637X/697/2/1071
- Basu, S. (2000, September). Magnetic Fields and the Triaxiality of Molecular Cloud Cores. ,

- 540(2), L103-L106. doi: 10.1086/312885
- Batista, P. I., Vecchi, M., Vecchi, M., Maurin, D., Derome, L., Boudaud, M., . . . Serpico, P. D. (2019, July). Is the B/C slope in AMS-02 data actually telling us something about the diffusion coefficient slope ? In *36th international cosmic ray conference (icrc2019)* (Vol. 36, p. 145). doi: 10.22323/1.358.0145
- Beattie, J. R., Krumholz, M. R., Skalidis, R., Federrath, C., Seta, A., Crocker, R. M., . . . Kriel, N. (2022, October). Energy balance and Alfvén Mach numbers in compressible magneto-hydrodynamic turbulence with a large-scale magnetic field. *MNRAS*, *515*(4), 5267-5284. doi: 10.1093/mnras/stac2099
- Bell, A. R. (1978, January). The acceleration of cosmic rays in shock fronts - I. *MNRAS*, *182*, 147-156. doi: 10.1093/mnras/182.2.147
- Bell, A. R., & Lucek, S. G. (2001, March). Cosmic ray acceleration to very high energy through the non-linear amplification by cosmic rays of the seed magnetic field. *MNRAS*, *321*(3), 433-438. doi: 10.1046/j.1365-8711.2001.04063.x
- Benyamin, D., Nakar, E., Piran, T., & Shaviv, N. J. (2016, July). The B/C and Sub-iron/Iron Cosmic Ray Ratios—Further Evidence in Favor of the Spiral-Arm Diffusion Model. *ApJ*, *826*(1), 47. doi: 10.3847/0004-637X/826/1/47
- Bergström, L., Bringmann, T., & Edsjö, J. (2008, November). New positron spectral features from supersymmetric dark matter : A way to explain the PAMELA data ? *Physical Review D*, *78*(10), 103520. doi: 10.1103/PhysRevD.78.103520
- Binns, W. R., Bose, R. G., Braun, D. L., Brandt, T. J., Daniels, W. M., De Nolfo, G. A., . . . Wiedenbeck, M. E. (2013, January). The Super-TIGER Experiment. In *International cosmic ray conference* (Vol. 33, p. 502).
- Binns, W. R., Israel, M., Wiedenbeck, M., Cummings, A., Leske, R., Mewaldt, R., . . . von Roseninge, T. (2019, July). Elemental Source Composition Measurements and the Origin of Galactic Cosmic Rays. In *36th international cosmic ray conference (icrc2019)* (Vol. 36, p. 36). doi: 10.22323/1.358.0036
- Biskamp, D. (2003). *Magnetohydrodynamic Turbulence*.
- Blandford, R. D., & Ostriker, J. P. (1978, April). Particle acceleration by astrophysical shocks. *ApJL*, *221*, L29-L32. doi: 10.1086/182658
- Blasi, P. (2009, July). Origin of the Positron Excess in Cosmic Rays. *Physical Review Letters*, *103*(5), 051104. doi: 10.1103/PhysRevLett.103.051104
- Blasi, P., Amato, E., & Serpico, P. D. (2012, August). Spectral Breaks as a Signature of Cosmic Ray Induced Turbulence in the Galaxy. *Physical Review Letters*, *109*(6), 061101. doi: 10.1103/PhysRevLett.109.061101
- Bloemen, J. B. G. M., Strong, A. W., Mayer-Hasselwander, H. A., Blitz, L., Cohen, R. S., Dame, T. M., . . . Lebrun, F. (1986, January). The radial distribution of galactic gamma rays. III - The distribution of cosmic rays in the Galaxy and the CO-H2 calibration. , *154*, 25-41.
- Bobik, P., Boella, G., Boschini, M. J., Consolandi, C., Della Torre, S., Gervasi, M., . . . Tacconi, M. (2012, February). Systematic Investigation of Solar Modulation of Galactic Protons for Solar Cycle 23 Using a Monte Carlo Approach with Particle Drift Effects and Latitudinal Dependence. *ApJ*, *745*(2), 132. doi: 10.1088/0004-637X/745/2/132
- Bobik, P., Boella, G., Boschini, M. J., Consolandi, C., Della Torre, S., Gervasi, M., . . . Tacconi, M. (2013, January). Latitudinal Dependence of Cosmic Rays Modulation at 1 AU and

- Interplanetary Magnetic Field Polar Correction. *Advances in Astronomy*, 2013, 793072. doi: 10.1155/2013/793072
- Bolatto, A. D., Wolfire, M., & Leroy, A. K. (2013, August). The CO-to-H₂ Conversion Factor. *ARAAS*, 51(1), 207-268. doi: 10.1146/annurev-astro-082812-140944
- Borriello, E., Maccione, L., & Cuoco, A. (2012, March). Dark matter electron anisotropy : A universal upper limit. *Astroparticle Physics*, 35(8), 537-546. doi: 10.1016/j.astropartphys.2011.12.001
- Boschini, M. J., Della Torre, S., Gervasi, M., Grandi, D., Jóhannesson, G., La Vacca, G., ... Tacconi, M. (2020, October). Inference of the Local Interstellar Spectra of Cosmic-Ray Nuclei $Z \leq 28$ with the GALPROP-HELMOD Framework. *ApJs*, 250(2), 27. doi: 10.3847/1538-4365/aba901
- Boulares, A., & Cox, D. P. (1990, December). Galactic Hydrostatic Equilibrium with Magnetic Tension and Cosmic-Ray Diffusion. , 365, 544. doi: 10.1086/169509
- Braginskii, S. I. (1965, January). Transport Processes in a Plasma. *Reviews of Plasma Physics*, 1, 205.
- Bringmann, T., Donato, F., & Lineros, R. A. (2012, January). Radio data and synchrotron emission in consistent cosmic ray models. , 2012(1), 049. doi: 10.1088/1475-7516/2012/01/049
- Burlaga, L. F., Florinski, V., & Ness, N. F. (2015, May). In Situ Observations of Magnetic Turbulence in the Local Interstellar Medium. , 804(2), L31. doi: 10.1088/2041-8205/804/2/L31
- Burlaga, L. F., Ness, N. F., Gurnett, D. A., & Kurth, W. S. (2013, November). Evidence for a Shock in Interstellar Plasma : Voyager 1. *ApJL*, 778(1), L3. doi: 10.1088/2041-8205/778/1/L3
- Burn, B. J. (1966, January). On the depolarization of discrete radio sources by Faraday dispersion. *MNRAS*, 133, 67. doi: 10.1093/mnras/133.1.67
- Büsching, I., de Jager, O. C., Potgieter, M. S., & Venter, C. (2008, May). A Cosmic-Ray Positron Anisotropy due to Two Middle-Aged, Nearby Pulsars? *ApJ Letters*, 678(1), L39. doi: 10.1086/588465
- Bustard, C., & Zweibel, E. G. (2021, June). Cosmic-Ray Transport, Energy Loss, and Influence in the Multiphase Interstellar Medium. *ApJ*, 913(2), 106. doi: 10.3847/1538-4357/abf64c
- Bykov, A. M. (2014, November). Nonthermal particles and photons in starburst regions and superbubbles. *A&A Review*, 22, 77. doi: 10.1007/s00159-014-0077-8
- Bykov, A. M., Ellison, D. C., Marcowith, A., & Osipov, S. M. (2018, February). Cosmic Ray Production in Supernovae. *Space Science Reviews*, 214(1), 41. doi: 10.1007/s11214-018-0479-4
- Cabral, B., & Leedom, L. C. (1993). Imaging vector fields using line integral convolution. In *Proceedings of the 20th annual conference on computer graphics and interactive techniques* (pp. 263–270).
- Calore, F., Di Mauro, M., & Donato, F. (2014, November). Diffuse γ -Ray Emission from Galactic Pulsars. , 796(1), 14. doi: 10.1088/0004-637X/796/1/14
- Casandjian, J.-M. (2015, June). Local Hi Emissivity Measured with Fermi-LAT and Implications for Cosmic-Ray Spectra. *ApJ*, 806(2), 240. doi: 10.1088/0004-637X/806/2/240

- Casandjian, J.-M., Ballet, J., Grenier, I., & Remy, Q. (2022, December). Evidence for Large-scale Excesses Associated with Low H I Column Densities in the Sky. I. Dust Excess. *ApJ*, 940(2), 116. doi: 10.3847/1538-4357/ac9731
- Cash, W. (1979, March). Parameter estimation in astronomy through application of the likelihood ratio. *ApJ*, 228, 939-947. doi: 10.1086/156922
- Chandrasekhar, S., & Fermi, E. (1953, July). Magnetic Fields in Spiral Arms. *ApJ*, 118, 113. doi: 10.1086/145731
- Compton, A. H., & Getting, I. A. (1935, June). An Apparent Effect of Galactic Rotation on the Intensity of Cosmic Rays. *Physical Review*, 47(11), 817-821. doi: 10.1103/PhysRev.47.817
- Condon, J. J., & Ransom, S. M. (2016). *Essential Radio Astronomy*.
- Cowsik, R., Pal, Y., Tandon, S., & Verma, R. (1967). Steady state of cosmic-ray nuclei—Their spectral shape and path length at low energies. *Physical Review*, 158(5), 1238.
- Cox, D. P. (2005, September). The Three-Phase Interstellar Medium Revisited. , 43(1), 337-385. doi: 10.1146/annurev.astro.43.072103.150615
- Cristofari, P., Gabici, S., Terrier, R., & Humensky, T. B. (2018, September). On the search for Galactic supernova remnant PeVatrons with current TeV instruments. *MNRAS*, 479(3), 3415-3421. doi: 10.1093/mnras/sty1589
- Crutcher, R. M. (1999, August). Magnetic Fields in Molecular Clouds : Observations Confront Theory. , 520(2), 706-713. doi: 10.1086/307483
- Crutcher, R. M., Wandelt, B., Heiles, C., Falgarone, E., & Troland, T. H. (2010, December). Magnetic Fields in Interstellar Clouds from Zeeman Observations : Inference of Total Field Strengths by Bayesian Analysis. *ApJ*, 725(1), 466-479. doi: 10.1088/0004-637X/725/1/466
- Cummings, A. C., Stone, E. C., Heikkila, B. C., Lal, N., Webber, W. R., Jóhannesson, G., . . . Porter, T. A. (2016, November). Galactic Cosmic Rays in the Local Interstellar Medium : Voyager 1 Observations and Model Results. *ApJ*, 831(1), 18. doi: 10.3847/0004-637X/831/1/18
- Dame, T. M., & Thaddeus, P. (2022, September). A CO Survey of the Entire Northern Sky. *ApJs*, 262(1), 5. doi: 10.3847/1538-4365/ac7e53
- Dampe Collaboration. (2022, November). Detection of spectral hardenings in cosmic-ray boron-to-carbon and boron-to-oxygen flux ratios with DAMPE. *Science Bulletin*, 67(21), 2162-2166. doi: 10.1016/j.scib.2022.10.002
- DAMPE Collaboration, Ambrosi, G., An, Q., Asfandiyarov, R., Azzarello, P., Bernardini, P., . . . Zimmer, S. (2017, December). Direct detection of a break in the teraelectronvolt cosmic-ray spectrum of electrons and positrons. *Nature*, 552(7683), 63-66. doi: 10.1038/nature24475
- Davies, R. D., Booth, R. S., & Wilson, A. J. (1968, December). Interstellar Magnetic Fields determined from Zeeman Effect Measurements. *Nature*, 220(5173), 1207-1210. doi: 10.1038/2201207a0
- Davis, L. (1951, Mar). The Strength of Interstellar Magnetic Fields. *Physical Review*, 81, 890-891. doi: 10.1103/PhysRev.81.890.2
- di Bernardo, G., Evoli, C., Gaggero, D., Grasso, D., Maccione, L., & Mazziotta, M. N. (2011, February). Implications of the cosmic ray electron spectrum and anisotropy measured

- with Fermi-LAT. *Astroparticle Physics*, 34(7), 528-538. doi: 10.1016/j.astropartphys.2010.11.005
- Dickey, J. M., Mebold, U., Stanimirovic, S., & Staveley-Smith, L. (2000, June). Cold Atomic Gas in the Small Magellanic Cloud. *ApJ*, 536(2), 756-772. doi: 10.1086/308953
- Dogiel, V. A., Ivlev, A. V., Chernyshov, D. O., & Ko, C. M. (2020, November). Formation of the Cosmic-Ray Halo : Galactic Spectrum of Primary Cosmic Rays. *ApJ*, 903(2), 135. doi: 10.3847/1538-4357/abba31
- Draine, B. T. (1986, May). Multicomponent, reacting MHD flows. *MNRAS*, 220, 133-148. doi: 10.1093/mnras/220.1.133
- Draine, B. T. (2011). *Physics of the Interstellar and Intergalactic Medium*.
- Drury, L. O., Aharonian, F. A., & Voelk, H. J. (1994, July). The gamma-ray visibility of supernova remnants. A test of cosmic ray origin. *A&A*, 287, 959-971. doi: 10.48550/arXiv.astro-ph/9305037
- Erlykin, A. D., & Wolfendale, A. W. (2015, July). The spectral shapes of hydrogen and helium nuclei in cosmic rays. *Journal of Physics G Nuclear Physics*, 42(7), 075201. doi: 10.1088/0954-3899/42/7/075201
- Everett, J. E., & Zweibel, E. G. (2011, October). The Interaction of Cosmic Rays with Diffuse Clouds. *ApJ*, 739(2), 60. doi: 10.1088/0004-637X/739/2/60
- Evoli, C. (2018, December). *The cosmic-ray energy spectrum*. Zenodo. Retrieved from <https://doi.org/10.5281/zenodo.2360277> doi: 10.5281/zenodo.2360277
- Evoli, C., Blasi, P., Morlino, G., & Aloisio, R. (2018, July). Origin of the Cosmic Ray Galactic Halo Driven by Advected Turbulence and Self-Generated Waves. *Phys. Rev. Letters*, 121(2), 021102. doi: 10.1103/PhysRevLett.121.021102
- Evoli, C., Gaggero, D., Grasso, D., & Maccione, L. (2008, October). Cosmic ray nuclei, antiprotons and gamma rays in the galaxy : a new diffusion model. *Journal of Cosmology and Astroparticle Physics*, 2008(10), 018. doi: 10.1088/1475-7516/2008/10/018
- Evoli, C., Gaggero, D., Grasso, D., & Maccione, L. (2012, May). Common Solution to the Cosmic Ray Anisotropy and Gradient Problems. , 108(21), 211102. doi: 10.1103/PhysRevLett.108.211102
- Evoli, C., Gaggero, D., Vittino, A., Di Mauro, M., Grasso, D., & Mazziotta, M. N. (2018, July). Cosmic-ray propagation with DRAGON2 : II. Nuclear interactions with the interstellar gas. *JCAP*, 2018(7), 006. doi: 10.1088/1475-7516/2018/07/006
- Farmer, A. J., & Goldreich, P. (2004, April). Wave Damping by Magnetohydrodynamic Turbulence and Its Effect on Cosmic-Ray Propagation in the Interstellar Medium. *ApJ*, 604(2), 671-674. doi: 10.1086/382040
- Federrath, C. (2016, December). Magnetic field amplification in turbulent astrophysical plasmas. *Journal of Plasma Physics*, 82(6), 535820601. doi: 10.1017/S0022377816001069
- Fermi, E. (1949, April). On the Origin of the Cosmic Radiation. *Physical Review*, 75(8), 1169-1174. doi: 10.1103/PhysRev.75.1169
- Field, G. B., Goldsmith, D. W., & Habing, H. J. (1969, March). Cosmic-Ray Heating of the Interstellar Gas. , 155, L149. doi: 10.1086/180324
- Finkbeiner, D. P. (2003, June). A Full-Sky H α Template for Microwave Foreground Prediction. *ApJ S*, 146, 407-415. doi: 10.1086/374411
- Gabici, S., & Aharonian, F. A. (2007, August). Searching for Galactic Cosmic-Ray Pevatrons

- with Multi-TeV Gamma Rays and Neutrinos. *ApJ Letters*, 665(2), L131-L134. doi: 10.1086/521047
- Gabici, S., Evoli, C., Gaggero, D., Lipari, P., Mertsch, P., Orlando, E., ... Vittino, A. (2019, January). The origin of Galactic cosmic rays : Challenges to the standard paradigm. *International Journal of Modern Physics D*, 28(15), 1930022-339. doi: 10.1142/S0218271819300222
- Gaggero, D., Maccione, L., Di Bernardo, G., Evoli, C., & Grasso, D. (2013, July). Three-Dimensional Model of Cosmic-Ray Lepton Propagation Reproduces Data from the Alpha Magnetic Spectrometer on the International Space Station. *Physical Review Letters*, 111(2), 021102. doi: 10.1103/PhysRevLett.111.021102
- Gaggero, D., Urbano, A., Valli, M., & Ullio, P. (2015, April). Gamma-ray sky points to radial gradients in cosmic-ray transport. , 91(8), 083012. doi: 10.1103/PhysRevD.91.083012
- Gaustad, J. E., McCullough, P. R., Rosing, W., & Van Buren, D. (2001, November). A Robotic Wide-Angle H α Survey of the Southern Sky. *PASP*, 113(789), 1326-1348. doi: 10.1086/323969
- Génolini, Y., Serpico, P. D., Boudaud, M., Caroff, S., Poulin, V., Derome, L., ... Vecchi, M. (2017, December). Indications for a High-Rigidity Break in the Cosmic-Ray Diffusion Coefficient. *Physical Review Letters*, 119(24), 241101. doi: 10.1103/PhysRevLett.119.241101
- Ginzburg, V. L., & Syrovatskii, S. I. (1964). *The Origin of Cosmic Rays*.
- Gleeson, L. J., & Axford, W. I. (1968, December). Solar Modulation of Galactic Cosmic Rays. *ApJ*, 154, 1011. doi: 10.1086/149822
- Goldreich, P., & Sridhar, S. (1995, January). Toward a Theory of Interstellar Turbulence. II. Strong Alfvénic Turbulence. *ApJ*, 438, 763. doi: 10.1086/175121
- Gong, M., Ostriker, E. C., & Kim, C.-G. (2018, May). The X_{CO} Conversion Factor from Galactic Multiphase ISM Simulations. *ApJ*, 858(1), 16. doi: 10.3847/1538-4357/aab9af
- Green, D. A. (2015, December). Constraints on the distribution of supernova remnants with Galactocentric radius. , 454(2), 1517-1524. doi: 10.1093/mnras/stv1885
- Grenier, I. A., Black, J. H., & Strong, A. W. (2015, August). The Nine Lives of Cosmic Rays in Galaxies. *ARAA*, 53, 199-246. doi: 10.1146/annurev-astro-082214-122457
- Grenier, I. A., Casandjian, J.-M., & Terrier, R. (2005, Feb). Unveiling Extensive Clouds of Dark Gas in the Solar Neighborhood. *Science*, 307(5713), 1292-1295. doi: 10.1126/science.1106924
- Han, J. L. (2017, August). Observing Interstellar and Intergalactic Magnetic Fields. *ARAA*, 55(1), 111-157. doi: 10.1146/annurev-astro-091916-055221
- Hasselmann, K., & Wibberenz, G. (1970, December). A Note on the Parallel Diffusion Coefficient. *ApJ*, 162, 1049. doi: 10.1086/150736
- Haud, U., & Kalberla, P. M. W. (2007, May). Gaussian decomposition of HI surveys. III. Local HI. , 466(2), 555-564. doi: 10.1051/0004-6361:20065796
- Heiles, C., & Crutcher, R. (2005). Magnetic Fields in Diffuse HI and Molecular Clouds. In R. Wielebinski & R. Beck (Eds.), *Cosmic magnetic fields* (Vol. 664, p. 137). doi: 10.1007/3540313966_7
- Heiles, C., & Troland, T. H. (2003, April). The Millennium Arecibo 21 Centimeter Absorption-Line Survey. II. Properties of the Warm and Cold Neutral Media. *ApJ*, 586(2), 1067-1093.

- doi: 10.1086/367828
- Hennebelle, P., & Falgarone, E. (2012, November). Turbulent molecular clouds. *A&A Review*, 20, 55. doi: 10.1007/s00159-012-0055-y
- Heyvaerts, J., & Priest, E. R. (1983, January). Coronal heating by phase-mixed shear Alfvén waves. *A&A*, 117, 220-234.
- HI4PI Collaboration, Ben Bekhti, N., Flöer, L., Keller, R., Kerp, J., Lenz, D., . . . Staveley-Smith, L. (2016, October). HI4PI : A full-sky HI survey based on EBHIS and GASS. *A&A*, 594, A116. doi: 10.1051/0004-6361/201629178
- Hillas, A. M. (2006, October). The cosmic-ray knee and ensuing spectrum seen as a consequence of Bell's self-magnetized SNR shock acceleration process. In *Journal of physics conference series* (Vol. 47, p. 168-177). doi: 10.1088/1742-6596/47/1/021
- Hooper, D., Blasi, P., & Serpico, P. D. (2009, January). Pulsars as the sources of high energy cosmic ray positrons. *JCAP*, 2009(1), 025. doi: 10.1088/1475-7516/2009/01/025
- Hopkins, P. F., Squire, J., Chan, T. K., Quataert, E., Ji, S., Kereš, D., & Faucher-Giguère, C.-A. (2021, March). Testing physical models for cosmic ray transport coefficients on galactic scales : self-confinement and extrinsic turbulence at \sim GeV energies. *MNRAS*, 501(3), 4184-4213. doi: 10.1093/mnras/staa3691
- Hörandel, J. R. (2003, May). On the knee in the energy spectrum of cosmic rays. *Astroparticle Physics*, 19(2), 193-220. doi: 10.1016/S0927-6505(02)00198-6
- Iroshnikov, P. S. (1964, February). Turbulence of a Conducting Fluid in a Strong Magnetic Field. , 7, 566.
- Jenkins, E. B., & Tripp, T. M. (2011, June). The Distribution of Thermal Pressures in the Diffuse, Cold Neutral Medium of Our Galaxy. II. An Expanded Survey of Interstellar C I Fine-structure Excitations. , 734(1), 65. doi: 10.1088/0004-637X/734/1/65
- Jiang, Y.-F., & Oh, S. P. (2018, February). A New Numerical Scheme for Cosmic-Ray Transport. *ApJ*, 854(1), 5. doi: 10.3847/1538-4357/aaa6ce
- Jóhannesson, G., Porter, T. A., & Moskalenko, I. V. (2018, March). The Three-dimensional Spatial Distribution of Interstellar Gas in the Milky Way : Implications for Cosmic Rays and High-energy Gamma-ray Emissions. *ApJ*, 856(1), 45. doi: 10.3847/1538-4357/aab26e
- Jokipii, J. R. (1966, November). Cosmic-Ray Propagation. I. Charged Particles in a Random Magnetic Field. *ApJ*, 146, 480. doi: 10.1086/148912
- Jones, C. F., Crawford, J. H., Engelage, J., Guzik, G. T., Mitchell, W. J., Waddington, J. C., . . . Wefel, P. J. (1990, January). The Leaky Box : An Idea Whose Time is Up? In *21st international cosmic ray conference (icrc21)* (Vol. 3, p. 333).
- Joubaud, T., Grenier, I. A., Ballet, J., & Soler, J. D. (2019, November). Gas shells and magnetic fields in the Orion-Eridanus superbubble. *A&A*, 631, A52. doi: 10.1051/0004-6361/201936239
- Joubaud, T., Grenier, I. A., Casandjian, J. M., Tolksdorf, T., & Schlickeiser, R. (2020, March). The cosmic-ray content of the Orion-Eridanus superbubble. *A&A*, 635, A96. doi: 10.1051/0004-6361/201937205
- Kachelrieß, M., Moskalenko, I. V., & Ostapchenko, S. (2019, December). AAfrag : Interpolation routines for Monte Carlo results on secondary production in proton-proton, proton-nucleus and nucleus-nucleus interactions. *Computer Physics Communications*, 245, 106846. doi: 10.1016/j.cpc.2019.08.001

- Kachelrieß, M., & Ostapchenko, S. (2012, August). Deriving the cosmic ray spectrum from gamma-ray observations. *Phys. Rev. D*, 86(4), 043004. doi: 10.1103/PhysRevD.86.043004
- Kalberla, P. M. W., & Haud, U. (2015, June). GASS : The Parkes Galactic All-Sky Survey. Update : improved correction for instrumental effects and new data release. *A&A*, 578, A78. doi: 10.1051/0004-6361/201525859
- Kamae, T., Karlsson, N., Mizuno, T., Abe, T., & Koi, T. (2006, August). Parameterization of γ , $e^{+/-}$, and Neutrino Spectra Produced by p-p Interaction in Astronomical Environments. *ApJ*, 647(1), 692-708. doi: 10.1086/505189
- Kamal Youssef, F., & Grenier, I. (2024). Cosmic-ray diffusion in two local filamentary clouds. *A&A*. *A&A*.
- Kennel, C. F., & Engelmann, F. (1966, December). Velocity Space Diffusion from Weak Plasma Turbulence in a Magnetic Field. *Physics of Fluids*, 9(12), 2377-2388. doi: 10.1063/1.1761629
- Kerszberg, D., Kraus, M., Kolitzus, D., Egberts, K., Funk, S., Lenain, J., ... Vincent, P. (2017). The cosmic-ray electron spectrum measured with HESS. In *International cosmic ray conference, [cri215]*.
- Kim, J.-G., Gong, M., Kim, C.-G., & Ostriker, E. C. (2023, January). Photochemistry and Heating/Cooling of the Multiphase Interstellar Medium with UV Radiative Transfer for Magnetohydrodynamic Simulations. *ApJs*, 264(1), 10. doi: 10.3847/1538-4365/ac9b1d
- Kissmann, R. (2014, March). PICARD : A novel code for the Galactic Cosmic Ray propagation problem. *Astroparticle Physics*, 55, 37-50. doi: 10.1016/j.astropartphys.2014.02.002
- Kolmogorov, A. (1941, January). The Local Structure of Turbulence in Incompressible Viscous Fluid for Very Large Reynolds' Numbers. *Akademiia Nauk SSSR Doklady*, 30, 301-305.
- Kraichnan, R. H. (1965, July). Inertial-Range Spectrum of Hydromagnetic Turbulence. *Physics of Fluids*, 8(7), 1385-1387. doi: 10.1063/1.1761412
- Krüger, H., Strub, P., Grün, E., & Sterken, V. J. (2015, October). Sixteen Years of Ulysses Interstellar Dust Measurements in the Solar System. I. Mass Distribution and Gas-to-dust Mass Ratio. *ApJ*, 812(2), 139. doi: 10.1088/0004-637X/812/2/139
- Krymskii, G. F. (1977, June). A regular mechanism for the acceleration of charged particles on the front of a shock wave. *Akademiia Nauk SSSR Doklady*, 234, 1306-1308.
- Kulsrud, R., & Pearce, W. P. (1969, May). The Effect of Wave-Particle Interactions on the Propagation of Cosmic Rays. *ApJ*, 156, 445. doi: 10.1086/149981
- Kulsrud, R. M. (2005). *Plasma Physics for Astrophysics*.
- Kulsrud, R. M., & Cesarsky, C. J. (1971, March). The Effectiveness of Instabilities for the Confinement of High Energy Cosmic Rays in the Galactic Disk. *Astrophys. Letters*, 8, 189.
- Lagage, P. O., & Cesarsky, C. J. (1983, September). The maximum energy of cosmic rays accelerated by supernova shocks. *A&A*, 125, 249-257.
- Lallement, R., Babusiaux, C., Vergely, J. L., Katz, D., Arenou, F., Valette, B., ... Capitanio, L. (2019, May). VizieR Online Data Catalog : Galactic interstellar dust Gaia-2MASS 3D maps (Lallement+, 2019). *VizieR Online Data Catalog*, J/A+A/625/A135. doi: 10.26093/cds/vizieR.36250135
- Lazarian, A. (2016, December). Damping of Alfvén Waves by Turbulence and Its Conse-

- quences : From Cosmic-ray Streaming to Launching Winds. *ApJ*, 833(2), 131. doi: 10.3847/1538-4357/833/2/131
- Leike, R. H., Glatzle, M., & Enßlin, T. A. (2020, July). Resolving nearby dust clouds. *A&A*, 639, A138. doi: 10.1051/0004-6361/202038169
- Lingenfelter, R. E. (2018, November). Cosmic rays from supernova remnants and superbubbles. *Advances in Space Research*, 62(10), 2750-2763. doi: 10.1016/j.asr.2017.04.006
- Lipari, P. (2019, February). Spectral shapes of the fluxes of electrons and positrons and the average residence time of cosmic rays in the Galaxy. *Physical Review D*, 99(4), 043005. doi: 10.1103/PhysRevD.99.043005
- Liszt, H., Gerin, M., & Grenier, I. (2019, July). Standing in the shadow of dark gas : ALMA observations of absorption from dark CO in the molecular dark neutral medium of Chamaeleon. *A&A*, 627, A95. doi: 10.1051/0004-6361/201935436
- López-Coto, R., Parsons, R. D., Hinton, J. A., & Giacinti, G. (2018, December). Undiscovered Pulsar in the Local Bubble as an Explanation of the Local High Energy Cosmic Ray All-Electron Spectrum. *Physical Review Letters*, 121(25), 251106. doi: 10.1103/PhysRevLett.121.251106
- Lorimer, D. R., Faulkner, A. J., Lyne, A. G., Manchester, R. N., Kramer, M., McLaughlin, M. A., ... Crawford, F. (2006, October). The Parkes Multibeam Pulsar Survey - VI. Discovery and timing of 142 pulsars and a Galactic population analysis. , 372(2), 777-800. doi: 10.1111/j.1365-2966.2006.10887.x
- Luo, Q., Feng, J., & Tam, P.-H. T. (2023, March). Explaining the Hardening Structures of Helium Spectrum and Boron to Carbon Ratio through Different Propagation Models. *Galaxies*, 11(2), 43. doi: 10.3390/galaxies11020043
- magazine. (1928, July). Popular science monthly. In (Vol. 113(1), p. 13). Popular Science Publishing, New York.
- Maurin, D., Donato, F., Taillet, R., & Salati, P. (2001, July). Cosmic Rays below $Z=30$ in a Diffusion Model : New Constraints on Propagation Parameters. *ApJ*, 555(2), 585-596. doi: 10.1086/321496
- Mazziotta, M. N., Cerutti, F., Ferrari, A., Gaggero, D., Loparco, F., & Sala, P. R. (2016, August). Production of secondary particles and nuclei in cosmic rays collisions with the interstellar gas using the FLUKA code. *Astroparticle Physics*, 81, 21-38. doi: 10.1016/j.astropartphys.2016.04.005
- Mori, M. (2009, June). Nuclear enhancement factor in calculation of Galactic diffuse gamma-rays : A new estimate with DPMJET-3. *Astroparticle Physics*, 31(5), 341-343. doi: 10.1016/j.astropartphys.2009.03.004
- Mozer, F. S., & Pritchett, P. L. (2010, January). Magnetic field reconnection : A first-principles perspective. *Physics Today*, 63(6), 34. doi: 10.1063/1.3455250
- Murphy, R., & Supertiger Collaboration. (2016, March). Abundances of Ultra-Heavy Galactic Cosmic Rays from the SuperTIGER Instrument. In *Aps april meeting abstracts* (Vol. 2016, p. S13.003).
- Murray, C. E., Stanimirović, S., Goss, W. M., Dickey, J. M., Heiles, C., Lindner, R. R., ... Hennebelle, P. (2015, May). The 21-SPONGE HI Absorption Survey I : Techniques and Initial Results. *ApJ*, 804(2), 89. doi: 10.1088/0004-637X/804/2/89
- Murray, C. E., Stanimirović, S., Goss, W. M., Heiles, C., Dickey, J. M., Babler, B., & Kim, C.-

- G. (2018, October). The 21-SPONGE H I Absorption Line Survey. I. The Temperature of Galactic H I. *ApJs*, 238(2), 14. doi: 10.3847/1538-4365/aad81a
- Neyman, J., & Pearson, E. S. (1933, January). On the Problem of the Most Efficient Tests of Statistical Hypotheses. *Philosophical Transactions of the Royal Society of London Series A*, 231, 289-337. doi: 10.1098/rsta.1933.0009
- Nguyen, H., Dawson, J. R., Miville-Deschênes, M. A., Tang, N., Li, D., Heiles, C., ... Finger, R. (2018, July). Dust-Gas Scaling Relations and OH Abundance in the Galactic ISM. *ApJ*, 862(1), 49. doi: 10.3847/1538-4357/aac82b
- Nuñez-Castiñeyra, A., Grenier, I. A., Bournaud, F., Dubois, Y., Kamal Youssef, F. R., & Hennebelle, P. (2022, May). Cosmic-ray diffusion and the multi-phase interstellar medium in a dwarf galaxy. I. Large-scale properties and γ -ray luminosities. *arXiv e-prints*, arXiv :2205.08163. doi: 10.48550/arXiv.2205.08163
- Ohira, Y., & Ioka, K. (2011, March). Cosmic-ray Helium Hardening. *ApJ Letters*, 729(1), L13. doi: 10.1088/2041-8205/729/1/L13
- Orlando, E., & Strong, A. (2013, December). Galactic synchrotron emission with cosmic ray propagation models. *MNRAS*, 436(3), 2127-2142. doi: 10.1093/mnras/stt1718
- Panov, A. D., Adams, J. H., Ahn, H. S., Bashinzhagyan, G. L., Watts, J. W., Wefel, J. P., ... Fazely, A. R. (2009, June). Energy spectra of abundant nuclei of primary cosmic rays from the data of ATIC-2 experiment : Final results. *Bulletin of the Russian Academy of Sciences, Physics*, 73(5), 564-567. doi: 10.3103/S1062873809050098
- Parizot, E. (2014, November). Cosmic Ray Origin : Lessons from Ultra-High-Energy Cosmic Rays and the Galactic/Extragalactic Transition. *Nuclear Physics B Proceedings Supplements*, 256, 197-212. doi: 10.1016/j.nuclphysbps.2014.10.023
- Parker, E. N. (1965, January). The passage of energetic charged particles through interplanetary space. *Planetary and Space Science*, 13(1), 9-49. doi: 10.1016/0032-0633(65)90131-5
- Pineda, J. L., Langer, W. D., Velusamy, T., & Goldsmith, P. F. (2013, June). A Herschel [C ii] Galactic plane survey. I. The global distribution of ISM gas components. , 554, A103. doi: 10.1051/0004-6361/201321188
- Planck Collaboration, Abergel, A., Ade, P. A. R., Aghanim, N., Alves, M. I. R., Aniano, G., ... Zonca, A. (2014, November). Planck 2013 results. XI. All-sky model of thermal dust emission. *A&A*, 571, A11. doi: 10.1051/0004-6361/201323195
- Planck Collaboration, Ade, P. A. R., Aghanim, N., Alina, D., Alves, M. I. R., Armitage-Caplan, C., ... Zonca, A. (2015, April). Planck intermediate results. XIX. An overview of the polarized thermal emission from Galactic dust. *A&A*, 576, A104. doi: 10.1051/0004-6361/201424082
- Planck Collaboration, Ade, P. A. R., Aghanim, N., Arnaud, M., Ashdown, M., Aumont, J., ... Zonca, A. (2011, December). Planck early results. XIX. All-sky temperature and dust optical depth from Planck and IRAS. Constraints on the “dark gas” in our Galaxy. *A&A*, 536, A19. doi: 10.1051/0004-6361/201116479
- Planck Collaboration, Fermi Collaboration, Ade, P. A. R., Aghanim, N., Aniano, G., Arnaud, M., ... Zonca, A. (2015, October). Planck intermediate results. XXVIII. Interstellar gas and dust in the Chamaeleon clouds as seen by Fermi LAT and Planck. *A&A*, 582, A31. doi: 10.1051/0004-6361/201424955
- Porter, T. A., Jóhannesson, G., & Moskalenko, I. V. (2022, September). The GALPROP

- Cosmic-ray Propagation and Nonthermal Emissions Framework : Release v57. *ApJ Supp.*, 262(1), 30. doi: 10.3847/1538-4365/ac80f6
- Pothead, M., Gaggero, D., Storm, E., & Weniger, C. (2018, October). On the progressive hardening of the cosmic-ray proton spectrum in the inner Galaxy. , 2018(10), 045. doi: 10.1088/1475-7516/2018/10/045
- Priest, E., & Forbes, T. (2000, January). *Magnetic reconnection : MHD theory and applications*.
- Ptuskin, V. (2012, December). Propagation of galactic cosmic rays. *Astroparticle Physics*, 39, 44-51. doi: 10.1016/j.astropartphys.2011.11.004
- Ptuskin, V., Zirakashvili, V., & Seo, E.-S. (2010, July). Spectrum of Galactic Cosmic Rays Accelerated in Supernova Remnants. *ApJ*, 718(1), 31-36. doi: 10.1088/0004-637X/718/1/31
- Recchia, S., Blasi, P., & Morlino, G. (2016, October). On the radial distribution of Galactic cosmic rays. *MNRAS*, 462(1), L88-L92. doi: 10.1093/mnras/slw136
- Recchia, S., & Gabici, S. (2018, February). Non-linear acceleration at supernova remnant shocks and the hardening in the cosmic ray spectrum. *MNRAS*, 474(1), L42-L46. doi: 10.1093/mnras/slx191
- Recchia, S., Gabici, S., Aharonian, F. A., & Vink, J. (2019, May). Local fading accelerator and the origin of TeV cosmic ray electrons. *Physical Review D*, 99(10), 103022. doi: 10.1103/PhysRevD.99.103022
- Remazeilles, M., Dickinson, C., Banday, A. J., Bigot-Sazy, M. A., & Ghosh, T. (2015, August). An improved source-subtracted and destriped 408-MHz all-sky map. *MNRAS*, 451(4), 4311-4327. doi: 10.1093/mnras/stv1274
- Remy, Q., Grenier, I. A., Marshall, D. J., & Casandjian, J. M. (2017a, May). Cosmic rays, gas and dust in nearby anticentre clouds. I. CO-to-H₂ conversion factors and dust opacities. *A&A*, 601, A78. doi: 10.1051/0004-6361/201629632
- Remy, Q., Grenier, I. A., Marshall, D. J., & Casandjian, J. M. (2017b, May). Cosmic rays, gas and dust in nearby anticentre clouds. I. CO-to-H₂ conversion factors and dust opacities. *A&A*, 601, A78. doi: 10.1051/0004-6361/201629632
- Remy, Q., Grenier, I. A., Marshall, D. J., & Casandjian, J. M. (2018, March). Cosmic-rays, gas, and dust in nearby anticentre clouds. II. Interstellar phase transitions and the dark neutral medium. *A&A*, 611, A51. doi: 10.1051/0004-6361/201730797
- Schlickeiser, R. (2002). *Cosmic Ray Astrophysics*.
- Schlickeiser, R., Caglar, M., & Lazarian, A. (2016, June). Cosmic Rays and MHD Turbulence Generation in Interstellar Giant Molecular Clouds. *ApJ*, 824(2), 89. doi: 10.3847/0004-637X/824/2/89
- Schlickeiser, R., Webber, W. R., & Kempf, A. (2014, May). Explanation of the Local Galactic Cosmic Ray Energy Spectra Measured by Voyager 1. I. Protons. *ApJ*, 787(1), 35. doi: 10.1088/0004-637X/787/1/35
- Skalidis, R., & Tassis, K. (2021, March). High-accuracy estimation of magnetic field strength in the interstellar medium from dust polarization. *A&A*, 647, A186. doi: 10.1051/0004-6361/202039779
- Sofue, Y., Nakanishi, H., & Ichiki, K. (2019, May). Magnetic field and ISM in the local Galactic disc. , 485(1), 924-933. doi: 10.1093/mnras/stz407

- Sokoloff, D. D., Bykov, A. A., Shukurov, A., Berkhuijsen, E. M., Beck, R., & Poezd, A. D. (1998, August). Depolarization and Faraday effects in galaxies. *MNRAS*, 299(1), 189-206. doi: 10.1046/j.1365-8711.1998.01782.x
- Soler, R., Terradas, J., Oliver, R., & Ballester, J. L. (2016, July). The role of Alfvén wave heating in solar prominences. *A&A*, 592, A28. doi: 10.1051/0004-6361/201628722
- Starck, J. L., & Pierre, M. (1998, March). Structure detection in low intensity X-ray images. *A&AS*, 128, 397-407. doi: 10.1051/aas:1998150
- Stecker, F. W., & Jones, F. C. (1977, November). The galactic halo question : new size constraints from galactic gamma -ray data. , 217, 843-851. doi: 10.1086/155631
- Stone, E. C., Cummings, A. C., McDonald, F. B., Heikkila, B. C., Lal, N., & Webber, W. R. (2013, July). Voyager 1 Observes Low-Energy Galactic Cosmic Rays in a Region Depleted of Heliospheric Ions. *Science*, 341(6142), 150-153. doi: 10.1126/science.1236408
- Stone, E. C., Frandsen, A. M., Mewaldt, R. A., Christian, E. R., Margolies, D., Ormes, J. F., & Snow, F. (1998, July). The Advanced Composition Explorer. , 86, 1-22. doi: 10.1023/A:1005082526237
- Strong, A., Porter, T., Digel, S., Jóhannesson, G., Martin, P., Moskalenko, I., ... Orlando, E. (2010). Global cosmic-ray-related luminosity and energy budget of the milky way. *The Astrophysical Journal Letters*, 722(1), L58.
- Strong, A. W., & Mattox, J. R. (1996, April). Gradient model analysis of EGRET diffuse Galactic γ -ray emission. , 308, L21-L24.
- Strong, A. W., & Moskalenko, I. V. (1998, December). Propagation of Cosmic-Ray Nucleons in the Galaxy. *ApJ*, 509(1), 212-228. doi: 10.1086/306470
- Strong, A. W., Moskalenko, I. V., & Ptuskin, V. S. (2007, November). Cosmic-Ray Propagation and Interactions in the Galaxy. *Annual Review of Nuclear and Particle Science*, 57(1), 285-327. doi: 10.1146/annurev.nucl.57.090506.123011
- Strong, A. W., Orlando, E., & Jaffe, T. R. (2011, October). The interstellar cosmic-ray electron spectrum from synchrotron radiation and direct measurements. *A&A*, 534, A54. doi: 10.1051/0004-6361/201116828
- Tibaldo, L., Digel, S. W., Casandjian, J. M., Franckowiak, A., Grenier, I. A., Jóhannesson, G., ... Strong, A. W. (2015, July). Fermi-LAT Observations of High- and Intermediate-velocity Clouds : Tracing Cosmic Rays in the Halo of the Milky Way. *ApJ*, 807(2), 161. doi: 10.1088/0004-637X/807/2/161
- Tielens, A. G. G. M. (2010). *The Physics and Chemistry of the Interstellar Medium*.
- Tomassetti, N. (2012, June). Origin of the Cosmic-Ray Spectral Hardening. *ApJ Letters*, 752(1), L13. doi: 10.1088/2041-8205/752/1/L13
- van de Hulst, H. C., Muller, C. A., & Oort, J. H. (1954, May). The spiral structure of the outer part of the Galactic System derived from the hydrogen emission at 21 cm wavelength. *Bulletin of the Astronomical Institutes of the Netherlands*, 12, 117.
- Volk, H. J., & McKenzie, J. F. (1981, January). Characteristics of cosmic ray shocks in the presence of wave dissipation. In *International cosmic ray conference* (Vol. 9, p. 246-249).
- Vranjes, J., & Krstic, P. S. (2013, June). Collisions, magnetization, and transport coefficients in the lower solar atmosphere. *A&A*, 554, A22. doi: 10.1051/0004-6361/201220738
- Walsh, N., Binns, W., Israel, M., Murphy, R., Rauch, B. F., Ward, J., ... Waddington, C. J.

- (2019, July). SuperTIGER Abundances of Galactic Cosmic-Rays for the Charge Interval $Z=41-56$. In *36th international cosmic ray conference (icrc2019)* (Vol. 36, p. 147). doi: 10.22323/1.358.0147
- Webber, W. R., Lee, M. A., & Gupta, M. (1992, May). Propagation of Cosmic-Ray Nuclei in a Diffusing Galaxy with Convective Halo and Thin Matter Disk. *ApJ*, 390, 96. doi: 10.1086/171262
- Weinrich, N., Boudaud, M., Derome, L., Génolini, Y., Lavalle, J., Maurin, D., ... Weymann-Despres, G. (2020, July). Galactic halo size in the light of recent AMS-02 data. *A&A*, 639, A74. doi: 10.1051/0004-6361/202038064
- Westerhout, G. (1957, May). The distribution of atomic hydrogen in the outer parts of the Galactic System. *Bulletin of the Astronomical Institutes of the Netherlands*, 13, 201.
- Wielebinski, R. (2005). Magnetic Fields in the Milky Way, Derived from Radio Continuum Observations and Faraday Rotation Studies. In R. Wielebinski & R. Beck (Eds.), *Cosmic magnetic fields* (Vol. 664, p. 89). doi: 10.1007/3540313966_5
- Wilks, S. S. (1938). The Large-Sample Distribution of the Likelihood Ratio for Testing Composite Hypotheses. *The Annals of Mathematical Statistics*, 9(1), 60 – 62. Retrieved from <https://doi.org/10.1214/aoms/1177732360> doi: 10.1214/aoms/1177732360
- Wolfire, M. G., Hollenbach, D., & McKee, C. F. (2010, June). The Dark Molecular Gas. *ApJ*, 716(2), 1191-1207. doi: 10.1088/0004-637X/716/2/1191
- Wolfire, M. G., Hollenbach, D., McKee, C. F., Tielens, A. G. G. M., & Bakes, E. L. O. (1995, April). The Neutral Atomic Phases of the Interstellar Medium. *ApJ*, 443, 152. doi: 10.1086/175510
- Xu, J., & Han, J. L. (2019, July). Magnetic fields in the solar vicinity and in the Galactic halo. *MNRAS*, 486(3), 4275-4289. doi: 10.1093/mnras/stz1060
- Xu, S., & Lazarian, A. (2022, March). Cosmic Ray Streaming in the Turbulent Interstellar Medium. *ApJ*, 927(1), 94. doi: 10.3847/1538-4357/ac4dfd
- Yamamoto, A. (2003, January). BESS-Polar Long Duration Balloon Flights at Antarctica to Search for Primordial Antiparticle. *Progress of Theoretical Physics Supplement*, 151, 240-245. doi: 10.1143/PTPS.151.240
- Yan, H., & Lazarian, A. (2002, December). Scattering of Cosmic Rays by Magnetohydrodynamic Interstellar Turbulence. *Phys. Rev. Letters*, 89(28), 281102. doi: 10.1103/PhysRevLett.89.281102
- Yang, R., Aharonian, F., & Evoli, C. (2016, June). Radial distribution of the diffuse γ -ray emissivity in the Galactic disk. , 93(12), 123007. doi: 10.1103/PhysRevD.93.123007
- Yang, R.-z., Jones, D. I., & Aharonian, F. (2015, August). Fermi-LAT observations of the Sagittarius B complex. , 580, A90. doi: 10.1051/0004-6361/201425233
- Yoon, Y. S., Anderson, T., Barrau, A., Conklin, N. B., Coutu, S., Derome, L., ... Wu, J. (2017, April). Proton and Helium Spectra from the CREAM-III Flight. *ApJ*, 839(1), 5. doi: 10.3847/1538-4357/aa68e4
- Yoshida, T., Yamamoto, A., Mitchell, J., Abe, K., Fuke, H., Haino, S., ... Yoshimura, K. (2004, January). BESS-polar experiment. *Advances in Space Research*, 33(10), 1755-1762. doi: 10.1016/j.asr.2003.05.017
- Yuan, Q., Zhang, B., & Bi, X.-J. (2011, August). Cosmic ray spectral hardening due to dispersion in the source injection spectra. *Physical Review D*, 84(4), 043002. doi:

10.1103/PhysRevD.84.043002

- Yusef-Zadeh, F., Arendt, R. G., Wardle, M., Heywood, I., Cotton, W., & Camilo, F. (2022, February). Statistical Properties of the Population of the Galactic Center Filaments : the Spectral Index and Equipartition Magnetic Field. , *925*(2), L18. doi: 10.3847/2041-8213/ac4802
- Yusef-Zadeh, F., Wardle, M., Arendt, R., Hewitt, J., Hu, Y., Lazarian, A., . . . Heywood, I. (2024, January). Detection of large-scale synchrotron radiation from the molecular envelope of the Sgr B cloud complex at the Galactic centre. , *527*(1), 1275-1282. doi: 10.1093/mnras/stad3203
- Zatsepin, V. I., & Sokolskaya, N. V. (2006, October). Three component model of cosmic ray spectra from 10 GeV to 100 PeV. *A&A*, *458*(1), 1-5. doi: 10.1051/0004-6361:20065108
- Zirnstein, E. J., Heerikhuisen, J., Funsten, H. O., Livadiotis, G., McComas, D. J., & Pogorelov, N. V. (2016, February). Local Interstellar Magnetic Field Determined from the Interstellar Boundary Explorer Ribbon. *ApJ Letters*, *818*(1), L18. doi: 10.3847/2041-8205/818/1/L18
- Zweibel, E. G. (2013, May). The microphysics and macrophysics of cosmic rays. *Physics of Plasmas*, *20*(5), 055501. doi: 10.1063/1.4807033
- Zweibel, E. G. (2017, May). The basis for cosmic ray feedback : Written on the wind. *Physics of Plasmas*, *24*(5), 055402. doi: 10.1063/1.4984017

